MICROCRYSTALLINE SILICON SOLAR CELLS: THEORY, DIAGNOSIS AND STABILITY

Thèse présentée à la Faculté des Sciences
Institut de Microtechnique
Université de Neuchâtel

Pour l'obtention du grade de docteur ès sciences

Par

Fanny Sculati-Meillaud

Acceptée sur proposition du jury :
Prof. A. Shah, directeur de thèse,
Prof. C. Ballif, rapporteur,
Prof. ass. E. Vallat-Sauvain, rapporteur
Prof. M. C. Lux-Steiner, rapporteur
Prof. A. N. Tiwari, rapporteur
Dr. M. Vanecek, rapporteur

Soutenue le 10 juillet 2006
Université de Neuchâtel

2006

Université de Neuchâtel unine

FACULTE DES SCIENCES
Secrétariat-Décanat de la faculté
- Rue Emile-Argand 11
- CP 158
- CH-2009 Neuchâtel

IMPRIMATUR POUR LA THESE

Microcrystalline silicon solar cells : theory, diagnosis and stability

Fanny SCULATI-MEILLAUD

UNIVERSITE DE NEUCHATEL

FACULTE DES SCIENCES

La Faculté des sciences de l'Université de Neuchâtel,
sur le rapport des membres du jury

Mmes E. Vallat-Sauvain, M.C. Lux-Steiner (Berlin, D),
MM. A. Shah (directeur de thèse), C. Ballif,
A.N. Tiwari (ETH Zürich) et M. Vanecek (Prague CZ)

autorise l'impression de la présente thèse.

Neuchâtel, le 27 novembre 2006

Le doyen :

J.-P. Derendinger

UNIVERSITE DE NEUCHATEL
FACULTE DES SCIENCES
Secrétariat-décanat de la faculté
Rue Emile-Argand 11 - CP 158
CH-2009 Neuchâtel

■ Téléphone : +41 32 718 21 00 ■ Fax : +41 32 718 21 03 ■ E-mail : secretariat.sciences@unine.ch ■ www.unine.ch/sciences

Table of contents

1. Introduction 1
1.1 Motivation 1
1.2 Amorphous silicon (a-Si:H) 2
1.3 Microcrystalline silicon (µc-Si:H) 6
1.4 Outline of the thesis 7
2. Characterization techniques 9
2.1 Current density -voltage J(V) measurement 9
2.2 External quantum efficiency measurement 10
2.3 Micro-Raman spectroscopy 11
2.4 Fourier-Transform Photocurrent Spectroscopy (FTPS) 13
3. Theoretical limits for the main parameters of single-junction and tandem solar cells as a function of bandgap energy 17
3.1 Introduction 17
3.2 Pn junction 18
3.2.1 Ideal pn junction 18
3.2.2 Theoretical limits for the pn junction 21
3.2.3 Semi-experimental limits for pn junction 26
3.3 Pin junction 26
3.4. Single-junction solar cell 26
3.4.1 Limit for short-circuit current density J_{sc} 27
3.4.2 Limits for open-circuit voltage V_{oc}, fill factor FF and efficiency η 28
3.5 Tandem solar cell 35
3.6 Conclusions 39
3.6.1 Single-junction solar cells 39
3.6.2 Tandem solar cells 39
4. Diagnosis of thin-film microcrystalline silicon solar cells 41
4.1 Introduction 41
4.2 Variable Illumination Measurements (VIM) 42

4.2.1 Theory (pn/pin junctions) 42
4.2.2 Effects of recombination current density (J_{rec}), shunt resistance (R_{sh}) and defect-related absorption (α(0.8 eV)) on fill factor (FF) losses 48
4.2 Dark J(V) 54
4.2.1. a-Si:H 54
4.2.2. μc-Si:H 54
4.2.3 Dark J(V) measurements 54
4.3 Effect of i-layer thickness on the $\mu^0\tau^0$-product of solar cells and individual i-layers 55
4.3.1 Introduction 55
4.3.2 a-Si:H and μc-Si:H layers..56
4.3.3 a-Si:H and μc-Si:H cells...58
4.4 Variable gas flow series 62
4.4.1 Samples 62
4.4.2 VIM measurements 63
4.5 Pin and nip dilution series: light-soaking...66
4.5.1 Samples 66
4.5.2 VIM measurements 67
4.5.3 FTPS measurements 68
4.5.4 Dark J(V) measurements 69
4.6 Solar cells with low shunt resistance 72
4.6.1 Samples 72
4.6.2 VIM measurements 72
4.7 Conclusions...73
5. Light-induced degradation of thin-film microcrystalline...... silicon (μc-Si:H) solar cells 77
5.1 Introduction...77
5.2 Light-induced degradation: observations and models......................78
5.2.1 Observations...78
5.2.2 Models (from a-Si:H) 80
5.3 Samples 81
5.4 Light-soaking and annealing conditions, characterization techniques 83

5.5 Initial parameters of the solar cells 84

5.6 Light-induced degradation kinetics 86

5.7 Light-induced degradation as a function of crystallinity 88

5.7.1 Electrical parameters 88
5.7.2 Shunt resistance and collection voltage 94
5.7.3 Defect-related absorption 97

5.8 Defect annealing 100

5.8.1 Electrical parameters 100
5.8.2 Defect-related absorption 100

5.9 Annealing kinetics 102

5.10 Model for light-induced defect creation and annealing in μc-Si:H solar cells 106

6. Proton-induced degradation of thin-film microcrystalline silicon (μc-Si:H) solar cells 111

6.1 Introduction 111

6.2 Proton irradiation: observations and models 112

6.2.1. Observations 112
6.2.2 Models 115

6.3 Samples 116

6.4 Irradiation and annealing conditions, characterization techniques 116

6.5 High-energy proton irradiation 119

6.5.1 Proton-induced degradation 119
6.5.2 Defect Annealing 129
6.5.3 Model for high-energy proton defect creation and annealing in μc-Si:H 133

6.6 Low-energy proton irradiation 133

6.6.1 Proton degradation as a function of crystallinity 133
6.6.2 Defect annealing 142
6.6.3 Model for low-energy proton defect creation and annealing in μc-Si:H 144

6.7 Comparison of light-induced and proton-induced degradation in μc-Si:H solar cells 145

6.8 Conclusions..147
7. Final Conclusions... 151
References... 155
Acknowledgements 159
Annexe 1 161

Keywords:

Thin-film solar cells, microcrystalline silicon, characterization techniques, light-induced degradation, proton-induced degradation, defect density

Summary:

This thesis is focused on microcrystalline silicon solar cells deposited by Very High Frequency Plasma Enhanced Chemical Vapor Deposition (VHF PE-CVD) technique. Microcrystalline silicon is a mixed material, composed of an amorphous phase and of nanocrystalline grains: it exhibits a wide range of microstructures depending on both the deposition conditions and the substrate material. Various characterization techniques were used in this work as diagnostic tools for defective solar cells, in our case solar cells presenting low fill factor values (FF).

A collection model, originally developed for amorphous silicon solar cells, has been adapted to microcrystalline silicon solar cells, and the empirical relationships established were compared to actual measurements on various solar cells (dilution series, gas series and individual solar cells). An excellent correspondence between the predictions and the measurements was thus shown, validating the capacity of the tools employed in this work for solar cells diagnosis. In addition, an original model has been developed for the calculation of the upper limits for the electrical parameters of pin junctions, as a function of the material's bandgap. We thus demonstrated that large gains in short-circuit current density were still possible with microcrystalline silicon solar cells.

Then, the stability of microcrystalline silicon solar cells under light-soaking and proton irradiation was investigated by means of electrical, as well as sub-bandgap absorption measurements. Amorphous silicon thin-film solar cells are known to suffer from the Staebler-Wronski effect, which consists of a degradation of the electrical parameters under illumination. This effect is completely reversible under thermal annealing but it represents, nevertheless, a limiting factor regarding the use of amorphous silicon in solar cells. The stability of microcrystalline silicon solar cells, that are partly composed of amorphous silicon, was, thus, of very high interest: we showed that microcrystalline silicon solar cells degrade, albeit in a "softer" and slower way than amorphous silicon solar cells. We observed that the amplitude of the light-induced degradation is a function of the crystallinity of the sample: cells with a medium crystallinity (which are, with respect to conversion efficiency, the optimum cells) present a relative efficiency reduction in the order of 5%.

Finally, the stability of μc-Si:H solar cells under high-energy and low-energy proton irradiation was also studied: here, we showed that microcrystalline silicon solar cells degrade and recover differently depending on the energy of the proton

radiation. A simple model is proposed for light-induced and proton-induced degradation of microcrystalline silicon solar cells. In the case of light-soaking, we conclude that the defects are situated at the surface of the nanocrystals, whereas, in the case of protons irradiation, the defects are directly created within the nanocrystals.

Mots clés:

Cellules solaires en couche mince, silicium microcristallin, techniques de caractérisation, dégradation lumineuse, dégradation par protons, densité de défauts

Résumé:

Cette thèse traite des cellules solaires en silicium microcristallin déposées par la technique du dépôt chimique en phase vapeur assisté par plasma à très haute fréquence (Very High Frequency Plasma Enhanced Chemical Vapor Deposition, VHF PE-CVD). Le silicium microcristallin est un matériau composé d'une phase amorphe et de nanocristaux: différentes microstructures existent selon les conditions de fabrication et le type de matériau sur lequel la cellule solaire est déposée. Diverses techniques de caractérisation ont été employées dans ce travail comme outils de diagnostic pour des cellules solaires défectueuses, dans notre cas des cellules solaires présentant de basses valeurs du facteur de forme (FF).

Un modèle de collection, à l'origine développé pour les cellules solaire en silicium amorphe, a été adapté pour les cellules solaires en silicium microcristallin, et les relations établies de façon empirique ont été comparées aux mesures réalisées sur diverses cellules solaires (série en dilution, série à cristallinité constante et des cellules solaires individuelles) Une excellente adéquation entre les prédictions et les mesures a ainsi été démontrée, mettant en évidence le pouvoir des outils de diagnostic développés et employés dans ce travail. En outre, un modèle original a été développé pour le calcul des limites supérieures des paramètres électriques des jonctions pin, en fonction de la bande d'énergie interdite du matériau. Nous avons ainsi mis en évidence que de larges gains en courant étaient encore possibles avec les cellules solaires en silicium microcristallin.

Ensuite, la stabilité des cellules solaire en silicium microcristallin sous illumination et faisceau de protons a été étudiée au moyen de mesures électriques et optiques (absorption). Les cellules solaires en couche mince de silicium amorphe sont connues pour souffrir de l'effet de Staebler-Wronski, qui correspond à une dégradation des paramètres électriques sous illumination. Cet effet est entièrement réversible sous recuits thermiques mais il représente, néanmoins, un facteur limitant concernant l'utilisation du silicium amorphe pour les cellules solaires. La stabilité des cellules solaires en silicium microcristallin, qui se composent en partie de silicium amorphe, était ainsi un sujet de haute importance: nous avons montré que les cellules solaires microcristallines dégradent, mais de façon plus lente et moindre que celles en silicium amorphe. Nous avons observé que l'amplitude de la dégradation induite par la lumière dépend de la cristallinité de l'échantillon: les cellules solaires avec une cristallinité moyenne (qui présentent l'efficacité de

conversion la plus élevée) présentent une perte relative en efficacité de l'ordre de 5%.

Finalement, la stabilité des cellules solaires microcristallines sous irradiation de protons d’énergie haute et basse a également été étudiée: ici, nous avons prouvé que les cellules solaires en silicium microcristallin dégradent et récupèrent différemment selon l'énergie du faisceau de proton. Un modèle simple est proposé pour la dégradation des cellules solaires microcristallines, telle qu’induite par l’exposition à la lumière et aux protons de basse et haute énergie. Dans le cas de la dégradation lumineuse, nous concluons que les défauts créés se situent à la surface des nanocristaux, tandis que dans le cas de l’irradiation par protons les défauts sont créés à l’intérieur même des nanocristaux.

.

Table of symbols:

μc-Si:H	Hydrogenated microcrystalline silicon
a-Si:H	Hydrogenated amorphous silicon
c-Si	(Mono-)crystalline silicon
LPCVD	Low pressure chemical vapor deposition
PECVD	Plasma enhanced chemical vapor deposition
VHF	Very-high frequency
SiH_4	Silane
H_2	Hydrogen
SC	Silane concentration, i.e. the ratio of the silane flow over the total gas flow: SC = $[SiH_4]/[SiH_4]+[H_2]$
TCO	Transparent conductive oxide
ZnO	Zinc Oxide
J(V)	Current density-voltage measurement
EQE	External Quantum Efficiency measurement
CPM	Constant Photocurrent Method
PDS	Photothermal Deflection Spectroscopy
FTIR	Fourier-Transform Infrared Spectroscopy
FTPS	Fourier-Transform Photocurrent Spectroscopy
VIM	Variable Illumination measurement
J_{sc}	Short-circuit current density
V_{oc}	Open-circuit voltage
FF	Fill factor
η	Efficiency
α(0.8 eV)	Defect-related absorption (as measured at 0.8 eV)
E_0	Urbach parameter
ϕ_c	Raman crystallinity factor evaluated at a wavelength of 633 nm (or 514 nm)
X_c	Raman crystalline volume fraction

1. Introduction

1.1 Motivation

Solar energy can be divided into two categories: thermal energy and photovoltaic (PV) energy, which is the direct conversion of light into electricity. The history of photovoltaic energy started in 1839 when A.-E. Becquerel discovered the photovoltaic effect. In 1954, Chapin et al. announced the first "usable" solar cell, based on silicon, which had about 6% conversion efficiency [1]. Nowadays, PV market is largely dominated by the monocrystalline silicon (c-Si) and the polycrystalline silicon (poly-Si) technologies, that reach laboratory conversion efficiencies around 25%. However, thin-film silicon constitutes one of the most promising ways for low-cost photovoltaic solar cells and modules. Indeed, in silicon thin-film technology, only a very thin layer of silicon is used (the photoactive layer thickness is only about 1.5 µm). Compared to this, wafer-based technology (c-Si and poly-Si) requires silicon thicknesses of hundreds of micrometers.

Thus, even if research cells show current record conversion efficiencies only between 10 and 15%, thin-film technology implies a substantial potential for cost reduction due to cheap deposition processes, compatible with large area and mass production, as well as a large choice of rigid or flexible substrates (glass, metal, plastic, etc). In addition, silicon thin-film technology requires far less fabrication energy than wafer-based technology: the energy payback time of thin film silicon modules is, therefore, consequently reduced.

Thin-film silicon solar cells are either amorphous or microcrystalline. Hydrogenated microcrystalline silicon (µc-Si:H) was introduced in 1968 [2] and the first µc-Si:H solar cells were deposited in our group, at the Institute of Microtechnology of Neuchâtel (IMT), by J. Meier et al. in 1994 [3]. In the IMT laboratory, amorphous and microcrystalline silicon are deposited by very-high frequency (VHF) plasma enhanced chemical vapor deposition (PECVD), from a gas mixture of silane (SiH_4) and hydrogen (H_2). The microstructure of the resulting thin-film layers and solar cells strongly depends on the silane concentration (SC), wich is defined as the gas flow ratio $SC=[SiH_4]/[SiH_4+H_2]$ as used for deposition of the photoactive layer (intrinsic layer) [4-5]. At high SC, mostly amorphous material is fabricated, whereas a low SC (i.e. a high H_2 gas flow) leads to highly microcrystalline growth. The "transistion" from fully amorphous to microcrystalline growth is sharp: variation of silane concentration by 1% around the transistion leads to the occurrence of either amorphous or microcrystalline microstructure [6]

It was reported that single-junction µc-Si:H solar cells with the highest efficiencies are those deposited with silane concentration close to the

microcrystalline/amorphous transition [7]. Nowadays, μc-Si:H solar cells are fabricated in different laboratories, with electrical conversion efficiencies in the order of 9 to 10 % [8, 9]. The best μc-Si:H solar cells present fill factor values up to 74% [9]; such values are very close to the theoretical upper limit we will establish in Chapter 3 for the pin diodes. Nevertheless, for a long time, fill factor values were limited to values up to 70%. The chapter 4 will, thus, treat in detail the technological reasons that can actually limit the fill factor: high recombination in the intrinsic layer, low shunt resistance, as well as high series resistance are all the three hold responsible for those relatively low values of FF in single-junction microcristalline silicon solar cells.

The issue of whether microcrystalline silicon is stable under light-soaking is also a main part of the present thesis and an issue of high interst that will be treated in Chapter 5, whereas stability under high and low-energy proton irradiation will be considered in Chapter 6. Finally, all three types of degradation will be compared and simple models will be suggested for light-induced and proton-induced degradation mechanisms.

1.2 Amorphous silicon (a-Si:H)

Amorphous silicon (a-Si:H) is composed of silicon atoms which are spatially arranged on a lattice that presents only short range order (i.e. the lattice is not really random). Compared to crystalline silicon (c-Si), the average bond angles between neighboring atoms are distorted, as schematically shown in Fig. 1.1. Some bonds are even broken and result in so-called "dangling bonds". Nevertheless, the presence of hydrogen during the deposition of (hydrogenated) amorphous silicon leads to the passivation of a large part of these dangling bonds.

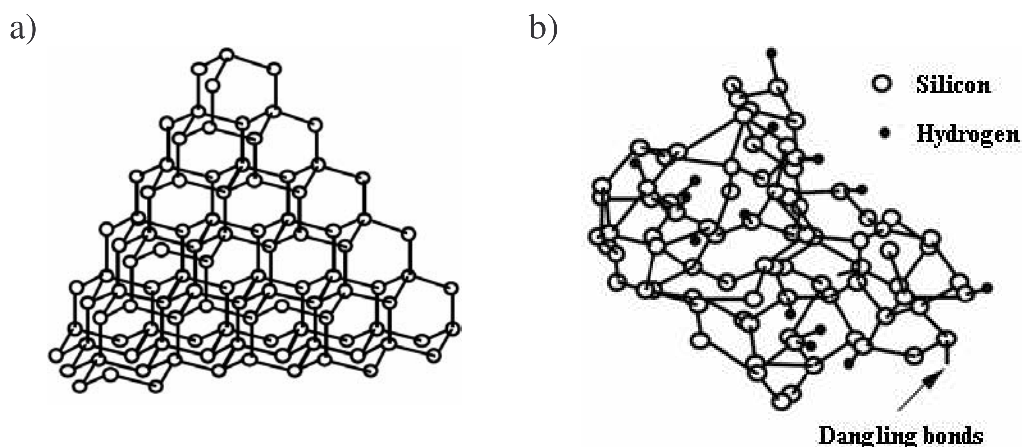

Figure 1.1. Lattice of (a) crystalline silicon (FCC, diamond-like lattice), (b) hydrogenated amorphous silicon, with Si-Si and Si-H bonds, as well as dangling bonds.

The two main deviations of the lattice of a-Si:H – bond distortion and dangling bonds – as compared to the translation invariant crystalline lattice of c-Si, lead to an electronic band structure with localized states within the (mobility) bandgap, see Fig. 1.2. The bond distortion results in bandtails near the valence and conduction bands: in these bandtails, the electrons' (or holes') wavefunctions are spatially localized and do not participate directly in the electronic transport. The (non-passivated) dangling bonds create deep, highly localized, electronic states near the middle of the bandgap. These defects, that act as the main recombination centers in a-Si:H, can either be positively charged (i.e. unoccupied, D^+), neutral (i.e. occupied by one electron, D^0) or negatively charged (i.e. occupied by two electrons, D^-). The dangling bonds act as recombination centers for the free electrons and holes, and lead to two recombination paths: one over D^0/D^- and one over D^+/D^0.

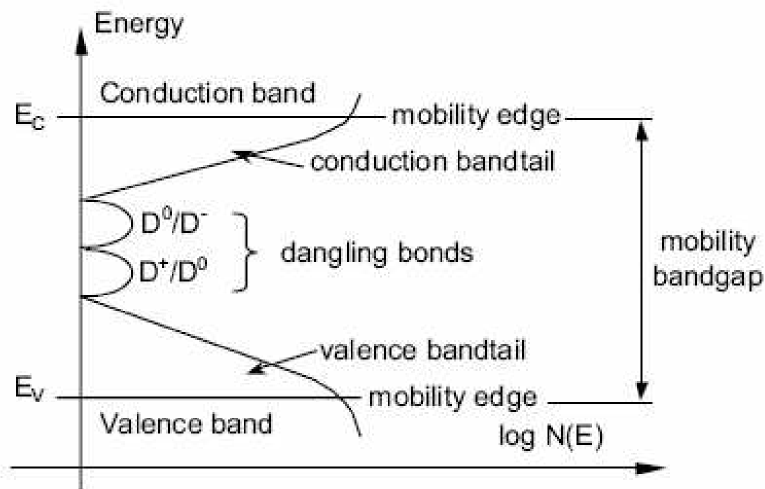

Figure 1.2. Density of states N(E) for intrinsic a-Si:H. Within the mobility bandgap (delimited by E_c and E_V), the states are localized (dangling bonds and bandtails).

Amorphous silicon (and microcrystalline silicon as well) is, thus, a very defective material with carriers' diffusion lengths so low that it must be used in pin (or nip) configuration. The pin (nip) configuration is composed of a p-doped layer, an intrinsic (i-) layer and a n-doped layer. The n and p layers are doped by adding, during the deposition process, phosophine (PH_3) or diborane (B_2H_6) to the silane gas. The thickness of the doped layers is in the order of 20-30 nm, whereas the thickness of the intrinsic layer is of 0.3 to 0.5 μm for a-Si:H, 1 to 2 μm for μc-Si:H.

The thin-film solar cell is then obtained by contacting the pin junction with a front transparent conductive oxide (TCO) and a back conductive contact (either a TCO layer and/or a metallic contact), as presented in Fig 1.3. Since the mobility of the electrons is larger than that of the holes in a-Si:H and μc-Si:H, light should always enter from the p-layer side: pin cells must, thus, be deposited on transparent substrates whereas nip cells can be deposited on opaque substrates, too.

The most often used transparent conductive oxide in IMT laboratory is Zinc

Oxide (ZnO), obtained by low-pressure chemical vapor deposition (LP-CVD) [10]. LP-CVD ZnO is a rough substrate and, thus, an effective light diffuser that enhances light-trapping within the solar cell. Another kind of TCO used in the samples presented in this thesis is sputtered-etched ZnO [8]. The roughness of the ZnO is, in this case, obtained by chemical etch of the (as deposited flat) sputtered ZnO.

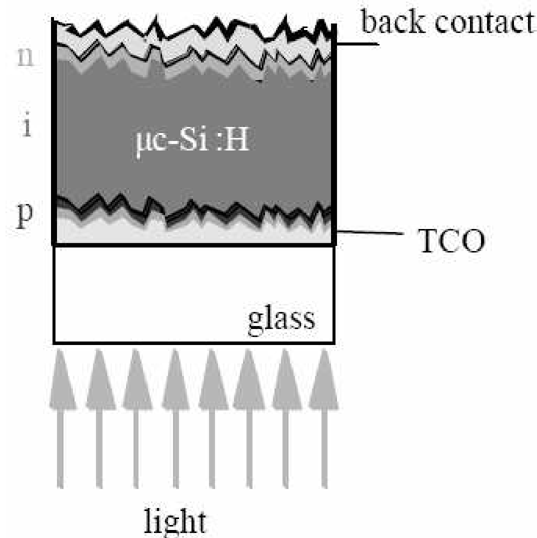

Figure 1.3. Scheme of a typical pin structure, as used for a-Si:H and μc-Si:H single-junction thin film solar cells. The front contact is a transparent conductive oxide (TCO); the back conductive contact is either a TCO layer and/or a metallic contact. In case of a nip structure, it is the n layer that is deposited on top of the substrate, here glass. In the nip configuration light enters the device from the top, last deposited, p-layer.

Due to low temperature PECVD deposition process (~200°C), various types of substrates can be used: rigid (such as glass) or flexible (such as diverse forms of plastics, included PET for example). The main deposition parameters used to obtain amorphous or microcrystalline silicon with the PECVD deposition technology are: (a) the plasma excitation frequency, (b) the power injected into the plasma, and (c) the silane concentration. Nevertheless, it should be mentioned that many other parameters, such as temperature, pressure, chamber and electrode geometries, or the substrate itself, can modify the amorphous/microcrystalline growth mode [11].

Transition from amorphous to microcrystalline silicon is obtained in the region of the deposition parameters' space where the plasma frequency or the power are high, or for low silane concentration (higher hydrogen content). A review of the VHF-PECVD technique for the deposition of a-Si:H and μc-Si:H solar cells is presented in [12].

Nowadays, the major drawback for commercial use of amorphous silicon is its degradation under light-soaking, called the Staebler-Wronski effect [13]. This

degradation effect will be discussed in detail in Chapter 5, in the case of µc-Si:H. Another weakness of present, commercially produced, a-Si:H thin film solar modules is their relatively low conversion efficiency, in the order of 6.5% [14]. In comparison, crystalline (c-Si) or polycrystalline (poly-Si) silicon modules show, in practice, values between 10% to 15% [15].

However, a-Si:H can be advantageously combined with µc-Si:H to form “micromorph” tandem solar cells. A "micromorph" tandem consists of a top (through which light enters first) a-Si:H cell, deposited on a bottom µc-Si:H cell. Compared to amorphous silicon, microcrystalline silicon absorbs light within a wider spectral range, as can be seen in Fig 1.4. This difference in the range of absorption of a-Si:H and µc-Si:H is due to different bandgap energy values E_g: the bandgap of a-Si:H is equal to 1.75 eV, while the bandgap of µc-Si:H is lower with 1.1 eV (similar to crystalline silicon (c-Si)).

Nevertheless, within its range of absorption, the absolute value of the absorption coefficient of a-Si:H (non-direct gap) is higher than that of µc-Si:H (indirect gap). Therefore, such a combination of materials takes advantage of a larger part of the solar spectrum (as compared to single-junction cells) and the tandem (double-junction) solar cell conversion efficiency is consequently increased, with up to 13.4% for mini-modules (910 x 455 mm^2), as demonstrated by Kaneka Corp. (initial efficiency, with interlayer) [16]. Kaneka Corp. also exhibits initial efficiencies up to 15.1% with triple-junction modules [16]. A part of Chapter 3 is focused on the theoretical treatment of such “micromorph” tandem with the establishment of an upper limit for the conversion efficiency.

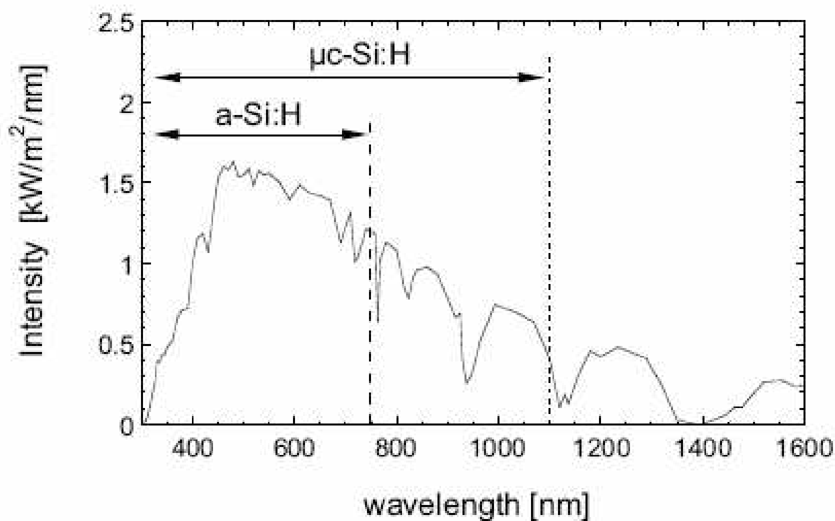

Figure 1.4. Spectral distribution of the AM 1.5 solar spectrum incident on the earth's surface. The spectral range absorbed by a-Si:H and µc-Si:H is indicated.

Chapters 2 and 4 describe experimental characterization techniques that allow one to investigate the origin of losses in the electrical parameters of actual defective devices.

1.3 Microcrystalline silicon (μc-Si:H)

Microcrystalline silicon is a complex material that is composed of crystalline and amorphous silicon phases, plus grain boundaries, see Fig. 1.5. We know, from previous studies by Transmission Electron Microscopy (TEM), that μc-Si:H exhibits a wide range of microstructure, depending on the silane concentration used for the deposition (a larger amount of hydrogen leads to a more crystalline material [6]), and the substrate roughness [11]. Grain boundaries between large conglomerates of nanocrystals, as well as the nanocrystals' surface itself, are source of defects, although the high content of hydrogen, as incorporated in the μc-Si:H material during its deposition, passivates most of the dangling bonds present [17]. In addition, cracks and voids have been observed, that may easily lead to electrical shunts with a consequent reduction in the fill factor of the solar cells. The effect of shunts on the fill factor will be quantified in Chapter 4.

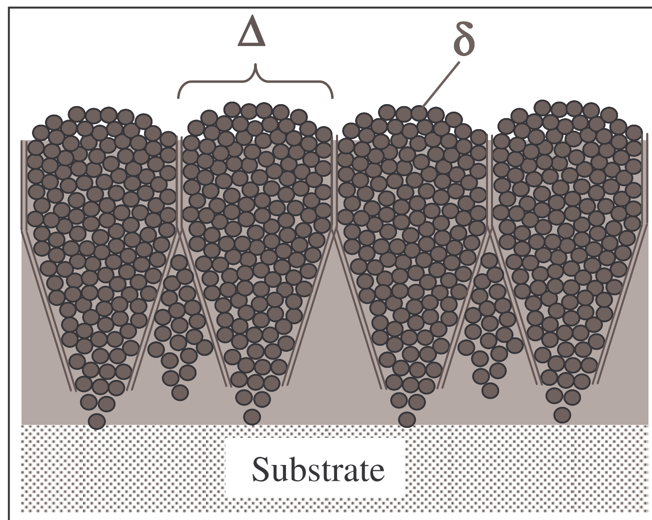

Figure 1.5 from [18] Scheme of a μc-Si:H layer microstructure: pencil-like conglomerates (Δ) formed by a multitude of nanocrystals (δ) (in black), plus voids represented by the narrow lines; in grey the amorphous phase.

It will be confirmed in the present thesis, that the solar cells with the highest efficiencies are those with a medium average crystallinity; i.e. in these cells, only half of the material's volume is crystalline, the rest is amorphous. Due to this rather high fraction of amorphous material, the question of whether these “best” cells are, or not, subject to light-induced degradation is of great importance. This issue will be treated in detail in Chapter 5, where we will demonstrate that μc-Si:H solar cells are indeed subject to light-induced degradation, but in a “softer” and slower way than a-Si:H solar cells. We will introduce a simple model where we suggest that light-induced defects are linked to the passivation of nanocrystals by the amorphous phase (i.e. linked to the grain boundaries as present inside the conglomerates). The degradation observed in μc-Si:H is completely reversible under thermal annealing, similarly to that in a-Si:H.

Due to its very complex microstructure, we don't have, as yet, a clear picture of the electronic density of states of μc-Si:H. Nevertheless, we expect the distribution of density of states to be very similar to that of a-Si:H, with a lower bandgap (1.1 eV) and narrower bandtails. In the present thesis, we will evaluate the defect density of the intrinsic layer of our μc-Si:H solar cells from sub-bandgap absorption measurements. Indeed, the absorption value at 0.8 eV (α(0.8 eV)) is assumed to be proportional to the defect density in the μc-Si:H intrinsic layer [19]. We will give further experimental evidences (see Chapters 5 and 6) that support this assumption.

1.4 Outline of the thesis

Besides this introduction chapter, the present thesis contains the following chapters:

- Chapter 2 summarizes the experimental techniques that were used to characterize the μc-Si:H solar cells used in this work: J(V) curves under AM 1.5 illumination and External quantum efficiency (EQE) measurements were used to evaluate the electrical device parameters. Micro-Raman spectroscopy was used for the evaluation of the amorphous and crystalline volume fractions (i.e. for the evaluation of the crystallinity) of the intrinsic layer in the μc-Si:H solar cells, and Fourier-Transform Photocurrent Spectroscopy (FTPS) was used to measure sub-bandgap absorption, which gives information about the defect density in the intrinsic layer.

- Chapter 3 concerns the theory of pn and pin junctions and the calculations of upper limits for the electrical parameters (J_{sc}, V_{oc}, FF, η) of single-junction solar cells, as a function of the material's bandgap energy. Three different models will be considered for the calculation of these limits, two based on the pn junction theory and experimental observations, and one original model established in this thesis for pin junctions. We will show that the largest gains still to be achieved regarding present μc-Si:H solar cells can be made on the short-circuit current density. The upper limits for conversion efficiency of tandem (double-junction) solar cells will also be calculated as a function of the materials' bandgap energies. It will be, thus, demonstrated that the “micromorph” tandem, composed of an a-Si:H solar cell deposited on top of a μc-Si:H solar cell, indeed represents an optimum combination of materials.

- Chapter 4 is focused on the application of various characterization techniques as tools for quantitative diagnostic of problematic solar cells, in our case solar cells presenting low fill factor values. We will demonstrate that J(V) measurements at variable illumination (i.e. VIM technique) allows the separation of the effects of (a) an increase of recombination (i.e. a decrease of the active material's “quality”), (b) a low shunt resistance and (c) a high series resistance, on the

reduction of the fill factor with respect to an ideal (theoretical) FF value. A collection model, originally developed for a-Si:H solar cells, will be adapted to μc-Si:H solar cells, and the empirical relationships established compared to actual measurements on various solar cells (dilution series, gas series and individual solar cells).

- The stability of μc-Si:H solar cells under light-soaking will be studied in detail in Chapter 5: we will show that μc-Si:H solar cells degrade, albeit in a "softer" and slower way than a-Si:H. The light-induced degradation in μc-Si:H is, similarly to that in a-Si:H, completely reversible under thermal annealing. We observe that the amplitude of the light-induced degradation is a function of the crystallinity ϕ_c of the sample: cells with $\phi_c \sim 50\%$ (which are, with respect to conversion efficiency, the optimum cells) present a relative efficiency reduction in the order of 5%. It will be shown that light-induced degradation is consequent to an increase of recombination in the intrinsic layer, revealed by an increase of the defect-related absorption α(0.8 eV) and a reduction of the collection voltage of the device. Fill factor is the parameter that shows the largest light-induced decrease: we show that its relative loss can be well quantified by the reduction in the collection voltage of the solar cell. A simple model is proposed for light-induced degradation, where we assume that light-induced defects, created in the amorphous phase, somehow dispersively diffuse to the nanocrystals' surface, where they deteriorate passivation (by the amorphous phase) and electrical transport properties.

- Chapter 6 deals with the stability of μc-Si:H solar cells under high-energy and low-energy proton irradiation. We will show that μc-Si:H solar cells degrade and recover differently depending on the energy of the proton radiation. In the case of protons of high energy, the degradation is completely reversible under thermal annealing, whereas with low-energy proton irradiation, permanent damage is created. Indeed, the low-energy protons (H^+) are implanted within the intrinsic layer, instead of merely crossing it. The amplitude of the degradation is observed, similarly to light-induced degradation, to depend on the crystallinity of the photoactive layer of the device. But, in the case of proton radiation, the solar cells with the highest crystallinity are those showing the largest degradation. We suggest a simple model for low and high-energy degradation, where the defect creation within the crystalline phase is, this time, responsible for the degradation.

- Chapter 7 will be the last chapter, containing overall conclusions as well as a discussion about the three types of degradation studied in this work and the corresponding models presented.

2. Characterization techniques

2.1 Current density -voltage J(V) measurement

Current density-voltage J(V) measurement is a fundamental electrical characterization technique used for solar cells' performance evaluation. It is carried out, in our laboratory, with a WACOM sun simulator, which spectrum is close to the AM 1.5 solar spectrum, and which intensity is equal to 100 mW/cm^2. Generally, J(V) curves are measured on several individual solar cells (typical size: 5 x 5 mm) which are structured either by lift-off (see [20]) or laser scribing on a 4 cm x 4 cm substrate. Values given in this work for the electrical device parameters are average values generally measured on 4-5 individual solar cells.

A typical J(V) curve of a solar cell is shown in Fig 2.1:

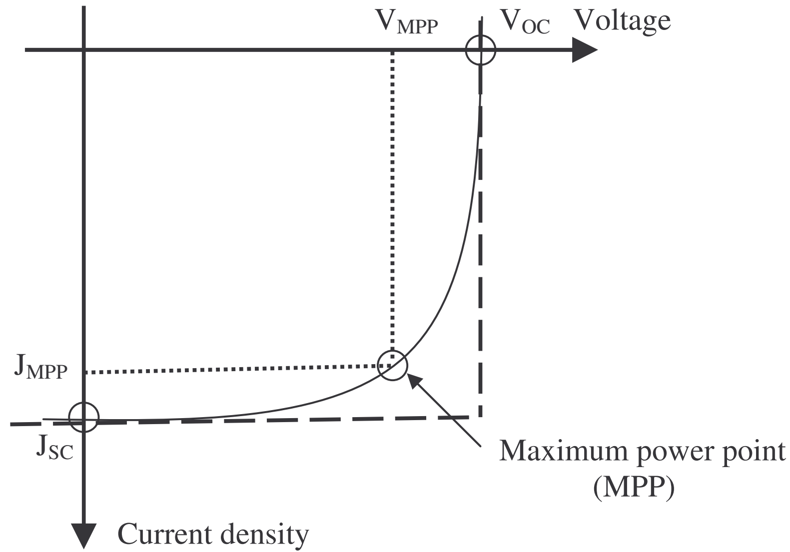

Fig. 2.1. Typical current density-voltage J(V) curve of a microcrystalline silicon solar cell under illumination. The open-circuit voltage (V_{oc}) and the short-circuit current density (J_{sc}) are indicated, as well as the maximum power point corresponding to the maximum current density J_{MPP} and maximum voltage V_{MPP}.

The open-circuit voltage V_{oc} is measured when no current flows through the solar cell, whereas the short-circuit current density J_{sc} is measured when the voltage is equal to zero. The fill factor FF is defined as:

$$FF = \frac{J_{MPP} \cdot V_{MPP}}{J_{sc} \cdot V_{oc}} \qquad (2.1)$$

where J_{MPP} and V_{MPP} are the current density and voltage corresponding to the maximum power produced by the solar cell.

V_{oc} and FF are evaluated from J(V) measurements, whereas J_{sc} is usually

established from external quantum efficiency measurements (see § 2.2), for 2 reasons: (a) the active area of the solar cell, which is necessary to determine the current density, is not always well defined, and (b) the spectrum produced by the sun simulator does not exactly correspond to AM 1.5.

The efficiency of the solar cell η is the ratio of the maximum power over the incident light power (P_{light}):

$$\eta = \frac{J_{MPP} \cdot V_{MPP}}{P_{light}} = \frac{J_{sc} \cdot V_{oc} \cdot FF}{P_{light}} \quad (2.2);$$

AM 1.5 spectrum corresponds to P_{light} = 100 mW/cm^2 or 1000 W/m^2.

J(V) measurements can also be performed in the dark or with variable illumination intensities; the techniques are then called "Dark J(V)" and "VIM". Both techniques will be detailed in Chapter 4.

2.2 External quantum efficiency measurement

External quantum efficiency (EQE) is a measure of the probability for an incident photon at a given wavelength to create an electron/hole pair that will contribute to the external current density of the solar cell. It includes the probability for the photon to be absorbed in the device (i.e. it includes optical reflection losses), and, also, the probability for the photogenerated carriers to reach the external contacts without recombining.

The measurement can be performed under a voltage bias in order to superimpose an external electrical field to the internal field of the solar cell. Experimentally, the solar cell is illuminated with a chopped light beam crossing a monochromator. The solar cell current density $J(E_{photon})$ is measured and divided by the product of the elementary charge q and the incident flux of photons ϕ (as determined with a calibrated reference detector, which quantum efficiency is known):

$$EQE = \frac{J(E_{photon})}{q\phi(E_{photon})} \quad (2.3)$$

2.3 Micro-Raman spectroscopy

Micro-Raman spectroscopy is a characterization technique used to evaluate the average crystalline volume fraction (i.e. the crystallinity) of the microcrystalline intrinsic layers present in our solar cells. Raman scattered light can either be:

1. Elastically scattered (Rayleigh scattering): the scattered light has the same wavelength (frequency) that the incident light; this scattering mode is largely predominant.
2. Inelastically scattered (Raman scattering): the scattered light has a different wavelength (frequency) than the incident light; this scattering mode only represents a very small fraction ($10^{-5} – 10^{-7}$) of the total scattered light.

The Raman effect results from the interaction of vibrational and/or rotational modes of molecules (or atoms in a crystal) with the electromagnetic radiation, i.e. of photons-phonons interactions. In a solid, the incident photons interact with the atomic lattice of the material in such a way that energy is either gained or lost, so that the scattered photons are shifted in frequency. The difference in energy between the incoming and outgoing photons corresponds to the energy of vibrations (phonons for a crystal) of the probed material. The frequency shift is, thus, characteristic of the phonon distribution in the material. In our case, Micro-Raman spectroscopy is used to measure the relative amount of amorphous and crystalline phases in our microcrystalline material.

Practically, the incident light is either an Argon laser (Ar, λ = 514 nm) or a Helium Neon laser (HeNe, λ = 633 nm), which beam is focused through a microscope on the sample's surface. The penetration depth is given by $1/(2\alpha)$, with α the absorption coefficient of the material at the wavelength considered. In the case of µc-Si:H, 514 nm and 633 nm correspond to penetration depths in the order of around 50 nm and 500 nm, resp. Thus, Ar laser is used to probe the (p/i and i/n) interfaces mainly, whereas HeNe laser is used to evaluate the average crystalinity through the total intrinsic layer thickness.

A Raman spectrum is the plot of the intensity of the Raman scattered light as a function of the scattered light wavenumber, expressed in absolute shift (cm^{-1}) relatively to the excitation's laser wavelength, see the example of Fig. 2.2.

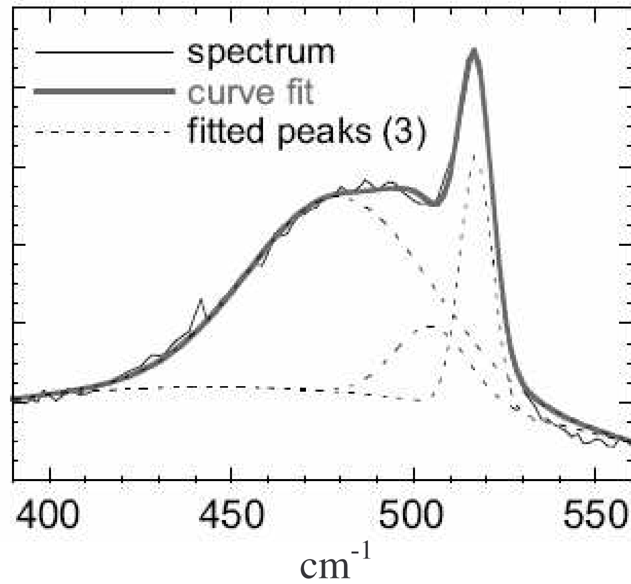

Figure 2.2 Typical Raman spectrum of a µc-Si:H solar cells, with a Raman crystallinity factor ϕ_c (see below) equal to ~ 50%. The dotted lines represent the 3 gaussian peaks used to fit the spectrum: one centered at 480 cm^{-1}, one centered at ~ 510 cm^{-1} and one centered at ~520 cm^{-1}.

The Raman spectra is fitted with 3 gaussian peaks: one at 480 cm^{-1}, typical of amorphous silicon; one at ~510 cm^{-1} attributed to crystallites with sizes in the order of 5 to 10 nm; the third peak, at ~ 520 cm^{-1}, corresponds to “bulk” crystalline silicon (c-Si). The Raman crystallinity factor ϕ_c is then evaluated from the integrated areas of the peaks (I) using the following relationship:

$$\phi_c = \frac{I_{510} + I_{520}}{I_{480} + I_{510} + I_{520}} \qquad (2.4)$$

The Raman crystallinity factor is, thus, calculated for the top and the bottom sides of the solar cell; the <u>average</u> Raman crystallinity factor is then calculated as the average value of that of the top and of the bottom. The (average) ϕ_c gives an approximate value (± 20% relative error, depending on ϕ_c) for the crystalline volume fraction of the intrinsic layer [21].

More details about Micro-Raman Spectroscopy and practical conditions of measurement (set-up, laser beam power, etc.) can be found in [18].

2.4 Fourier-Transform Photocurrent Spectroscopy (FTPS)

The absorption spectrum of intrinsic layers has been used for years to monitor the quality of amorphous silicon by assessing the residual absorption below bandgap, with sensitive techniques such as photothermal deflection spectroscopy (PDS) [22] or constant photocurrent method (CPM) [23]; the Fourier-Transform Photocurrent Spectroscopy (FTPS) method has been derived from CPM.

Unlike PDS, CPM and FTPS can be applied to intrinsic layer characterization within working devices/solar cells. All 3 techniques allow the evaluation of: the optical gap, the Urbach slope (which is a measure of bandtails disorder) and the defect-related absorption, which, in amorphous silicon, is known to be proportional to dangling bond density. The typical absorption spectra of crystalline silicon (c-Si), amorphous silicon (a-Si:H) and μc-Si:H are shown in Fig. 2.3:

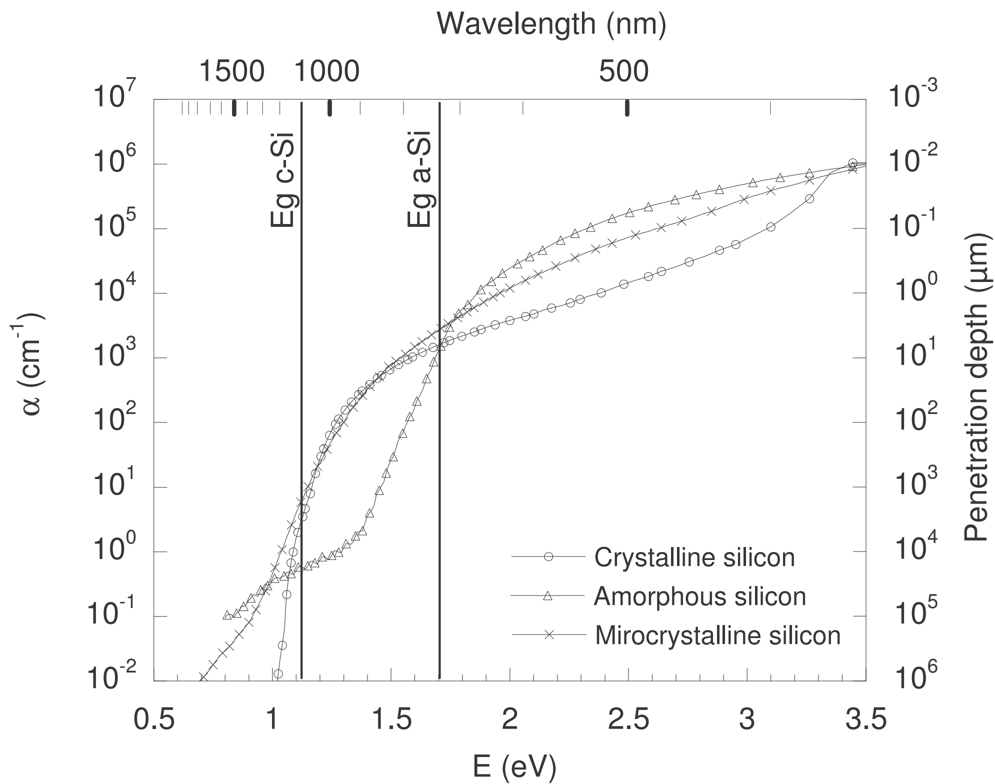

Figure 2.3 from ref [11]. Absorption spectra of crystalline, amorphous and microcrystalline silicon, as measured from CPM. The penetration depth, i.e. the inverse of the absorption coefficient α, is plotted on the right axis.

In the region just below the gap (1.1 eV for μc-Si:H, 1.75 eV for a-Si:H) the absorption coefficient stems from optical transition involving band tail states. The absorption in that region increases exponentially with the photon energy, forming the so-called Urbach tail.

It is characterized by the exponential slope E_0 of the absorption spectrum and determined by fitting the absorption curve using the following formula:

$$\alpha = \alpha_0 \cdot e^{E/E_0} \quad (2.5),$$

where α_0 is the exponential pre-factor.

In amorphous silicon the Urbach tail roughly extends from 1.5 to 1.7 eV and its slope is characterized by an Urbach parameter E_0 with a value between 40 and 60 meV. E_0 can be related to material disorder [24]. The value of E_0 generally depends on the temperature, however, in the case of a-Si:H, the disorder is mostly static and relates to strained bounds. Note that the Urbach tail also exists in crystalline silicon (a typical value of E_0 = 9.6 meV was reported in [25] for room temperature measurement).

Fourier-Transform Photocurrent Spectroscopy has been developed by M. Vanecek et al., based on Fourier-Transform Infrared (FTIR) spectroscopy [19, 26].) FTPS provides measurements of the absorptance spectrum of silicon-based thin-films over 6 orders of magnitude, in the sub-bandgap region as well as above it. The set-up of FTPS measurement is presented in Fig. 2.4.:

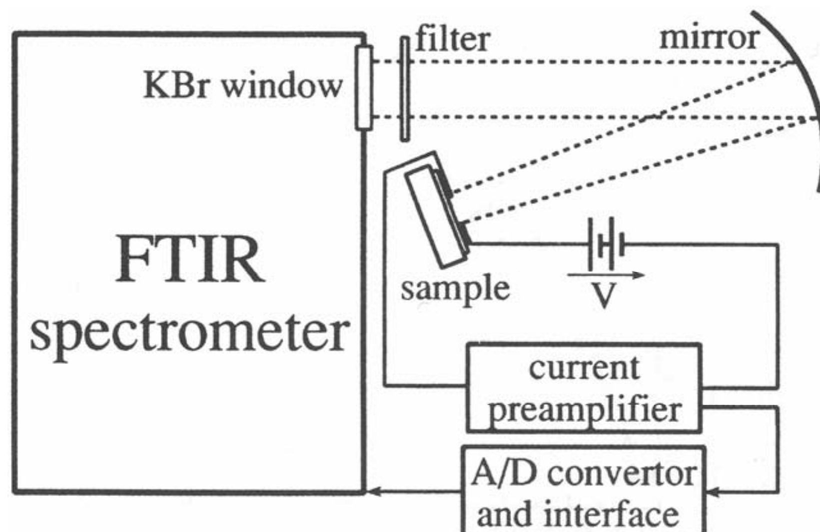

Figure 2.4 from ref [26]. Set-up of FTPS measurement.

Inside the FTIR spectrometer (not shown here), the beam from a light source (either halogen lamp or glow-bar) is directed through a variable aperture. Then, it enters a Michelson Interferometer equipped with one fixed and one movable mirror that constantly moves back and forth along a rail. The position of the movable mirror is recorded by counting the number of interference fringes from a helium-neon laser beam that follows the same path as the main beam in the interferometer. The main beam is recomposed with a beam splitter and externally focused on the

sample. The sample works here as a detector, either in a coplanar contact configuration, or transverse configuration (photovoltaic mode). A voltage bias can applied between the contacts, in order to extract the photocurrent or to bias the solar cell. The photocurrent is then pre-amplified and sent back to the spectrometer through an A/D converter.

The absorbance spectrum of interest (roughly from 0.6 eV to 2 eV) extends over at least 6 orders of magnitude; however, current amplifiers have a dynamic range of "only" approximately 3 orders of magnitude for a given sensitivity. The technical solution is, thus, to decompose the light spectrum into 2 spectral regions. For such purpose, two optical filters are placed on the beam path: a red (so-called KC14) filter used to measure the spectrum for the measurement range between 2 and 1.2 eV and a 5mm-thick Si wafer coated with antireflection layer for that between 1.2 and 0.6 eV. The two FTPS spectra obtained are then put together to form the whole FTPS spectrum from 0.6 eV up to 2eV.

The FTPS spectrum obtained is proportional to the absorptance of the sample, which is equal to the absorption coefficient α for $\alpha d < 0.1$ (with d the intrinsic layer thickness). This condition is fulfilled here for photon energies below 1.4 eV. In order to get comparable absorption spectra, the FTPS spectrum must, then, be calibrated; here, they were calibrated at 1.35 eV, by setting the absorption coefficient of the µc-Si:H cells to the value of crystalline silicon. In this thesis, we will assume that the absorption value at 0.8 eV is proportional to the defect density of the µc-Si:H intrinsic layer, as indicated from comparison of sub-bandgap absorption and Electron Spin Resonance (ESR) measurements [19]. In a-Si:H, it is the absorption value at 1.2 eV which is considered to be proportional to the bulk defect density. In the case of µc-Si:H, α(1.2 eV) corresponds to band-to-band absorption of silicon nanocrystals, see Fig 2.4.

With the calibration procedure chosen, defect-related absorption α(0.8 eV) is assumed to originate only from defects within the crystalline phase [27] or at the surface of the nanocrystals. Still, we cannot exclude that some part of the absorption signal at 0.8 eV is due to the amorphous phase; this issue still need to be investigated. Furthermore, it must be mentioned that comparable absorption spectra in this work have been established and measured on devices with similar rough TCO (transparent conductive oxide), i.e. with rough interfaces. The calibration method proposed here is not validated for comparison of i-layer material quality in cells deposited on TCO's with varying roughness or change in free carrier absorption (FCA).

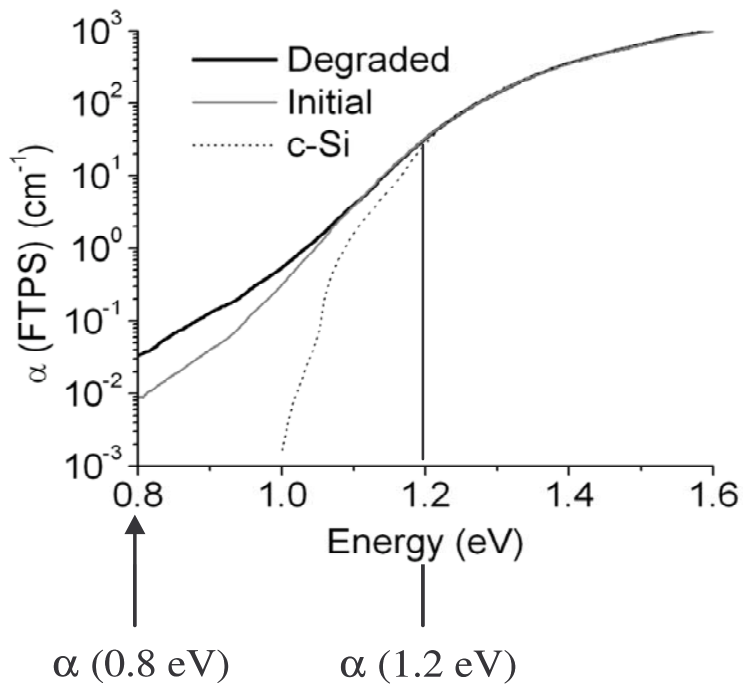

Figure 2.4 Fourier-transform photocurrent spectroscopy (FTPS) spectra for the initial and degraded states of a nip solar cell, where the intrinsic layer has an (average) Raman crystallinity factor ϕ_c = 25%. The FTPS spectra are calibrated at 1.35 eV on the value of the absorption coefficient of crystalline silicon (c-Si).

3. Theoretical limits for the main parameters of single-junction and tandem solar cells as a function of bandgap energy

3.1 Introduction

As mentioned in Chapter 1, thin-film silicon single-junction and tandem solar cells constitute one of the most promising options for further decreasing the fabrications costs of solar cells. However, the conversion efficiency of thin-film silicon solar cells remains relatively low when compared to that of wafer-based crystalline silicon (c-Si) solar cells, or even other forms of thin-film solar cells, such as CIGS and CdTe solar cells. The conversion efficiency is a measure of the generation, and potential recombination, of the electron-hole pairs created by photon absorption. It is limited by basic physical considerations, such as the type of semiconductor used and its range of absorption, defined by the bandgap energy: photons with an energy lower than the bandgap are negligibly absorbed.

Another source of efficiency limitation in solar cells is the thermalization of electrons and holes: an electron-hole pair created by a highly energetic photon quickly thermalizes, i.e. relaxes back to the edges of the carrier bands; the excess energy is dissipated as heat. Thus, even though the photon's energy is much larger than the bandgap, only one single electron-hole pair is generated. The maximum achievable efficiency is, thus, limited to about 44% of the whole solar spectra [28].

Further physical and technical restrictions exist that confine the efficiency to values well below the theoretical "ideal" limit: one typical example is the increased recombination rate of electron-hole pairs due to bandgap states as present in amorphous (a-Si:H) and microcrystalline (μc-Si:H) silicon. Moreover, actual solar cells are in general too thin to absorb all the "useful" photons with energies above bandgap; light-trapping techniques are, thus, necessary to increase the light path and the photon absorption probability. These techniques are, however, not fully effective as yet.

In this chapter, fundamental limits for short-circuit current density (J_{sc}), open-circuit voltage (V_{oc}), fill factor (FF) and efficiency (η) as a function of the bandgap (E_g) will be presented for a-Si:H and μc-Si:H single-junction and tandem solar cells. These basic limitations are established from thermodynamical considerations on radiative recombination, semi-empirical considerations based on the classical pn diode equation and an original coarse model established for pin diodes.

The limits obtained will be discussed in relation to actual experimental values of J_{sc}, V_{oc}, FF and η for a-Si:H and μc-Si:H: it will, thus, be confirmed that for single-junction solar cells, major efficiency gains should be achieved by increasing the short-circuit current density through better light-trapping. Concerning tandem solar

cells the pair of materials “amorphous/microcrystalline silicon” is confirmed to be the optimal combination.

3.2 Pn junction

3.2.1 Ideal pn junction

The dark current density for a pn junction is given by:

$$J_{dark} = J_0 \left[\exp\left(\frac{qV}{kT} \right) - 1 \right] \qquad (3.1),$$

where J_0 is the reverse saturation current density, V the voltage, q the elementary charge, k the Boltzmann constant and T the absolute temperature.

The detailed derivation of this expression will not be given here; it can, for example, be found in [29, 30].

For a pn diode without surface recombination, the reverse saturation current represents the diffusion current of minority carriers generated in the neutral regions; it is expressed by:

$$J_0 = qn_i^2 \frac{D_n}{L_n N_A} + \frac{D_p}{L_p N_D} \approx \frac{qn_i^2}{N_D} \sqrt{\frac{D_p}{\tau_p}} \quad \text{if} \quad N_D >> N_A \qquad (3.2),$$

where D_n and D_p are the diffusion constant of the electrons and holes resp., L_n and L_p the diffusion lengths, n_i the intrinsic carrier density, N_A and N_D the acceptors and donors density and τ_p lifetime of the holes.

J_0 values in the order of 10^{-12} A/cm^2 are, thus, obtained for crystalline silicon (c-Si) [31]. Such values correspond, according to equ (3.1), to dark (diffusion) current densities J_{dark} between $5 \cdot 10^{-11}$ A/cm^2 and $5 \cdot 10^{-4}$ A/cm^2 for forward voltages between 0.1 and 0.5 V (T = 293 °K).

In the calculation for the ideal diode, generation and recombination currents are considered to be negligible in the depletion region. In reality, this is not true and generation/recombination processes that take place in the depletion region also contribute to the dark current. Under forward bias, both the concentrations of holes and electrons exceed the equilibrium values; the net recombination rate is maximum in the depletion region where the intrinsic Fermi level E_i is halfway between the quasi-Fermi levels E_{Fp} and E_{Fn}. This is the case in the middle of the depletion layer, as can be seen in Fig. 3.1 (b):

(a) (b)

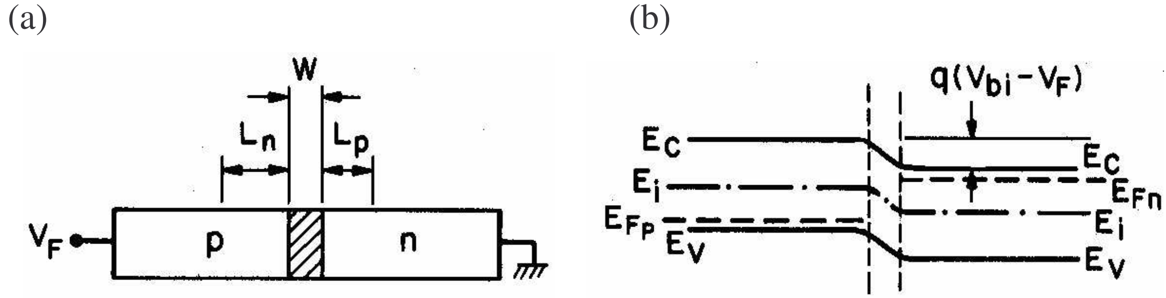

Figure 3.1. (a) Schematic cross-section and (b) energy band diagram of a pn junction under forward bias, as published in [30]: W is the depletion region width and L_n and L_p are the diffusion lengths of electrons and holes, respectively.

The recombination current density is established by integrating the net recombination rate over the whole depletion region; it is given by [30]:

$$J_{rec} = \frac{qWn_i}{2\tau_r} \exp\left(\frac{qV}{2kT}\right) \quad (3.3),$$

where W is the depletion region width and τ_r is the effective recombination lifetime given by $1/\sigma_0 v_{th} N_t$, with $\sigma_0 = \sigma_n = \sigma_p$ the electron (hole) capture cross section, v_{th} the thermal velocity and N_t the concentration of recombination centres.

This expression is obtained by assuming that the net recombination current is maximum over the total depletion region: this assumption is false, but necessary to obtain an analytical expression for J_{rec} (see for example [32]). Considering equ. (3.3), as well as taking into account characteristic parameters values for c-Si, one obtains for the current density J_{rec} values between 10^{-9} A/cm^2 and 10^{-5} A/cm^2, for forward voltages between 0 and 0.5 V (T= 293 °K).

The total forward dark current density can finally be expressed by the sum of the diffusion current density, as given in equ. (3.1), and the recombination current density of equ. (3.3) (for V > 3kT):

$$J_{dark} \approx \frac{qn_i^2}{N_D}\sqrt{\frac{D_p}{\tau_p}} \exp\left(\frac{qV}{kT}\right) + \frac{qWn_i}{2\tau_r} \exp\left(\frac{qV}{2kT}\right) \sim \exp\left(\frac{qV}{nkT}\right) \quad (3.4),$$

with n defined as the ideality factor: n=1 when the diffusion current dominates and n=2 when the recombination current dominates. When both currents are of comparable magnitudes, n is between 1 and 2.

This result is different from the one obtained for reverse bias: in this case, at room temperature, the dark current contribution due to thermal generation from the depletion layer is larger than the diffusion current, see e.g. [31]. Under forward

bias, the predominance of one current over the other one depends on the voltage applied, as can be seen in Fig. 3.2 where experimental results on silicon and GaAs pn diodes are reproduced:

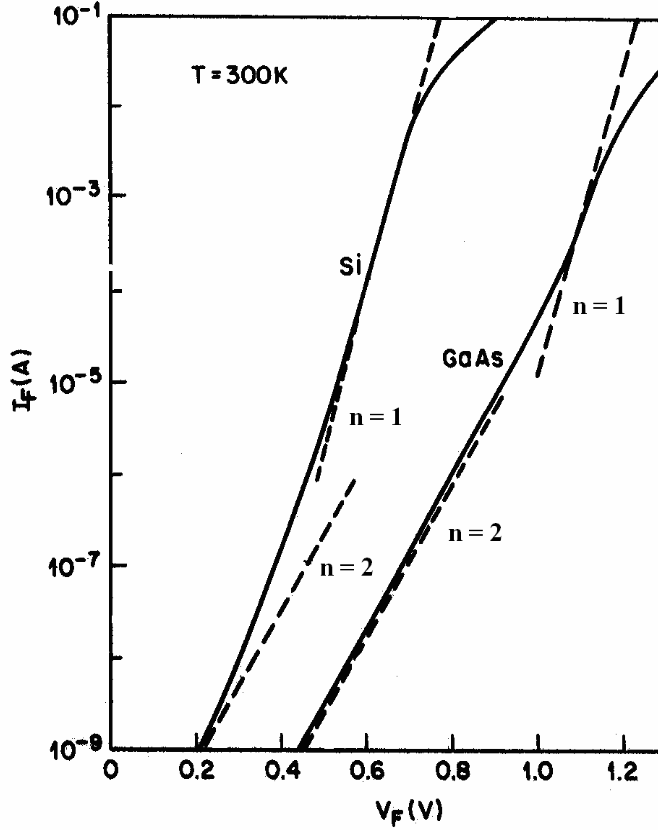

Figure 3.2 from ref [30]. Forward current-voltage characteristics of silicon and GaAs pn diodes at 300 °K: n represents the ideality factor, as introduced in equ. (3.4)

According to Fig. 3.1, this observation can be explained by considering that, for increased forward bias, both (a) the electrostatic potential across the depletion region, and (b) the width of the depletion region, decrease. Indeed, (a) results in an increase of the diffusion current in comparison to the drift current, whereas (b) results in a reduction of the generation (recombination) current. This corresponds to values of n tending towards 1 for high forward bias.

Finally, the J(V) characteristic of a single-junction pn solar cell under illumination can be written as the linear superposition of the photogenerated current density J_L and the dark current density of the cell (see [30, 33]):

$$J = J_0 \left[\exp\left(\frac{qV}{nkT} \right) - 1 \right] - J_L \tag{3.5}$$

This superposition principle is not valid when considering amorphous and

microcrystalline silicon pin junctions (even with n=2): a recombination term must be added, as will be presented in detail in Chapter 4.

The open-circuit voltage V_{oc} can be deduced from equ. (3.5) with the condition J = 0:

$$qV_{oc} = nkT \cdot \ln\left(\frac{J_L}{J_0}\right) \quad \text{with} \quad \left(\frac{J_L}{J_0} + 1 \approx \frac{J_L}{J_0}\right) \qquad (3.6),$$

and the reverse saturation current density J_0 can be expressed as function of the bandgap energy E_g:

$$J_0 = J_{00} \cdot \exp\left(-E_g / nkT\right) \qquad (3.7)$$

Finally, equ. (3.6) can be rewritten as:

$$qV_{oc} = E_g + nkT \cdot \ln\left(J_L / J_{00}\right) \qquad (3.8)$$

Values for the pre-factor J_{00} will be established according to (a) two models developed by Green [33] and Kiess [34] for pn junctions, (b) one model developed in the present thesis for pin junctions.

3.2.2 Theoretical limits for the pn junction

A first completely theoretical limit, the "detailed balance limit" was presented in 1961 by Shockley and Queisser [28], based on thermodynamical considerations. They based their considerations on the concept that, in solar cells, the carriers' generation due to light absorption has a counterpart: the radiative recombination.

Shockley and Queisser estimated the maximum achievable efficiency as a function of the semiconductor bandgap for three different cases:

(a) First, they considered the very simple (unrealistic) case of a spherical solar cell, at a temperature T_c = 0 °K, surrounded by a blackbody at a temperature T_s, as presented in Fig 3.3 (a). They, thus, established what they called the "ultimate efficiency";

(b) Second, they considered a planar solar cell and a blackbody at the same temperature $T_s = T_c > 0$°K, i.e. the sun and the solar cell are in thermal equilibrium;

(c) Finally, they considered the real case, with T_s (6000 °K) > T_c (300°K). The blackbody radiations fall upon the planar cell at a small solid angle ω_s. This case is schematically presented in Fig. 3.3 (b):

(a) (b)

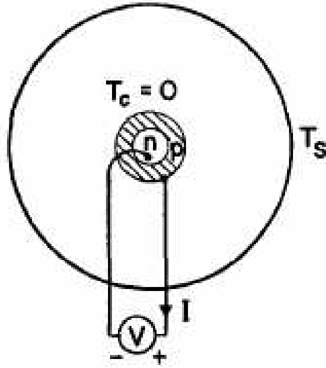

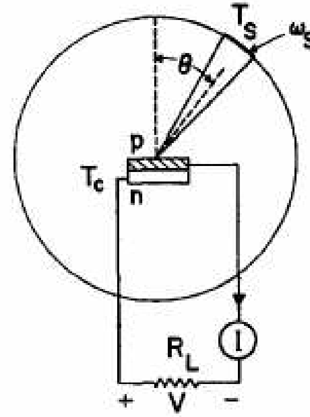

Figure 3.3 from ref [28]. (a) a spherical solar cell surrounded by a blackbody at temperature T_s, the solar cell is at temperature T_c = 0 °K, (b) a planar cell with radiations coming from a spherical sun at a small solid angle ω_s and an angle of incidence θ.

For their calculations Shockley and Queisser assumed that:

- The sun and the solar cell are both blackbodies and the rate of photons emitted is expressed according to Planck's distribution formulas;
- Every photon with an energy greater or equal to the bandgap energy produces only one electron-hole pair;
- The recombination is totally radiative.

Let us consider that the cell has an area A subject to radiation; its output power is given by:

$$P_{out} = h\nu_g A Q_s \quad (3.9),$$

with h the Planck's constant, ν_g the bandgap frequency and Q_s the rate of photons of frequency greater than ν_g, per unit area per unit time, emitted by the blackbody at a temperature T_s (expressed by Planck's formulas, see [28]).

On the other hand, the incident power is given by:

$$P_{in} = AP_s \quad (3.10),$$

with P_s the total energy density for blackbody radiation at a temperature T_s, per unit area per unit time, (expressed by Planck's formulas, see [28]).

The "ultimate" efficiency u is, thus, given by:

$$u(\nu_g, T_s) = P_{out} / P_{in} = h\nu_g Q_s(\nu_g, T_s) / P_s(\nu_g, T_s) \qquad (3.11)$$

Let us define the ratio $x_g = E_g / kT_s$, with $E_g = h\nu_g = qV_g$ the bandgap energy and k the Boltzmann's constant: the "ultimate" efficiency u is a function of x_g, as presented in Fig. 3.4:

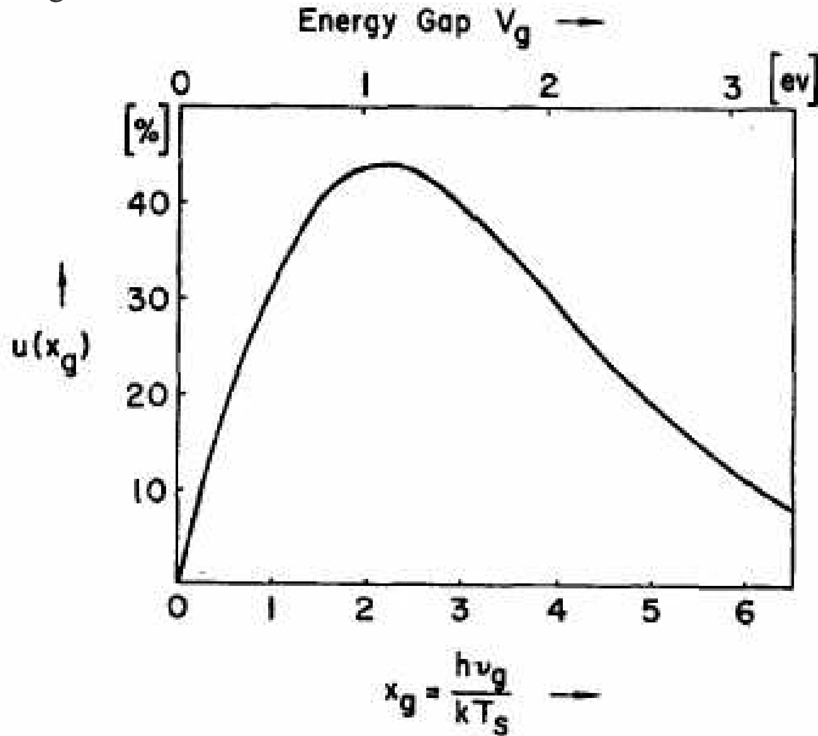

Figure 3.4 from ref [28]. Ultimate efficiency u as a function of x_g and the bandgap energy for T_s = 6000 °K

The maximum of efficiency thus established is equal to 44% corresponding to a bandgap energy of 1.1 eV. The "ultimate" efficiency achievable is limited to such (low) values because each photon (even those of an energy much larger than the bandgap energy) produces only one single electron-hole pair, due to thermalization processes [29, 33].

Then, Shockley and Queisser determined the current-voltage relationship under steady-state conditions for the planar solar cell in thermal equilibrium with the blackbody. They considered that non-radiative processes also take place in the cell and they established an expression for the dark current density, that is similar to the one previously given in equ. (3.1) for the ideal pn diode:

$$J = J_0 [\exp(qV / kT_c) - 1] \qquad (3.12),$$

where the reverse saturation current density J_0 is expressed by:

$$J_0 = q[F_{c0} + R(0)] \qquad (3.13),$$

where F_{c0} and R(0) are the rate (per unit area per unit time) of radiative, resp. non-radiative, recombination in thermal equilibrium. The radiative recombination current density is given by $q \cdot F_{c0}$, with F_{c0}:

$$F_{c0} = t_c Q_c \qquad (3.14),$$

with t_c the probability that an incident photon of energy greater than E_g is absorbed by the solar cell and produces an electron-hole pair, and Q_c the rate of photons of frequency greater than ν_g, per unit area per unit time, emitted by the blackbody at a temperature T_c (expressed by Planck's formulas, see [28]).

For an energy gap of 1.1 eV and a temperature of 300 °K ($T_c = T_s$), Q_c is equal to $1.7 \cdot 10^3$ cm^{-2} sec^{-1} (see Planck's formulas [28] and [35]). The radiative recombination current density, expressed by $q \cdot F_{c0,}$ is, thus, equal, for $t_c = 1$, to $2.7 \cdot 10^{-16}$ A/cm^2, according to equ. (3.14).

If we define f_c as the fraction of the recombination-generation rate which is radiative, $f_c = F_{c0} / \lfloor F_{c0} + R(0) \rfloor$, equ. (3.13) can be rewritten:

$$J_0 = qF_{c0} / f_c \qquad (3.15)$$

Considering that existing solar cells have dark current densities in the order of 10^{-12} A/cm^2, whereas $q \cdot F_{c0}$ was found to be equal to $2.7 \cdot 10^{-16}$ A/cm^2, we obtain that f_c is in reality equal to $\sim 10^{-4}$ (instead of 1, as previously assumed).

Let us now consider the final case where the cell is subject to solar radiation energy, i.e. the cell and the blackbody are not in thermal equilibrium any more with T_s (6000 °K) much larger than T_c (300 °K).

Equ. (3.12) becomes:

$$J = J_0 [\exp(qV / kT_c) - 1] - J_{sc} \qquad (3.16),$$

with the short-circuit current density J_{sc} expressed by:

$$J_{sc} = q \cdot (F_s - F_{c0}) \approx qF_s \qquad (3.17),$$

where F_s is the number of electron-hole pairs generated by solar radiation, per unit area per unit time ($F_s >> F_{c0}$), i.e. $J_{sc} = J_L$, the photogenerated current density.

The open-circuit voltage is obtained by solving equ. (3.16) for J=0:

$$V_{oc} = (q/kT_c) \ln[(J_{sc}/J_0) + 1] \qquad (3.18),$$

whereas the maximum power produced by the cell is assessed by maximising the I(V) equation.

Shockley and Queisser determined the fill factor by dividing the maximum power produced by the cell by its nominal power $I_{sc} \cdot V_{oc}$; the values thereby obtained for FF are presented in Fig 3.5 as a function of the normalized open-circuit voltage v_{oc}:

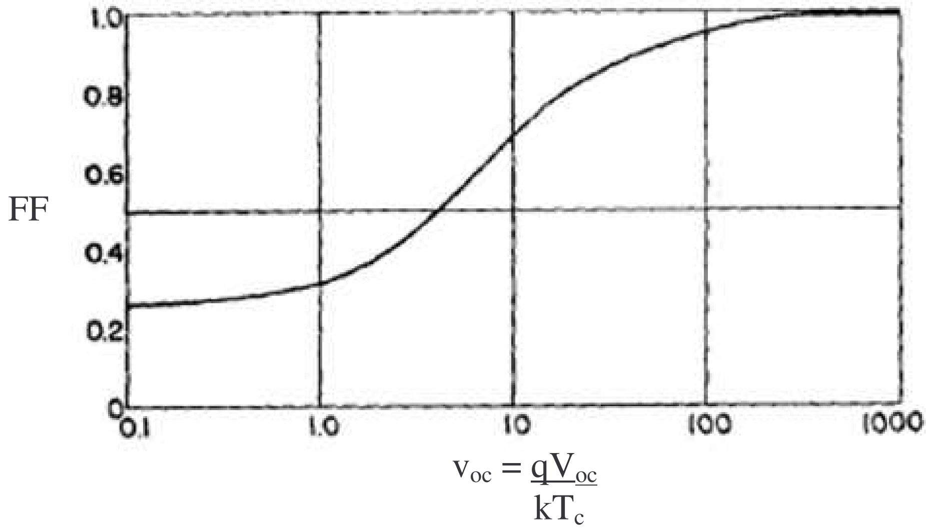

Figure 3.5 from ref [28]. Fill factor as a function of the normalized open-circuit voltage $v_{oc} = qV_{oc}/ kT_c$

This numerical relationship was assessed by computing both (a) values of FF and (b) values of V_{oc}, as functions of the maximum power voltage V_M. The result is very similar to the empirical expression published by Green [33]:

$$FF = \frac{v_{oc} - \ln(v_{oc} + 0.72)}{v_{oc} + 1} \qquad (3.19),$$

valid for values of the normalized open-circuit voltage v_{oc} (qV_{oc}/kT) that are larger than 10.

A maximum efficiency limit of about 30 % was thus finally established by Shockley and Queisser for E_g = 1.1 eV, considering only radiative recombination (f_c =1) and unconcentrated 6000 °K black body radiation. For AM 1.5 spectrum, the maximum efficiency achievable is a little bit larger with 32.9 % [36].

Kiess and Rehwald [34] also calculated a limit for the conversion efficiency as a function of bandgap energy, by considering only radiative recombination and AM 1.5 spectrum. They first established a theoretical limit for the open-circuit voltage and then assumed a constant fill factor value of FF = 0.85 to establish the limit for the efficiency. They thus obtained, for E_g = 1.1 eV, a V_{oc} limit of 0.86 V

leading to an efficiency limit of 30.6 %. Details of their calculations will be presented in § 3.4.2.

3.2.3 Semi-experimental limits for pn junction

Efficiency calculations have been carried out since the beginning of the photovoltaic technology development, to guide the research activity: already in 1955, Prince published results on the solar cells efficiency as a function of bandgap energy [37], followed by Loferski the year after [38]. These calculations were based on empirical values for the solar cell characteristic parameters. More recently, Green [33] also published a semi-empirical limit based on experimental data that will be presented in details later (see equ. (3.21)).

3.3 Pin junction

All the theoretical and empirical limits previously presented and published for single-junction solar cells were calculated by considering a pn junction. Pn junctions are indeed employed for crystalline silicon; conversely, amorphous and microcrystalline silicon are used in pin configurations, as they are very defective materials and need an internal electric field to assist in collection.

The pn junction limits will therefore be adapted to pin configuration: we will first consider the limits established by Kiess and Green, and then, additional losses in open-circuit voltage and fill factor due to the pin configuration will be estimated considering two distinct effects:

a) the diminution of the photogenerated current in pin solar cells due to additional recombination in the intrinsic layer, and
b) the increase of the dark (reverse) current of thin-film silicon pin diodes, as can be attributed to thermal generation current from mid-gap defect states (dangling bonds).

These calculations for the pin junction will be given in paragraph § 3.4.2 hereafter. Efficiency limitations for tandem (double-junction) solar cells will also be considered in § 3.5; it will be confirmed that the tandem “micromorph” (a-Si:H/μc-Si:H) solar cell, as pioneered and developed in our group [3], indeed corresponds to an optimum combination of bandgap values.

3.4. Single-junction solar cell

All the limits presented below have been calculated numerically using the tabulated numerical values for the AM 1.5 spectrum and various numerical and analytic expressions which will be derived step by step in the paragraph § 3.4.2.

3.4.1 Limit for short-circuit current density J_{sc}

The upper limit for the short-circuit current density J_{sc} was computed by considering the normalized AM 1.5 spectrum (IEC 904-3), and by assuming that each photon with an energy $h\nu \geq E_g$ (where h is the Planck constant, ν is the frequency, equal to c/λ with c the speed of light and λ the wavelength, and E_g is the energy gap of the semiconductor material considered) is absorbed and converted into a single electron-hole pair that can be collected at short-circuit condition. J_{sc} is, thus, expressed by:

$$J_{sc} = q \int_0^{\lambda(E_g)} \phi_s(\lambda)\, d\lambda \qquad (3.20),$$

with q the elementary charge, λ (E_g) the wavelength that corresponds to the bandgap energy, and ϕ_s the normalized AM 1.5 solar spectrum.

This results in J_{sc} values, calculated from (3.20), as a function of the material's bandgap energy E_g, as presented in Fig. 3.6:

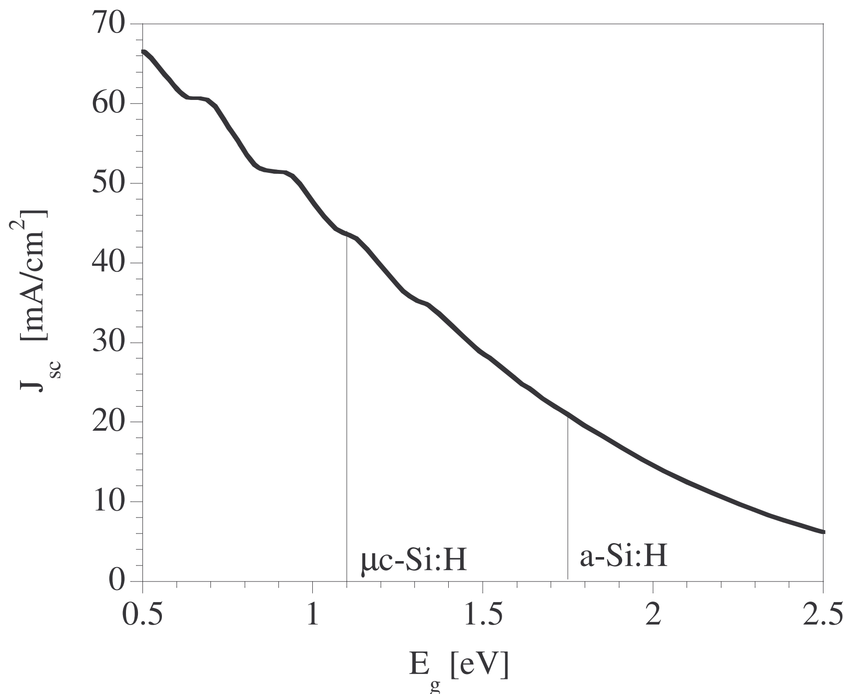

Figure 3.6. Upper limit of the short-circuit current density J_{sc} as a function of the bandgap energy E_g of the solar cell material, under AM1.5 illumination.

Microcrystalline silicon solar cells have an energy gap of 1.1 eV, corresponding to the theoretical upper limit J_{sc} = 43.6 mA/cm^2; a-Si:H solar cells have an energy gap of 1.75 eV, corresponding to J_{sc} = 21.1 mA/cm^2. In practice, however, values of $J_{sc} \approx$ 20-27 mA/cm^2 [8, 9] and $J_{sc} \approx$ 14-18 mA/cm^2 [14] are the actual short-circuit current density values obtained by several laboratories for μc-Si:H and a-Si:H solar cells, respectively. These values are, thus, well below the theoretical upper limits.

However, the theoretical upper limits were established by considering that all the photons with an energy larger than E_g are absorbed: this corresponds to the ideal case of an infinitely thick cell with no reflection at the front side. In practice, a-Si:H and µc-Si:H solar cells are relatively thin and do have additional reflection and transmission optical losses. In present solar cell research, gains in short-circuit current density are therefore sought by means of light-trapping techniques, such as the use of textured TCOs [39] and back reflectors [40].

3.4.2 Limits for open-circuit voltage V_{oc}, fill factor FF and efficiency η

a) Open-circuit voltage V_{oc} and reverse saturation current density J_0

a.1) pn junction

Green [33] gives a lower limit, based on experimental data, for the reverse saturation current density J_0 in a pn junction, as previously presented in equ. (3.7), that corresponds to:

$$J_{00} = 1.5 \cdot 10^{8} \quad [\text{mA/cm}^2] \tag{3.21}$$

On the other hand, based on thermodynamical considerations, Kiess and Rehwald [34] give the following limit for V_{oc} (pn junction, n=1):

$$qV_{oc} = E_g + kT \cdot \ln\left[\left(\frac{h^3 c^2}{2\pi kT}\right) \cdot \left(\frac{\dot{N}_{incident}}{E_g^2}\right)\right] \quad \text{with } \dot{N}_{incident} = J_{sc}/q \tag{3.22}$$,

which corresponds to a similar relationship as that previously given in equ. (3.8).

Kiess and Rehwald's limit was established by considering that:

- Each photon absorbed produces only one single electron-hole pair (impact ionization is neglected);
- The absorbed flux of photons is equal to the photon flux emitted by radiative recombination of carriers within kT of the band edge.

We will demonstrate that equ (3.22) is, thus, equivalent to the V_{oc} limit, as established by Shockley and Queisser and presented as equ (3.18). Let us start by expressing the rate of photons emitted by the sun, as described by Planck's distribution [34]:

$$f(v) = 2\pi v^2 \Delta v / \left(c^2 \left[\exp(hv/kT_s) - 1\right]\right) \tag{3.23}$$

Considering only photons in a range kT_c of the band edge, i.e. $h\Delta v = kT_c$ [34], equ (3.23) becomes:

$$f(\nu) = \frac{2\pi kT_c}{h^3c^2} \cdot \frac{E_g^2}{\left[\exp(E_g/kT_c) - 1\right]} \tag{3.24}$$

By combining equ. (3.24) and the expression for the reverse saturation current density as established by Shockley and Queisser (equ. (3.15)), we obtain that (for $f_c = 1$ and $F_{c0} = f(\nu)$ the rate of radiative recombination):

$$J_0 = qf(\nu) = \frac{2\pi kT_c q}{h^3c^2} \cdot \frac{E_g^2}{\left[\exp(E_g/kT_c) - 1\right]} \quad (3.25),$$

which leads, according to their V_{oc} limit (equ (3.18)), to:

$$V_{oc} = \frac{kT_c}{q} \ln\left[\frac{J_{sc}}{\frac{2\pi kTq}{h^3c^2} \cdot \frac{E_g^2}{\left[\exp(E_g/kT_c) - 1\right]}}\right] \quad (3.26),$$

that, in its turn, becomes, with $J_{sc} = q \cdot \dot{N}_{incident}$:

$$V_{oc} = \frac{kT_c}{q} \ln\left[\frac{h^3c^2}{2\pi kT} \cdot \frac{\dot{N}_{incident}}{E_g^2} \cdot \left[\exp(E_g/kT_c) - 1\right]\right] \quad (3.27),$$

which is indeed equal to equ. (3.22), since $\exp(E_g/kT_c) >> 1$.

According to equ. (3.8), equ. (3.27) corresponds to:

$$J_{00} = \left(\frac{2\pi kT_c}{h^3c^2}\right) \cdot q \cdot E_g^2 \quad [\text{A/cm}^2] \quad (3.28),$$

which becomes, for T_c = 25°C ($kT_c \approx$ 25 meV):

$$J_{00} = 4 \cdot 10^5 \cdot E_g^2 \quad [\text{mA/cm}^2] \text{ with } E_g \text{ in [eV]} \tag{3.29}$$

For c-Si, i.e. for E_g = 1.1 eV, such a J_{00} value corresponds, according to equ. (3.7), to $J_0 \sim 4{\cdot}10^{-14}$ mA/cm^2. For comparison, the value given by Green as equ. (3.21), corresponds to $J_0 \sim 1.2{\cdot}10^{-11}$ mA/cm^2.

a.2) pin junction

As previously mentioned, a-Si:H and μc-Si:H materials are used in pin-type solar cells, because of their too large defect density. We will therefore establish a specific limit for pin junction configuration: additional losses in V_{oc} (and in FF) due to this configuration will be assumed to be the consequence of two separate effects:

(a) additional recombination in the intrinsic layer ;

(b) thermal generation/recombination contribution to the dark current due to mid-gap defects (dangling bonds).

The recombination in the intrinsic layer of a pin diode can be considered at first as a recombination source added to the electrical equivalent circuit for photovoltaic solar cells, see Chapter 4, § 4.1, and [41]. The linear superposition of the dark current and the photogenerated current, as considered in equ. (3.5) for ideal pn junctions, is, thus, not valid anymore: the illuminated J(V) characteristic for pin solar cells should now be written as (with $T = T_c$, the device temperature):

$$J = J_0 \left[\exp\left(\frac{qV}{nkT} \right) - 1 \right] + J_{rec} - J_L \qquad (3.30),$$

with the recombination current density J_{rec} a function of the photogenerated current J_L. Based on [41], we may assume, as coarse approximation that $J_{rec} \approx 0.8 \cdot J_L$ for $V \approx V_{oc}$. Indeed, we may define that, at $V = V_{oc}$:

$$J_{rec} = J_L \cdot \left(\frac{V_{bi} - V_{int}}{V_{bi} - V_{oc}} \right) \qquad (3.31),$$

with V_{bi} the built-in voltage and V_{int} the intersection voltage at which the J(V) curves, as measured at variable illumination intensities, cross, see Fig. 3.7.

With $V_{bi} \sim 1$ V, $V_{int} \sim 0.63$ V and $V_{oc} \sim 0.54$, as measured for the typical sample of Fig. 3.7, equ (3.31) indeed gives $J_{rec} \sim 0.81 \cdot J_L$.

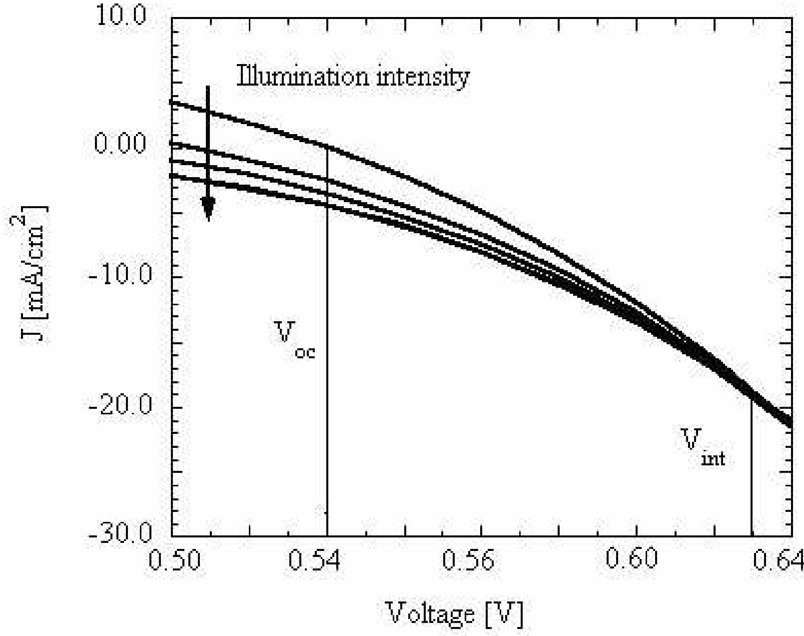

Figure 3.7 J(V) curves of a typical µc-Si:H solar cell measured at various light intensities: one can observe that all the curves cross at a single intersection voltage V_{int} (see [42] for similar observations in a-Si:H).

A lower limit for the reverse saturation current density in pin diodes can be estimated considering that the dark current density is thermally generated from mid-gap defects. This current density may then be written as :

$$J_{00} = (1/\tau_{gen})\, d_i\, q\, N_{db} \quad (3.32),$$

with τ_{gen} the "coefficient" of thermal generation in the intrinsic layer, d_i the intrinsic layer thickness, q the elementary charge and N_{db} the dangling bond density.

Dark current measurements carried out in our own group [31] as well as in the Paris' group by P. Roca et al. [43] have yielded reverse saturation currents in the order of $J_{th} \approx 10^{-12}$ A/cm^2 for a-Si:H diodes of a thickness of ~ 2 µm, at room temperature. C. Miazza [31] even estimated that J_{th} could be as low as 10^{-13} A/cm^2. We may, thus, assume, considering $\tau_{gen} \sim 10^{-9}$ s [31, 44], $d_i \sim 2$ µm, $N_{db} \sim 10^{15}$ cm^{-3}, that J_{00} is in the order of:

$$J_{00,\ pin} = 5 \cdot 10^4 \text{ [mA/cm}^2\text{]} \quad (3.33),$$

for state-of-the-art a-Si:H pin diodes. This value is taken as a first approximation for µc-Si:H diodes also, as defect densities are quite similar in this case [12]. Nevertheless, it must be mentioned that for µc-Si:H, much larger values of the reverse saturation current density J_0 are, thus, obtained since the gap is lower: $J_0 \sim 10^{-5}$ mA/cm^2 for E_g = 1.1 eV. The validity of this approximation will be confirmed in Chapter 4 (§ 4.5) where dark current measurements of µc-Si:H solar cells will be presented.

Note that this J_{00} value must be considered together with n = 2 (in equ (3.7)) in order to obtain realistic values for the solar cell parameters. Furthermore, our calculation assumes that thermal generation takes places in the entire intrinsic layer. In fact, the current density, as expressed in equ. (3.33), corresponds to an additional contribution to the reverse saturation current, in supplement to the "pn-diode" current densities as given in equ. (3.7) with a J_{00} value from equ. (3.21) or equ. (3.29). As a coarse approximation, only this additional contribution is taken into account (with n=2) for the calculation of our pin diode limits, as presented in Figs. 3.8, 3.9 and. 3.10 hereafter.

The limits for V_{oc} (E_g) are calculated:

- For pn diodes: from equ. (3.8) with n=1, based on models by Green (equ. (3.21)) and Kiess (equ. (3.29));
- For pin diodes: from equ. (3.30) with J = 0, $J_{rec} = 0.8 \cdot J_L$ and n=2, and our original approximation for pin junctions (equ. (3.33)).

The calculated limits for V_{oc} (E_g) are presented in Fig. 3.8:

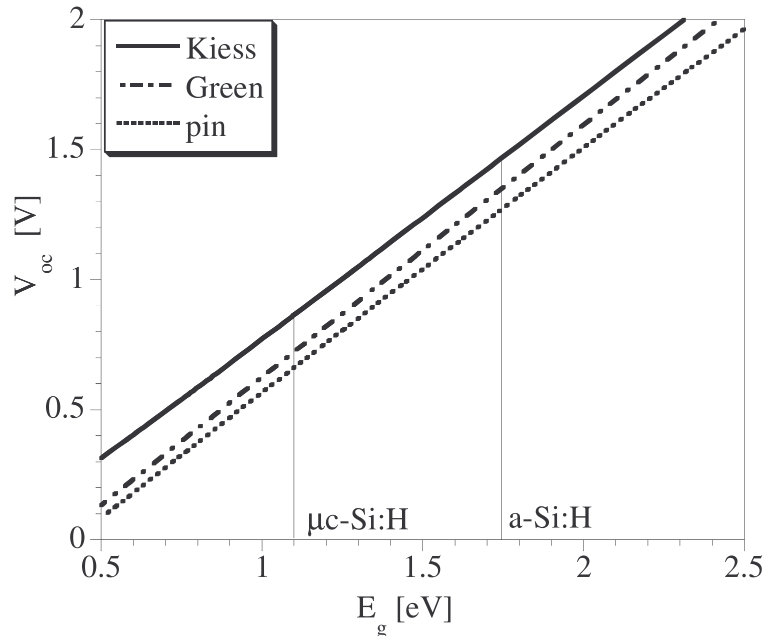

Figure 3.8. Upper limits of the open-circuit voltage as a function of the bandgap energy of the solar cell material: limit calculation based on Kiess' model, Green's model and our new coarse approximation for pin diodes.

The "fundamental" limit as obtained above for the pin junction is almost reached by present µc-Si:H solar cells that possess an open-circuit voltage $V_{oc} \approx 0.55$-0.60 V, see for example [9]. On the other hand, according to Fig. 3.7, around 0.3 V could still be gained with a-Si:H solar cells (currently $V_{oc} \sim 0.9$ V, see [14, 16]).

b) Fill factor FF and efficiency η

As previously mentioned, the fill factor FF can be expressed by:

$$FF = (J_{MPP} \cdot V_{MPP}) / (J_{sc} \cdot V_{oc}) \tag{3.34}$$

where J_{MPP} and V_{MPP} are the current density and the voltage at the maximum power point. J_{MPP} and V_{MPP} are obtained by maximising the (J·V) product by differentiation, considering the diode equation with n=1 (pn configuration) or n=2 (pin configuration).

The recombination current density, such as previously considered for the calculation of the open-circuit voltage, is again taken into account for the calculation of the pin junction fill factor limit. In addition, a fill factor limit is established for our interpretation of Kiess' model too (equ. (3.29)), instead of only considering FF = 0.85 as in the original paper by Kiess and Rehwald [34]. The calculated curves FF(E_g) are presented in Fig 3.9:

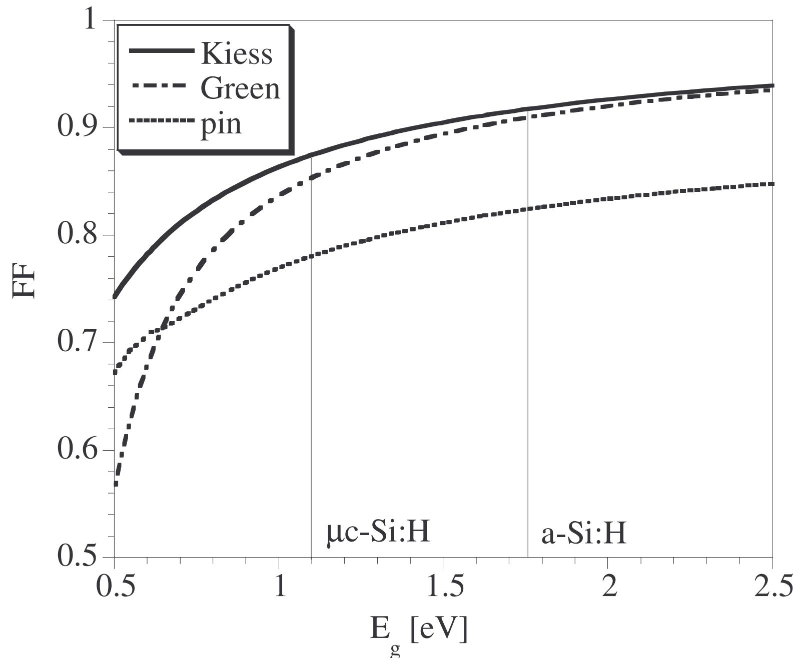

Figure 3.9. Upper limits of the fill factor as a function of the bandgap energy E_g of the solar cell material: limit calculated from our interpretation of Kiess' model, calculated based on Green's model and our new coarse approximation for pin diodes.

It can be seen in Fig 3.9 that the value for the fill factor limit as established for the pin junction with E_g = 1.1. eV is very similar to the values currently obtained with actual μc-Si:H solar cells; the latter having FF values up to 75 % [8, 9]. This limit was established from the coarse assumption of (a) a dark current from thermal generation from mid-gap defects and an additional recombination current, and (b)

an ideality factor n=2. In reality, dark J(V) measurement of µc-Si:H solar cells confirm that the situation is much more complicated with values of n ranging from 1.2 to 1.5, depending on the µc-Si:H sample measured (see Chapter 4).

Finally, the limit for the solar cell conversion efficiency can be computed by multiplying $J_{sc}\cdot V_{oc}\cdot$ FF and by dividing by the incident light energy. This yields the curves $\eta(E_g)$ of Fig. 3.10:

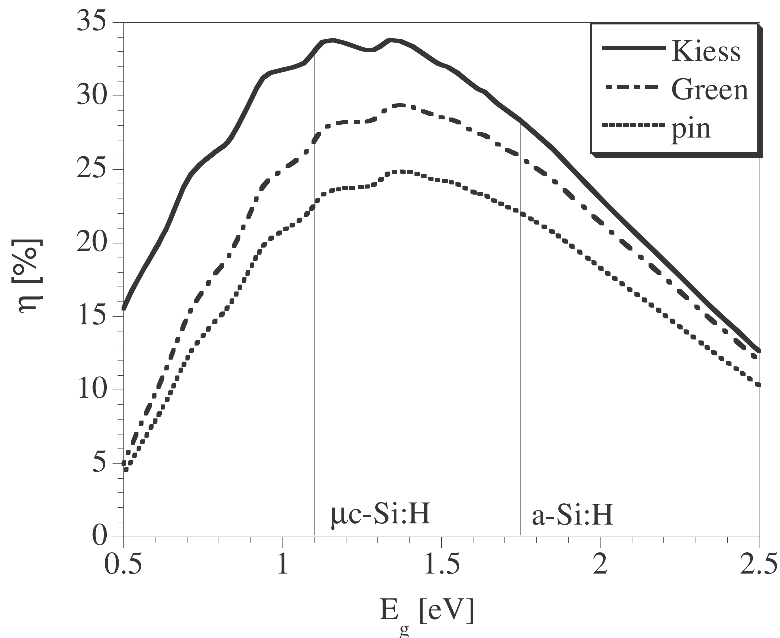

Figure 3.10. Upper limits of the conversion efficiency (for AM.15 spectrum) as a function of the bandgap energy E_g of the solar cell material: limit from our interpretation of Kiess' model, limit calculated based on Green's model and our new coarse approximation for pin diodes.

We, thus, obtain an upper limit for the efficiency, for E_g =1.1 eV, equal to:

- 33.2 % based on Kiess' model;
- 27.2 % based on Green's model;
- 23.0 % for the pin junction.

In all three cases, the maximum conversion efficiency of the AM 1.5 spectrum would be achieved for a semiconductor with E_g ~ 1.4 eV. The efficiency limit assessed from Kiess' model is, as would be expected, equal to the one published by Luque et al [36], established from Shockley and Queisser's theory. Nowadays, best existing single-junction µc-Si:H solar cells present efficiencies in the order of 10 % [8, 9]. The large difference observed between experimental and theoretical values is mainly due to the short-circuit current density, which is only in the order of 20-27 mA/cm^2 in typical present µc-Si:H solar cells instead of 43.6 mA/cm^2, as theoretically (ideally) predicted.

3.5 Tandem solar cell

As previously mentioned in Chapter 1, tandem solar cells are composed of two stacked cells, called the top and the bottom cell, which are deposited on top of each other. Such tandem cells are particularly interesting for thin-film silicon technology, as they allow one (a) to increase the limits in conversion efficiency (by enlarging the spectral range of absorption) as well as (b) to reduce degradation effects (by the use of thinner layers), see [16, 40].

From the theoretical point of view, a tandem cell is interesting if the bandgap of the two cells can be properly adjusted. Indeed, let us consider a single-junction solar cell with a gap $E_g^* = 1.4$ eV (that corresponds to the bandgap for maximum conversion efficiency under AM 1.5 illumination spectrum, see Fig. 3.10) with its short-circuit current density J_{sc}^*, open-circuit voltage V_{oc}^* and fill factor FF^* values. Now, select a top cell with $E_{g,\,top} > E_g^*$ and a bottom cell with $E_{g,\,bottom} < E_g^*$, more of less symmetrically to E_g^*, as schematically presented in Fig 3.11.

This combination corresponds to the “micromorph” (a-Si:H/µc-Si:H) tandem solar cell:

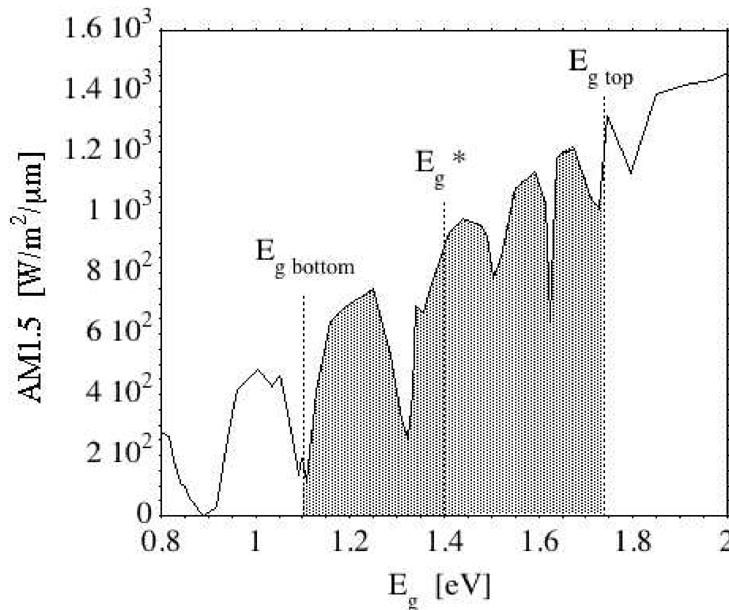

Figure 3.11. AM 1.5 spectra and basic principle of the tandem cell concept with bandgap matching; the shaded area corresponds to the photogenerated current of the bottom cell under the assumption that each photon with $h\nu > E_g$ is absorbed.

Tandem solar cells are connected in series, i.e. the voltage of the tandem is the sum of the voltages of both “partial” cells, whereas the current is limited to the lowest current of the two “partial” cells. Current matching (i.e. $J_{sc,\,top} = J_{sc,\,bottom}$) is, thus, critical for such tandem solar cells and limits the choice of the bandgap combination, as can bee seen from Fig. 3.12:

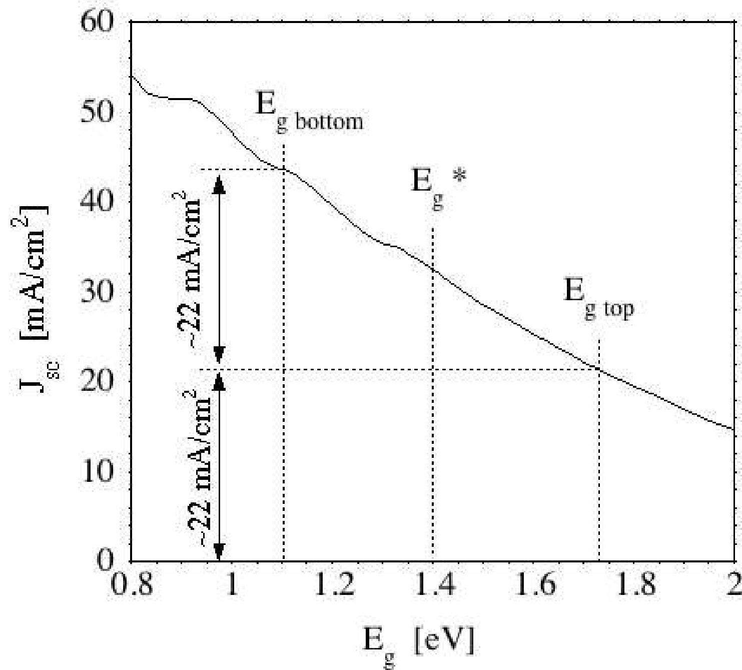

Figure 3.12. Upper limit of the short circuit current density J_{sc} as a function of the bandgap energies $E_{g,\ top}$ and $E_{g,\ bottom}$ of a tandem solar cell, under AM1.5 illumination

Fig. 3.12 shows that current matching is indeed obtained when $E_{g,\ top} \approx$ 1.75 eV and $E_{g,\ bottom} \approx$ 1.1 eV, yielding to $J_{sc,\ top} \approx J_{sc,\ bottom} \approx$ 22 mA/cm^2. If $E_{g,\ top}$ or $E_{g,\ bottom}$ are shifted towards higher, resp. lower values, the current balance between the 2 cells is altered, favouring the top or the bottom cell, thus limiting even more the current of the complete tandem solar cell.

The “micromorph” tandem can, thereby, be confirmed to lead “theoretically” to the highest conversion efficiency limit; a similar conclusion was presented by Luque et al [45], as well as Coutts et al. [46]. Both obtained very different limits: 38% for Luque et al. and 24 % for Coutts et al.; depending on the model we used for the solar cell junction, we obtain values ranging from 45% to 35% (see results hereafter). Luque et al considered very similar conditions to ours (ideal conditions, with no optical losses), whereas Coutts et al considered larger values for the reverse saturation current density, as well as optical losses (due to the transparent conductive oxide (TCO) layers mainly).

In our case, we computed the efficiency limits for tandem solar cells, as a function of the bandgap energy of both materials, by considering:

(a) A perfect balance between top and bottom cell current densities;

(b) The ideal case, where the bottom cell absorbs all the light transmitted by the top cell (which is considered to be infinitely thick).

Efficiency limits were first established for the simple case of a tandem composed of two pn junctions according to Kiess' and Green's models; the results are presented in Figs. 3.13 (a) and (b) as a function of the bandgap energy of the bottom and top cells:

(a)

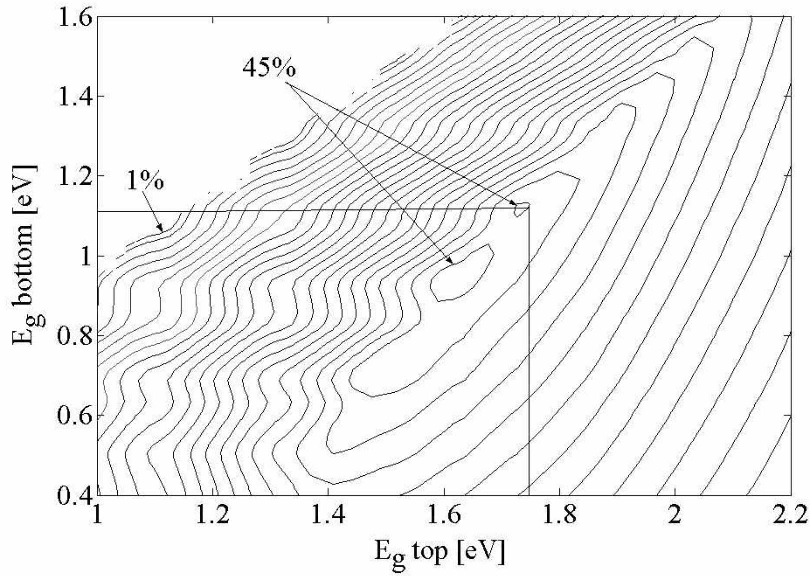

(b)

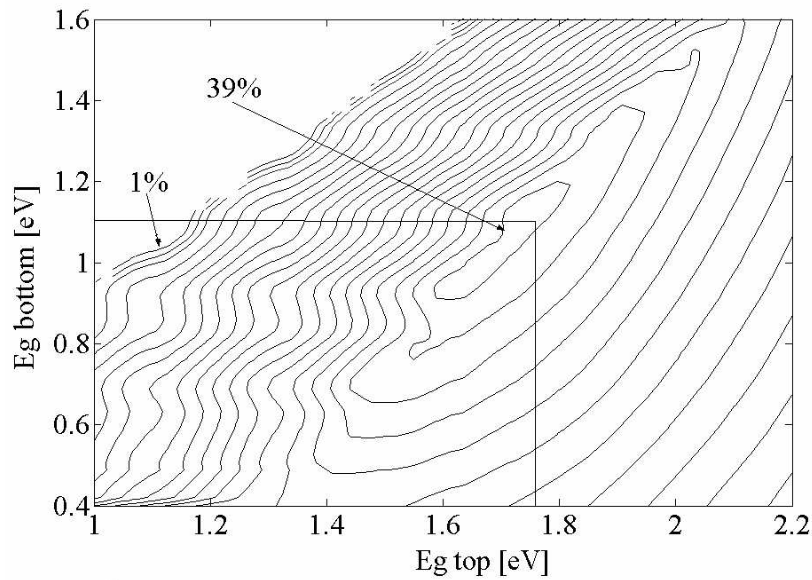

Figure 3.13. Upper limits of the efficiency of p-n/p-n tandem solar cell as a function of the bandgap energies $E_{g,\,top}$ and $E_{g,\,bottom}$, based on (a) Kiess' limit, and (b) Green's limit. The straight lines correspond to the μc-Si:H/a-Si:H tandem (1.1 eV/1.75 eV)

Fig 3.13 clearly shows that the combination 1.1 eV and 1.75 eV indeed presents the highest efficiency with $\eta = 45\%$ and 39%. It must be noted that even for

bandgap combination well away from the optimal combination, the efficiency achievable is still much higher than for single-junction solar cells (see for example $E_{g,\ bottom}$ = 1.4 eV and $E_{g,\ top}$ = 1.8 eV corresponding to a GaInP/GaAs tandem, with $\eta \sim 29\%$ according to the limit based on Green's model).

We then performed the same calculation for pin/pin junctions (under the same conditions as previously considered for single-junction solar cells: an additional recombination in the intrinsic layer, a generation/recombination contribution to the dark current due to mid-gap defects and an ideality factor n = 2, see §3.4.2, (a2)).

The result is presented in Fig. 3.14:

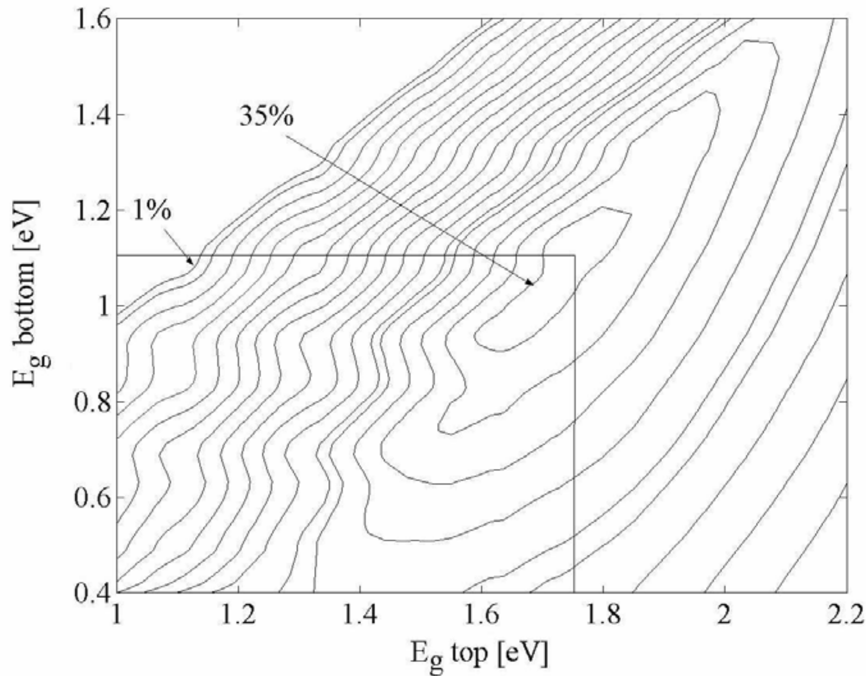

Figure 3.14. Upper limit of the efficiency of pin/pin tandem solar cell as a function of the bandgap energies $E_{g,\ top}$ and $E_{g,\ bottom}$. The straight lines correspond to the μc-Si:H/a-Si:H tandem (1.1 eV/1.75 eV)

The efficiency limit thus established is lower than for pn/pn junction, with a maximum of η = 35% for the μc-Si:H/a-Si:H tandem solar cell. However, efficiency values presently obtained with this type of tandem cells are much lower, in the order of 12 to 13.5% [16, 40]. The highest efficiencies are obtained when a zinc oxide intermediate reflector (ZIR) is employed between the two “partial” cells. Indeed, the path light is, thus, increased in the top cell leading to a higher short-circuit current density (the top cell is, in practice, generally the one that limits the current of the tandem, because the amorphous cell must be kept thin to avoid degradation effects).

3.6 Conclusions

3.6.1 Single-junction solar cells

Fundamental limits for pn and pin single and double-junction solar cells were established from the extension of well-known theoretical and semi-empirical considerations on pn junctions, as well as from an original model developed for pin junctions. These limits are, especially for the short-circuit current density J_{sc}, much higher than present values, and indicate scope and direction for further improvements that may still be obtained, e.g. by light-trapping and materials' research.

Losses in V_{oc}, FF and η due to the pin configuration have been assumed to be the consequence of both an additional recombination in the intrinsic layer, and a generation/recombination contribution to the dark current due to mid-gap defects (dangling bonds), with the ideality factor taken as n = 2. Even if these assumptions are a coarse approximation to the reality, the limits obtained for V_{oc} and FF for μc-Si:H solar cells are very close to the actual values. J(V) dark measurements of μc-Si:H solar cells show that the ideality factor is in fact lower than 2 (n is between 1.2 and 1.5, see Chapter 4, § 4.5.4), whereas the reverse saturation current densities J_0 are well in the order of magnitude of the J_0 value that was considered for the calculation of the pin limits. This would suggest that the limits we established are somewhat lower than the actual values achievable. Further work should be carried out to try to identify the exact nature of the dark current measured in our μc-Si.H pin solar cells.

Concerning a-Si:H, the limits established showed that higher values of V_{oc} and FF should be achievable; but, again, our assumption should be compared to actual measurements before establishing any conclusion. Wronski et al. have been actively working on dark J(V) measurements of amorphous silicon solar cell, trying to separate the effect of the bulk and the effect of the interfaces (especially the p-i interface) [47, 48]. Further work should, in our opinion, be undertaken in that direction (as discussed in Chapter 4 as well).

Finally, Coutts and al showed that the conductivity properties (mobility and carrier concentration) of the solar cell TCO (Transparent conductive oxide) also limit the efficiency that can be obtained for tandem cells; similar conclusion may certainly be drawn for single-junction solar cells.

3.6.2 Tandem solar cells

Considering tandem solar cells, the "micromorph" tandem (a-Si:H/μc-Si:H) was confirmed to correspond to an optimum combination for double-junction solar cells with an efficiency limit of 35%. This value is far above the present values

achieved (13.5% initial, with intermediate reflector), due to the very coarse and simple assumptions used for the numerical calculations. Nevertheless, a useful efficiency "map" of the bandgap combinations was thus established, confirming the choice of the silicon-based tandem actually developed.

Present research on the "micromorph" tandem solar cells is focused on the development of effective intermediate reflectors (Zinc Oxide Intermediate reflector-ZIR), as previously described (in p. 38): recently, Meier et al [14], as well as Dominé et al [40] showed that the use of such a ZIR leads to a relative increase of the short-circuit current density of the top (amorphous) cell of up to 25%.

4. Diagnosis of thin-film microcrystalline silicon solar cells

4.1 Introduction

Chapter 2 presented the classical, basic, measurement techniques employed for the electrical characterization of thin-film amorphous and microcrystalline silicon solar cells, such as:

- Classical J(V) curves at 100 mW/cm^2 (1 sun);
- External Quantum Efficiency curves [EQE (hν)], that can be performed at different values of bias voltage;

J(V) curves at 1 sun give information on the open-circuit voltage and the fill factor values, whereas EQE (hν, V_{bias}) gives information on the short-circuit current density (by integration of the EQE curve) and on the collection within the intrinsic layer (as evaluated from the EQE response in the red part of the spectra, i.e. between 700 and 1000 nm, for μc-Si:H). On the other hand, the EQE response in the shorter wavelengths provides insights into potential collection problems at the p-i interface.

More sophisticated characterization techniques have, as well, already been introduced in Chapter 2, notably:

- Micro-Raman spectroscopy;
- Fourier-transform photocurrent spectroscopy (FTPS);

Micro-Raman spectroscopy allows one to evaluate the intrinsic layer crystallinity (as measured with a HeNe laser at 633 nm), whereas FTPS probes the absorption coefficient α(hν) of the intrinsic layer and gives information about defect density (via α(0.8 eV)) and about the structural disorder (via the Urbach parameter E_0).

In this chapter, two additional characterization methods will be presented as diagnostic tools, for investigating faults in design and fabrication that may have a limiting effect on μc-Si:H and a-Si:H solar cell performances:

- Variable Illumination measurement (VIM);
- Dark J(V) measurement.

The entire package of diagnostic tools will then be applied to three different cases, mainly to investigate losses in fill factor, in connection with:

(a) Light-soaking study of two μc-Si:H solar cells series;

(b) A gas flow series;

(c) Individual μc-Si:H solar cells with low fill factors.

4.2 Variable Illumination Measurements (VIM)

4.2.1 Theory (pn/pin junctions)

The Variable Illumination measurement (VIM) method [41] consists in measuring the J(V) curves of the solar cells at different illumination intensities. In our case we used intensities ranging from one sun, i.e. from 100 mW/cm^2, down to 0.1 mW/cm^2, with a WACOM solar spectral simulator. Variable illumination is obtained by means of neutral (metallic) grey filters, which allow one to vary the intensity without modifying the spectra.

As previously presented in Chapter 3, the J(V) characteristic of a single-junction ideal pn solar cell under illumination can be written as the linear superposition of the photogenerated current density J_L and the dark current density of the cell:

$$J = J_0\left[\exp\left(\frac{qV}{nkT}\right)-1\right]-J_L \qquad (4.1),$$

with J_0 the reverse saturation current density, V the voltage, q the elementary charge, k the Boltzmann constant, T the absolute temperature and n the ideality factor: n=1 when the diffusion current dominates and n=2 when the recombination current dominates. When both currents are of comparable magnitudes, n is between 1 and 2.

However, this superposition principle is not valid in its simple form when considering amorphous and microcrystalline silicon pin junctions (even with n=2): a recombination term must be added, as introduced by Merten et al. [41, 49]. Indeed, Kusian et al [42] showed that the J(V) curves of a-Si:H solar cells, as measured under variable illumination, all cross at a single intersection voltage value $V_{int} > V_{oc}$; such a behavior cannot be described using the superposition principle in its simple form, such as given in equ. (4.1). Similar observations were made for µc-Si:H silicon solar cells (see Chapter 3). Consequently, Merten et al. introduced the equivalent circuit of Fig. 4.1, valid for thin-film silicon solar cells.

In previous equivalent circuits, J_{rec} and R_{sh} were included into a parallel resistance R_p. Here, the current sink J_{rec} is a function of J_L and V and depends on the intrinsic layer "quality", whereas the shunt resistance R_{sh} originates from micro-shunts at the edges (resulting from the device structuration process) or in the bulk of the cell (resulting from the material's microstructure such as voids, or from particles). The series resistance R_s is given by the resistance of the contacts and by the TCO sheet resistance (as in the case of series-interconnected cells or very large cells, depending on the location of the contact to the TCO). The electrical behavior of the ideal diode D is described by equ. (4.1), and characterized by the parameters J_0 and n. J_0 is related to the material's bandgap, the defect density N_d and the intrinsic layer thickness d_i.

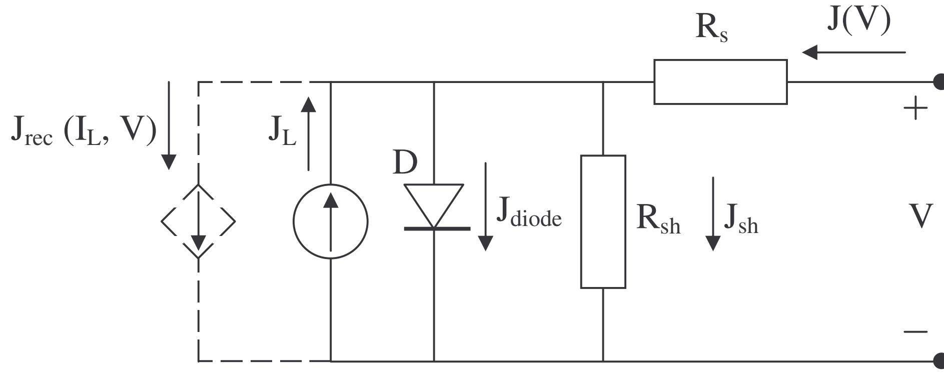

Figure 4.1. Equivalent circuit for pin (or nip)-type solar cells [41] with J_L the photogenerated current density, D the ideal diode, R_{sh} the shunt resistance, R_s the series resistance and, dashed lines, the recombination current density (which is a function of J_L and V)

This equivalent circuit is, thus, very useful for cell diagnostic, as it splits up the parallel resistance of the usual equivalent circuit into 2 distinct parts: a recombination part (represented by J_{rec}) and "true" physical (linear and non-linear) shunts (represented by R_{sh}). Merten et al. showed that there is, over 5 decades of light intensity, an excellent fit between J(V) curves calculated from this model and experimental J(V) characteristics for typical a-Si:H solar cells. In the present chapter, this model is introduced and compared to experimental data for µc-Si:H solar cells. In our formal approach, we are adding the collection current density J_{coll}, and the dark diode current density J_{diode}:

$$J_{total} = J_{coll} + J_{diode} \tag{4.2}$$

J_{diode} is given by the drift-diffusion diode model, as contained in equ. (4.1); for a pin diode J_{coll} is given by:

$$J_{coll} = J_{rec} + J_{sh} - J_L \quad (4.3),$$

with [41, 49]:

$$J_{rec}(V) = (d_i \cdot J_L)/(E_{eff} \cdot (\mu\tau)_{eff}) \quad (4.4),$$

where:

- $(\mu\tau)_{eff} = 2 \cdot \dfrac{\mu_n^0 \tau_n^0 \cdot \mu_p^0 \tau_p^o}{\mu_n^0 \tau_n^0 + \mu_p^0 \tau_p^0}$ is the effective mobility-lifetime product of the intrinsic layer; the mobility-lifetime product is defined, for electrons, as $\mu_n^0 \tau_n^0 = \mu_n^o \cdot \dfrac{1}{v_{th} N_{db} \sigma_n^0}$ with μ_n^0 the electron band mobility, v_{th} the thermal velocity, N_{db} the dangling bond density and σ_n^0 the capture cross-section of the neutral dangling bonds. The definitions are exactly similar for holes.

- $E_{eff} \approx (V_{bi} - V)/(\varphi(V) \cdot d_i)$ is the effective electric field within the intrinsic layer: V_{bi} is the built-in voltage, V the external applied voltage, d_i the intrinsic layer thickness and φ a correction factor taking into account the deformation of the electric field E(x). φ is a function of the applied voltage (as well as of the intrinsic layer thickness): the deformation of the electric field may, in fact, be assumed to be negligible, for relatively thin cells, at short-circuit conditions and, especially, under reverse bias (i. e. here we may postulate: φ = 1). On the other hand, the relative deformation of the electric field, as well as the correction factor φ, both increase as we approach the maximum power point [50, 51]. Furthermore, there is often, within the intrinsic layer of μc-Si:H solar cells, a deformation of the electric field that is due to oxygen contamination [51]; this will also lead to an increase in the value of φ.

Equ. (4.4) can, thus, be rewritten:

$$J_{rec}(V) = (\varphi(V) \cdot d_i^2 \cdot J_L)/((\mu\tau)_{eff} \cdot (V_{bi} - V)) \quad (4.5)$$

Equs. (4.2) and (4.3) contribute to the basic theoretical model for a-Si:H or μc-Si:H pin type diodes. They replace the superposition principle of pn diode given in equ. (4.1). In fact, equs. (4.2) and (4.3) correspond to an “extended” form of the superposition principle, which has so far only been derived experimentally and intuitively. However, a solid collection model underlies equ. (4.3), in which Merten et al considered that the photocurrent is voltage-dependent, unlike the photocurrent in the pn junction model, which is generally assumed to be constant [33]). The voltage dependence is introduced by the recombination current $J_{rec}(V)$, as introduced in equ. (4.5) (see also Chapter 3, § 3.4.2 (a2)). A very similar model was, in fact, introduced by Crandall [53] (see [50] for a discussion/comparison of both collection models). Crandall also introduced the collection length L_c, defined as the sum of the drift lengths of the electrons and holes.

We will, in order to simplify the formalism, assume that all the recombination centers (dangling bonds) in the material are neutral and we will consider the “normalized” $\mu^0\tau^0$-product ($\mu_n^0\tau_n^0 = \mu_p^0\tau_p^0 = \mu^0\tau^0$), as introduced in [50]. In reality, dangling bonds are not always all neutral; they are, especially at the p/i and i/n interfaces, positively and negatively charged, resp. However J. Hubin et al showed [52] that this effect can be neglected for a-Si cells; his considerations are certainly also valid for μc-Si cells. Under this assumption, $(\mu\tau)_{eff}$ is, thus, equal to $\mu^0\tau^0$.

According to [52], the collection length is defined as:

$$L_c = \mu^0\tau^0 E_{eff} = \mu^0\tau^0 \left[(V_{bi} - V)/d_i\right] \quad (4.6),$$

and the collection current density J_{coll} is then expressed by (if $R_{sh} \rightarrow \infty$):

$$J_{coll} = qGL_c(1-\exp(-d_i/L_c)) = qGd_i(L_c/d_i)[1-\exp(-d_i/L_c)] \quad (4.7),$$

with q the elementary charge, G the generation rate and d_i the intrinsic layer thickness. Indeed, J_{coll} is given by:

$$J_{coll} = J_p + J_n = qE(\mu_p p + \mu_n n) \quad (4.8),$$

with E the electric field, μ_p and μ_n the hole and electron mobility, resp., and p and n the hole and electron density; the latter are expressed as a function of the position x within the intrinsic layer:

$$p = G\tau_p[1-\exp(-x/l_p)] \text{ and } n = G\tau_n[1-\exp(x-L/l_n)] \quad (4.9),$$

where τ_p and τ_n are the recombination time for holes and electrons, resp., and l_p and l_n are the hole and electron drift lengths. According to Crandall, equ. (4.7) is, thus, obtained by substituting equ. (4.9) into equ. (4.8), evaluated at the position where $p/\tau_p = n/\tau_n$, i.e. where the recombination rate is maximum.

By combining equs. (4.6) and (4.7), with $qGd_i = J_{sc} = J_L$, and by approximating the exponential function, we obtain:

$$J_{coll} \approx J_L\,(1-(d_i/L_c)) \approx J_L\left[1-(d_i^{\,2}/[\mu^0\tau^0(V_{bi}-V)])\right] \quad (4.10),$$

which is equivalent to equ. (4.3) (with J_{rec} given by equ. (4.5)) without the additional term J_{sh}, introduced by Merten et al.

The current density through physical micro-shunts is given by:

$$J_{sh} \approx V/R_{sh} \quad (4.11)$$

It must be noted that R_{sh} is expressed in <u>kΩ·cm²</u> (instead of Ω or kΩ as expressed in SI base units). This unit was chosen because of the use of current density (in mA/cm^2); R_{sh}, R_s and R_{sc} will, thus, all be expressed in <u>kΩ·cm²</u> in the further calculations of this chapter.

The collection voltage is defined as (see also [41]):

$$V_{coll} = \frac{\mu^0\tau^0 \cdot V_{bi}^2}{d_i^2} \quad (4.12);$$

it can be expressed as a function of the collection length (at V = 0V) through the expression:

$$V_{coll} = L_c(0V)\cdot\frac{V_{bi}}{d_i} \quad (4.13)$$

In case of electric field deformation, φ is larger than 1 and equ. (4.12) becomes:

$$V_{coll} = \frac{\mu^0 \tau^0 \cdot V_{bi}^2}{d_i^2 \cdot \varphi} \quad (4.14)$$

According to [40], let us define the short-circuit current resistance R_{sc}:

$$R_{sc} = (\partial V / \partial J)_{V=0} \quad (4.15)$$

R_{sc} thus corresponds to the reciprocal of the slope of the J(V) curve at V= 0, as shown in Fig. 4.2 below:

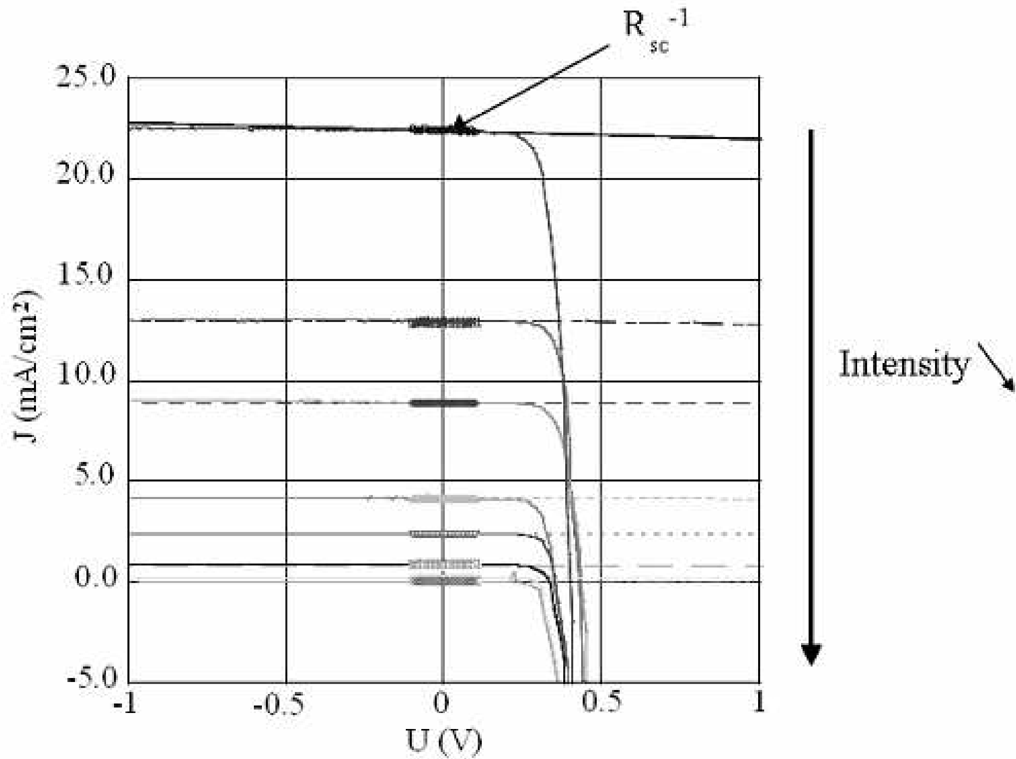

Figure 4.2. VIM curves of a typical microcrystalline silicon solar cell, with the reciprocal of the short-circuit resistance R_{sc}: the value of R_{sc} tends toward the shunt resistance value R_{sh} for low illumination intensities ([41, 50] and equ. (4.17))

For low illumination intensity (below ~10^{-2} suns), R_{sc} is determined by the diode term and the shunt losses of equs. (4.2) and (4.3) (see [50]). Furthermore, we may assume that the dark diode term is (at V = 0V) often negligible with respect to the shunt resistance. We, thus, obtain:

$$R_{sc}^{-1} \approx \frac{1}{R_{sh}} + \frac{qI_o}{nkT} \approx \frac{1}{R_{sh}} \quad (4.16)$$

For medium illumination intensity (~10^{-2} sun – 1 sun), R_{sc} is limited by the recombination term of equ. (4.3) [41, 50]; it is expressed by:

$$R_{sc} \approx \frac{\mu^o \tau^0 V_{bi}^2}{d_i^2} \cdot \frac{1}{J_{sc}} = V_{coll} / J_{sc} \tag{4.17}$$

The collection voltage V_{coll} can, thus, be experimentally assessed from measurements of R_{sc} as a function of J_{sc}^{-1} (= J_L^{-1}), as illustrated by Fig. 4.3:

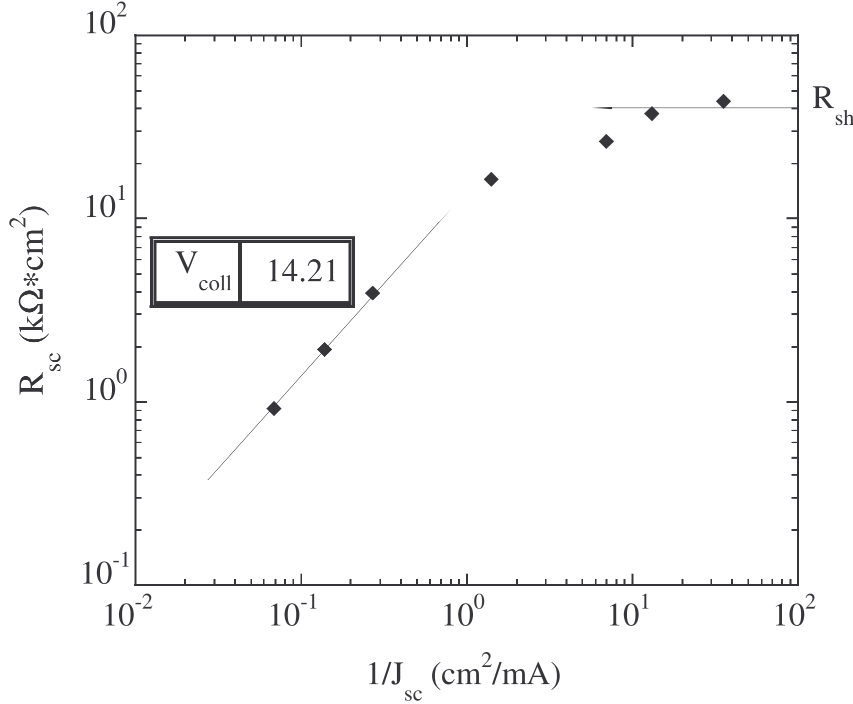

Figure 4.3. Short-circuit resistance R_{sc} as a function of the reciprocal of the short-circuit current density J_{sc}^{-1} for a typical μc-Si:H solar cell (of Raman crystallinity factor ϕ_c ~ 50%): the straight line corresponds to a fit of the linear part of the curve according to equ. (4.17). The curve tends asymptotically towards R_{sh}, for high J_{sc}^{-1}.

Finally, the effective (or normalized) $\mu^0\tau^0$-product can be evaluated from the values of the collection voltage and the intrinsic layer thickness according to equs. (4.14) and (4.17). But, care must then be taken to compare only values of $\mu^0\tau^0$-products as established from cells of similar i-layer thickness (see § 4.3).

Furthermore, we will see in § 4.3 that the VIM technique cannot be used under all circumstances to gain information on the intrinsic layer material's quality, i.e. on $\mu^0\tau^0$-product, since VIM is much more sensitive to defective interfaces or microstructure gradients than coplanar transport measurements, such as Steady-State Photoconductivity (SSPC) or Steady-State Photocarrier Grating (SSPG), typically used for the measurement of $\mu^0\tau^0$-products in layers on glass. Defective interfaces will influence the electric field deformation (i.e. the correction factor φ will be larger than 1).

4.2.2 Effects of recombination current density (J_{rec}), shunt resistance (R_{sh}) and defect-related absorption (α(0.8 eV)) on fill factor (FF) losses

From the equivalent circuit presented before, we will establish empirical relationships between losses in fill factor and values of:

(a) The circuit parameters: J_{rec}, R_{sh}, R_s

(b) The defect-related absorption α(0.8 eV) of the intrinsic layer material

In the case (a), an increase in J_{rec} is physically due to an increased recombination within the intrinsic layer of the material, e.g. as obtained by light-induced degradation of μc-Si.H solar cells. A decrease in R_{sh} can be, in practice, due to imperfect device structuration or localized shunts (due to dust/ZnO particles for example), whereas an increase in R_s indicates a too large resistance of the contacts. In the case (b), the defect-related absorption can be varied e.g. by light-soaking the solar cells or by modifying the intrinsic layer fabrication conditions. Here, we focus on situations where the variations of V_{oc} and J_{sc} are negligible with respect to the variations of FF. We will consider <u>absolute</u> losses in FF with respect to an ideal fill factor value of FF_0 = 75% as achieved in our lab with best μc-Si:H solar cells [9]. This ideal value is very close to the theoretical upper limit established in Chapter 3, that is FF ~ 78% for μc-Si:H solar cells.

Fig. 4.4 schematically represents the variation of an "ideal" J(V) curve (with FF = 75%) when J_{rec} is strongly increased :

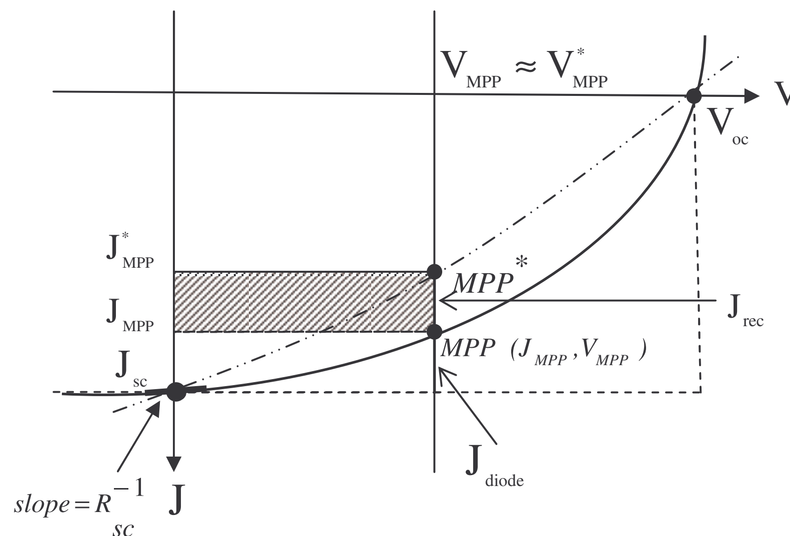

Figure 4.4 Schematic representation of J(V) curves for the "ideal" cell (plain curve) and for a cell with strong recombination losses (dashed curve). The dashed area corresponds to the fill factor loss (under the assumption that J_{sc}, V_{oc} and V_{MPP} remain the same, and that only J_{MPP} is reduced)

We will consider three different situations that lead experimentally to a decrease of FF:

(a) Light-soaking with an increase of J_{rec} and α(0.8 eV). In that case we observed that, as assumed here, variations of J_{sc}, V_{oc} and V_{MPP} are negligible. Furtheremore, the shunt resistance R_{sh} is not modified (see Chapter 5): for simplification we will consider, in this case, $R_{sh} \sim \infty$. We will also consider that R_s remains constant.

(b) Low values of R_{sh} ($R_{sh} \leq$ ~10 kΩ·cm^2) due to micro-shunts;

(c) Large values of the series resistance R_s ($R_s \geq$ ~10 Ω·cm^2) due e.g. to high TCO sheet resistance.

The case (a) will be discussed in details and experimental results will confirm the empirical relationship established hereafter. The case (b) will also be discussed and compared to experimental results, whereas (c) will only be treated theoretically. More complete investigations on this subject should, thus, still be performed.

a) FF decrease due to light-induced degradation

a.1) µc-Si:H

Let us consider the following situation for µc-Si:H:

(1) V_{oc} and J_{sc} are not essentially changed by degradation, as schematically presented in Fig. 4.4 (within ± 2.5 % according to Chapter 5). According to our model of Fig. 4.4 and the assumptions (2) to (6) hereafter, these slight variations should correpond to low FF losses (δFF less than 5%). For larger δFF, the deformation of the electric field increases, as we go from for short-circuit conditions (V=0) towards the maximum power point MPP ($V=V_{MPP}$). However, to simplifiy the calculations we will set φ (V_{MPP}) ≈ 1; subsequently, we will show that our experimental results are well fitted this way, even for fill factor losses larger than 5% (see Figs. 4.11, 4.16).

(2) The maximum power point (MPP) is always at approximately the same voltage V_{MPP} (within ± 5 %);

(3) $V_{MPP} \approx 0.5 \cdot V_{bi} \approx 0.5 \cdot V$ (we assume $V_{bi} \approx 1$ eV for µc-Si:H);

(4) In the ideal case J_{rec} can be neglected, i.e. $J_{sc} = J_L$;

(5) $V_{MPP} \approx 0.9\ V_{oc}$ (as experimentally observed, see [9] for example);

(6) $J_{MPP,\ ideal} \approx 0.83\ J_{sc}$ (also see [9]);

All these assumptions lead to:

(7) $J_{MPP,\ ideal} - J_{MPP,\ deg} = \Delta J_{MPP} = J_{rec,\ deg}$

Now, with FF_0 equal to the ideal value of 75%, we obtain from (5) and (7) that

$$FF_0 - FF_{deg} = \delta FF = \frac{V_{MPP} \cdot \Delta J_{MPP}}{J_{sc} \cdot V_{oc}} = \frac{J_{rec,deg}}{J_{sc}} \cdot \frac{V_{MPP}}{V_{oc}} \approx 0.9 \cdot \frac{J_{rec,deg}}{J_{sc}} \tag{4.18}$$

By combining equs. (4.5) and (4.18), we can write:

$$\delta FF \approx 0.9 \cdot \frac{\varphi(V_{MPP}) \cdot d_i^2}{(\mu^0\tau^0)_{deg} \cdot (V_{bi} - V_{MPP})} \tag{4.19}$$

With the assumption (3) we obtain typical values of δFF for μc-Si:H as given by (with $d_i^2 = cm^2$ and $\mu^0\tau^0 = cm^2/V$):

$$\delta FF \approx 90\% \cdot \frac{\varphi(V_{MPP}) \cdot d_i^2}{(\mu^0\tau^0)_{degr} \cdot 0.5V} \tag{4.20}$$

If we now look at the collection voltage V_{coll}, we find from equs. (4.14), (4.17) and (4.18):

$$\delta FF\ (\%) \approx \varphi(V_{MPP}) \cdot \frac{V_{bi}}{V_{coll}} \cdot \frac{V_{MPP}}{V_{oc}} \approx \varphi(V_{MPP}) \cdot \frac{V_{bi}}{V_{coll}} \cdot 90 \tag{4.21}$$

with $V_{bi} \sim 1V$ and V_{coll} that can be directly obtained from VIM measurements.

a.2) a-Si:H

Empirical relationships can be established in a similar manner for amorphous silicon; however, some of the above assumptions must then be modified:

(1) In a-Si:H, V_{oc} is limited to about 0.9 V (instead of the ideal limit which is around 1.3 V, see Chapter 3) and we do not know the exact reason for this limitation: it is certainly due (partly at least) to the impossibility of pushing the Fermi-level near to the conduction band (in n-doped a-Si:H layers) or near to the valence band (in p-doped layers), see for example [29]. The situation is actually more complex when we use μc-Si:H p- and n-doped layers within a-Si:H pin (nip) solar cells.

(2) The ratios of V_{MPP}/V_{oc} and J_{MPP}/J_{sc} given in the assumptions (5) and (6) above

are slightly lower for a-Si:H: $V_{MPP} \approx 0.8 \cdot V_{oc}$, $J_{MPP,\ ideal} \approx 0.8 \cdot J_{sc}$ (see for example [14])

(3) In a-Si:H solar cells, there is always, and especially in the degraded state, a considerable deformation of the electric field. To take this into account, one may consider here $\varphi \approx 2$ in equ. (4.14).

(4) Mainly because of interface effects (the highest densities of states are at p/i and n/i interfaces), $\mu^0\tau^0$ is relatively low in the relatively thin a-Si:H solar cells (in the order of $5 \cdot 10^{-8}$, see results presented later in § 4.3.3).

(5) $d_i \approx 0.2 - 0.4\ \mu m$ in a-Si:H solar cells

We, thus, obtain for a-S:H solar cells the approximate expression, with $V_{bi} = 1V$, $V_{MPP} \sim 0.7\ V$ and $\varphi = 2$:

$$\delta FF \approx 90\% \cdot \frac{2 \cdot d_i^2}{(\mu^0\tau^0)_{degraded} \cdot 0.3V} \tag{4.22}$$

and

$$\delta FF \approx \frac{V_{bi}}{V_{coll}} \cdot \frac{V_{MPP}}{V_{oc}} \approx \frac{V_{bi}}{V_{coll}} \cdot 80\% \tag{4.23}$$

Experimentally, losses of fill factor in the order of 5% are measured after light-soaking of a-Si:H cells with intrinsic layer thickness equal to $d_i \approx 0.3\ \mu m$. These observations are in rough agreement with our expressions, considering that for such an i-layer thicknesses, equ. (4.22) gives the absolute loss $\delta FF = 4.8\%$ (i.e. FF = 70.2%) with $\mu^0\tau^0 \approx 5 \cdot 10^{-8}\ cm^2/V$, whereas equ. (4.23) gives the absolute loss $\delta FF = 5.3\%$ (i.e. FF = 69.7%) with $V_{coll} \sim 15V$, as measured in a-Si:H solar cells [50].

b) <u>FF decrease due to shunts (low R_{sh})</u>

From the equivalent circuit of Fig. 4.1, we obtain:

$$\Delta J_{MPP} = \frac{V_{MPP}}{R_{sh}} \tag{4.24}$$

and equ. (4.18) becomes:

$$\delta FF = \frac{V_{MPP} \cdot \Delta J_{MPP}}{J_{sc} \cdot V_{oc}} = \frac{V_{MPP}}{J_{sc}} \cdot \frac{V_{MPP}}{V_{oc}} \cdot \frac{1}{R_{sh}} \tag{4.25}$$

- in μc-Si:H: V_{MPP}/J_{sc} ~ 0.025 kΩ·cm² (V_{MPP} ~ 0.5 V, J_{sc} ~ 20 mA/cm²),
- in a-Si:H: V_{MPP}/J_{sc} ~ 0.05 kΩ·cm² (V_{MPP} ~ 0.7 V, J_{sc} ~ 14.5 mA/cm²),

Equ. (4.25) thus gives:

- $\delta FF\,(\%) \approx 2 \cdot \frac{1}{R_{sh}}$ for μc-Si:H, R_{sh} in kΩ·cm² (4.26)
- $\delta FF\,(\%) \approx 4 \cdot \frac{1}{R_{sh}}$ for a-Si:H, R_{sh} in kΩ·cm² (4.27)

We will show in § 4.6 that the low FF values of the μc-Si:H solar cells used in this work are mainly due to low collection voltages and not to low shunt resistances.

c) FF decrease due to series resistance (large R_s)

There are 2 issues here:

(1) R_s will mainly affect V_{MPP} and not J_{MPP},

(2) If we look at the current paths within the TCO (transparent conductive oxide) R_s depends on the solar cell geometry (surface): it depends on how far the current has to travel, essentially in the front TCO, which has a finite resistance (ρ ≠ 0).

The loss in fill factor can be assessed either from the series resistance R_s, as established from VIM measurements (not from R_{sc} but from R_{oc}, going up to 2 to 3 suns, see [41])), or from the sheet resistance R_{sheet} of the TCO. Current good μc-Si:H solar cells present R_s values in the order of 2-3 Ω·cm², wheras the sheet resistance of the TCO should be lower than 10 $\Omega/_{sq}$ [39, 55].

From (1), we obtain:

$$\delta FF = \frac{\Delta V_{MPP} \cdot J_{MPP}}{J_{sc} \cdot V_{oc}} \tag{4.28}$$

ΔV_{MPP} is given by (from the equivalent circuit of Fig. 4.1):

$$\Delta V_{MPP} = R_s \cdot J_{MPP} \tag{4.29}$$

Equ. (4.28) thus becomes:

$$\delta FF = \frac{\Delta V_{MPP} \cdot J_{MPP}}{J_{sc} \cdot V_{oc}} = \frac{R_s \cdot J^2_{MPP}}{J_{sc} \cdot V_{oc}} \quad (4.30)$$

For μc-Si:H, we can roughly estimate J_{MPP} as being 18 mA/cm^2 for J_{sc} equal to 22 mA/cm^2; we assume V_{oc} ~ 530 mV (see assumption (6) in § 4.2.2 (a)); this gives us:

$$\delta FF\ (\%) \approx 3 \cdot R_s \text{, with } R_s \text{ in } \Omega \cdot cm^2 \quad (4.31)$$

In [56], Shah et al established that the power loss ΔP/P of a thin-film solar cell, as induced by the sheet resistance R_{sheet} of the TCO layer, can be expressed by:

$$\frac{\delta P}{P} = \frac{w^2 \cdot R_{sheet}}{3} \cdot \frac{J_{MPP}}{V_{MPP}} \quad (4.32),$$

where w is the width of the cell stripe. Equ. (4.32) was established considering the Joule losses within the TCO layer, as incorporated into the following geometry:

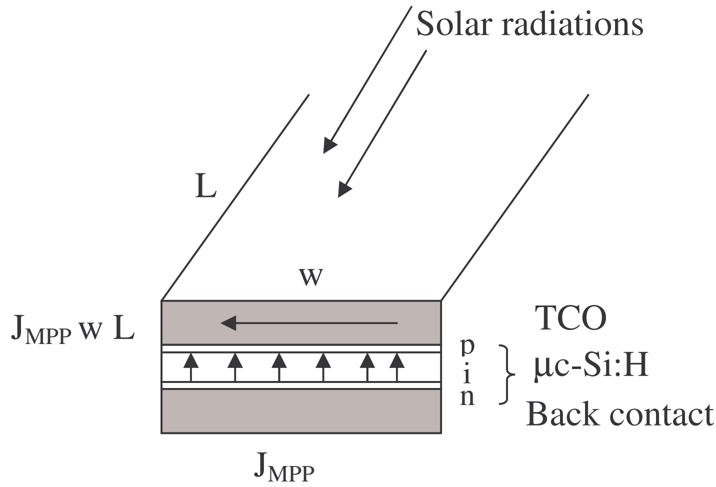

Figure 4.5 Scheme of the solar cell geometry (in nip configuration) with w the width and L the length of the cell stripe (serveral stripes are connected in series to form a module) (see also [55]).

From the assumption (5) of § 4.2.2 (a), we get, for μc-Si:H, $V_{MPP} \approx 480$ mV; we can, thus, rewrite equ. (4.32):

$$\frac{\delta P}{P} (\%) \approx 1.3 \cdot w^2 \cdot R_{sheet}, \; R_{sheet} \text{ in } \Omega/_{sq} \quad (4.33)$$

Under our assumptions, we can consider that δP/P=δFF/FF; with FF_0 = 75%, we therefore obtain:

$$\delta FF\ (\%) \approx w^2 \cdot R_{sheet}\text{, } R_{sheet} \text{ in } \Omega \qquad (4.34)$$

With the equivalent circuit introduced in this paragraph, we were able to predict losses in FF due to light-soaking (increase of recombination current density), shunts and high series resistance. These predictions will be compared and discussed in relationship with experimental observations, for the first two cases, in paragraphs § 4.4 and 4.5.

4.2 Dark J(V)

Dark J(V) measurements allow one to establish the experimental values of the reverse saturation current density J_0 and the ideality factor n, to be used in the preceding "theoretical" model (equs. (4.2 - 4.3) and Fig 4.1). J(V) dark curves are generally characterized by an ideality factor that is independent of the voltage; n has a value between 1 and 2 [57, 58]. According to the "classical" pn diode theory, n is such as: n=1 when the diffusion current dominates and n=2 when the recombination current dominates. When both currents are of comparable magnitudes, n is between 1 and 2 (see Chapter 3 and [30]). For pin diode junctions, no rigorous theory has been developed as yet; by intuitive extension from the pn diode theory, one may assume that n tending towards 2 is associated with the case of an "ideal" pin diode where defect density is uniform [51]. Nevertheless, some authors report that n tending towards 1 may be associated with the case where interface (p/i and/or i/n) recombination dominates [59].

4.2.1. a-Si:H

Detailed investigations have been carried out, for many years, on J(V) dark characteristics of a-Si:H solar cells [57, 58]. Attention was more particularly focused on the effect of light-soaking on J(V) dark characteristics: contributions associated with bulk recombination were observed in such situations [60, 61]. More recently, Deng et al. associated the increase of J_0 and n due to light-soaking to modifications of the energy distribution of the bandgap defects [62].

4.2.2. µc-Si:H

Detailed investigations of dark J(V) characteristics have not been carried out for µc-Si:H as yet; however, we can mention that Klein et al [63] also observed an increase of J_0 and n with light-soaking, especially for cells of low crystalline volume fraction. They attributed this increase to a larger light-induced defect density, and, thus, to an increased recombination, in the amorphous phase.

4.2.3 Dark J(V) measurements

Fig 4.6 shows an example of dark J(V) measurement, carried out at room temperature (T = 293 °K), for a typical µc-Si:H solar cell; we established the

experimental values of J_0 and n by fitting such a dark J(V) curve with the dark diode equation (as contained in equ. (4.1)).

In Chapter 3, we assumed, for the calculation of the theoretical limits in the pin configuration, that the reverse saturation current J_0 was equal to ~ 10^{-5} mA/cm^2 for μc-Si:H. This range of value is confirmed by the dark measurements performed on both our pin and nip series that give J_0 values in the order of 10^{-5} – 10^{-6} mA/cm^2.

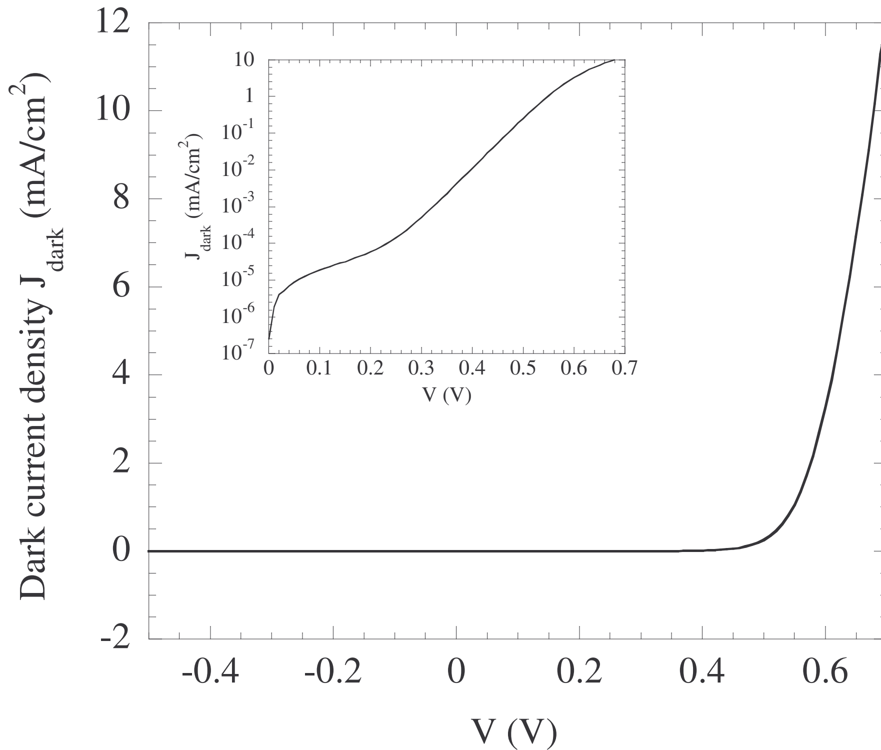

Figure 4.6. Dark J(V) measurement of a typical microcrystalline silicon solar cell (of medium crystallinity, ϕ_c ~ 50%): linear and logarithmic representation.

4.3 Effect of i-layer thickness on the $\mu^0\tau^0$-product of solar cells and individual i-layers

4.3.1 Introduction

In this paragraph we will focus on the experimental evaluation of $\mu^0\tau^0$-products (= $(\mu\tau)_{eff}$, see remark on the bottom of p. 44) by three different techniques:

- Photoconductivity (SSPC);
- Steady-state photocarrier grating (SSPG); and
- Variable Illumination measurement (VIM)

for thickness series of annealed and degraded a-Si:H layers and cells, as well as thickness series of μc-Si:H solar cells and layers. Note that whereas SSPC and SSPG will be jointly used to evaluate layers grown on glass, and are measurements

performed in the coplanar configuration (transport path parallel to the substrate), VIM will be applied to complete solar cells and is performed in the transverse configuration (transport path perpendicular to the substrate plane). Furthermore, SSPC and SSPG are techniques based on photoconductive methods which probe that part of the layers with the best transport properties, whereas VIM is a technique based on the J(V) curves which takes into account the recombination integrated over the entire depth of the intrinsic layer.

In a-Si:H and μc-Si:H solar cells, the $\mu^0\tau^0$-products are deduced from VIM measurements according to equ (4.17), whereas $\mu^0\tau^0$-products cannot be measured by a single experiment in a-Si:H and μc-Si:H layers, as both neutral and charged defects always coexist in such layers. $\mu^0\tau^0$-products were, thus, experimentally established in layers from measurements of the mobility-recombination lifetime products $\mu^0\tau^R$, for both majority and minority carriers. $\mu^0\tau^0$ corresponds to the value that the measured $\mu^0\tau^R$-products would take if all the defects in the material were neutral. SSPC and SSPG are two methods used to analyze coplanar electronic transport of a photoconductive semiconductor, such as silicon thin films under illumination. In these measurement techniques, a steady-state condition between generation and recombination of free carriers is achieved by steadily illuminating the sample.

SSPC gives information about the photoconductivity σ_{photo}, whereas SSPG gives access to the ambipolar diffusion length L_{amb}. Details on these methods can be found in [64, 65]. The application of the SSPG method to μc-Si:H layers is more delicate than for a-Si:H; its validity was discussed in detail in [66].

$\mu^0\tau^0$-products were established from σ_{photo}, and L_{amb} combining the two following equations:

$$\sigma_{photo} = q \cdot \left(\mu^0 n_f + \mu^0 p_f\right) = q \cdot G \cdot \left(\mu^0 \tau_n^R + \mu^0 \tau_p^R\right) \qquad (4.35) \text{ and}$$

$$L_{amb}^2 = \frac{kT}{q} \cdot \frac{\mu_n^0 \tau_n^R \cdot \mu_p^0 \tau_p^R}{\mu_n^0 \tau_n^R \cdot \mu_p^0 \tau_p^R} \cdot C \qquad (4.36),$$

where n_f and p_f are the free electron and hole density, resp., μ_n^0 and μ_p^0 their mobility, τ_n^R and τ_p^R their recombination time, G is the generation rate, k is the Boltzmann factor, T is the absolute temperature, q is the elementary charge and C is a correction factor, with a value between 1 and 2 [66].

4.3.2 a-Si:H and μc-Si:H layers

The samples consist of several annealed and degraded a-Si:H layers, as well as of μc-Si:H layers, with thicknesses between 0.3 and 2.8 μm. The $\mu^0\tau^0$-products

established by the combination of SSPG and SSPC techniques are presented as a function of the layer thickness in Fig. 4.7. Degraded device-grade a-Si:H layers posses the lowest $\mu^0\tau^0$-products, equal to about 10^{-7} cm^2/V.

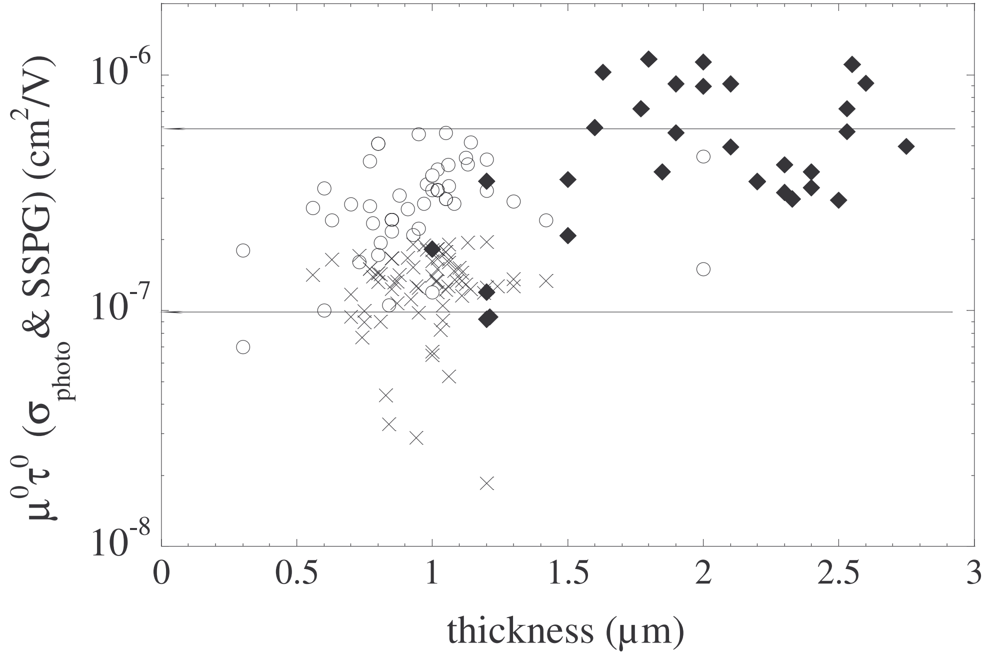

Figure 4.7. $\mu^0\tau^0$-products of various μc-Si:H layers (black diamonds) as well as degraded (crosses) and annealed a-Si:H layers (empty dots), established from SSPC and SSPG measurements, as a function of the layer thickness. The lines are guides to the eye.

Fig. 4.7 shows that $\mu^0\tau^0$-products of μc-Si:H layers (deposited on glass) present a relatively slight dependence on the layer thickness (which varies over one full decade), especially for thin layers below 1.5 μm. We suggest that the slight dependence observed is linked to defect gradients. Indeed, it is known that the microstructure of μc-Si:H layers evolves with accumulated layer thickness. Such evolution results in crystallinity gradients and possibly in defect gradients as well [11]. Nevertheless, for layers which are more than 1.5 μm thick, absolute values of $\mu^0\tau^0$ as measured on μc-Si:H layers are independent of the layer thickness. Here, <u>coplanar</u> transport properties are no longer affected by defect gradients or by microstructure/crystallinity gradients (see also [67]).

The average values of $\mu^0\tau^0$-products, as presented in Fig 4.7, are listed in Table 4.1:

Layer	measured $\mu^0\tau^0$ – product [cm^2/V]
Best a-Si:H (empty dots) (annealed state)	$6 \cdot 10^{-7}$
Characteristic a-Si:H (empty dots) (annealed state)	$4 \cdot 10^{-7}$
Characteristic a-Si:H (crosses) (degraded state)	$1x10^{-7}$
Best μc-Si:H (empty diamonds)	$1x10^{-6}$
Characteristic μc-Si:H (black diamonds)	$6x10^{-7}$

Table 4.1. Typical $\mu^0\tau^0$-products of a-Si:H and μc-Si:H layers established from SSPC and SSPG measurements

4.3.3 a-Si:H and μc-Si:H cells

After the thickness series of layers as described above, thickness series of annealed and degraded a-Si:H cells, as well as thickness series of μc-Si:H cells were evaluated by VIM. $\mu^0\tau^0$-products were established from equ. (4.17) by setting $V_{bi} = 1$ V; they are presented as a function of the i-layer thickness in Fig. 4.8:

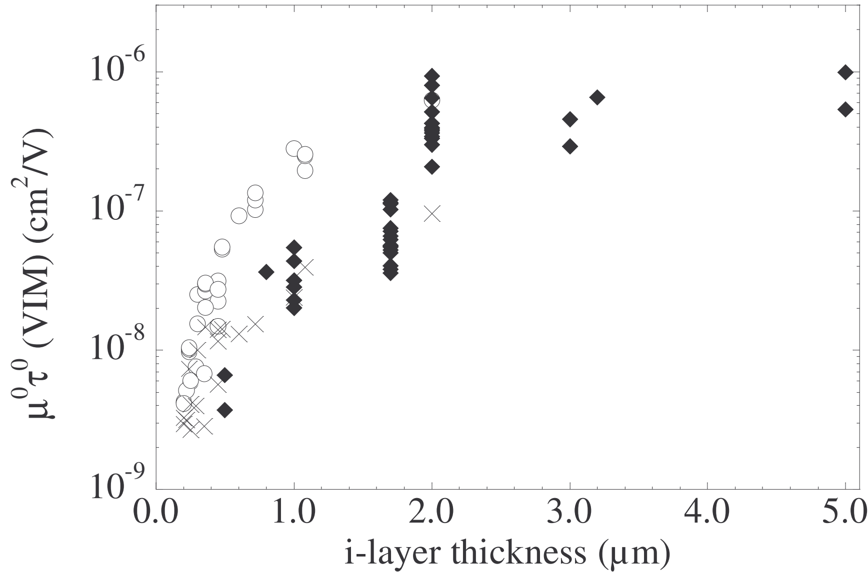

Figure 4.8. $\mu^0\tau^0$-products of various a-Si:H (empty dots: annealed state, crosses: degraded state) and μc-Si:H solar cells (black diamonds) established from VIM measurements, as a function of the intrinsic layer thickness

In contrast with $\mu^0\tau^0$-products as measured in layers by SSPC/SSPG, $\mu^0\tau^0$-products as evaluated by VIM in a-Si:H and μc-Si:H solar cells show a strong dependence on the intrinsic layer thickness, especially for cells with an intrinsic

layer thickness smaller than 3 μm, as shown in Fig. 4.8. This strong dependence of the $\mu^0\tau^0$-products with i-layer thickness is again assumed to be caused by defective interfaces or by crystallinity gradients. But, this time, VIM has been used to measure the $\mu^0\tau^0$-products and VIM is a transverse "integrative" electronic measurement technique that presents a high sensitivity to defects or microstructure gradient's presence, even for i-layer thickness over 1.5 μm. Moreover, we can see from Figs. 4.7 and 4.8 that $\mu^0\tau^0$-products measured in cells, in transverse geometry by VIM, are up to a factor 10 lower than $\mu^0\tau^0$-product values measured in layers, in a coplanar geometry, by SSPG/SSPC (that are photoconductive techniques).

Defect density gradients have been studied extensively with PDS (Photothermal Deflection Spectroscopy) measurements. PDS is a very sensitive technique for measuring optical absorption, by evaluating the variations in sample temperature due to the latter [22]. PDS is used to evaluate the defect density in a similar way as FTPS (Fourier Transform Photocurrent Spectroscopy (FTPS), see § 2.4). However, unlike FTPS, which is a photoconductive method, PDS is (like VIM) an integrative method. Indeed, the heating of the sample physically depends on the integral of the absorption over the whole sample depth.

Based on results of PDS measurements, Jackson et al. proposed a very simple defect density model for a-Si:H layers. This defect density model accounts for surface/interface and bulk effects, with both the surface and interface layers considered as two-dimensional structures [68]. Curtins et al. later introduced what they considered a more realistic model by assuming that the defect density is an exponentially decaying distribution [69]. Jackson's model assumes that the defect density thickness distribution is of the form:

$$n_D(z) = N_s \cdot \delta(z) + N_b \qquad (4.37),$$

where N_s is the surface/interface defect density (in cm^{-2}), N_b is the bulk defect density (in cm^{-3}), $\delta(z)$ the delta function, and z the axis of (intrinsic) layer growth. The term $N_s \cdot \delta(z)$ includes both contributions of the defective layer at $z = 0$ (interface) and of the one at $z = d$ (surface).

After integration of such a distribution, one obtains that the average defect density is given by:

$$N_D(d) = d^{-1} \cdot \int_0^d n_D(z) dz = N_s / d + N_b \qquad (4.38)$$

According to this expression, a linear plot of the defect density versus the reciprocal layer thickness results in a straight line: its intersect with the vertical axis gives the value of the bulk density N_b and its slope equals the surface/interface defect density N_s. In the case of the defect model of Curtins et al., the slope is not constant and depends on the layer thickness (see [69]).

Assuming that the effective recombination lifetime τ^0 is inversely proportional

to the recombination center density N_D, a linear relationship between the defect density and the reciprocal of the layer thickness d^{-1} implies a linear relationship between the reciprocal of the $\mu^0\tau^0$-products and d^{-1}, if μ^0 is assumed to be constant over the i-layer thickness. Indeed, let us designate with R(z) the local recombination function, this quantity varies with the i-layer depth z; τ^0 is, thus, given by:

$$\tau^0 = \tau_{eff} = \frac{n_f \cdot d}{\int_0^d R(z)\,dz} \approx const \cdot \frac{d}{\int_0^d R(z)\,dz} \qquad (4.39),$$

where n_f is the density of free photogenerated electrons ($n_f = p_f$), which is assumed to be constant over the i-layer thickness d.

Now, by taking μ^0 constant, we obtain that:

$$\frac{1}{\mu^0\tau^0} \approx \frac{const'}{d} \cdot \int_0^d R(z)\,dz \approx \frac{const''}{d} \cdot \int_0^d n_D(z)\,dz \approx const'' \cdot \left[N_s / d + N_b\right] \qquad (4.40)$$

Thus, if we postulate that defect density $n_D(z)$ varies according to the "Ansatz" (4.38) of Jackson et al., we simply obtain that $(\mu^0\tau^0)^{-1}$ should vary linearly with the reciprocal of the i-layer thickness (1/d). In reality, Fig. 4.9 shows that $(\mu^0\tau^0)^{-1}$ varies exponentially with d^{-1}:

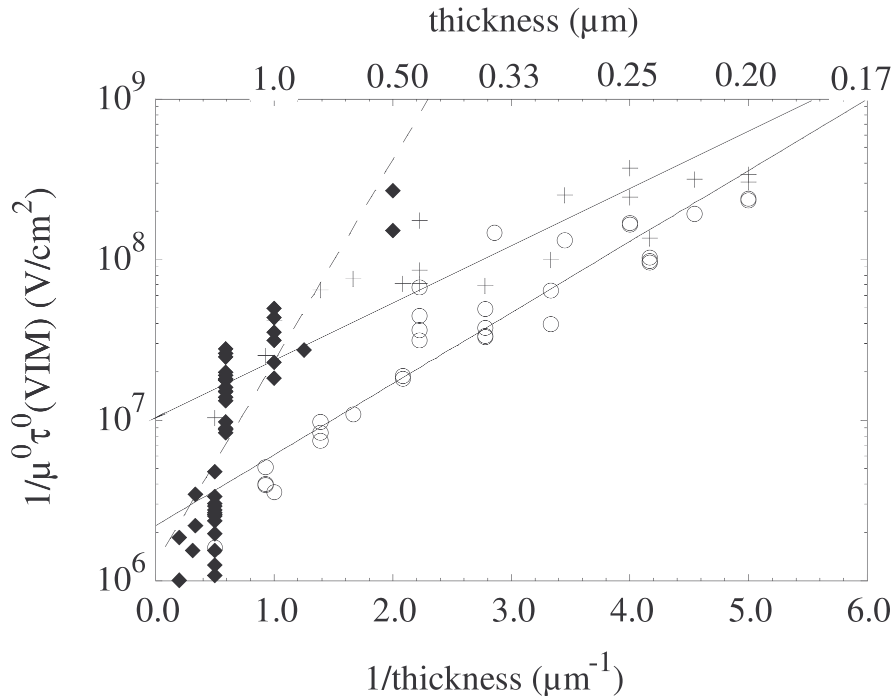

Figure 4.9. $\mu^0\tau^0$-products of various a-Si:H (empty dots: annealed state, crosses: degraded state) and µc-Si:H solar cells (black diamonds) established from VIM measurements, in logarithm scale as a function of the reciprocal of the i-layer thickness.

According to Fig 4.8, the $(\mu^0\tau^0)^{-1}$ values can be well fitted with:

$$\frac{1}{\mu^0\tau^0} = k \cdot \exp\left[k^{'}(1/d)\right] \quad (4.41),$$

with k and k' two numerical constants (different in all three cases).

Such an exponential function can be rather well approximated by a linear function for large i-layer thickness, i.e. when $k'\cdot(1/d) < \sim 0.5$. In that case, if we consider Jackson's model (equ. 4.40), we have:

$$\frac{1}{\mu^0\tau^0} = k \cdot \exp\left[k^{'}(1/d)\right] \approx k \cdot (1 + \frac{k^{'}}{d}) \approx k^{"} \cdot \left[N_b + \frac{N_s}{d} \right] \quad (4.42),$$

i.e. we obtain that k is proportional to the bulk density N_b, whereas $k \cdot k^{'}$ is proportional to the interface/surface defect density N_s

Thus, according to Fig. 4.8, for such "larger" thicknesses, the μc-Si:H solar cells present the highest interface/surface defect density N_s (i.e. the steepest slope), followed by degraded and annealed a-Si:H solar cells, resp. If we assume that the interfaces, as present along the crystalline grains in μc-Si:H solar cells can be neglected, N_s (as in Jackson's model) represents probably, above all, the defect density at the p/i interface (for pin cells) or at the n/i interface (for nip cells). The high surface defect density observed in μc-Si:H solar cells is then related to growth and possible contamination problems at these interfaces.

For thinner i-layer thicknesses, i.e. for d values below 1 μm, the exponential function cannot be approximated with a linear function any more and the defect density model by Jackson et al. is not applicable. This is not surprising, as in reality, interfaces can not be modeled by delta functions, as they are regions of finite dimensions, where perturbations and additional defects due to growth problems and contamination decrease with something like an exponential function. Similarly, Favre [70] observed that Jackson's as well as Curtin's models could not be applied, for a-Si:H layers, for thicknesses below 0.81 μm.

To conclude, we observed that for layers thicker than 1.5 μm, the coplanar electronic transport, and, thus, the $\mu^0\tau^0$-product, is no longer affected by any defect gradient. Consequently the $\mu^0\tau^0$-product evaluated in layers thicker than 1.5 μm in coplanar geometry is a reliable material quality parameter. On the other hand, transverse electronic measurements, as done by VIM on a-Si:H and μc-Si:H solar cells, are affected over a longer distance by the presence of defects or crystallinity gradient: the $\mu^0\tau^0$ values of solar cells showed a marked thickness dependency for i-layer thicknesses up to approximately 3 μm. Moreover, as already stated, there is a factor 10 between the absolute values for $\mu^0\tau^0$-products as measured in layers and those measured in solar cells. This can be attributed to the fact that the

measurements on layers are based on coplanar, photoconductive methods, which only “probe” the most conductive part of the bulk of the layer, whereas measurements on cells are based on VIM, i.e. on J(V) curves, which “probe” the whole depth of the intrinsic layer within the pin solar cell.

$\mu^0\tau^0$-products should, thus, strictly be compared, in solar cells, if they are taken from VIM measurements performed on cells of similar intrinsic layer thickness.

4.4 Variable gas flow series

In this paragraph, we will show how VIM and FTPS can be used as diagnostic tools to investigate the main reason for a drop of fill factor, as observed when the hydrogen flow is decreased during the deposition of pin μc-Si:H solar cells.

4.4.1 Samples

The samples consist in μc-Si:H solar cells deposited under “high pressure depletion” (HPD) conditions, so as to increase the deposition rate, whilst maintaining intrinsic layer quality. However, the HPD method generally requires very high gas flows, especially H_2 flows; economically, this requirement can be a serious disadvantage. Roschek at al. [71] investigated the fabrication of μc-Si:H solar cells under such HPD conditions, at 13.56 MHz, but with step-wise reduced H_2 flow rates. The TCO used consist of sputtered etched Zinc Oxide [8].

The silane dilution was adjusted in such a way, as to keep the Raman crystallinity factor ϕ_c (approximately) constant, at about 60 to 65%. It was observed, in this case, that the FF drops from 72.4 % to 66.2 % when the H_2 flow rate is reduced from 750 sccm to 50 sccm, see Table 4.2:

H_2 flow (sscm)	i-layer thickness (μm)	J_{sc} (mA/cm^2)	V_{oc} (mV)	FF (%)	η (%)
750	1.29	21.9	538	72.4	8.5
360	1.29	21.8	527	69.3	8.0
150	1.32	21.9	505	69.2	7.6
50	1.09	21.7	502	66.2	7.2

Table 4.2. Values for the main parameters of the gas flow series: hydrogen flow, intrinsic layer thickness, short-circuit current density J_{sc}, open-circuit voltage V_{oc}, fill factor FF and efficiency η. For more details, see also [71].

4.4.2 VIM measurements

As can be seen in Fig. 4.10, the collection voltage and the fill factor both increase with increased hydrogen flow:

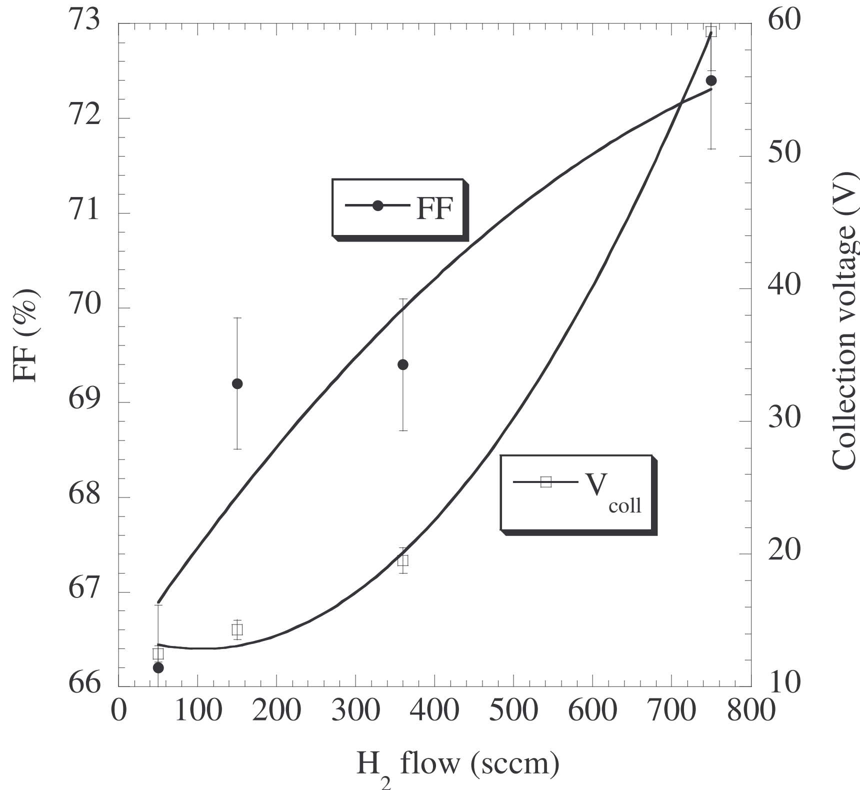

Figure 4.10. Collection voltage (measured by VIM) and fill factor as a function of hydrogen flow. Lines are only guides to the eye.

It can be clearly seen from Fig. 4.10 that the collection voltage drops from 59.4 V to 12.5 V when the hydrogen flow decreases from 750 to 50 sccm. According to equ. (4.21) previously introduced, this should correspond to absolute losses in fill factor equal to 1.5% and 7.2%, with respect to the ideal value of FF = 75%, i.e. FF values of 73.5% and 67.8%, resp. We observe that the correlation between losses in FF and collection voltage, as expressed in equ. (4.21), is indeed confirmed, as shown in Fig. 4.11.

This increase of the collection voltage with hydrogen flow is consistent with observations done on EQE (External Quantum efficiency) curves: an increase of EQE at 700 nm is observed under reverse bias for the sample deposited with 50 sccm of H_2, confirming that all carriers are not collected under short-circuit condition. On the contrary, no variation of EQE is measured under reverse bias for the sample deposited with 750 sccm of H_2, see Fig. 4.12.

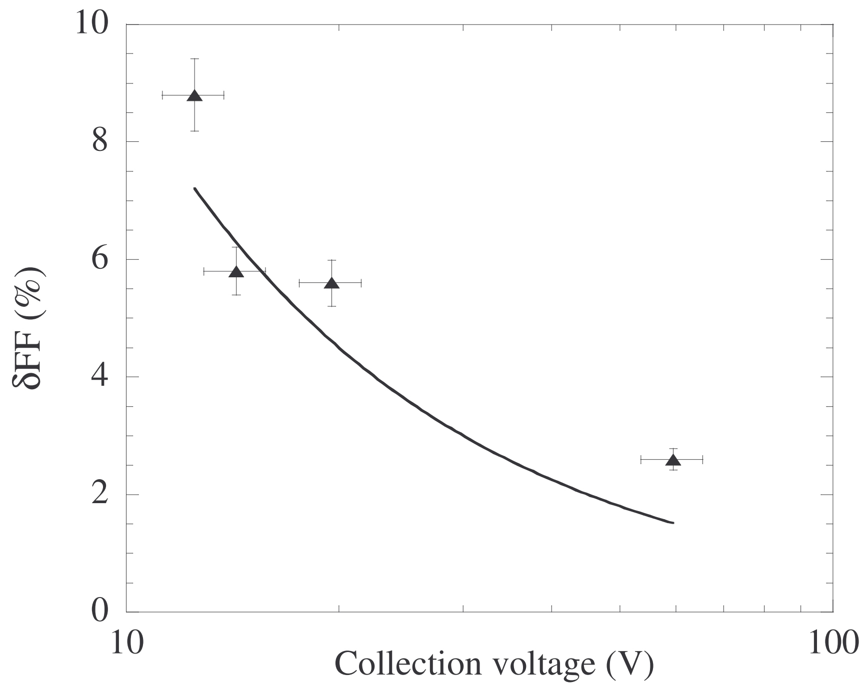

Figure 4.11. Absolute loss of fill factor (FF_0 = 75%, see §4.2.2) as a function of collection voltage. The curve is a fit to equ. (4.21).

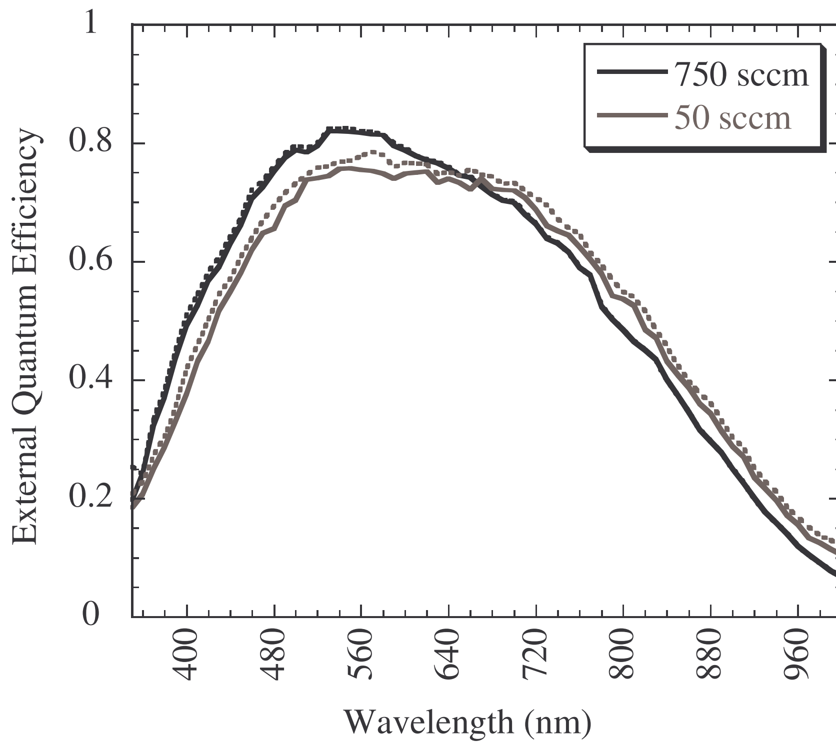

Figure 4.12. External quantum efficiency curves at open-circuit voltage and under reverse bias (plain and dashed curves, resp.), for two samples deposited with 50 and 750 sccm of H_2.

4.4.3 FTPS measurements

If we now look at (sub-bandgap) defect-related absorption, as established by Fourier-Transform photocurrent spectroscopy (FTPS) at 0.8 eV (see Chapter 2), we observe a decrease of α(0.8 eV) with H_2 flow as presented in Fig. 4.13:

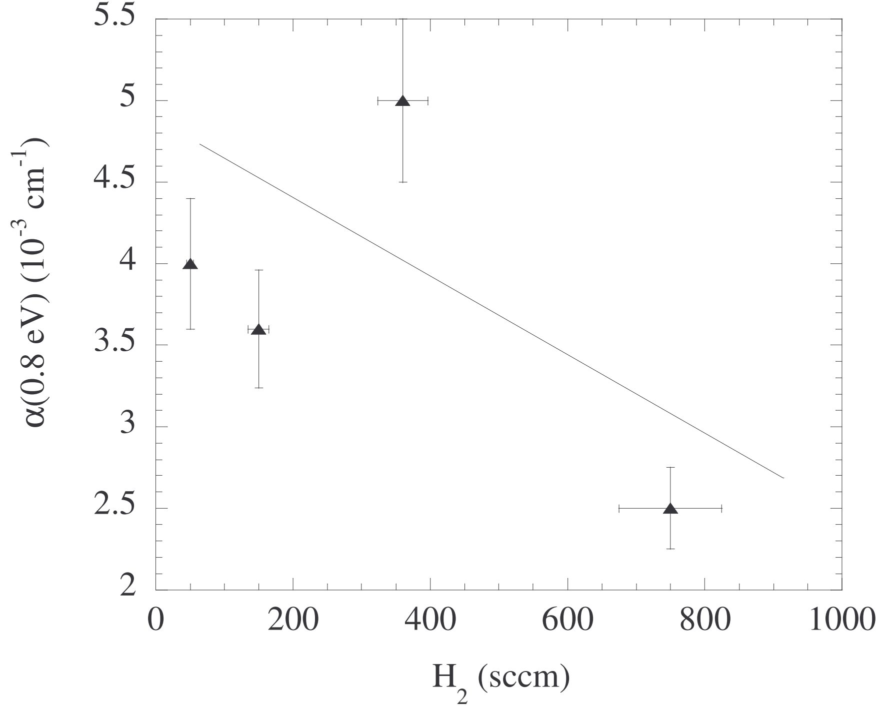

Figure 4.13. Defect-related absorption as a function of hydrogen flow. The line is merely a guide for the eye.

Fig. 4.14 shows as tendency a rough proportionality between the loss of fill factor δFF and the defect absorption α(0.8 eV), as may be expected from equ. (4.20) (by assuming that μ^0 and d_i are constant, and τ^0 is inversely proportional to α(0.8 eV)). Nevertheless, more data is necessary here to confirm this tendency. According to Fig. 4.14, the FF value equal to 66.2% (δFF = 8.8 %) should correspond to a value of α(0.8 eV) in the order of $5.5 \cdot 10^{-3}$ cm^{-1} instead of $4 \cdot 10^{-3}$ cm^{-1}, as actually measured. This means that the fill factor suffers a stronger reduction, than what could be solely explained by the increase in α(0.8 eV), i.e. in defect density. Indeed, the fill factor values at low gas flow rates are limited because of low values of the collection voltage V_{coll}. We suggest that these low collection voltage are due to a stronger oxygen incorporation at low gas flow rates, leading to a reduction in the electrical field E_{eff}. Indeed, according to equs. (4.5) and (4.12):

$$V_{coll} \propto \mu^0 \tau^0 E_{eff} \propto \frac{1}{\alpha(0.8\,eV)} \cdot E_{eff} \qquad (4.43);$$

i.e. for a similar defect-related absorption value (i.e. a similar defect density), a

decrease in the electric field due to contamination leads to a further, proportional, decrease of the collection voltage.

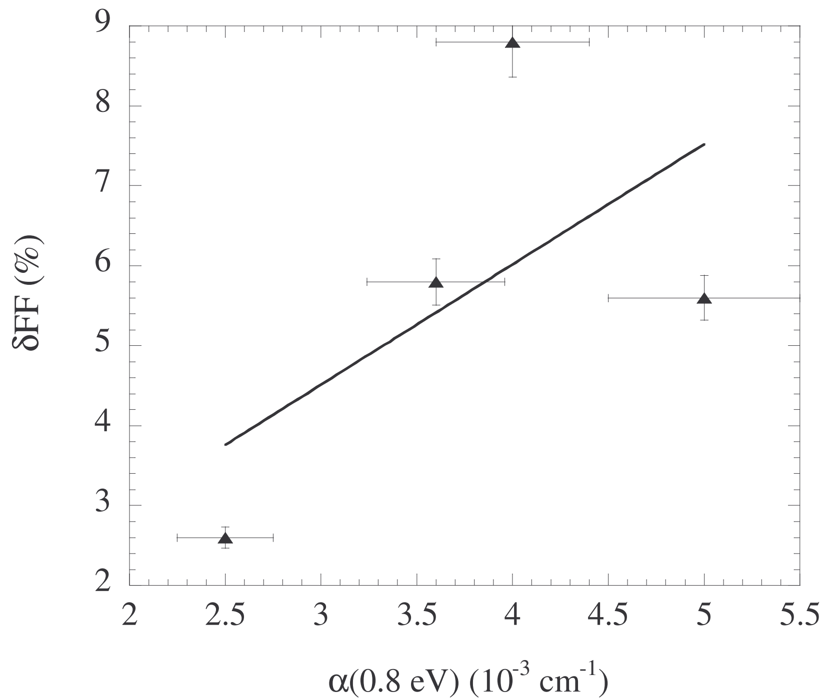

Figure 4.14. Absolute loss of fill factor (FF_0 = 75%, see § 4.2.2) as a function of defect-related absorption. The curve is a proportional fit.

Finally, it should be noticed that the Urbach parameter E_0 (see Chapter 2) decreases with increasing hydrogen flow: 39.6 eV for the sample of 50 sccm of H_2 and 35.8 for this of 750 sccm of H_2, indicating of a modification of the "network" disorder (strained bonds). From previous measurements preformed with FTPS, an increase of α(0.8 eV) (due to variations in the deposition process (such as silane dilution) or due to proton-induced degradation) is invariably associated with a proportional increase of E_0 (see [11] and Chapter 6). On the other hand, in the case of light-induced degradation, this relationship between E_0 and α(0.8 eV) is not observed (see Chapter 5).

4.5 Pin and nip dilution series: light-soaking

In this paragraph, we want to check whether the predicted reduction in FF with an increase of α(0.8 eV) (i.e. with an increase of the defect density) is verified for light-induced degradation.

4.5.1 Samples

The samples consist of two series of μc-Si:H solar cells: one series of pin cells and one of nip cells, of varying crystallinity. Both series were light-soaked for 1000h; detailed results and the dependence of light-induced degradation on

crystallinity will be presented in Chapter 5. The fill factor (FF) is the solar cell parameter that is the most affected by light-soaking, all other parameters present only variations that are lower than 2.5%. Moreover, FF was observed to be maximal for samples of intermediate crystallinity: this maximum corresponds to a minimum in defect-related absorption and to a maximum in collection voltage.

4.5.2 VIM measurements

VIM measurements show that the degradation observed under light-soaking is associated with a decrease of the collection voltage V_{coll}; furthermore, no significant variation of the shunt resistance is observed, see Fig. 4.15 (caption), below:

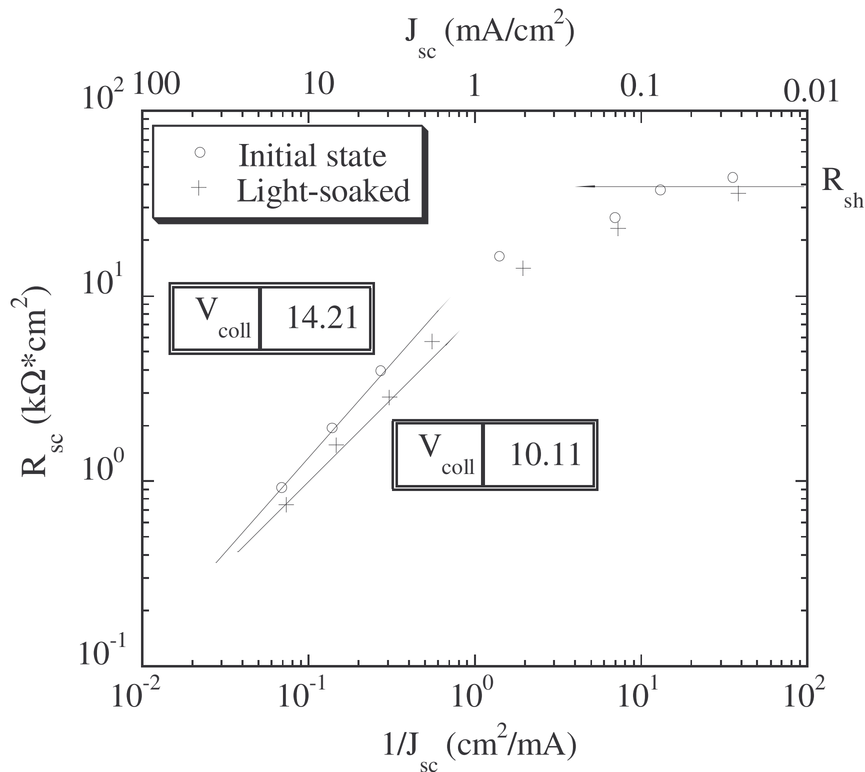

Figure 4.15. Short-circuit resistance R_{sc} as a function of the reciprocal of the short-circuit current density J_{sc}^{-1} for the pin sample of medium crystallinity. The J_{sc} values are also indicated. The straight line corresponds to a linear fit according to equ. (4.17). The curves tend asymptotically towards the same value R_{sh}, for high J_{sc}^{-1}: we can thus conclude that the shunt resistance in this device is not affected by light-soaking.

Let us now consider the absolute loss of fill factor, as induced by light-soaking, as a function of the collection voltage, presented in Fig. 4.16:

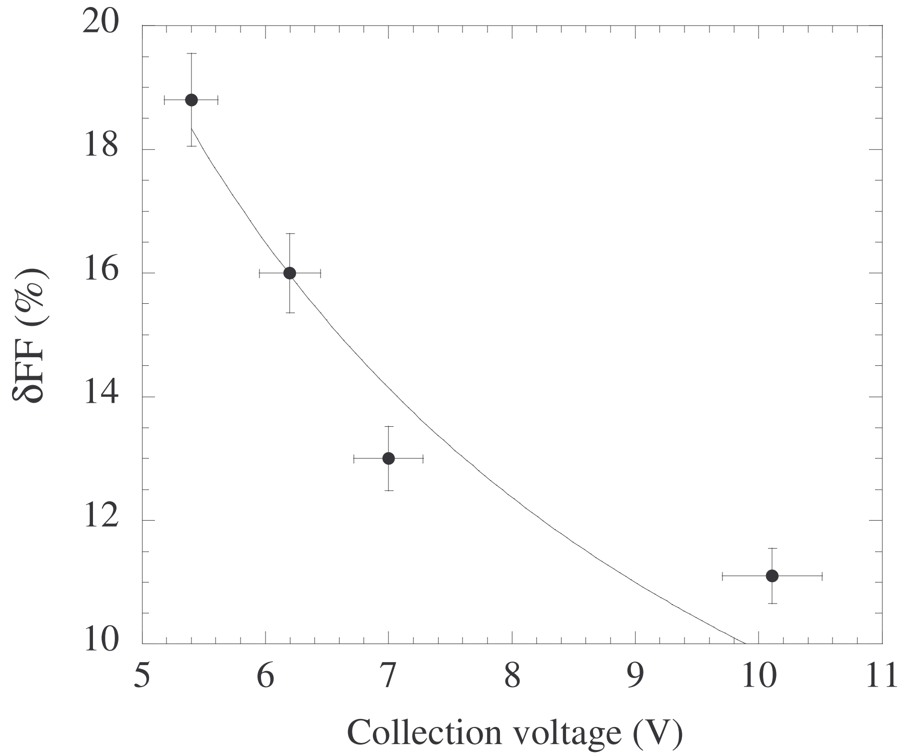

Figure 4.16. Absolute loss of fill factor due to light-soaking with respect to the ideal value FF_0 = 75% as a function of collection voltage for the nip dilution series. The lowest reduction in fill factor is obtained for the nip cells with the highest crystallinity. The curve is a fit to equ. (4.21). Similar values of δFF and V_{coll} were obtained for the pin series (not presented here).

4.5.3 FTPS measurements

Here, we confirm that light-induced losses in fill factor can be correlated with an increase in defect-related absorption: indeed, Fig. 4.17 shows that δFF is proportional to α(0.8eV) in the degraded state, as expected from equ. (4.20), for the nip series (similar results were obtained for the pin series, not shown here).

We can, thus, conclude that the reductions of FF observed when light-soaking the cells of our μc-Si:H pin and nip series are well fitted by the empirical relationships established from the equivalent circuit introduced in this Chapter. In the framework of this model, the main electrical loss (i.e. FF drop) due to light-soaking can be attributed to an increased recombination in the intrinsic layer. The experimental results on light-soaking, thus, validate, together with the results previously obtained with the gas series, the simple model proposed for μc-Si:H.

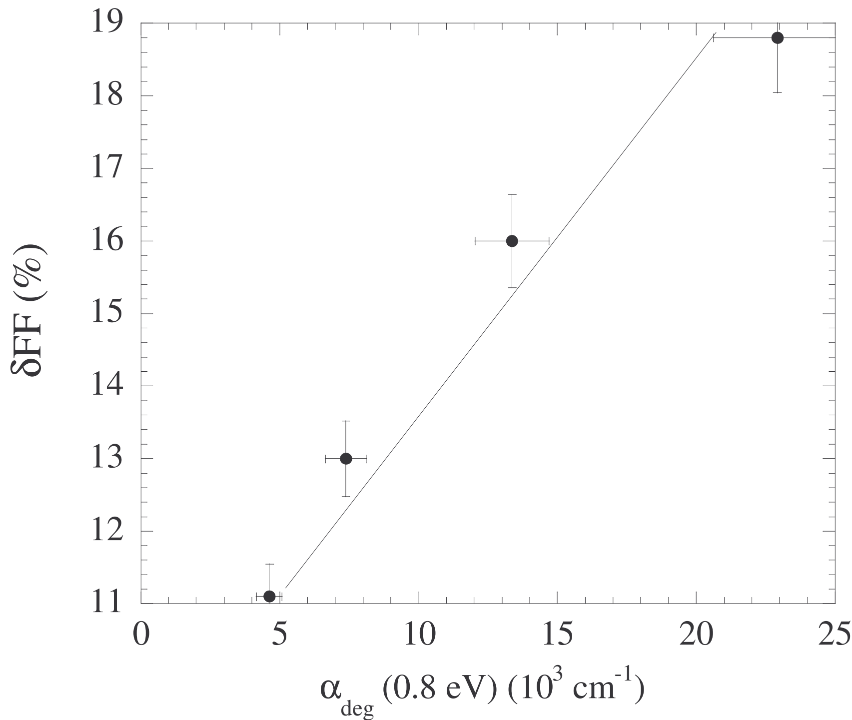

Figure 4.17. Absolute loss of fill factor due to light-soaking as a function of defect-related absorption, in the degraded state, of the cells of the nip series; the line is a proportional fit, according to equ. (4.20)

4.5.4 Dark J(V) measurements

As previously mentioned, we assumed in Chapter 3 (theoretical limits) that the reverse saturation current J_0 was equal to ~ 10^{-6} mA/cm^2 for μc-Si:H. This range of values is confirmed by the dark J(V) measurements performed on both our pin and nip series, see for example Fig. 4.18 hereafter. Fig. 4.18 shows the variation of dark current density after light-soaking for the pin sample of medium crystallinity.

The observed change in dark J(V) corresponds to an increase of the ideality factor n from 1.3 to 1.5 and an increase of the reverse saturation current density J_0 from $2.1\cdot10^{-7}$ to $9.8\cdot10^{-6}$ mA/cm^2. An increase of n (not shown here) and an increase of J_0 (shown in Fig. 4.19, for the sample of medium crystallinity) was observed for all pin and nip samples with light-soaking. Similar results were reported by Klein et al who light-soaked μc-Si:H solar cells deposited by Hot-Wire CVD [62].

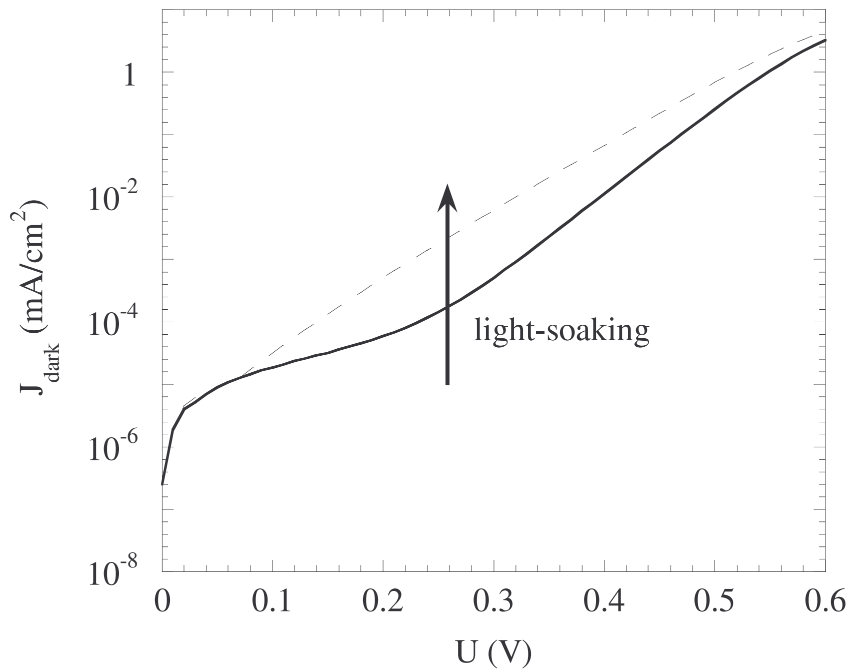

Figure 4.18. Dark J(V) measurement before (full line) and after (dotted line) light-soaking for the pin sample of medium crystallinity (ϕ_c ~ 50%), at room temperature (T = 293 °K)

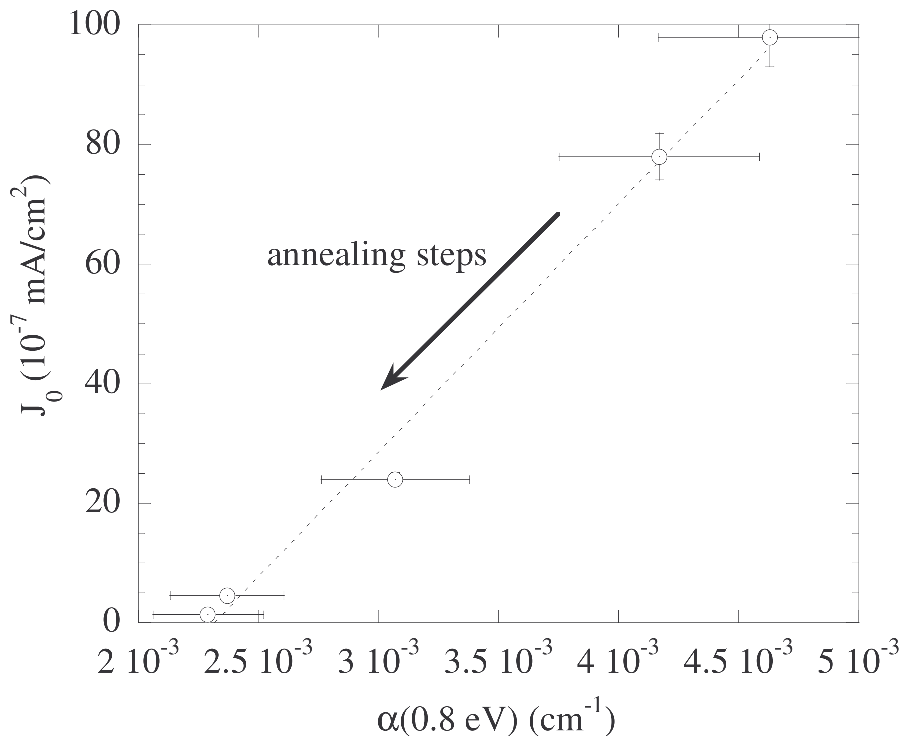

Figure 4.19 Reverse saturation current as a function of defect-related absorption after light-soaking and subsequent annealing steps for the pin sample of medium crystallinity (ϕ_c ~ 50%). The dotted line is a linear fit.

Fig. 4.19 shows that the reverse saturation current density J_0 decreases linearly with decreasing defect-related absorption α(0.8 eV). Since the FTPS spectra were calibrated at 1.35 eV with respect to the absorption value of crystalline silicon, defect-related absorption as measured at 0.8 eV is assumed to be proportional to the defect density of the (micro)crystalline phase (see Chapter 2, § 2.4)). Fig. 4.19, would, thus, indicate that the value of J_0 is directly linked, in μc-Si:H solar cells, to the density of such "microcrystalline" defects; we suggest (see Chapter 5) that these defects are situated at the surface of the nanocrystals. The ideality factor n decreases with defect-related absorption (not shown here) but also with crystallinity as can bee seen in Fig. 4.20:

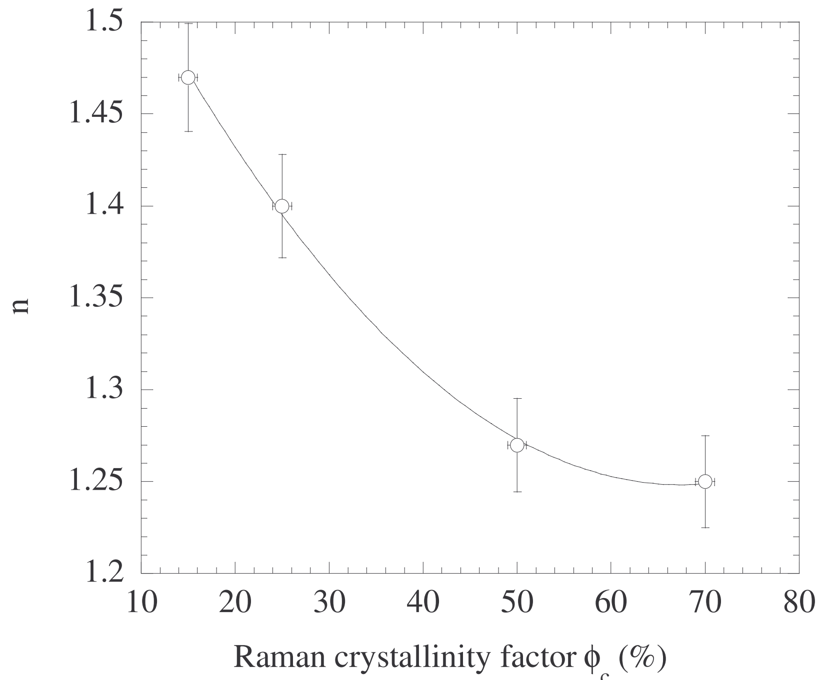

Figure 4.20. Ideality factor as a function of Raman crystallinity factor for the nip series (similar result for the pin series). The line is merely a guide for the eye. The reverse saturation current J_0 also decreases with crystallinity (not presented here).

This observation indicates a continuous variation of the ideality factor between the experimental value for mainly amorphous devices (n ~ 1.5), and for highly (micro)crystalline devices (n ~ 1.2). According to the theory for pn junction, the trend observed could be interpreted as a continuous variation of the type of transport with crystallinity: drift dominated transport at low ϕ_c and diffusion dominated transport at high ϕ_c. From the pin junction model (see § 4.2), this could suggest that bulk recombination is predominant at low ϕ_c, whereas it is interface recombination that is predominant at high ϕ_c. The increase of n with light-soaking is in agreement with the other observations, that indicate an increase of recombination within the intrinsic layer. Nevertheless, further work would be needed to confirm this interpretation.

4.6 Solar cells with low shunt resistance

4.6.1 Samples

In this paragraph, we will consider two pin µc-Si:H solar cells with a surface area of ~0.2 cm^2, structured on the same substrate, that present very similar FF under AM1.5 illumination: cell A: FF_A = 70.9 % and cell B: FF_B = 70.4 %, resp, but very different FF at low illumination (~10^{-2} sun): FF_A = 68.7% and FF_B = 29.2% resp. We will investigate if the difference in fill factor values observed between these two cells A and B can be explained by a low shunt resistance, due either to structuration problems or due to a localized shunt (e.g. from dust/ZnO particle or from voids).

4.6.2 VIM measurements

VIM measurements were carried out on both solar cells: Fig. 4.21 shows the short-circuit resistance R_{sc} as a function of J_{sc}^{-1}; we observe that the cell B saturates very quickly, leading to a R_{sh} value of ~ 3 kΩ·cm^2, whereas the cell A does not, as yet, saturate, even with R_{sc} values over ~ 40 kΩ·cm^2. We also observe a difference in the collection voltage V_{coll}, which is a little lower for the cell B:

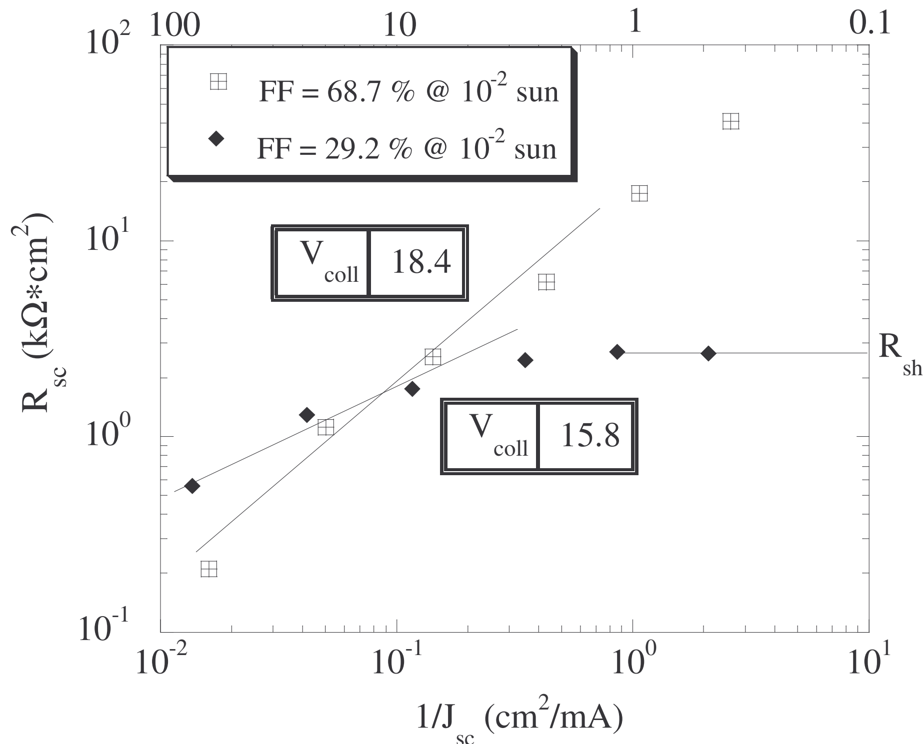

Figure 4.21. Short-circuit resistance R_{sc} as a function of the reciprocal of the short-circuit current density J_{sc}^{-1} for two pin µc-Si:H solar cells: the straight line corresponds to a fit of the linear part of the curve according to equ. (4.17).

The FF value at 10^{-2} AM 1.5 immediately indicates a shunt in the device which has a lower FF at AM 1.5. One single measurement at very low illumination thus allows the detection of whether a structured, individual, cell has a "localized" defect. From equ. (4.26), we obtain, for $R_{sc} = R_{sh} = 3$ kΩ·cm^2, a fill factor loss equal to 0.7%, whereas the loss is negligible for $R_{sc} \sim 40$ kΩ·cm^2. The difference between both FF at AM1.5 can, thus, be attributed to the shunt resistance.

Nevertheless, the fill factor reduction should not be considered with respect to the ideal value of 75%, because these cells have already collection deficiencies that limit their FF values. Indeed, the larger part of the loss observed is not related to shunts, but to the low collection voltages: $V_{coll} = 18.4$ V corresponds, according to equ. (4.21), to a fill factor reduction of $FF_0 - FF \sim 4.8$ %., i.e. to FF ~ 70.2 %, whereas $V_{coll} = 15.8$ V gives a reduction of 5.6 %, i.e. FF ~ 69.4 %.

In order to be able to validate our empirical expressions, cells with very high collection voltages ($V_{coll} \geq 70$V) and low R_{sh} ($R_{sh} \leq 1$ kΩ·cm^2) should be considered. Such cells could correspond to very good initial cells (FF ~ 75%) later shunted during the scribing process.

4.7 Conclusions

In the present chapter, an equivalent circuit and a "theoretical model" (system of equations) already introduced and validated by J. Merten [49] and J. Merten et al [41] for a-Si:H pin-type solar cells in 1995-1998, has been introduced for the description of μc-Si:H pin-type solar cells. The equivalent circuit/"theoretical model" still needs to be validated for μc-Si:H by systematically carrying out fits on a large number of different μc-Si:H solar cells and by measuring the collection voltage and shunt resistance for various illumination levels (between 10^{-3} and 1 sun). So far, in our own work, an excellent agreement between such measurements and an increase of defect-related absorption, as well as high shunt resistances, that both lead to a reduced FF value, has been noted. But our experience is limited. The model used can be considered to be an extension of the superposition principle (known for pn-type solar cells) to the case of pin-type solar cells, by adding a recombination current sink.

Variable illumination measurements (VIM) based on the equations of the model allow one to evaluate 3 major effects that often limit efficiency and adversely affect the fill factor of μc-Si:H solar cells:

(1) Collection losses due to low lifetimes of the photogenerated carriers (seen as a reduction in collection voltage V_{coll} and an increase of defect-related absorption α at 0.8 eV),

(2) Low shunt resistance R_{sh} due to micro-cracks and structuration problems,

(3) High series resistance R_s of the TCO layers.

The fill factor of µc-Si:H solar cells was assumed to ideally equal 75%, as achieved with actual best µc-Si:H solar cells [9]. In practice, one often obtains much lower fill factor values. The absolute difference δFF between the ideal fill factor (75%) and the actual value of fill factor can be written as:

$$\delta FF = \delta FF_{coll} + \delta FF_{shunt} + \delta FF_{series} \quad (4.44),$$

with (for µc-Si:H):

$$\delta FF_{coll}\,(\%) \approx \varphi(V_{MPP})\frac{V_{bi}}{V_{coll}}\cdot 90\ ,\ V_{bi} \sim 1V \quad (4.45),$$

$$\delta FF_{shunt}(\%) \approx 2\cdot\frac{1}{R_{sh}},\ R_{sh}\text{ in }\underline{k\Omega\cdot cm^2} \quad (4.46),$$

$$\delta FF_{series}\,(\%) \approx 3\cdot R_s,\ R_s\text{ in }\underline{\Omega\cdot cm^2} \quad (4.47),$$

where V_{coll}, R_{sh} and R_s can be easily measured by the VIM method, whereas the electric field deformation $\varphi(V_{MPP})$ must be assessed by numerical simulations (see e.g. [51]). For simplification we set $\varphi \approx 1$ at short-circuit conditions and at maximum power point as well. We showed that the above relationships can be applied with success to various practical cases of µc-Si:H solar cells (variable gas flow series, dilution series with and without light-soaking, strongly shunted cells). Note that in the illuminated J(V) measurements both parameters, R_{sc} and R_{oc}, that are determined directly from the slopes of the J(V) curves at V = 0 and at $V = V_{oc}$, respectively, contain contributions from recombination. Because of this fact, very low values of R_s cannot be easily measured, without strongly increasing the light intensity, as they are otherwise fully masked by the recombination. Indeed, in a-Si:H cells, for example, values of R_s lower than 3 $\Omega\cdot cm^2$ can not be measured under 1 sun illumination [55].

A further significant result exposed in this chapter is related to the measurement of $\mu^0\tau^0$-products of µc-Si:H layers (on glass) and of entire pin cells. In both cases, thickness series were studied. The in-depth analysis of this data allows us to conclude that:

(a) interface defects (on the p/i and i/n interface) play a major role in solar cells: the interface defect density is thereby observed to be greater in µc-Si:H solar cells than in a-Si:H solar cells. This is probably due to growth and contamination problems at the first interface (p/i or n/i interface depending on the configuration);

(b) VIM is a <u>transverse</u> (and "integrative") electronic measurement technique that therefore presents a high sensitivity to the presence of gradients in defect density or in microstructure: the values of the $\mu^0\tau^0$-products, as established

by VIM in solar cells, are therefore thickness dependent and a factor 10 lower in absolute value than values measured in coplanar geometry in layers. Care must thus be taken to compare $\mu\tau$-products in solar cells only if they are established from VIM measurements performed on solar cells of similar intrinsic layer thickness.

Dark J(V) measurements carried out on both a pin and a nip dilution series confirmed that, in pin junctions, the reverse saturation current depends on the defect density. Indeed, it was shown (for the first time to our knowledge), that in a μc-Si:H solar cell with medium crystallinity (ϕ_c ~ 50%), the reverse saturation current density J_0 increases linearly with the defect density, as monitored by the defect-related absorption α at 0.8 eV. In addition, the ideality factor was observed to decrease from n ~ 1.5 to n ~ 1.2 when the Raman crystallinity factor increases from ϕ_c = 15% to ϕ_c = 70%. From the pin junction collection model presented in this chapter, this could suggest that bulk recombination is predominant at low ϕ_c, whereas it is interface recombination that is predominant at high ϕ_c. Furthermore, the increase of n that is, as well, observed with light-soaking is in agreement with an increase of the recombination in the "bulk" of the intrinsic layer of μc-Si:H solar cells, as suggested in the next Chapter 5 (the word "bulk" including the interfaces between amorphous and (micro)crystalline phases).

Further investigations should be focused on applying the equs. (4.45) to (4.47) to a larger number of samples, among which another thickness series of μc-Si:H cells. Light-soaking and annealing measurements on such a series would give further precious information on the nature of the defects, by verifying if only the "bulk" defect density increases with light-soaking in μc-Si:H or if the interface defect density increases as well.

5. Light-induced degradation of thin-film microcrystalline silicon (µc-Si:H) solar cells

5.1 Introduction

This chapter presents the results of light-soaking studies on two series of thin-film pin and nip microcrystalline silicon (µc-Si:H) solar cells. The results will be discussed and compared to light-induced degradation, as observed in amorphous silicon (a-Si:H). Light-induced degradation of µc-Si:H solar cells will be assessed from measurements of the electrical parameters, as well as from sub-bandgap absorption spectra (defect-related absorption). Analogies between light-induced degradation and annealing in µc-Si:H and a-Si:H will be presented in detail.

In fact, two main issues are studied in this chapter:

- Are µc-Si:H solar cells of "medium" crystallinity (with a Raman crystallinity factor ~ 50%) stable under light-soaking (these cells have the highest initial efficiencies) ?
- If not, can we conclude that the amorphous phase is responsible for the degradation that is observed?

The first issue is of great importance for the application of µc-Si:H for low-cost single-junction and tandem (a-Si:H/ µc-Si:H) solar cells and modules.

After a short review of present models for light-induced degradation of a-Si:H and µc-Si:H solar cells and layers in § 5.2, we will describe the solar cells used for our study in § 5.3. Then, the light-soaking and annealing condition will be described in § 5.4, whereas the solar cells initial state will be fully characterized in § 5.5. In § 5.6 and 5.7, we will show that µc-Si:H solar cells degrade under light-soaking, albeit in a "softer" and slower way than amorphous devices. Furthermore, the relative amplitude of the degradation is a function of the crystallinity of the intrinsic layer incorporated in the solar cell: the lower the crystallinity, the higher the light-induced degradation. We will demonstrate more precisely that light-induced degradation is proportional to the ratio of the amorphous volume over the crystalline volume.

In § 5.8 we will show that light-induced degradation of µc-Si:H is totally reversible under thermal annealing and in § 5.9 we will give evidence that the kinetics of annealing is very similar to that of a-Si:H, albeit (again) slower. We will, thus, in § 5.10, suggest a simple model for light-induced degradation: in this simple model, defects that are created by light-soaking cause a deterioration of the nanocrystals' passivation, leading to a decrease of the electrical properties of the µc-Si:H solar cells .

5.2 Light-induced degradation: observations and models

Amorphous silicon has been known, for more than 20 years, to suffer from light-induced degradation; this degradation phenomenon is generally known as the Staebler-Wronski (SWE) effect [13]. We will summarize the major observations made, up to now, on light-induced degradation in a-Si:H and μc-Si:H layers and solar cells. Models developed for describing the Staebler-Wronski effect will also be briefly presented.

5.2.1 Observations

The following characteristic behaviours have been reported for thin-film amorphous and microcrystalline silicon layers and solar cells:

a) amorphous silicon (a-Si:H)

- layers:
  - A decrease in photoconductivity during illumination that results from a drop in the majority carrier μτ-product [13]. The decrease is approximately of one order of magnitude for illumination with a tungsten lamp of 200 mW/cm^2 [13]. For such illumination, a decrease in the dark conductivity of around 4 orders of magnitude was also observed [13];
  - A decrease of the photoluminescence intensity of the order of 50% after illumination with an argon ion laser light of 40 mW [72];
  - An increase of the defect-related absorption, as measured at 1.2 eV, by a factor of approximately 5 (see e.g. [73]);

All these behaviours are followed by quasi-saturation after ~1000h of illumination: the saturated values reached thereby depend on the temperature and defect generation rate (i.e. on the illumination level used for the degradation).

- solar cells:
  - A relative decrease in the electrical parameters that characterize the cell performance, of up to 40 % [74, 75], with the fill factor being the parameter that is the most affected by light-soaking. Typical degradation conditions used for a-Si:H solar cells consist in 1000 hours of light-soaking, under AM 1.5-like spectra, at 50°C. Under such conditions, quasi-saturation values of the electrical parameters are reached.
  - This type of degradation does not only occur under illumination, but also in the dark, under forward bias, when both types of carriers are injected into the intrinsic layer [76].

- The thicker the i-layer, the larger is the relative decrease of the electrical parameters (mainly the fill factor). Degradation can therefore be interpreted as depending on the total recombination within the intrinsic layer, which increases with increasing thickness. Thus, a-Si:H solar cells optimized for better stability have i-layer thicknesses lower than 500 nm.

Light-induced defects as created in a-Si:H layers and solar cells are metastable and degradation is observed to be reversible under thermal annealing: at annealing temperatures above 150°C, 2h are necessary to get back to the initial parameters [13, 77]. The defects have been identified as dangling bonds that act as recombination centers; the increase of the density of such recombination centers is responsible for the decrease observed in the fill factor of a-Si:H solar cells. Furthermore, the origin of the creation of dangling bonds has been deduced to be recombination itself. Indeed, in devices such as TFT (Thin Film Transistor), where no carrier recombination occurs in the active layer, no degradation has been observed.

b) microcrystalline silicon (μc-Si:H):

- layers:

  - Flückiger et al [78], as well as Liu et al. [79] observed light-induced degradation in μc-Si:H layers, but further measurements showed that post-oxidation could be taken as responsible for the increase of defect density that they observed.

- solar cells:

  - Fully μc-Si:H (i.e. cells with a Raman crystallinity factor ϕ_c ~ 80 - 90%) pin-type cells were shown to be practically stable under white light-soaking, with a relative decrease of the electrical parameters in the order of $\Delta FF < 2$ %, $\Delta V_{oc} < 2$ %, $\Delta J_{sc} < 1$ % [3];

  - Klein et al. [61] observed a degradation of μc-Si:H solar cells deposited by Hot-Wire (HW)-CVD: a relative decrease of efficiency of up to 10% was measured for samples with low crystallinity (i.e. $\phi_c < \sim 30\%$). For some of their samples, the fill factor is the parameter that degrades the most, for some others it is the short-circuit density J_{sc}. When applying a bias voltage, they observed a loss in external quantum efficiency in the short wavelengths (blue part of the spectra): they suggested that the amorphous phase was responsible for the degradation (Staebler-Wronski-like degradation mechanism). This was supported by dark J(V) measurements, showing a significant increase of both the reverse saturation current density and the diode quality factor, after light-soaking.

- A degradation of the amorphous phase as being the cause of µc-Si:H light-induced degradation was confirmed by Guha et al., who carried out light-soaking measurements using red and blue light [80]. They observed (a) a degradation when exposing their samples to blue light, as well as to white light (no filter), and (b) no degradation when exposing their devices to red light. Assuming that long wavelengths (red and infrared) are only absorbed in the (micro)crystalline phase, Guha et al. concluded that only the amorphous phase degrades.

  The same authors carried out further measurements using bias voltage [76]: this time, they observed that (a) a forward-bias current injection in the dark does not cause any degradation in the performance of µc-Si:H solar cells, whereas (b) a reverse bias enhances light-induced degradation. These phenomena are opposite to those observed in a-Si:H solar cells. Guha et al. suggested that the forward-injected carriers are mainly transported through the nanocrystals, where carrier recombination does not create metastable defects. The increased degradation under reverse bias was explained in terms of the heterogeneity of the material structure, via a "back-to-back" diode model.

5.2.2 Models (from a-Si:H)

Staebler and Wronski were the first to suggest that light-induced degradation observed in a-Si:H layers and solar cells was a consequence of the creation of additional localized gap states (dangling bonds), via the energy released by the recombination of photogenerated carriers. Over the years, many models have been developed to explain the creation and annealing of such light-induced defects in a-Si:H. The different models comprise:

- The bond-breaking model: in this model, first presented by Hirabayashi et al. [81] and Pankove et al. [82], the breaking of weak Si-Si bonds by prolonged illumination is established as a major mechanism for the creation of light-induced defects. Within the framework of this model, the increase of light-induced defect-related absorption with light-soaking time can be described by a power law increase, as introduced by Stutzmann et al. [83]. Such a power law increase was recently observed by Wronski et al in a-Si:H pin solar cells [84]. However, the power law does not allow one to describe the quasi-saturation experimentally observed after long light-soaking times ($t \geq 1000$ hours).

- The dispersive model: Redfield and Bube [85] introduced the dispersive model for the creation of light-induced defects in a-Si:H, and Jackson et al. [86] and Morigaki [87] for their annealing. In this model, the variations of defect density as a function of light-soaking conditions (i.e. temperature and generation rate), as well as analogous variations during annealing, are

interpreted in terms of the dispersive diffusion of hydrogen and described by a stretched exponential function. This stretched exponential function has the form (as given here for annealing):

$$N(t) = N(0) \cdot \exp\left[-\left(\frac{t}{\tau}\right)^{\beta}\right] \qquad (5.1),$$

where N is the light-induced defect (dangling bond) density, β and τ are the dispersive parameter and the effective time constant, respectively. The expression is slightly different for the degradation kinetics (presented later as equ. (5.3)).

The microscopic picture of light-induced degradation underlying this model is the following: bond-breaking is mediated through the dispersive motion of hydrogen within the amorphous network, i.e. hydrogen diffuses by sequences of trapping-detrapping and bond-breaking occurs as a consequence of hydrogen motion. By measuring the kinetics of dangling bond annealing at various temperatures, Jackson et al concluded that τ is thermally activated:

$$\tau = \tau_0 \cdot \exp\left(\frac{E_a}{kT_a}\right) \qquad (5.2),$$

with E_a the activation energy and T_a the annealing temperature. They also observed that β increases linearly with temperature.

For light-induced degradation in a-Si:H, Redfield and Bube [85] established a value of $\beta = 0.45$, whereas for annealing, Jackson et al [85] obtained values of: β (403°K) = 0.81, $\tau_0 = 1.8 \cdot 10^{-10}$ s and $E_a = 0.94$ eV.

We will later show that stretched exponential functions can also be used to describe creation and annealing of light-induced defects in μc-Si:H; however, different time constants and a different activation energy are established.

- Other models have been developed that will not be presented in detail here. However, we should mention the hydrogen collision model, developed by H. Branz [77], where dangling bonds are created by (recombination-induced) emission of hydrogen atoms from Si-H bonds and not by the breaking of weak Si-Si bonds.

5.3 Samples

The results presented in this chapter were obtained from measurements on two dilution series of μc-Si:H cells that were deposited by Very-High Frequency (VHF) PECVD in both nip and pin configurations. In the case of nip configuration, the

front TCO employed is LP-CVD ZnO (Zinc Oxide) (~ 2 µm thick), whereas the back TCO is sputtered etched ZnO deposited at the Forschungszentrum in Jülich, Germany (~ 0.6 µm thick) [8]. In the case of pin configuration, both types of Zinc Oxides are inverted (i.e. the p layer is deposited on sputtered etched ZnO). The doped layers have thicknesses in the order of 20-30 nm, whereas the intrinsic layer thickness is about 2 µm. Due to the relatively low deposition rate of µc-Si:H, the current trend is to use i-layers with thicknesses in the range of 1 µm. This trend should be beneficial for increasing the stability of µc-Si:H cells during the degradation process, if the process is here similar to the one observed for a-Si:H, which (according to our current understanding) seems to be the case. Nevertheless, surprisingly, Klein et al. [63] observed that in some cases, thicker cells showed a less pronounced light-induced degradation than their thinner counterparts (even for a comparable value of the crystalline fraction); the authors were unable to justify their observation.

Previous measurements done on two other series of pin and nip cells, deposited on LP-CVD ZnO [39] were published in [88], [89] and are presented in Appendix A1: we observed that the pin series degraded much more than the nip one and we attributed this difference in behavior to a contamination of the pin devices during their deposition process that had been carried out in a single chamber [88]. Indeed, our recent results, as presented below, confirm the better stability of the new pin series; these results are fully in accordance with the results obtained with the nip cells. These results suggest, thus, that contamination of the intrinsic layer may play a significant role with respect to device stability.

In order to avoid contamination problems, a double-chamber system was used for the deposition of each new series. The advantage of the double-chamber system is that the doped layers and the intrinsic layer are each deposited in their own chamber, reducing, thus, contamination of the intrinsic layer by dopant atoms. Nevertheless, we will observe that the new series are probably also contaminated, this time, by oxygen. The pin and nip samples studied here, thus, do not yet represent the best devices that can be fabricated at the moment [9]. They can, however, still be used to give indications on the expected behavior of state-of-the art µc-Si:H solar cells.

The deposition parameters of the doped layers were kept constant within a given series, whereas the silane dilution used for the deposition of the intrinsic layer was varied, leading to a variation in the crystallinity of the intrinsic layer. This is currently one of the major i-layer optimization steps of single-junction µc-Si:H solar cells.

The crystalline volume fraction of the intrinsic layers was assessed by Raman measurements (see § 2.3); it is approximated by the value of the ratio ϕ_c of the corresponding Raman intensities. ϕ_c is comprised between:

- 15 % and 70 % for the nip series (4 samples)
- 22 % and 66 % for the pin series (3 samples).

A fourth pin cell was fabricated with an i-layer deposited in two steps: the first i_1 layer was deposited with a lower silane concentration than the following i_2 layer. Such a variation of the silane dilution during the deposition of the intrinsic layer (called "hydrogen dilution profiling") implies the formation of fewer cracks and voids, leading to higher conversion efficiencies [90]. This cell has an "average" Raman crystallinity factor ϕ_c = 15%; its stability under light-soaking will be compared to that of the nip cell with the same crystallinity factor (see square symbol in Figs. 5.5 to 5.7).

5.4 Light-soaking and annealing conditions, characterization techniques

Both series were light-soaked under open-circuit conditions for 1000 hours, at a temperature of 50°C, under an AM 1.5-like spectrum (100 mW/cm^2). They were then annealed, under nitrogen flow, for 10 hours at sequentially increased temperature: 100°C, 130°C, 160°C and 180°C. Measurements of the degradation kinetics were carried out at room temperature on samples of medium and low crystallinity. Note that, as already mentioned in § 5.2 (b), the choice of the illumination spectra used for the degradation is essential. Indeed, in agreement with previously published data [80], our medium crystallinity (ϕ_c ~ 50%) solar cell, which defect-related absorption (see below) is increased by a factor ~ 1.5 after 100 hours of exposure to AM 1.5-like spectra, shows no degradation after 100 hours of exposure to red light (≥ 700 nm).

Open-circuit voltage (V_{oc}) and fill factor (FF) were obtained from J(V) measurements under a WACOM AM 1.5 sun simulator at 25°C, whereas short-circuit current density (J_{sc}) was obtained from external quantum efficiency (EQE) measurements.

The Fourier transform photocurrent spectroscopy (FTPS) technique was used to measure the sub-bandgap absorption spectra of the intrinsic layers as incorporated within the solar cells; the setup and measurement conditions are described in detail in § 2.4. The FTPS spectra were calibrated at 1.35 eV, by setting the absorption coefficient of the µc-Si:H cells studied here to the value of crystalline silicon; with this calibration procedure, we suppose that the absorption at 0.8 eV is mainly due to the crystalline phase (included the nanocrystals' surface). However, at this photon energy, a contribution from the amorphous phase may not be entirely excluded.

Micro-Raman spectroscopy was performed with a HeNe laser excitation beam (633 nm) to evaluate the average crystallinity factor of the intrinsic layer,

calculated as the arithmetical average of the Raman crystallinity factor as measured from the top and bottom of the samples (see § 2.3).

5.5 Initial parameters of the solar cells

As already mentioned, the most efficient microcrystalline silicon solar cells are those with an intrinsic layer of medium crystallinity (ϕ_c ~ 50%) [7]. This statement is verified for both dilutions series studied here: fig. 5.1 shows the conversion efficiency, after initial annealing (1h30, 180°C), as a function of the Raman crystallinity factor ϕ_c:

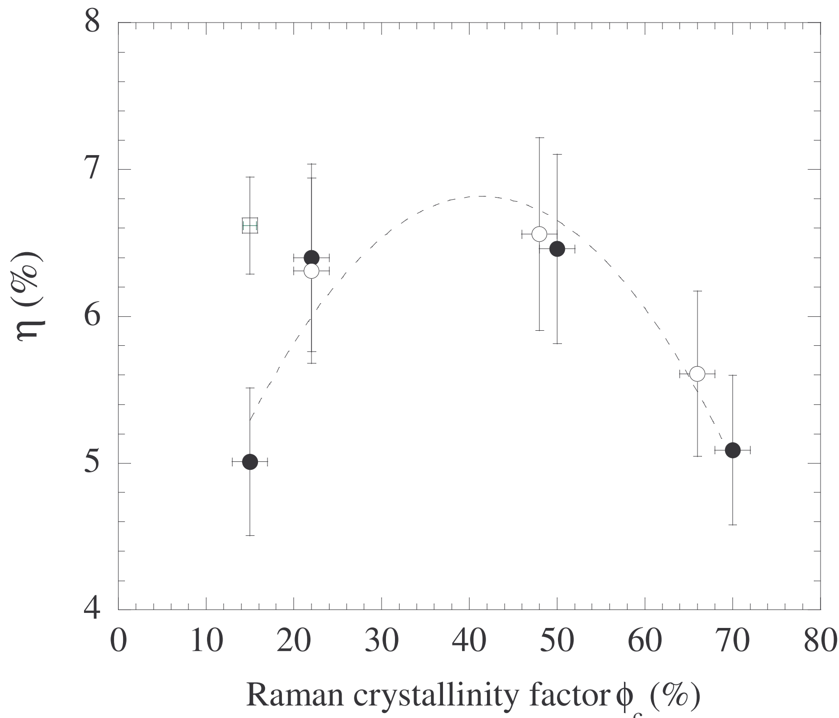

Figure 5.1. Conversion efficiency η as a function of Raman crystallinity factor ϕ_c for both series of cells: empty dots: pin series, black dots: nip series. The square symbol represents the pin cell with varying i-layer dilution. The dotted line is merely a guide for the eye.

The presence of an optimum conversion efficiency is clearly observable and occurs for Raman crystallinity factors in the order of 40 % to 50 %. Both series present a very similar trend. As expected from [90], the solar cell with the intrinsic layer deposited at variable dilution ($i_1 + i_2$) presents a higher efficiency than the nip cell with similar crystallinity.

The efficiency optimum corresponds to a minimum in defect-related absorption, as can be clearly seen in Fig. 5.2:

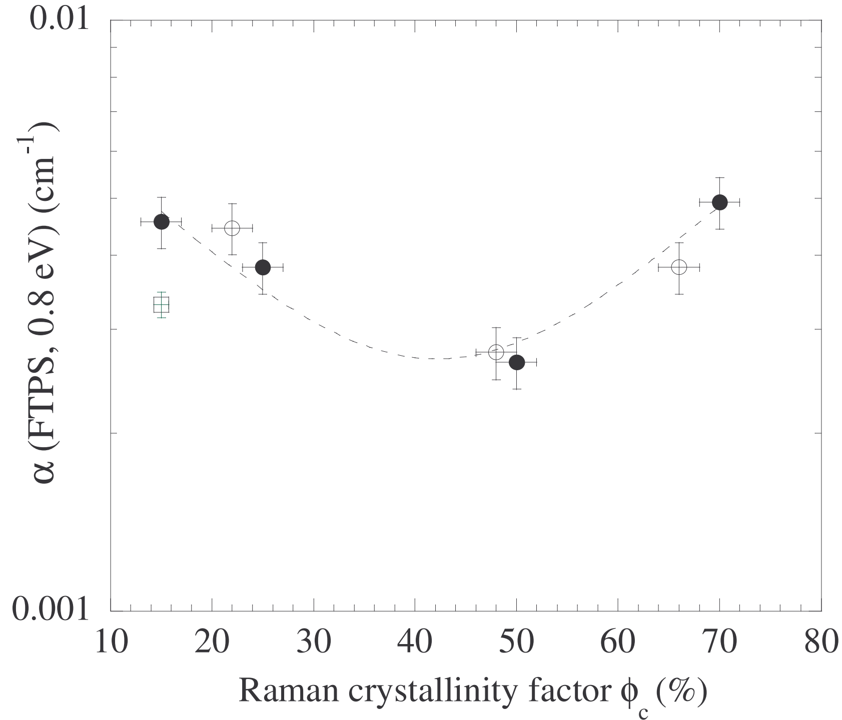

Figure 5.2. Defect-related absorption α(0.8 eV) as a function of Raman crystallinity factor ϕ_c for both series of cells: empty dots: pin series, black dots: nip series. The square symbol represents the pin cell with varying i-layer dilution. The dotted line is merely a guide for the eye.

We suggest that this optimum (highest conversion efficiency and lowest defect-related absorption), which is observed for a medium crystallinity factor, is related to the passivation of nanocrystals (grains) by amorphous silicon. Such a passivation mechanism was already observed for amorphous/crystalline interfaces [91, 92].

The sample with medium crystallinity would, thus, represent an "optimum" in passivation, whereas defect-related absorption would be higher for high ϕ_c, because there would not be enough amorphous material present to fully passivate the interface defects. The increase of α(0.8 eV) at low crystallinity factor is not so easy to explain in an intuitive way. Indeed, one knows [18] that for $\phi_c \leq 30\%$, the size of the nanocrystals is ~ 15-20 nm, and that this size does not noticeably vary with ϕ_c. Nevertheless, one could imagine that at these low values of crystalline volume fraction, the (micro)crystalline phase may be more defective, because crystalline growth is not "complete" and the phase is still rather disordered.

Moreover, Baia Neto et al [93] observed, by Electron Spin Resonance (ESR) measurements, that several types of defects are present when the amorphous fraction is high ($\phi_c \leq 30\%$). The ESR signature of these defects (i.e. their g value) does not correspond to the typical values for dangling bonds, as measured in fully a-Si:H layers.

5.6 Light-induced degradation kinetics

In order to follow the degradation kinetics of our μc-Si:H solar cells, 3 samples were chosen:

- 1 pin cell with $\phi_c = 48$ %;
- 1 nip cell with $\phi_c = 50$ %;
- 1 nip cell with $\phi_c = 15$ %.

Sequential measurements of sub-bandgap absorption (FTPS) were carried out after 20 minutes, 1h, 5h, 20h, 50h, 100h and 1000h of AM 1.5 light-soaking. The kinetics of defect-related absorption α(0.8 eV) during the degradation process is presented in Figure 5.3, as a function of light-soaking time:

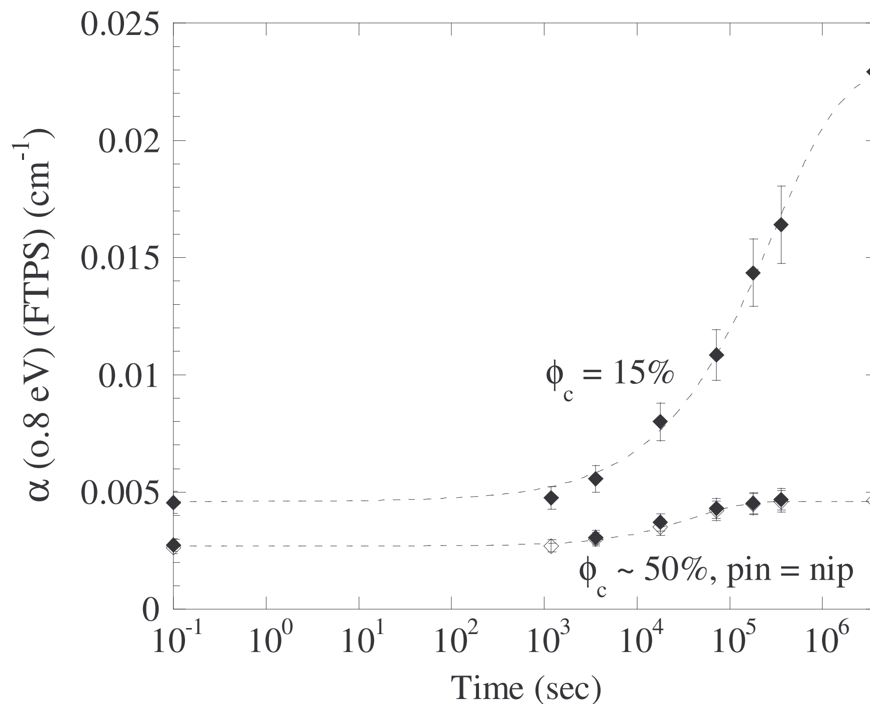

Figure 5.3. Defect-related absorption as a function of light-soaking time for a pin and a nip solar cell with medium crystallinity factor ϕ_c (empty and black diamonds, resp.), and a nip cell with low ϕ_c (black diamonds). The dotted lines are fits to equ. (5.3).

As already mentioned before, the kinetics of light-induced defect (dangling bond) creation in a-Si:H can be fitted with a stretched exponential function, as resulting from the dispersive model. This fit allows one to describe the evolution of the degradation over long time periods (as well as the apparent saturation behavior). In Fig. 5.3, we show that we can well fit our observations on the kinetics

of light-induced defect creation, also for the case of μc-Si:H solar cells of varying crystallinity, with such a stretched exponential function, as expressed by:

$$\alpha(0.8\,eV)(t) = \alpha_{ss}(0.8\,eV) - \left[\left(\alpha_{ss}(0.8\,eV) - \alpha_{initial}(0.8\,eV) \right) \cdot \exp\left(-\left(\frac{t}{\tau} \right)^{\beta} \right) \right] \quad (5.3),$$

where α_{ss} is the steady-state value (observed after a long time of light-soaking), $\alpha_{initial}$ is the initial value of defect-related absorption, β and τ are the dispersive parameter and the effective time constant, respectively.

From the fits of Fig 5.3, we can estimate that β ~0.6, independent of ϕ_c, whereas τ varies with crystallinity: $\tau = 6.6 \cdot 10^4$ s for $\phi_c = 50\%$ and $\tau = 3.1 \cdot 10^5$ s for $\phi_c = 15\%$. The increase of defect-related absorption with light-soaking time is, thus, observed to be slower than in a-Si:H, with, also, a larger measured value of β (β ~0.60 instead of 0.45 [86]). $\beta = 1$ would indicate an exponential relative increase of defect density with time, i.e. a mechanism of defect creation related with "normal" diffusion of hydrogen in the material (assuming that defect creation is "mediated" by hydrogen). According to the dispersive diffusion model proposed by Jackson et al. [87], by increasing the temperature, the limiting (dispersive-like) process, which is thermally activated, is less affected by the hydrogen trapping-detrapping process.

Let us now define the relative increase of defect-related absorption $\Delta\alpha$ (0.8 eV) as:

$$\Delta\alpha(0.8eV) = \left(\alpha_{degraded}(0.8eV) - \alpha_{initial}(0.8eV) \right) / \alpha_{initial}(0.8eV) \quad (5.4)$$

By combining equs. (5.3) and (5.4) we obtain that $\Delta\alpha$(0.8 eV) should increase with light-soaking time according to:

$$\Delta\alpha(0.8eV)(t) = \left(\frac{\alpha_{ss}(0.8\,eV) - \alpha_{initial}(0.8\,eV)}{\alpha_{initial}(0.8\,eV)} \right) \cdot \left[1 - \exp\left(\left(-\frac{t}{\tau} \right)^{\beta} \right) \right] \quad (5.5);$$

this is confirmed by the experimental results, as presented in Fig. 5.4:

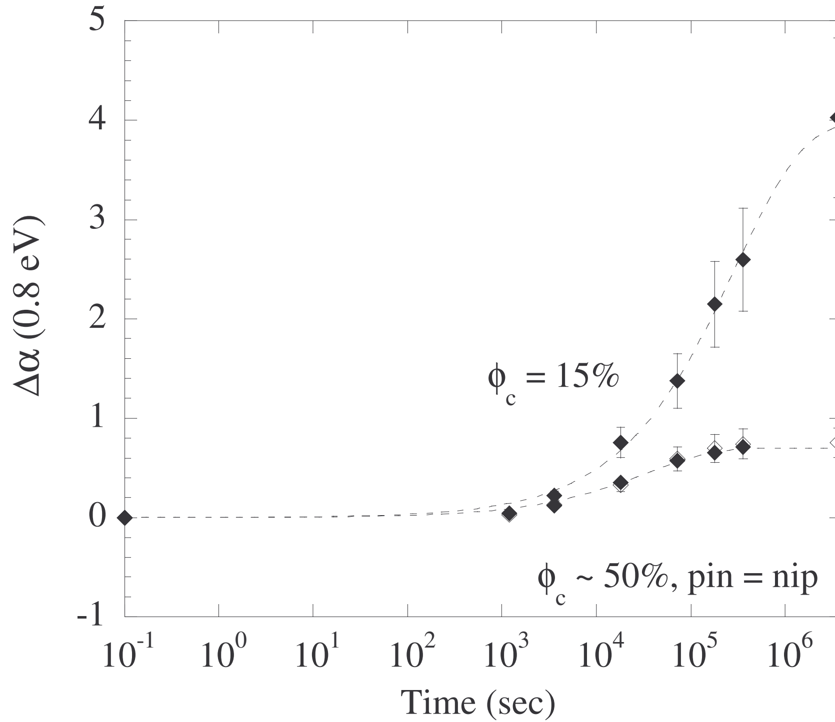

Figure 5.4 Relative defect-related absorption as a function of light-soaking time for a pin and a nip solar cell with medium crystallinity factor ϕ_c (empty and black dots, resp.), and a nip cell with low ϕ_c (black dots). The dotted lines are fits to equ. (5.5).

One could also fit the degradation kinetics with a power-law increase of α(0.8 eV), but then the quasi-saturation observed for long light-soaking time (> 500 hours) cannot be fitted anymore. Furthermore, in this case, the exponent would depend on the crystallinity, which is surprising. Indeed, in the bond-breaking model, the exponent in the power law results from the recombination function used in the model (the value 1/3 [88] results from monomolecular recombination). In our case, it would, thus, be surprising, if one had to postulate that the nature of the recombination process should depend on the crystallinity.

5.7 Light-induced degradation as a function of crystallinity

5.7.1 Electrical parameters

It must first be mentioned that the Raman crystallinity factors of the samples do not vary with light-soaking: the degradation observed here is, thus, clearly not due to structural or microstructural modifications (such as recrystallization).

The effect of light-soaking on the conversion efficiency of the nip and pin solar cells series is presented in Fig. 5.5; here, the relative (normalized) efficiency loss $\Delta\eta$ is presented as a function of the intrinsic layer Raman crystallinity factor ϕ_c. $\Delta\eta$ is defined as:

$$\Delta\eta = \left(\eta_{initial} - \eta_{degraded}\right) / \eta_{initial} \tag{5.6}$$

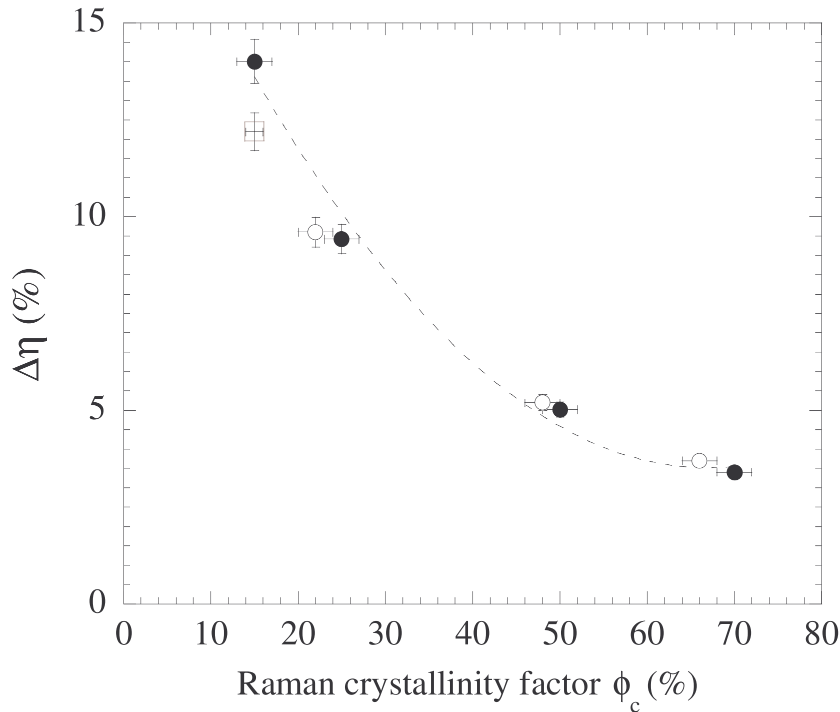

Figure 5.5. Relative light-induced loss of efficiency versus Raman crystallinity factor ϕ_c for both dilution series of cells (black dots: nip series, empty dots: pin series). The square symbol represents the pin cell with i-layer dilution profile. The dotted line is merely a guide for the eye.

Nip and pin series present very comparable relative losses of efficiency as a function of crystallinity: $\Delta\eta$ decreases with an increase in Raman crystallinity factor. This result is in agreement with the previous observations that highly μc-Si:H solar cells are not subject to noticeable light-induced degradation and agrees as well with the assumption that the amorphous matrix is the one that degrades. It should be noted that the pin cell with i-layer dilution profile shows a slightly lower degradation than the nip cell of similar crystallinity.

μc-Si:H solar cells with medium and high crystallinity factors are confirmed to be fairly stable with relative efficiency losses $\Delta\eta \leq 5\%$. Even μc-Si:H cells with a high amorphous fraction present relative losses lower than 15%, a value which is well below those that are obtained for light-soaking of a-Si:H cells ($\Delta\eta$ can be in the latter case as high as 40%, see [75], [76]).

Open-circuit voltage and short-circuit current density are observed to be rather stable under light-soaking with variations inferior to 2.5%. ΔV_{oc}, defined similarly to $\Delta\eta$, decreases linearly with the Raman crystallinity factor, as shown in Fig. 5.6 (a). On the other hand, ΔJ_{sc} is observed to be rather constant with relative losses between 1.5 and 2 %, see Fig 5.6 (b). The trend is very similar for both series.

(a)

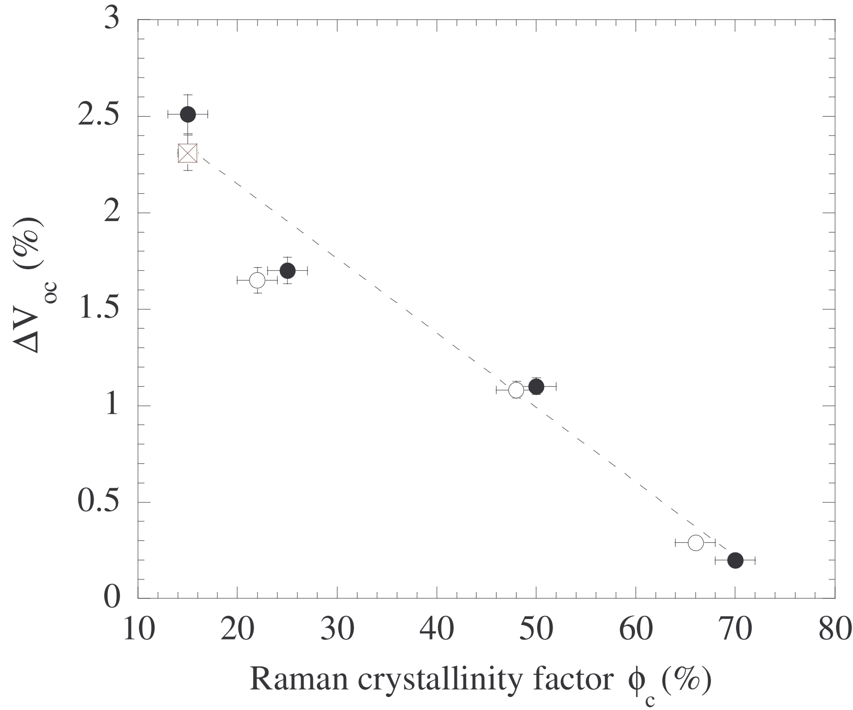

(b)

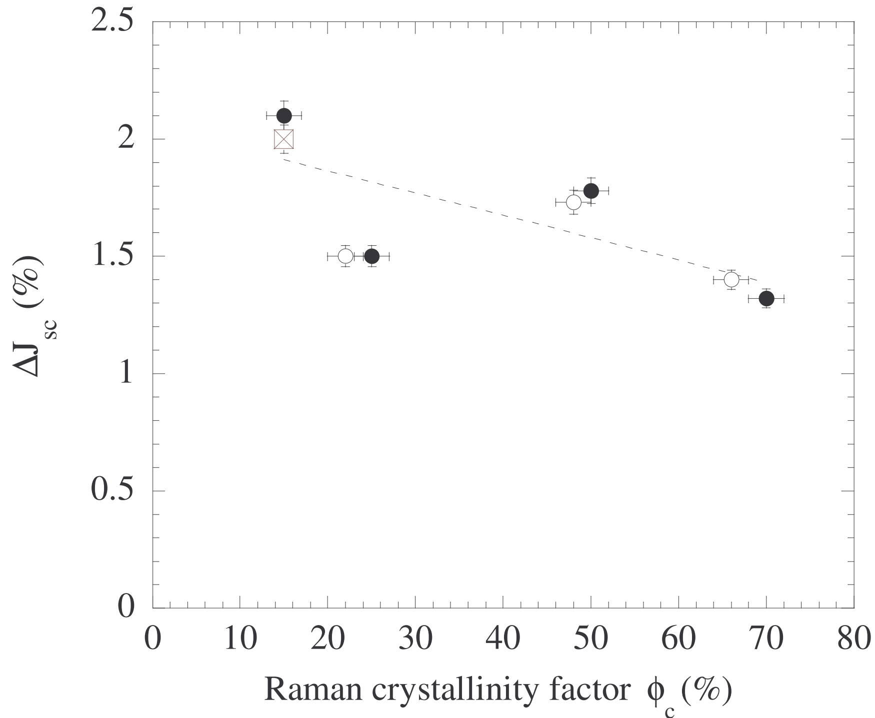

Figure 5.6 Relative light-induced loss of (a) open-circuit voltage, (b) short-circuit current density as a function of Raman crystallinity factor for both dilution series of cells (black dots: nip series, empty dots: pin series). The square symbol represents the pin cell with an i-layer dilution profile. The dotted line is merely a guide for the eye.

The relative light-induced decrease of J_{sc} shown in Fig. 5.6 (b) corresponds to a decrease of the External Quantum Efficiency (EQE) measurement in the red part of the spectra, i.e. in wavelengths over 650 nm, indicating a decrease in carriers collection. As previously mentioned, the fill factor is the parameter that is the most affected by light-soaking in a-Si:H and μc-Si:H solar cells; this is also observed for our pin and nip dilution series, as can be seen in Fig. 5.7 for the relative loss of fill factor, i.e. for ΔFF:

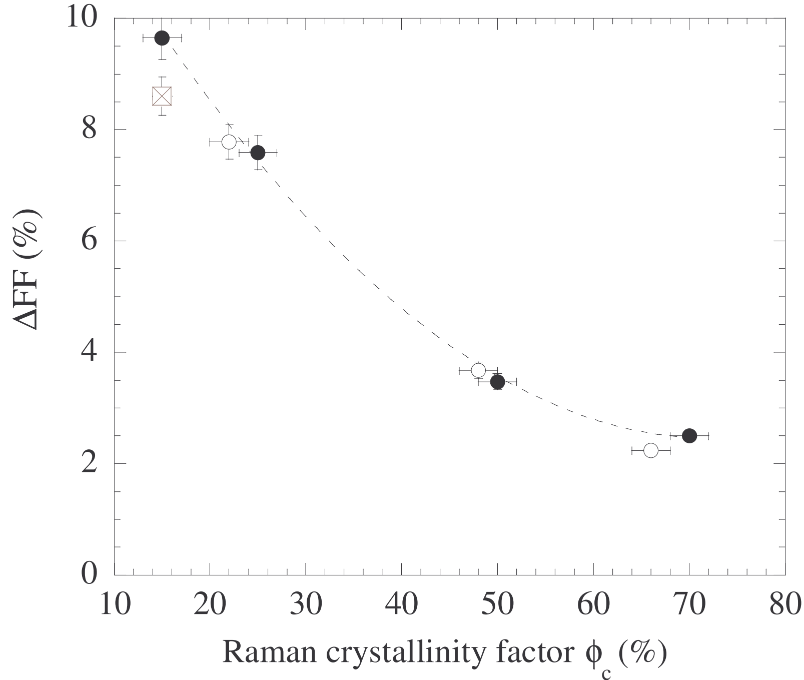

Figure 5.7. Relative light-induced loss of fill factor versus Raman crystallinity factor for both dilution series of cells (black dots: nip series, white dots: pin series). The square symbol represents the pin cell with an i-layer dilution profile. The dotted line is merely a guide for the eye.

In brief, the electrical parameters that are affected by light-induced degradation in μc-Si:H single junction solar cells are those which are adversely affected by an increase in i-layer recombination (i.e. FF, V_{oc} and J_{sc} in the red part of the EQE measurement). Our observations agree, thus, with a light-induced increase of recombination center density. We will confirm this in the next paragraph where the effect of an increase of defect-related absorption on the solar cells' electrical parameters will be discussed in more detail.

Relative losses of fill factor are observed to become less pronounced for cells with higher values of the crystallinity factor, similarly to the relative losses of efficiency Δη. The sample with an i-layer dilution profile (square symbol) is again observed to be more stable than the nip sample with a similar crystallinity factor.

The fill factor can, thus, be varied by light-soaking (or annealing) the device or by varying the Raman cyrstallinity factor of the i-layer, as can be seen in Fig. 5.8:

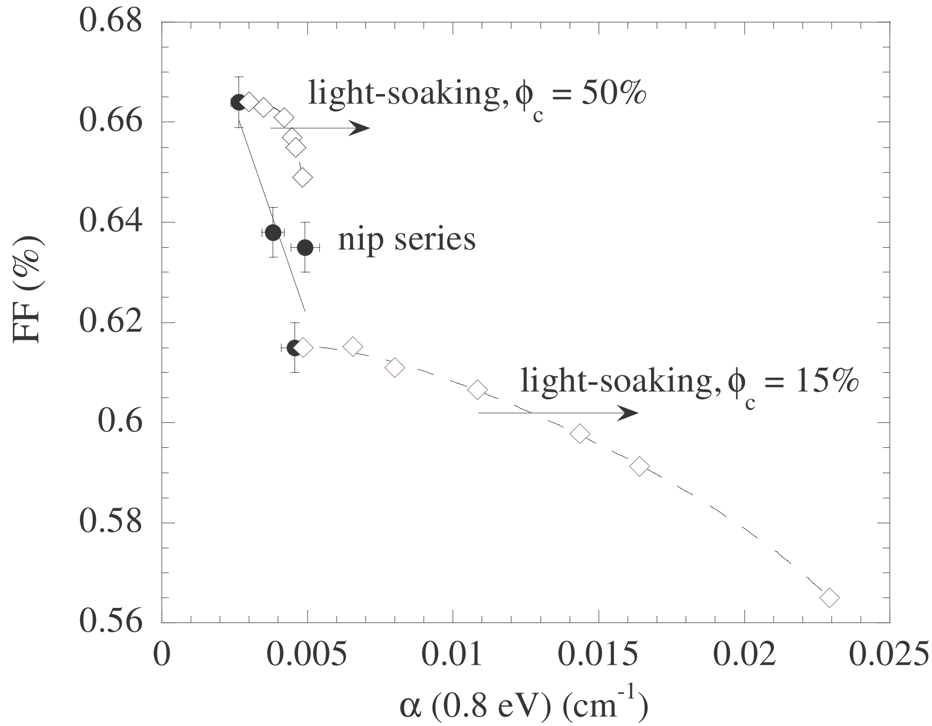

Figure 5.8. Variations of the fill factor, at initial state (black dots), and as observed during light-soaking (empty diamonds) for the nip dilution series, i.e. for cells with different values of the Raman crystallinity factor. Dotted lines are merely a guide for the eye. Similar results were obtained for the pin series (not presented here)

We observe that the variation in Raman crystallinity factor ϕ_c strongly affects the initial fill factor value: an increase of "fabrication-induced" defect-related absorption α(0.8 eV) by a factor of around 2 corresponds to a reduction of the fill factor by approximately 5%. In the case of light-soaking, the behavior of FF with α(0.8 eV) seems to depend on the Raman crystallinity factor ϕ_c:

- For the optimum cell (with ϕ_c = 50%), the effect of light-induced defects on the FF would be quite similar to that of "fabrication-induced" defects;
- For the mainly amorphous cell, a larger increase of α(0.8 eV) would be necessary to obtain a similar decrease in the fill factor.

But the representation of Fig. 5.8 can be misleading, as it is the relative loss in FF as a function of the relative increase in α(0.8 eV) that is representative of the effect of light-induced defects on the device's electrical parameters. Fig. 5.9, thus, presents $\underline{\Delta}$FF as a function of the relative increase in defect-related absorption $\underline{\Delta}\alpha$(0.8 eV) due to light-soaking. For comparison, the relative loss of fill factor with respect to the best initial value of FF (i.e. the fill factor value of the sample with ϕ_c = 50%, FF = 66.4%) is also shown for the nip dilution series, as a function of the relative variation of α(0.8 eV). In this case, the latter is due to the variations in Raman crystallinity factors of the as-deposited cells:

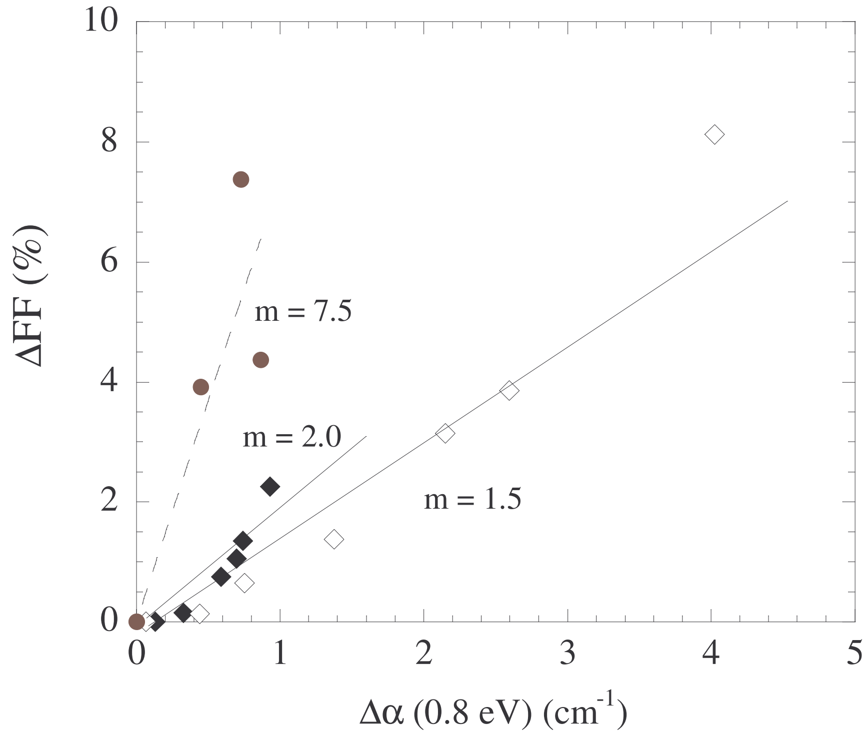

Figure 5.9. Relative light-induced loss of fill factor versus relative increase of defect-related absorption for 2 nip samples (black diamonds: sample with ϕ_c = 50 %, empty diamonds: ϕ_c = 15%). For comparison, we also plot, for the whole nip series and for the initial state, the difference between the FF of each cell and the FF of the best cell (black dots), as a function of the corresponding relative difference in measured defect absorption Δα(0.8 eV). Changes are brought about here by varying the Raman crystallinity of the cell, i.e. by varying the silane concentration during deposition. All dotted lines are proportional fits (as assumed for coarse approximation).

Fig. 5.9 shows that the behavior of ΔFF as a function of Δα (0.8 eV) can be more or less well fitted with a proportional relationship which slope varies with crystallinity: m = 1.5 ± 0.5 for ϕ_c = 15 %, m =2.0 ± 0.5 for ϕ_c = 50 % and m = 7.5 ± 0.5 when comparing the initial values of all cells fabricated. Once we plot ΔFF versus Δα(0.8 eV), we, thus, see that the variation of fill factor with increasing defect-related absorption is very similar in the case of light-soaking, for both solar cells, although they have very different values of Raman crystallinity. On the other hand, the plot that represents the differences in fill factor versus the differences in defect-related absorption, for the whole nip series with varying crystallinity in the "initial" state (after fabrication and first annealing), has a 3 times larger slope than the curves that are taken from the light-soaking process. This difference in the slopes suggests that defects created during light-soaking are different from those created by solar cell fabrication.

However, care must be taken when comparing these 3 curves. Indeed, by fitting with a proportional relationship, we assume that (see also Chapter 4, equ. (4.19 – 4.21):

$$\Delta FF \approx K(\varphi, d_i, \mu^0) \cdot \frac{\alpha(0.8\,eV)}{k} \qquad (5.7),$$

with K a constant that is a function of the electric field deformation φ, the i-layer thickness d_i and the effective mobility μ^0. Moreover, we assume that the effective lifetime τ^0 is proportional to the reciprocal of the defect-related absorption, i.e.:

$$\tau^0 \approx \frac{k}{\alpha(0.8\,eV)} \qquad (5.8),$$

where k is a constant that includes:

- the constant relating the defect density N_d and the defect-related absorption α(0.8 eV) for µc-Si:H (see [24] for constant values and calibration procedures in a-Si:H). M. Vanecek et al [19] estimated from Electron Spin Resonance (ESR) measurements that a spin density equal to $2 \cdot 10^{16}$ cm^{-3} corresponds to α(0.8 eV) = 0.12 cm^{-1}. Such a correspondence should be verified by ESR measurements on both our pin and nip series.
- the effective capture cross-sections of holes and electrons.

However, it is not evident that:

- in case of light-soaking, the electric field is not modified by light-induced defects, i.e. φ could increase with light-soaking;
- in case of crystallinity variation, the effective mobility μ^0 remains constant.

In fact, the assumption presented as equ. (5.7) is itself not evident, since the variations are normalized. Furthermore, it should be repeated here that defect-related absorption gives a signature that cannot be associated with any particular, specific defect; this is quite different from the situation in infrared spectroscopy, where each line is associated with a particular atomic bond. This will be even more clearly shown in chapter 6, where different types of defects, as created with proton radiation, all lead to an increase of α(0.8 eV).

5.7.2 Shunt resistance and collection voltage

The fill factor could in principle also be lower because of the presence of shunts along the cracks and voids that exist in µc-Si:H devices (see Chapter 4). We thus carried out variable illumination measurements (VIM), as introduced in chapter 4, to evaluate the "real" shunt resistance of the samples, in order to confirm that the variations in fill factor observed in Figs. 5.8 and 5.9 are indeed a consequence of an

increase of recombination (collection losses).

Fig. 5.10 shows the short-circuit resistance R_{sc} as a function of the inverse of the short-circuit current density J_{sc} for the nip series at initial state: for low illumination, i.e. high $1/J_{sc}$ values, R_{sc} tends to the shunt resistance R_{sh}; the collection voltage V_{coll} is assessed from the linear part of the R_{sc} (J_{sc}^{-1}) curves.

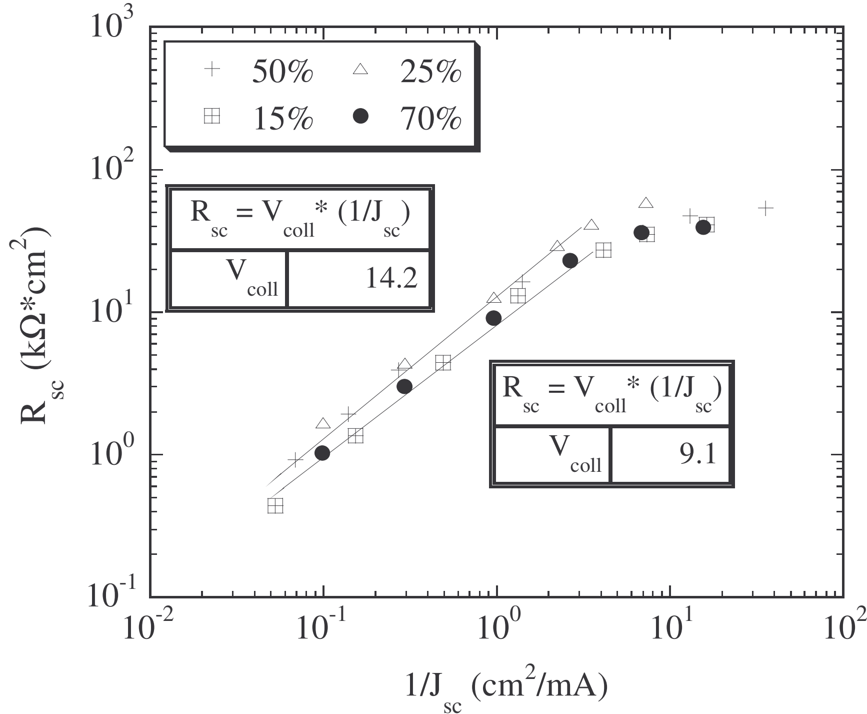

Figure 5.10 Short-circuit resistance R_{sc} as a function of the inverse of short-circuit current density for the nip dilution series at initial state.

Fig. 5.10 shows that all samples converge to similar values of shunt resistance R_{sh} indicating that shunts are not responsible for the variations of FF observed with Raman crystallinity factor, in initial (as fabricated) state, as previously shown in Fig. 5.8. On the other hand, the collection voltage V_{coll} varies with crystallinity: the highest value is obtained for the sample of ϕ_c = 50 % (V_{coll} = 14.2), the lowest for the sample of ϕ_c = 15 % (V_{coll} = 9.1). Similar results were obtained with the pin series (not presented here). As previously mentioned, such a range of low collection voltage values suggest that both pin and nip series are very probably contaminated by oxygen. VIM is, thus, a very useful technique that shows that, already in initial state, the collection voltage is too low: for good μc-Si:H solar cells, collection voltage values of up to 70 V can be measured.

The variation of FF with light-soaking can also be attributed to a decrease of the collection voltage, as can be seen in Fig. 5.11 for the mainly amorphous nip cell:

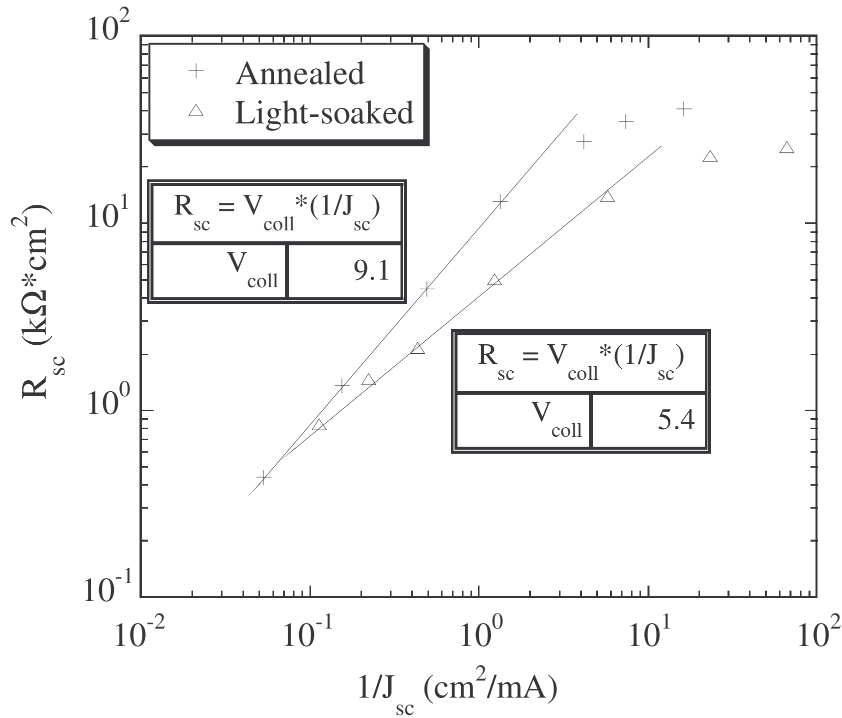

Figure 5.11 Short-circuit resistance R_{sc} as a function of the inverse of short-circuit current density for the nip sample of ϕ_c = 15 %, before and after light-soaking. The shunt resistance is not modified (within measurement errors) by light-soaking

The decrease of collection voltage observed is in good agreement with the empirical relationship presented in the previous Chapter 4 for the absolute loss of fill factor δFF between the ideal value FF_0 equal to 75%, and the actual, measured, value, as a function of the reciprocal of the collection voltage V_{coll}, expressed by:

$$\delta FF \approx \frac{1}{V_{coll}} \cdot 90\% \tag{5.9}$$

Indeed, we obtain:

- Before light-soaking: δFF equal to ~ 13 %, for a V_{coll} equal to 9.1 V
- After light-soaking: δFF equal to ~ 19 %, for a V_{coll} equal to 5.4 V

Moreover, as quantitatively discussed in Chapter 4, a reduction in the collection voltage is indeed expected when the defect density, as measured by α (0.8 eV), increases (the higher the defect density, the larger the recombination).

The decrease of the collection voltage is also consistent with External Quantum Efficiency (EQE) measurements, where a (slight) reduction is observed in the “red” part of the spectra, indicating a loss in the carriers’ collection efficiency.

5.7.3 Defect-related absorption

In the previous paragraph we have shown that μc-Si:H solar cells degrade under light-soaking. More particularly, we have seen that the electrical parameter of the devices which is the most sensitively affected by light-soaking is the fill factor. The decrease of FF can be attributed to an increase in defect density, as was previously discussed in Chapter 4. Here, we will discuss the effect of layer crystallinity on the degradation: more precisely, we will show that defect density, as measured by α(0.8 eV), is minimal for a Raman crystallinity factor equal to around 50%. Furthermore, we will show that the relative, light-induced, increase of defect-related absorption $\Delta\alpha$(0.8 eV) decreases proportionally to the ratio of the crystalline volume over the amorphous volume of the intrinsic layer. We will discuss only the results obtained for α(0.8 eV), but sub-bandgap measurements also give information about the Urbach parameter E_0; it should, still, be mentioned that:

- E_0 varies with crystallinity in a very similar trend as α(0.8 eV) (see Fig 5.14 (a) and (b) and [11]);
- E_0 is not modified by light-soaking (i.e. no increase of the "network" disorder (strained bonds) is observed; defects are only created near midgap).

FTPS spectra of initial and degraded states of the mostly amorphous nip cell (ϕ_c = 15 %) are presented in Fig. 5.13:

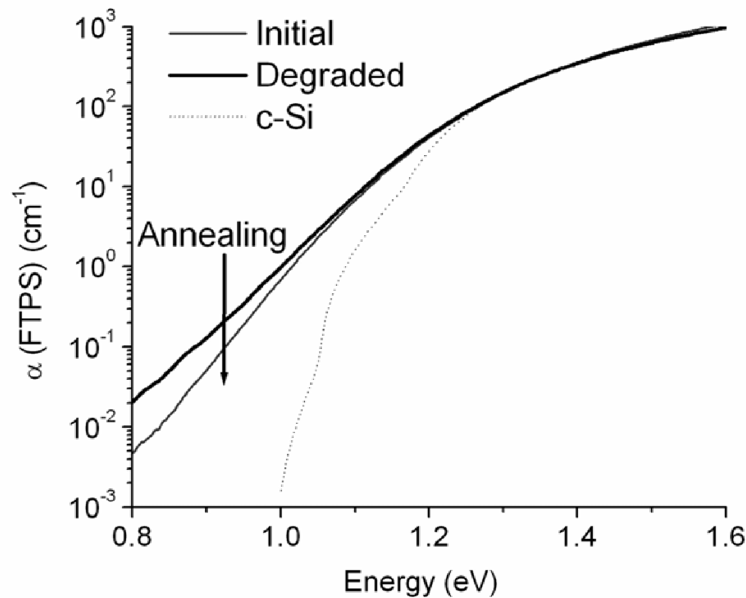

Figure 5.13. FTPS spectra in initial and degraded state for the nip cell with ϕ_c = 15 %.

Fig. 5.13 shows an increase in defect-related absorption of a factor 5 after degradation; in Figs. 5.14 (a) and (b), defect-related absorption is presented in initial and degraded state as a function of crystallinity, for both nip and pin series:

(a)

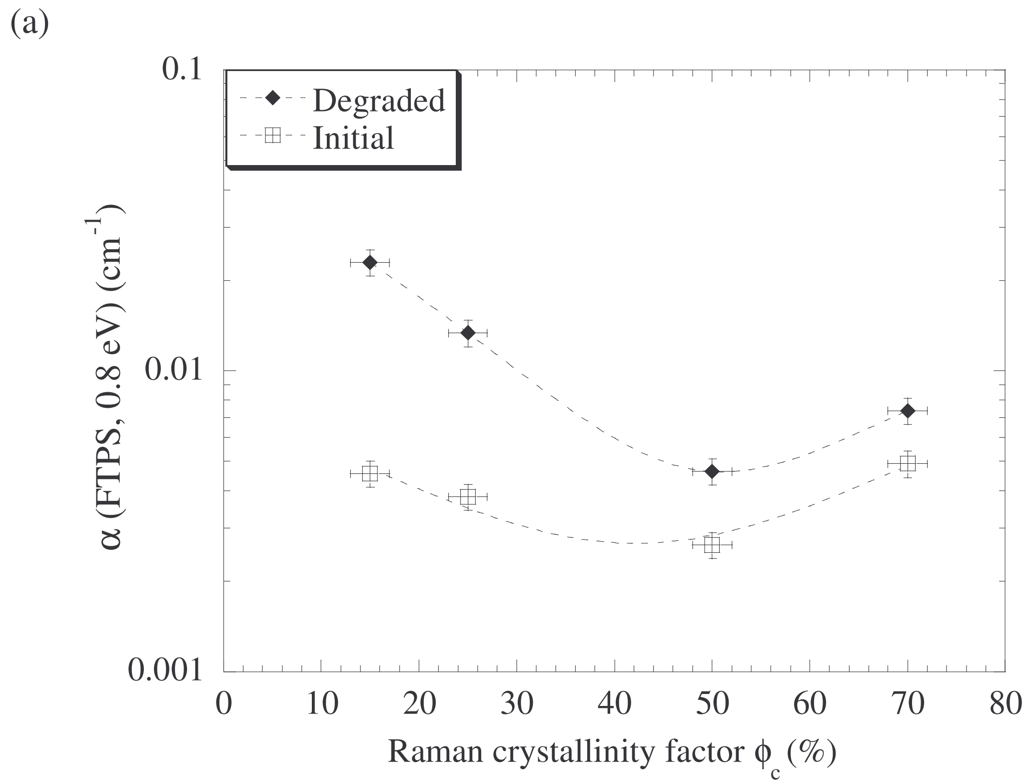

(b)

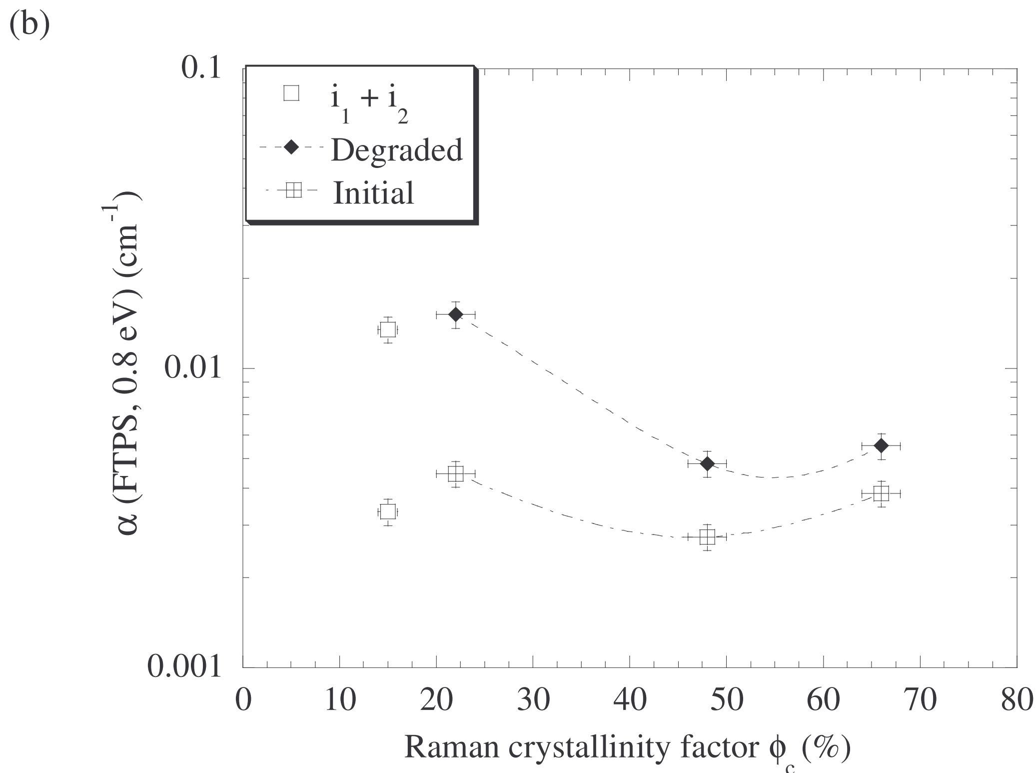

Figure 5.14. Defect-related absorption in initial and degraded state as a function of i-layer crystallinity for (a) nip dilution series, (b) pin dilution series. The dotted lines are merely guides for the eye.

Nip and pin series present very similar trends and it becomes apparent that highly μc-Si:H cells are subject to only very small variations of α(0.8 eV). This is in agreement with the low relative losses of efficiency observed for these cells under light-induced degradation. The minimum of absorption already observed in Fig. 5.2 in initial state is maintained in the degraded state as well. This means that even if the defect density of these "optimum cells" somewhat increases with light soaking, its value remains, in the degraded state, still lower than that of highly microcrystalline cells.

Furthermore, we observe that Δα(0.8 eV), as previously defined in equ. (5.4), is roughly proportional to the amorphous/crystalline volume ratio in the intrinsic layer of the device, see Fig. 5.15:

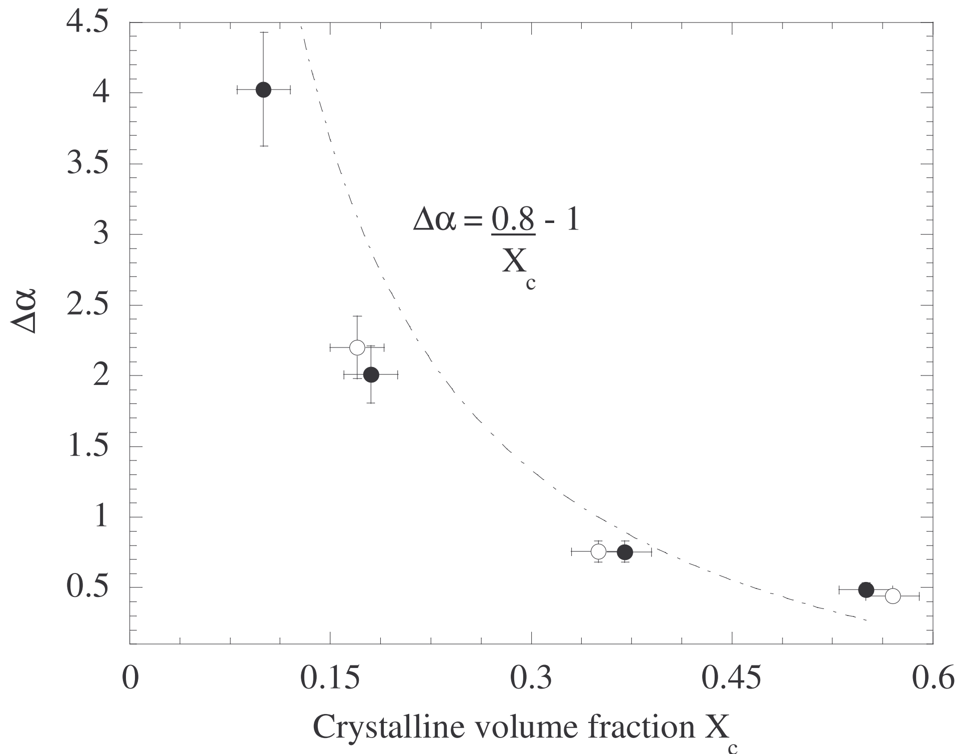

Fig. 5.15. Normalized light-induced defect-related absorption, as measured in the nip (black dots) and pin (empty dots) dilution series, as a function of i-layer crystalline volume fraction X_c.

Indeed, the crystalline volume fraction is basically defined as:

$$X_c = \frac{V_c}{V_{tot}} \quad (5.10),$$

where V_c and V_{tot} are the crystalline volume and the total volume of the sample, respectively. X_c can be calculated directly from ϕ_c, see [18] for the detailed calculation procedure.

The observed trend (dotted line) is, thus, described by the expression:

$$\Delta\alpha(0.8eV) \approx \frac{1}{X_c} - 1 \tag{5.11}$$

And $\Delta\alpha$(0.8 eV) decreases, therefore, according to the equation:

$$\Delta\alpha(0.8eV) \approx \frac{V_{tot} - V_c}{V_c} = \frac{V_a}{V_c} \tag{5.12}$$

Equ (5.12), thus, suggests that light-induced degradation is indeed related to the amorphous phase, as proposed by [63, 76, 80], but also related to the crystalline phase. Therefore, according to the results of Fig. 5.15, the variations of defect-related absorption, as measured at 0.8 eV, have to correspond to the creation of passivation defects in the crystalline phase; we are stipulating here that they correspond to defects at the surface of the nanocrystals. Furthermore, we also observed a dependence of the degradation kinetics as a function of intrinsic layer crystallinity (see Fig. 5.3). We will, thus, suggest a simple model, discussed further in § 5.10, where the light-induced defects must somewhat diffuse from the amorphous phase to the nanocrystals surface.

5.8 Defect annealing

Now that we have looked at the effect of light-soaking on the electrical parameters and sub-bandgap absorption value of the μc-Si:H pin and nip series, we will look at the effect of subsequent thermal annealing steps. We will show that the light-induced degradation observed is completely reversible under thermal annealing.

5.8.1 Electrical parameters

The effect of light-soaking and annealing steps on the solar cell relative efficiency $\Delta\eta$ (as was defined in equ. (5.6)) is presented in Fig. 5.16 for the nip series: we observe that the largest variations occur after the first annealing at 100°C, whereas total recovery (+/- 1%) appears after the annealing step at 180°C. Some cells even show, after the last annealing step, higher efficiencies than they initially had. Analogous results were obtained for the pin series (not presented here).

5.8.2 Defect-related absorption

Relative defect-related absorption, as defined in equ. (5.4), is similarly shown, in Fig. 5.17, for the nip series as a function of step-wise annealing steps. Again, the pin series, not shown here, presents a very similar trend with a total recovery after annealing at 160°C and above.

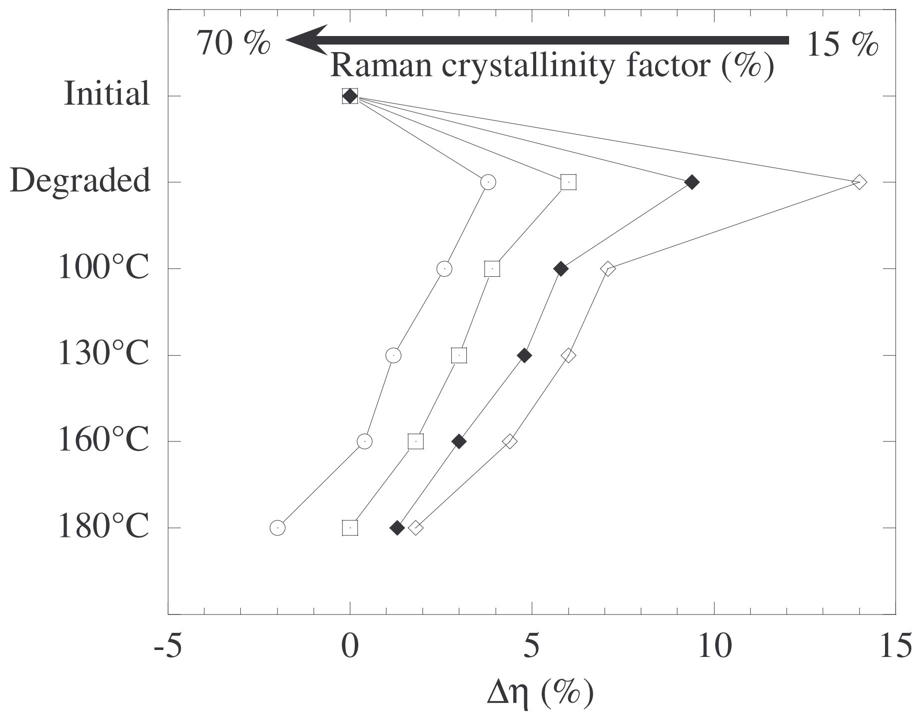

Figure 5.16. Relative efficiency as a function of step-wise annealing for the nip dilution series.

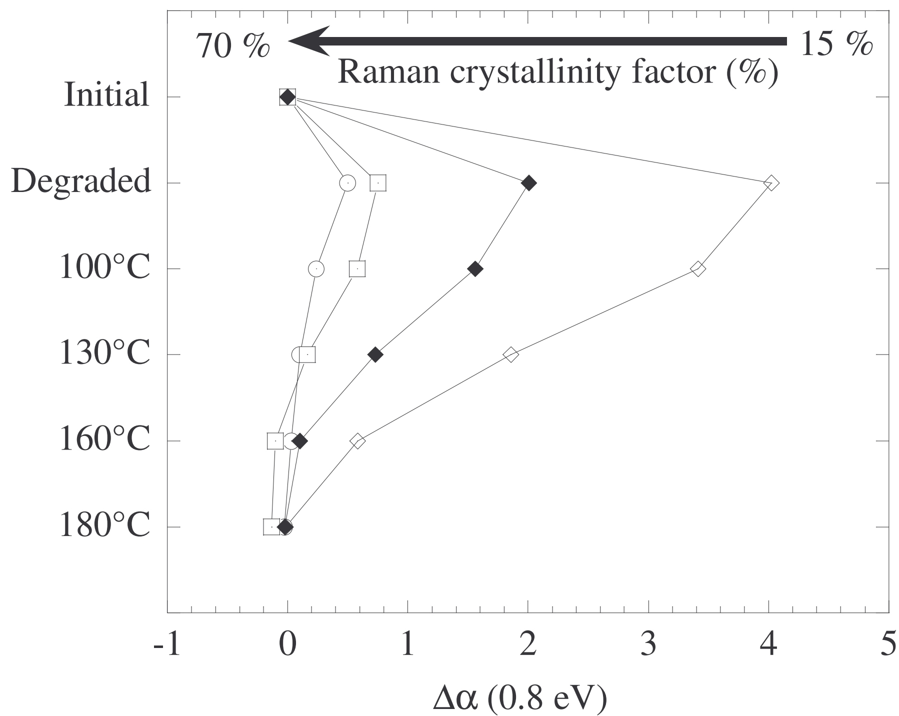

Figure 5.17. Relative defect-related absorption as a function of step-wise annealing for the nip dilution series.

5.9 Annealing kinetics

In § 5.6 we showed that the kinetics of light-induced degradation of pin and nip µc-Si:H solar cells incorporating an i-layer of varying crystallinity could be fitted with a stretched exponential function, as typically used to describe light-soaking in a-Si:H. We now want to check whether the kinetics of annealing can also be fitted with such a stretched exponential function. Therefore, in a further experiment, FTPS measurements of two nip solar cells with ϕ_c = 15% and ϕ_c = 50%, already characterized during light-soaking, were undertaken after 20 minutes, 1h, 2h, 5h, and 10 hours of annealing at T_a = 373 °K (100°C). The sample with ϕ_c = 15% was also measured during the annealing at T_a = 403 °K (130°C). The evolution of defect-related absorption α(0.8 eV) of these 3 devices with annealing time is presented in Fig. 5.18:

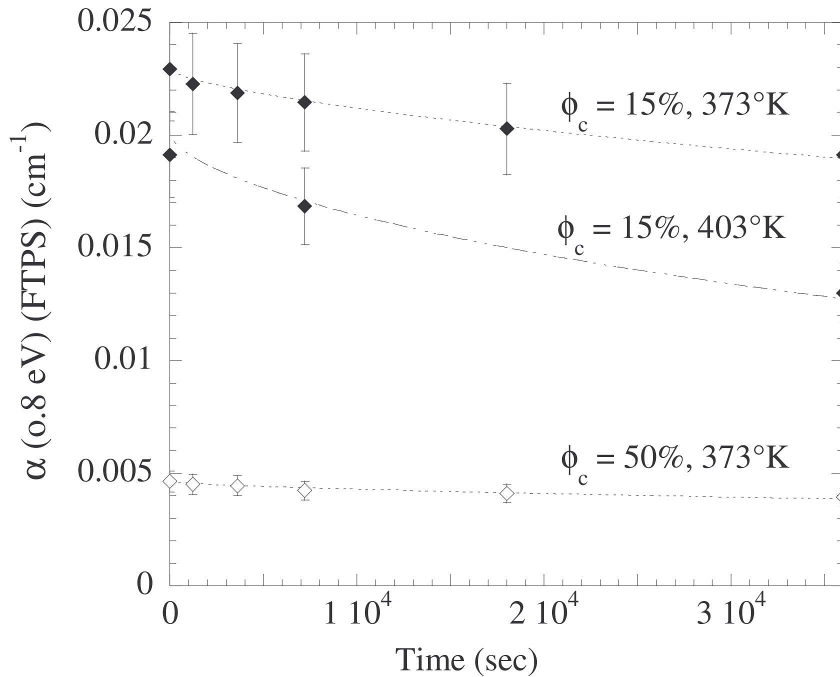

Fig. 5.18. Defect-related absorption as a function of annealing time for two nip cells, with Raman crystallinity factor ϕ_c = 15% (black diamonds) and 50% (empty diamonds): at 373°K for both cells and, additionally, at 403°K for the sample with ϕ_c = 15%. The dotted lines are fits to the equation (5.13).

In § 5.6, we showed that the creation of light-induced defects in µc-Si:H can be fitted with a stretched exponential function as predicted by the dispersive model (presented in § 5.1). This function can also be used to describe the kinetics of light-induced defect annealing, with the expression:

$$\alpha(0.8\,eV)(t)=\alpha_{ss}(0.8\,eV)\cdot\exp\left[-\left(\frac{t}{\tau}\right)^{\beta}\right] \quad (5.13),$$

where α_{ss} is the steady-state (after light-soaking) value of defect-related absorption,

τ a characteristic annealing time of the defects and t the annealing time; τ is a function of the annealing temperature, through the expression:

$$\tau = \tau_0 \cdot \exp\left(\frac{E_a}{kT_a}\right) \qquad (5.14),$$

with E_a the activation energy and T_a the annealing temperature.

By fitting the results presented in Fig 5.18 we obtain that the value of β is independent of ϕ_c, β ~ 0.69 for 373°K, whereas τ varies with crystallinity. Values of $\tau_0 = 9.6 \cdot 10^{-2}$ s for $\phi_c = 50\%$ and $\tau_0 = 6.6 \cdot 10^{-2}$ s for $\phi_c = 15\%$ are calculated from the fits and equ. (5.13). Conversely, E_a is independent of ϕ_c, as will be shown in Fig 5.22.

Fig. 5.19 shows that relative light-induced defect-related absorption Δα(0.8 eV) also decreases with annealing time and temperature according to a stretched exponential function, as expected from equ. (5.15) (derived from equ. (5.13):

$$\Delta\alpha(0.8\,eV)(t) = \left(\frac{\alpha_{ss}}{\alpha_{in}}\right)\left[\exp\left[-\left(\frac{t}{\tau}\right)^{\beta}\right]\right] - 1 \qquad (5.15)$$

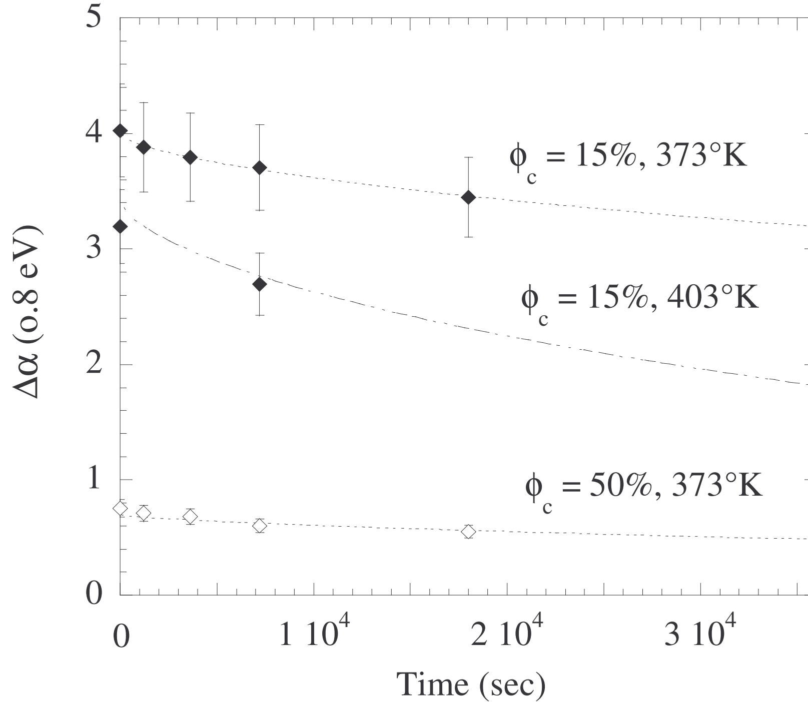

Figure 5.19 Relative light-induced defect-related absorption as a function of annealing time for two nip cells, with Raman crystallinity factor $\phi_c = 15\%$ (black diamonds) and 50% (empty diamonds): at 373°K for both cells and, additionally, at 403°K for the sample with $\phi_c = 15\%$. The dotted lines are fits according to equ. (5.15)

The kinetics of annealing are, thus, confirmed to be very similar to those of degradation, i.e. they can be well fitted with a stretched exponential function. The values of β, as measured for light-soaking and annealing, are slightly different (0.60 for T_{deg} = 323 °K and 0.69 for T_a = 373 °K); the values of τ also differ, by as much as 1 to 2 orders of magnitude. These variations are due to the difference between the degradation temperature (T_{deg} = 323°K) and the annealing temperatures (T_a = 373 °K and 403 °K). Indeed, from the dispersive diffusion model, it is expected that both β and τ are functions of the temperature: more precisely, β is proportional to the temperature in a-Si:H [86]. This is verified for µc-Si:H, and presented in Fig. 5.20:

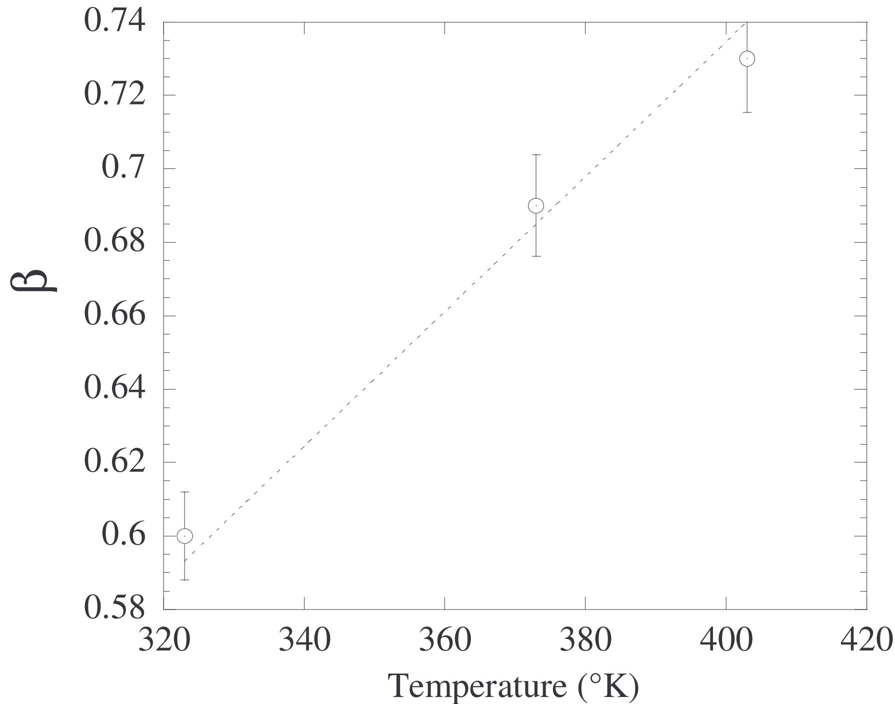

Figure 5.20. Dispersion parameter β as a function of temperature for light-soaking (T_{deg} = 323 °K) and for two annealing steps (T_a = 373 °K and 403 °K), for µc-Si:H nip cells. The dotted line is a proportional fit: $\beta = T/T_0$ with T_0 = 614 °K.

It must be mentioned that the values of β established for µc-Si:H are only slightly larger than those obtained for a-Si:H (see [86]), whereas values of the time constant τ differ by around 8 orders of magnitude between a-Si:H and µc-Si:H (see Table 5.1 at the end of this chapter). In the case of µc-Si:H, $\beta = T/T_0$ with T_0 = 544 °K instead of T_0 = 600 °K as in the case of a-Si:H. This confirms that the mechanism of light-induced degradation and annealing in µc-Si:H is not exactly the same as in a-Si:H.

Fig. 5.21 shows defect-related absorption for two nip cells (ϕ_c = 15 %, ϕ_c = 50 %) as measured after each of the 10 hours long annealing steps, at increasing temperatures:

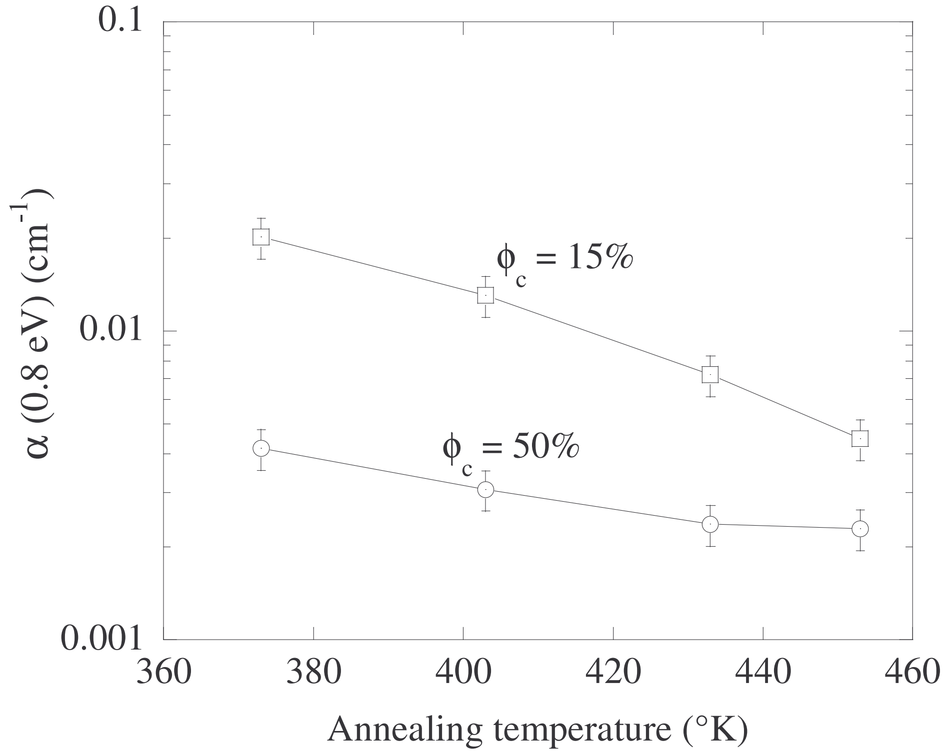

Fig. 5.21 Defect-related absorption reached, after 10h step-wise annealing of light-soaked nip samples, under N_2 flow. Lines are merely a guide for the eyes.

We observe that during the subsequent annealing steps, α(0.8 eV) decreases; the values of α(0.8 eV) obtained at the end of each subsequent annealing step can be described by a thermally activated behaviour, as expressed in equs. (5.13)-(5.14). The annealing behaviour is, thus, indeed similar to the one observed for a-Si:H samples, as presented in [94], but it is slower for μc-Si:H. The initial values are thereby not yet reached after 10 hours, as would have been the case for a-Si:H.

We already observed that the characteristic time τ is different for μc-Si:H than for a-Si:H, but what happens with the activation energy E_a? Fig 5.18 showed that β varies from 0.69 to 0.73 for annealing temperatures T_a ranging from 373 °K to 433 °K. We will, therefore make as a simplification the hypothesis that β is almost constant, β ~ 0.7, over the range of temperatures used here, so that the activation energy can then simply be derived from equ (5.13):

$$\left(\log\left[\frac{\alpha_0(0.8\,eV)}{\alpha_{10h}(0.8\,eV)}\right]\right)^{1/\beta} = C(\tau_0)\cdot\exp(-\frac{E_a}{kT_a}) \qquad (5.16)$$

Let us plot this logarithmic ratio as a function of $1/T_a$:

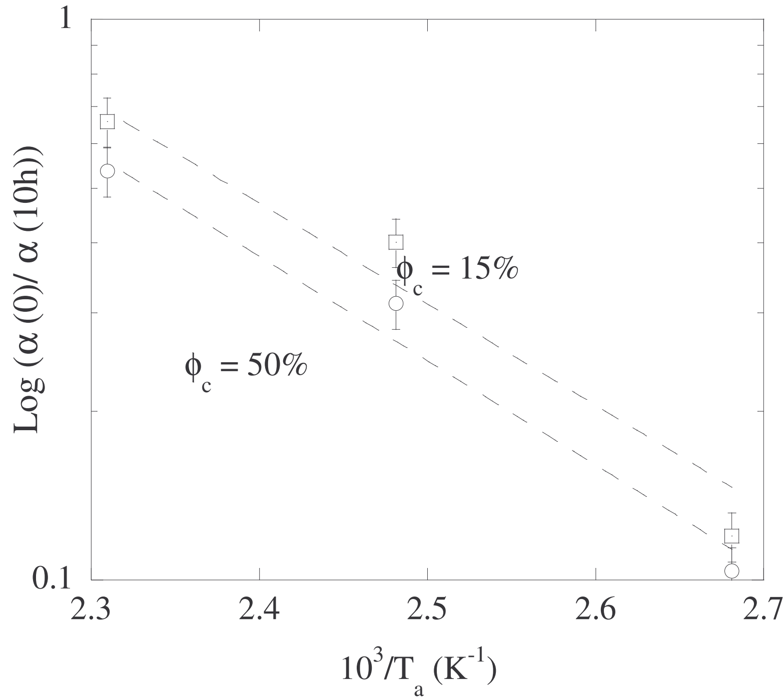

Fig. 5.22. Logarithmic value of the ratio of defect-related absorption before and after 10h annealing, in logarithmic scale, as a function of the reciprocal of the annealing temperature for 2 nip solar cells of different crystallinity. The dotted lines are fits to equ. (5.16)

We indeed observe a linear relationship, as is expected from equ. (5.16) (logarithm scale); the slope results in an activation energy E_a = 0.5 eV, independent of crystallinity. A similar value is obtained with the pin series (not presented here), as well as with the previously studied nip series, as presented in the Annex A1.

This value of activation energy is lower than the typical values obtained for light-induced defects in a-Si:H, which are in the order of 1 eV [86, 87]. This observation means that the defects, as created by light-soaking in µc-Si:H, are different from those created in a-Si:H: they can be annealed at a lower temperature.

5.10 Model for light-induced defect creation and annealing in µc-Si:H solar cells

The whole study of light-soaking presented in this chapter is based on the basic assumptions that in µc-Si.H solar cells, the defect density can be directly related to the absorption α as measured at 0.8 eV. Moreover, by calibrating the whole absorption spectra at 1.35 eV, we assumed that the overall absorption (at this photon energy) is dominantly in the (micro)crystalline phase [9].

We showed that there are striking similarities between µc-Si:H and a-Si:H, regarding the kinetics of creation and annealing of light-induced defects. In both cases the kinetics can be fitted with a stretched exponential function, such as

typically used when modeling diffusion mechanisms taking place in disordered systems.

Experimental values obtained for the parameters of the stretched exponential are listed in Table 5.1 for amorphous and microcrystalline silicon, for degradation as well as annealing. The values for a-Si:H are taken from references [84, 85], whereas the values for µc-Si:H have been measured in the present thesis:

kinetics	a-Si:H	µc-Si:H
degradation	stretched exponential (323 °K) $\beta = 0.45$, τ (323 °K) = ? E_a = ?	stretched exponential (323 °K): $\beta = 0.6 \neq \beta(\phi_c)$ τ (323°K) = $\tau(\phi_c)$ E_a = ?
annealing	stretched exponential: • β ↗ if T_a ↗ : β (373°K) ~ 0.60 • $\tau = f(T_a)$: $\tau_0 \sim 10^{-10}$ s $E_a \sim 1$ eV	stretched exponential: • β ↗ if T_a ↗ : β (373°K) = 0.69 • $\tau = f(\phi_c, T_a)$: τ_0 (15%) = 6.6 10^{-2} s τ_0 (50%) = 9.6 10^{-2} s $E_a \sim 0.5$ eV

Table 5.1. Parameters of the stretched exponential, as derived from fits of the kinetics of creation and annealing of light-induced defects in a-Si:H and µc-Si:H. Values for a-Si:H are taken from [86, 87].

It can be clearly seen in Table 5.1 that the time constant, dispersive factor and activation energy, as derived from fits with the stretched exponential functions, are different in µc-SI:H than those found in a-Si:H. The activation energy and the dispersive parameters do not depend on the crystallinity of the samples, whereas the time constant does. We, thus, observed that the sample of "medium" crystallinity (ϕ_c = 50%) degraded and recovered faster than the highly amorphous sample (ϕ_c = 15%).

To summarize we observed for µc-Si:H:

- A relative increase of α(0.8 eV) roughly proportional to the ratio of the crystalline volume over the amorphous volume (see Equ. 5.12);
- A "softer" and slower light-induced degradation with respect to a-Si:H, with a lower activation energy and longer time constants.

Klein et al. [63], as well as Guha et al. [76, 80], suggested that the amorphous phase is responsible for the light-induced degradation observed. Nevertheless, absorption at 0.8 eV cannot be caused by defects in the "bulk" of the amorphous phase (such defects would absorb at 1.2 eV); furthermore, from our results, we deduce that the defects observed in μc-Si:H are somehow related with both the amorphous phase and the (micro)crystalline phase. We, thus, think that they could be defects on the surface of the nanocrystals, i.e. passivation defects. This proposition is based on the well-known observation that a crystalline silicon surface can be efficiently passivated by a thin layer of amorphous silicon [91, 92]. Thus, the degraded amorphous phase would be less efficient in passivating the nanocrystals, leading to the creation of metastable defects at the surface of the nanocrystals, defects that could be optically detected at 0.8 eV.

We suggest that the observation of $\Delta\alpha$(0.8 eV) decreasing as the ratio of the amorphous volume over the crystalline volume may be explained by considering that the average defect diffusion length (mediated by hydrogen dispersive diffusion, as assumed in a-Si:H) of the defects from the amorphous phase to the nanocrystals surface is smaller if the crystalline volume fraction is higher. Such an assumption would also be in agreement with the dependence of the time constant with the crystallinity. Nevertheless, it needs further investigations before it can be ascertain.

5.11 Conclusions

In this study, creation and annealing kinetics of light-induced defects in μc-Si:H solar cells of varying crystallinity was studied by Fourier-transform photocurrent spectroscopy (FTPS). Electrical characterization of the whole cells was also conducted, in the initial and degraded state, as a function of crystallinity. The increase in the FTPS absorption value at 0.8 eV was used to estimate the increase in the density of defects (as present in the microcrystalline phase), which is a consequence of light soaking, as well as the effect of subsequent annealing steps.

The lower is the crystallinity of the cells, the stronger is the light-induced degradation observed by us. This result is in accordance with previous investigations on a-Si:H and μc-Si:H solar cells. Mainly amorphous nip and pin cells (with ϕ_c = 15%) are shown to present relative efficiency reductions of up to 14%, due mostly to a decrease of the fill factor. An increase of α(0.8 eV) by a factor of around 5 was measured for these cells. On the other hand, highly crystalline cells (ϕ_c = 70%) present a relative efficiency decrease of only ~ 3%, combined with an increase of α(0.8 eV) by a factor of only 1.5. Light-induced degradation is shown to be completely reversible under thermal annealing (similarly to the Staebler-Wronski effect present in a-Si:H).

Cells with "medium" crystallinity factor (ϕ_c ~ 50%) are confirmed to be the "optimum cells" not only giving maximum efficiency, but also possessing

minimum defect-related absorption. After light-induced degradation, even if these cells present a relative efficiency reduction of around 5%, their defect density remains lower than that of highly crystalline cells, which show only very weak degradation. Considering that the pin and nip series studied here are probably contaminated by oxygen, we may expect a lower degradation for “state-of-the-art” pin and nip cells (such as presented in [9]) Therefore, light-soaking should not be such a severe issue in µc-Si:H as in a-Si:H. Further investigations should be carried out on the effect of the thickness of the intrinsic layer on the stability of µc-Si:H solar cells.

In our measurements, all the observed light-induced reductions of electrical performances of µc-Si:H solar cells could be attributed to an increased recombination within the active intrinsic layer. Moreover, the kinetics of light-induced defect creation and annealing in our µc-Si:H nip and pin series was shown to be very similar to those given in literature for a-Si:H, albeit slower. Moreover, the relative increase of defect-related absorption was shown to be roughly proportional to the ratio of the amorphous volume over the crystalline volume. We thus believe that light-induced defects as measured at 0.8 eV, correspond to “passivation” defects, situated at the surface of the nanocrystals. In order to explain the slower degradation kinetics in µc-Si:H, as compared with a-Si:H, and its dependence on crystallinity, we suggest that light-induced degradation of µc-Si:H is mediated by the dispersive diffusion of hydrogen in the amorphous phase, with a characteristic diffusion length given by the average distance between the nanocrystals. The diffusion length of the defects from the amorphous phase to the nanocrystals surface would, thus, be smaller if the crystalline volume fraction is higher

In order to complete and validate our model, Electron-spin resonance (ESR) measurements should now be carried out; indeed, with such measurements, one should be able to determine the exact microscopic nature of our so-called “passivation” defects. Furthermore, degradation measurements as a function of temperature should also be performed: they would allow the assessment of the activation energy of light-induced defect creation in µc-Si:H, and to check if this activation energy is equal to the one derived from the kinetics of annealing.

6. Proton-induced degradation of thin-film microcrystalline silicon (µc-Si:H) solar cells

6.1 Introduction

Amorphous silicon solar (a-Si:H) cells are known to present a better stability under high-energy (1-20 MeV) proton irradiation [95-97] as compared to crystalline (c-Si) silicon devices [96]. But, contrary to a-Si:H, µc-Si:H solar cells were shown to suffer from degradation when exposed to protons within this range of energy [95, 96]. In fact, the stability of thin-film µc-Si:H solar cells under proton radiation is investigated as a complementary study to light-soaking experiments, in order to gain further physical insight into defect creation and annealing in µc-Si:H solar cells.

Indeed, in the previous chapter, we came to the conclusion that light-induced degradation of the mixed amorphous/crystalline µc-Si:H material could be attributed to the degradation of the amorphous phase of the material, leading to the creation of passivation defects at the surface of the nanocrystals. Conversely, by studying proton irradiation, one expects to directly monitor the effect of the degradation of the crystalline phase. Both complementary studies where the two phases of the material are “independently” degraded should ultimately bring further information on the microscopic nature of electronically active defects.

We will show in this chapter that µc-Si:H solar cells degrade under both high and low-energy proton radiation; the amplitude of the degradation is a function of the crystallinity: highly crystalline cells show a relative efficiency loss of up to 26 % and 70 % after high and low-energy proton irradiation, resp. In the case of high- energy protons, degradation is observed to be completely reversible under thermal annealing, in contrast with the situation for low-energy protons. Indeed, the damage created by low-energy protons within the devices is maximized, since the protons are implanted within the intrinsic layer of the µc-Si:H solar cells.

This Chapter, thus, investigates the stability of 2 dilution series of pin and nip microcrystalline silicon (µc-Si:H) solar cells (the same as used for the light-soaking study) under high-energy (E ~2 MeV) and low-energy (E ~405 keV) proton irradiation. Variation of the electrical parameters and defect-related absorption will be considered as a function of irradiation type and subsequent annealing steps.

The Chapter will be focused on two main questions:

- Are µc-Si:H solar cells of “medium” crystallinity (ϕ_c ~ 50%) stable under high- and low-energy proton irradiation ?
- If not, can we conclude that the defects generated within the (micro)crystalline phase are responsible for the degradation of the electrical parameters observed?

These issues are similar to those that were considered in Chapter 5; however, as we shall see, the resistance to irradiation as a function of the device i-layer crystallinity is opposite to that observed for light-soaking. Indeed, in case of proton irradiation, the degradation of the electrical parameters is the largest for the μc-Si:H solar cells with the highest crystallinity. Nevertheless, in a similar manner as in the case of light-soaking, the fill factor is the parameter that shows the largest relative decrease for high-energy proton irradiation.

6.2 Proton irradiation: observations and models

6.2.1. Observations

Here we summarize the characteristic behaviors observed for thin-film amorphous and microcrystalline silicon layers and single-junction solar cells under both high- and low-energy proton irradiation. In order to distinguish between high- and low-energy protons, we fix the proton energy threshold at 1 MeV. Roughly speaking, high energy protons are mainly ionizing the material while they are crossing it. Consequent to the material's ionization, localized defects can be created. On the other hand, low energy protons (i.e. H^+) are implanted within the material and can, thus, damage the material by the displacement of original atoms from their equilibrium lattice site. Thus, both types of irradiation do not generate the same type of defects.

a) High-energy p^+ ($E \geq 1$ MeV)

This range of energy corresponds to that of protons as present in space or, for much higher energies (in the order of GeV), to conditions as prevalent for particle detectors in the field of high-energy physics:

a.1) Amorphous silicon (a-Si:H)

- layers:
  - Under 12 MeV p^+ radiation, a-Si:H thin films show almost no degradation for fluences ϕ_p below 10^{13} p^+/cm^2. On the other hand, for higher fluences, an increase of the defect density of a factor ~ 5 was estimated from sub-bandgap absorption measurements at 1.2 eV. The degradation observed is shown to be completely reversible under thermal annealing at 200°C during 12 minutes [98].
- solar cells:
  - For proton irradiation with an energy equal to 1 MeV, a-Si:H solar cells show a relative efficiency degradation of around 5% for a fluence $\phi_p = 10^{14}$ p^+/cm^2. The degradation increases for larger fluences, but, in a similar way as for a-

Si:H layers, the degradation is observed to be reversible under thermal annealing. Fill factor degrades with p^+ irradiation, whereas open-circuit voltage and short-circuit current density remain rather stable [99]. Nevertheless, this latter also decreases when fluences $\phi_p \geq 10^{16}$ p^+/cm^2 are employed. Yamaguchi showed that, for such value of proton energy, the magnitude of the degradation depends on the thickness of the intrinsic layer: the higher the thickness, the more pronounced the degradation [100].

- When exposed to protons with an energy ranging from several tenths of keV up to 5 MeV, a-Si:H solar cells present a relative loss of efficiency in the order of 20%. Here, fill factor is, again, the parameter that degrades the most, whereas open-circuit voltage and short-circuit current density remain rather constant [95].

- Not only a-Si:H single-junction solar cells have been tested under p^+ irradiation: a-Si:H particle sensors have also been exposed to protons of very high energies (24 GeV). These devices consist of a pin structure with i-layer thicknesses ranging from 10 to over 30 μm. When irradiated with a fluence equal to $4.5 \cdot 10^{14}$ p^+/cm^2, 32.6 μm thick a-Si:H pin diodes show an increase of the dark (leakage) current by up to a factor 5 [101].

a.2) Microcrystalline silicon (μc-Si:H)

J. Kuendig et al. [95] as well as J. Kuendig [96] studied the degradation of μc-Si:H layers and solar cells when exposed to proton beam of energies ranging from several tenths of keV up to 5 MeV; they observed:

- layers:

  - For a 2 μm thick layer: an increase of the sub-bandgap absorption (at 0.8 eV) of a factor ~ 2.5 accompanied by a decrease of the effective mobility-lifetime ($\mu^0\tau^0$) product and of the dark conductivity of a factor ~ 1.5 and 100, resp. The magnitude of the degradation was shown to depend on the thickness of the intrinsic layer (similarly as with a-Si:H layers): Kuendig et al. suggested that proton irradiation generates a non-uniform defect profile, with a higher defect density close to the surface. The degradation measured was fully reversible under thermal annealing (at 160°C).

- solar cells:

  - A relative loss of efficiency of 24.5%: the fill factor is the parameter that degrades the most with a relative loss of 11%. Short-circuit current density and open-circuit voltage show relative reductions of 9.4 and 6.3%, resp. After annealing for 10 hours at 140°C, all parameters come back to their initial values.

When exposed to high-energy protons, amorphous and microcrystalline silicon layers and solar cells degrade, but the defects created are metastable and the degradation is completely reversible under thermal annealing.

b) Low-energy p^+ (E < 1 MeV)

In the case of low-energy protons, the H^+-particle is implanted within the material and causes much more damage than high-energy protons, which, in majority, cross the whole device. The implantation of low-energy protons can, thus, be considered as an extreme case of device degradation.

b.1) Amorphous silicon (a-Si:H)

- diodes:

  - 1 μm and 32 μm thick a-Si:H diodes were irradiated with protons of E = 405 keV at a fluence ϕ_p of $3 \cdot 10^{13}$ p^+/cm^2. Both diodes show a significant drop in the photoconductivity; the dark (leakage) current is increased by up to 3 orders of magnitude [101]. The mobility-lifetime product ($\mu^0\tau^0$) of the electrons is also increased by one order of magnitude for the thin diode. According to SRIM (Stopping and Range of Ions in Matter [102]) calculations, such low-energy protons are implanted within the first 2.0 μm of the a-Si:H device (see details in §6.4). The irradiation is, thus, expected to degrade the region close to the p-doped layer in the case of the thick cell, whereas, for the thin diode, the situation is more similar to that of high-energy protons with protons crossing through the sample. Low-energy p^+ irradiation is, thus, expected to have a more detrimental effect on the thick diode, as confirmed by N. Wyrsch et al. who observed a permanent degradation of the thick diode. In contrast with this, proton-induced degradation of the 1 μm thick diode is completely reversible under thermal annealing. N. Wyrsch et al. suggest that 2 types of defects are involved: deep defects affecting electron collection and a shallower type of defects affecting hole collection.

b.2) Microcrystalline silicon (μc-Si:H)

- solar cells:

  - Microcrystalline silicon solar cells irradiated under the same conditions as mentioned above for the a-Si:H diodes (E ~ 405 keV, $\phi_p = 3 \cdot 10^{13}$ p^+/cm^2) showed a dramatic relative efficiency decrease of up to 80% [103]. Fill factor and short-circuit current density were the electrical parameters of the devices that presented the largest degradation. The relative degradation of the device's properties due to low- energy proton irradiation was shown to

be a function of Raman crystallinity: the higher the crystallinity, the larger the relative efficiency loss. Furthermore, the degradation was observed to be related to (a) an increase of the defect density (as established from sub-bandgap absorption measurement at 0.8 eV), as well as (b) to an increase of the Urbach parameter.

The degradation induced by such low-energy protons was observed to be only partially reversible under thermal annealing.

6.2.2 Models

According to Tada [104], there are 3 dominant types of interaction between the particles (protons, electrons, etc.) used for the irradiation, and the solar cell material:

(1) Inelastic collision with the atomic electrons: part of the kinetics energy of the particle is transferred to the electrons that are then either (a) in an excited electronic level or (b) ionized.

(2) Elastic collision with the atomic cores: two types of phenomena can be considered in this category: the Rutherford diffusion and the direct collision of the incident particle with an atomic core. In the first case, the incident particle, which is charged, can have Coulomb interactions with the positive charges of the atomic cores. If the energy that is transmitted to the core is large enough, the atom will be displaced form its initial position. Following this first displacement, the atom can, then, similarly interact with the other atoms of the material. In the second case, the incident particles directly interact with the atomic cores through elastic collisions. Nevertheless, the probability for this type of interaction is lower than for Rutherford diffusion, excepted for very energetic particles.

(3) Inelastic collision with the atomic cores: in this last case, the incident particle only loses part of its kinetics energy by interaction with an atomic core.

We will, thus, distinguish between ionization and displacement damages: in the first case, an electron bound to an atom or molecule absorbs enough energy from the external source (i.e. the proton beam) to escape from the potential barrier that confined it, leading to an increased local recombination of the photogenerated carriers. On the other hand, in the case of displacement damages, vacancies are created within the material's network. In the case of highly energetic protons, irradiation mainly causes ionization damages, whereas, in the case of low-energy protons, displacement damages are also produced. Ionization damages can be thermally annealed, whereas displacement damages are permanent.

a) High-energy proton degradation

Kishimoto et al. suggested that the larger radiation hardness of amorphous silicon as compared to crystalline silicon is related to its enhanced structural flexibility [105]. Indeed, structural rearrangements (like collective atomic motions) could cancel the damaging effects of displaced atoms and prevent the creation of deep defects. The essential points of this mechanism are both (a) the structural flexibility of the a-Si:H and (b) the electronic excitation induced in the material by the high-energy protons. The electronic excitation would supply the activation energy necessary for the atomic rearrangements. On the other hand, high-energy protons can produce permanent damage in c-Si due to the displacement of atoms from their original site in the "rigid" crystalline lattice.

b) Low-energy proton degradation

N. Wyrsch et al. suggested that the implantation of low energy protons consequent to the irradiation with a p+ beam of an energy E= 405 keV leads to the creation of two types of defects [101]:

(a) Deep defects affecting the collection of electrons: these defects are reversible under thermal annealing;

(b) A shallower type of defects affecting the collection of holes: these, permanent, defects are not reversible under thermal annealing.

6.3 Samples

The samples used for the two irradiation-hardness studies are the pin and nip dilution series previously used for the light-soaking study as presented in Chapter 5. Details on the fabrication conditions and initial characteristics of the devices can, thus, be found in paragraphs § 5.3 and 5.5. The Raman crystallinity factor of the nip dilution series is comprised between ϕ_c = 70 % and ϕ_c = 15 %, whereas the solar cells of the pin dilution series have Raman crystallinity factors between ϕ_c = 66 % and ϕ_c = 25 %. A fourth pin sample consists of a μc-Si:H cell with an i-layer dilution profile (see Chapter 5) and an "average" ϕ_c = 15 %.

6.4 Irradiation and annealing conditions, characterization techniques

Both dilution series were irradiated with a proton beam from a Van der Graaf accelerator located at the CAFI (Centre d'Analyse par Faisceau Ionique), Le Locle (Switzerland), under the following conditions:

- High-energy protons: the solar cells were irradiated with a p^+ beam of 2 MeV and a fluence of 2.5 10^{13} p^+/cm^2. The solar cells were perpendicularly

irradiated from the top side of the cells, as schematically shown in Fig. 6.1. No rotation was applied to the solar cells, as is sometimes reported in the literature (see for example [96]), to obtain a more in-depth uniform irradiation.

- Low-energy protons: the solar cells were irradiated with a p^+ beam of 405 keV, corresponding to an initial p^+ beam of 1.07 MeV (at the exit of the Van der Graaf accelerator) attenuated through a 12 μm aluminum foil. The fluence was, again, 2.5 10^{13} p^+/cm^2 and the geometry of the irradiation, after the aluminum foil, was strictly similar as in the case of high-energy protons.

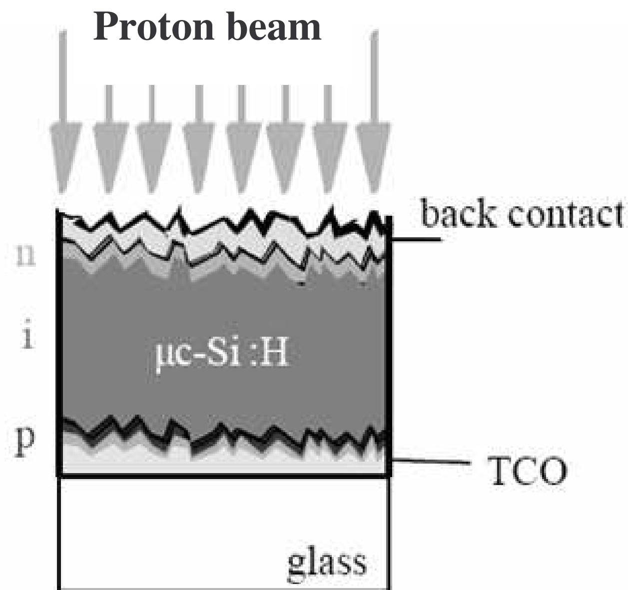

Figure 6.1. Geometry of the proton irradiation: the pin solar cell is irradiated from the n-side, through the back contact TCO (in our case, LP-CVD Zinc Oxide). In the case of nip configuration, the solar cell is irradiated from the p-side.

The irradiation conditions were simulated using the SRIM (Stopping and Range of Ions in Matter) software [102]; SRIM showed that:

- In the case of the 2 MeV p^+ beam, only a negligible fraction of the protons are "stopped" in the solar cell, the very large majority of the particles is transmitted through the device;
- In the case of low-energy proton irradiation, the situation is opposite, with most of the protons being "stopped" in the intrinsic layer of the solar cell. The depth distribution of the implanted protons is shown in Fig. 6.2: the maximum of the distribution, i.e. the most probable proton implantation depth, is centered at a distance equal to 15 μm that corresponds to the middle of the intrinsic layer. We can, thus, estimate the density of protons implanted to be approximately 10^{17} p^+/cm^3.

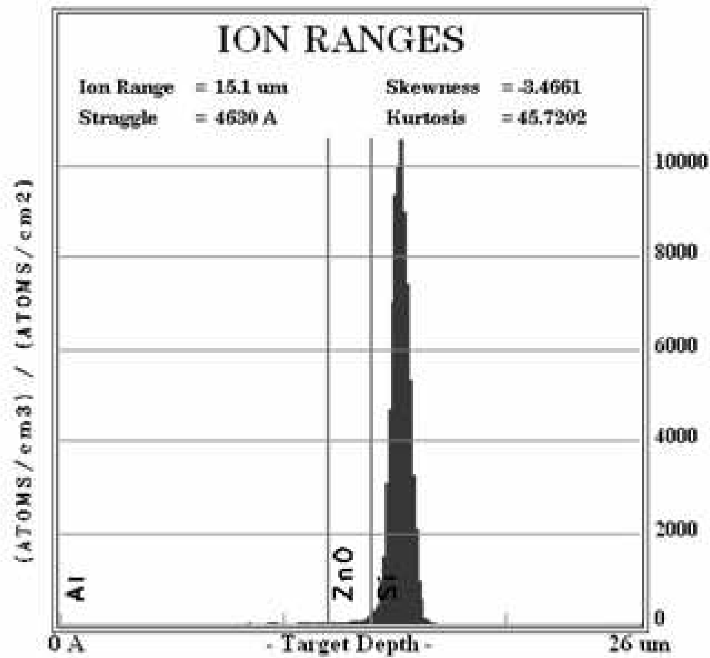

Figure 6.2 SRIM [102] simulation of the depth distribution of the low-energy protons: the maximum of the distribution, i.e. the most probable proton implantation depth, corresponds to the middle of the intrinsic layer.

We assume here that the degradation of the electrical parameters of the μc-Si:H single-junction solar cells is not due to a deterioration of the TCO; in the case of high-energy protons, the degradation is consequent to an increase of the defect density in the intrinsic layer of the solar cells. In the case of low-energy protons, some protons are also "stopped" in the Zinc Oxide, as can be seen in Fig. 6.2. However, here again, we assume that the degradation of the electrical parameters is not due to a deterioration of the TCO. Indeed, the degradation is, this time, not completely reversible, but we also observe that the defect-related absorption and the Urbach parameter do not return to their initial values. These both observations are experimental evidences that suggest that it is the Si-based material that degrades and does not fully recover. Nevertheless, in order to rule out the stability of the ZnO layers, which degradation could also lead to a decrease of the FF of the device, such ZnO layers should be irradiated under the same conditions as our solar cells and the resistivity of the ZnO layers measured before and after irradiation. This experiment was not made here and should be performed in the future.

After irradiation, annealing steps of 10h were carried out, under nitrogen flow, at increasing temperatures: 100°C, 130°C, 160°C and 180°C.

The characterization techniques employed are identical to those that were used for the light-soaking study (presented in Chapter 5), i.e.:

- Open-circuit voltage (V_{oc}) and fill factor (FF) were obtained from J(V) measurements under the AM 1.5 sun simulator at 25°C, whereas short-circuit

current density (J_{sc}) was obtained from the integration of the external quantum efficiency measurement.

- The Fourier transform photocurrent spectroscopy (FTPS) technique was used to measure sub-bandgap absorption spectra of the intrinsic layers as incorporated within the solar cells; the setup and measurement conditions are described in detail in § 2.4. The FTPS spectra were calibrated at 1.35 eV, by setting the absorption coefficient of the studied μc-Si:H cells to the value of crystalline silicon; by using this calibration procedure, we implicitly assume that the optical bandgap and its corresponding absorption coefficient are not affected by proton irradiation.
- Micro-Raman spectroscopy was performed with a HeNe laser excitation beam (633 nm) to evaluate the average crystallinity factor of the intrinsic layer, calculated as the arithmetical average of the 2 Raman crystallinity factors measured from the top and bottom of the samples (see § 2.3).

It must be mentioned here that the Raman crystallinity factors of the solar cells do not vary with high and low-energy proton irradiation; the degradation observed is, thus, not due to modifications of the microstructure.

6.5 High-energy proton irradiation

In this section, we will present the results of high-energy proton irradiation, as well as subsequent thermal annealing, on the electrical parameters of our μc-Si:H solar cells. We will show that the fill factor is the parameter that shows the largest decrease, followed by the short-circuit current density with external quantum efficiency losses in the long wavelengths (≥ 600 nm). We will also demonstrate that high-energy proton irradiation leads to an increase of defect-related absorption, as measured at 0.8 eV, indicating an increase of the defect density in the crystalline phase. A simple model for high-energy proton degradation and annealing will be introduced in the paragraph § 6.5.3.

6.5.1 Proton-induced degradation

a) Electrical parameters

The effect of high-energy proton irradiation on the conversion efficiency of the nip and pin solar cells series is presented in Fig. 6.3, with the relative efficiency loss $\Delta\eta$ as a function of the intrinsic layer Raman crystallinity factor ϕ_c. $\Delta\eta$ is defined as:

$$\Delta\eta = \left(\eta_{initial} - \eta_{degraded}\right) / \eta_{initial} \quad (6.1)$$

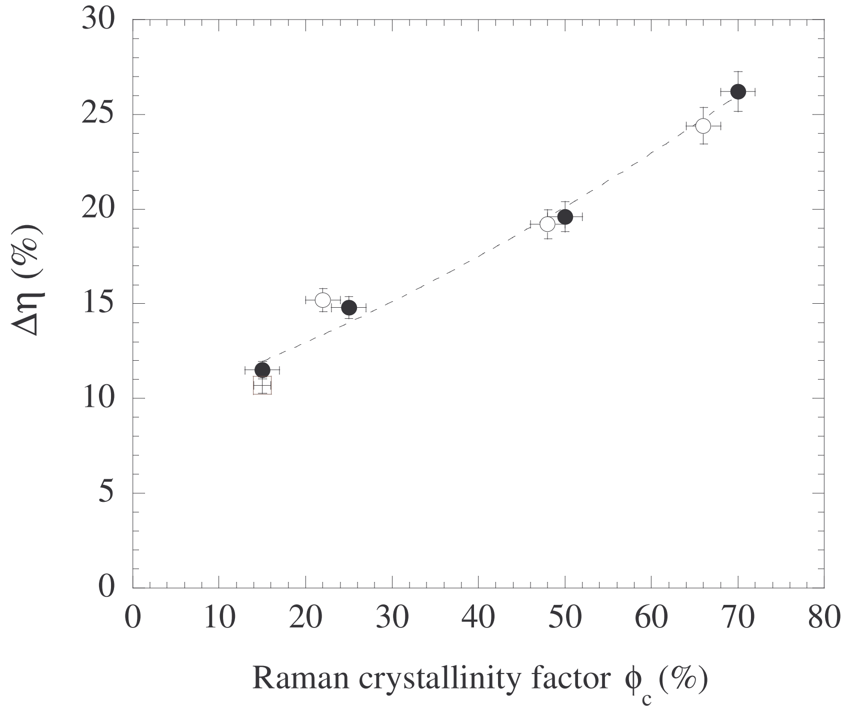

Figure 6.3. Relative high-energy proton-induced loss of efficiency as a function of Raman crystallinity factor ϕ_c, for both dilution series of cells (black dots: nip series, empty dots: pin series). The square symbol represents the pin cell with i-layer dilution profile. The dotted line is merely a guide for the eye.

Nip and pin series present very similar relative efficiency losses as a function of crystallinity: for both series, $\Delta\eta$ increases with Raman crystallinity factor ϕ_c. Furthermore, $\Delta\eta$ due to high-energy proton irradiation is of comparable order of magnitude as $\Delta\eta$ observed in the same series of devices after light-soaking (here: 10%-25%, light-induced degradation: 3%-15%), albeit its increase with ϕ_c is opposite.

This result is in agreement with the previous observations published in [95-96] that a-Si:H solar cells are not subject to noticeable high energy proton-induced degradation. Indeed, µc-Si:H solar cells with low crystallinity factors are confirmed to be more stable with relative efficiency losses $\Delta\eta \sim 10$ %. Highly µc-Si:H cells present relative losses up to 26 %, a value which is well below that obtained when µc-Si:H solar cells are irradiated with low-energy protons ($\Delta\eta$ can then be as high as 80%, see [102] and § 6.6). It should be noted that the pin cell with i-layer dilution profile degrades a little bit less than the nip cell of similar crystallinity, but it still presents a relative efficiency loss of approximately 10%.

As previously mentioned, the fill factor is the parameter that is most affected by high-energy proton irradiation in a-Si:H and µc-Si:H solar cells; this is also observed with these pin and nip dilution series, as can be seen in Fig. 6.4 for ΔFF, defined in a similar way as $\Delta\eta$:

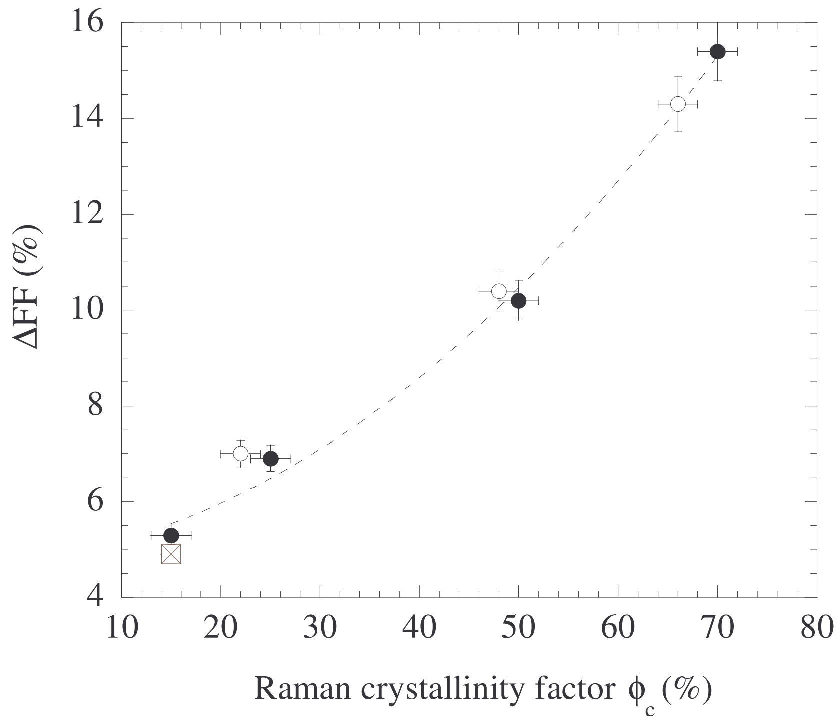

Figure 6.4. Relative high-energy proton-induced loss of fill factor as a function of Raman crystallinity factor ϕ_c for both dilution series of cells (black dots: nip series, empty dots: pin series). The square symbol represents the pin cell with i-layer dilution profile. The dotted line is merely a guide for the eyes.

The relative loss of short-circuit current density is presented in Fig. 6.5: we observe that the relative loss of fill factor and that of short-circuit current density become more pronounced with higher crystallinity. The external quantum efficiency curve (EQE), from which J_{sc} is calculated by integration, is presented in Fig. 6.6.

EQE is shown in initial state, after high energy proton irradiation and after annealing at 180°C, for the highly crystalline nip cell (ϕ_c = 70 %). Fig. 6.6 shows that the reduction in J_{sc} takes place in the "red" part of the spectrum, i.e. for wavelengths λ > ~600 nm. This decrease of EQE between 600 and 1000 nm indicates a reduction in the collection efficiency after irradiation with high-energy protons; this decrease of the collection is confirmed by a drop in the value of the collection voltage V_{coll} (see next section b)) and can be fully attributed to an increased recombination within the device (see section c)).

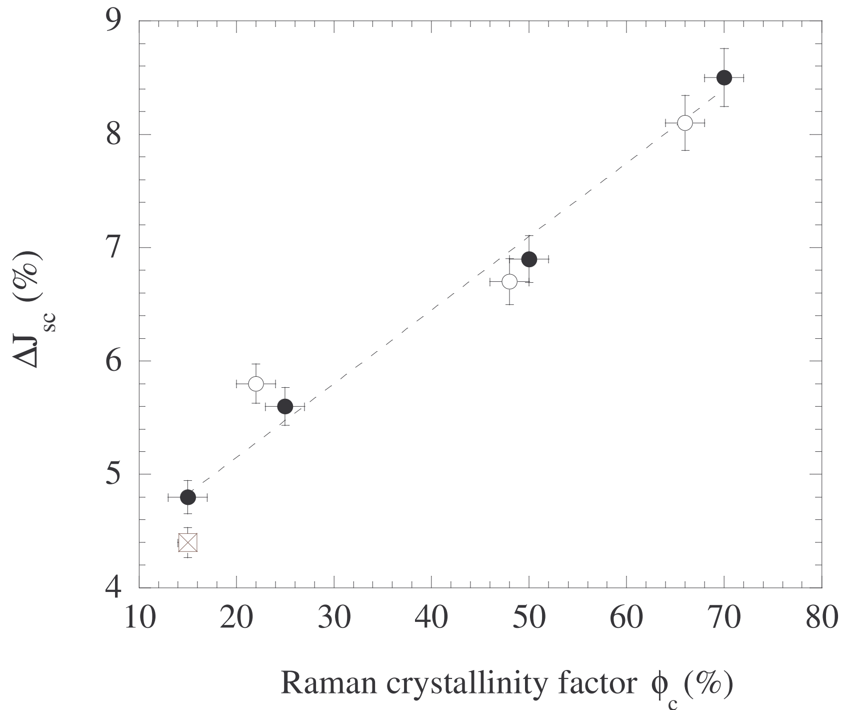

Figure 6.5. Relative high-energy proton-induced loss of short-circuit current density as a function of Raman crystallinity factor ϕ_c for both dilution series of cells (black dots: nip series, empty dots: pin series). The square symbol represents the pin cell with i-layer dilution profile. The dotted line is merely a guide for the eye.

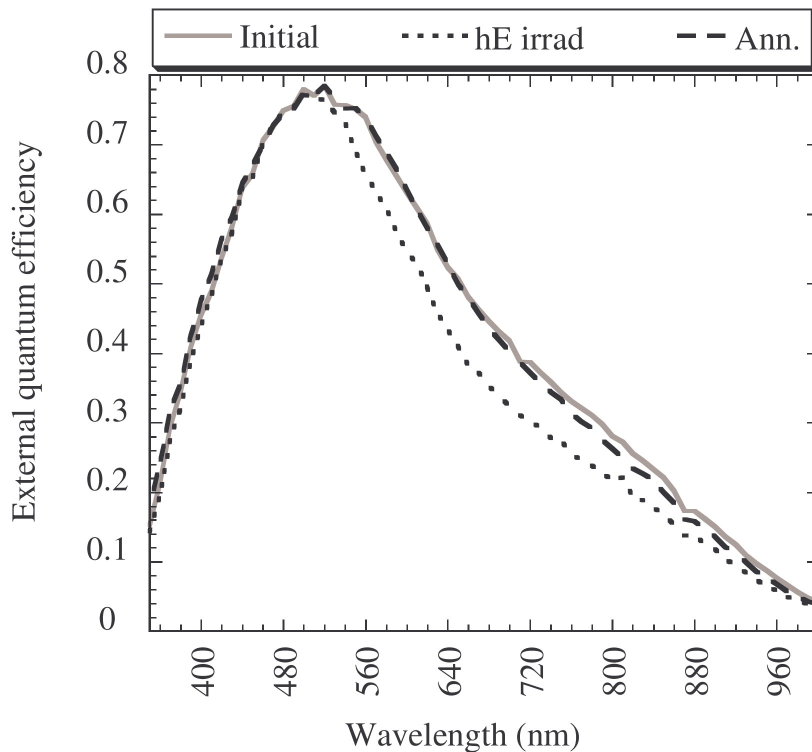

Figure 6.6. External quantum efficiency curves for initial and irradiated (high-energy p^+) states and after annealing at 180°C, for the 70 % crystalline nip cell.

The open-circuit voltage is also observed to decrease under high-energy proton irradiation; nevertheless the degradation is limited to relative losses below 5%. ΔV_{oc} increases linearly with the Raman crystallinity factor, as shown in Fig. 6.7:

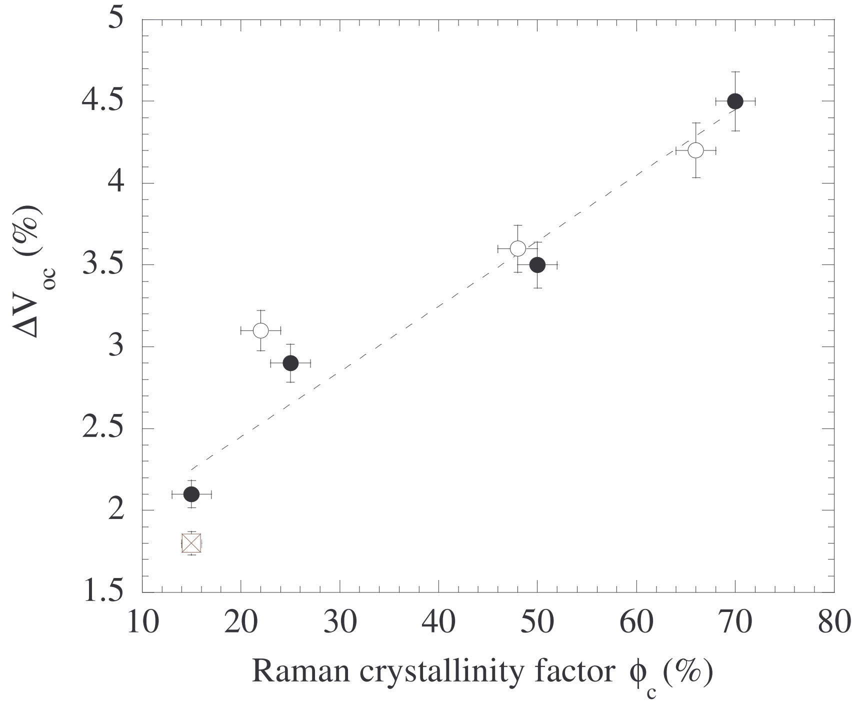

Figure 6.7. Relative high-energy proton-induced loss of open-circuit voltage as a function of Raman crystallinity factor ϕ_c for both dilution series of cells (black dots: nip series, empty dots: pin series). The square symbol represents the pin cell with i-layer dilution profile. The dotted line is merely a guide for the eye.

b) Shunt resistance and collection voltage

In this paragraph, we will show that high-energy proton irradiation leads to a reduction in the collection voltage, but not to a significant decrease in the shunt resistance R_{sh}. Fig. 6.8 presents the short-circuit resistance R_{sc} as a function of the reciprocal of the short-circuit current density J_{sc} for the nip solar cell with $\phi_c = 70$ %: for low illumination, i.e. for high $1/J_{sc}$ values, R_{sc} tends towards the shunt resistance R_{sh}. The collection voltage V_{coll} is assessed from the linear part of the R_{sc} (J_{sc}^{-1}) curves. The collection voltage of the highly crystalline nip solar cell decreases from $V_{coll} = 9.5$ V to $V_{coll} = 4.1$ V when irradiated with protons of 2 MeV.

According to chapter 4, such collection voltage values should correspond to absolute losses of fill factor δFF, with respect to $FF_0 = 75$ %, equal to (see equs. (4.21) or (5.9):

- In initial state: δFF ~ 9.5 %, for a V_{coll} equal to 9.5 V;
- After irradiation with 2 MeV protons: δFF ~ 22 %, for a V_{coll} equal to 4.1 V

The absolute reductions in the fill factor expected are in good agreement with the actual values of δFF measured, since: δFF = 11 % (i.e. FF = 64 %) in initial state and δFF = 21 % (i.e. FF = 54%) after irradiation.

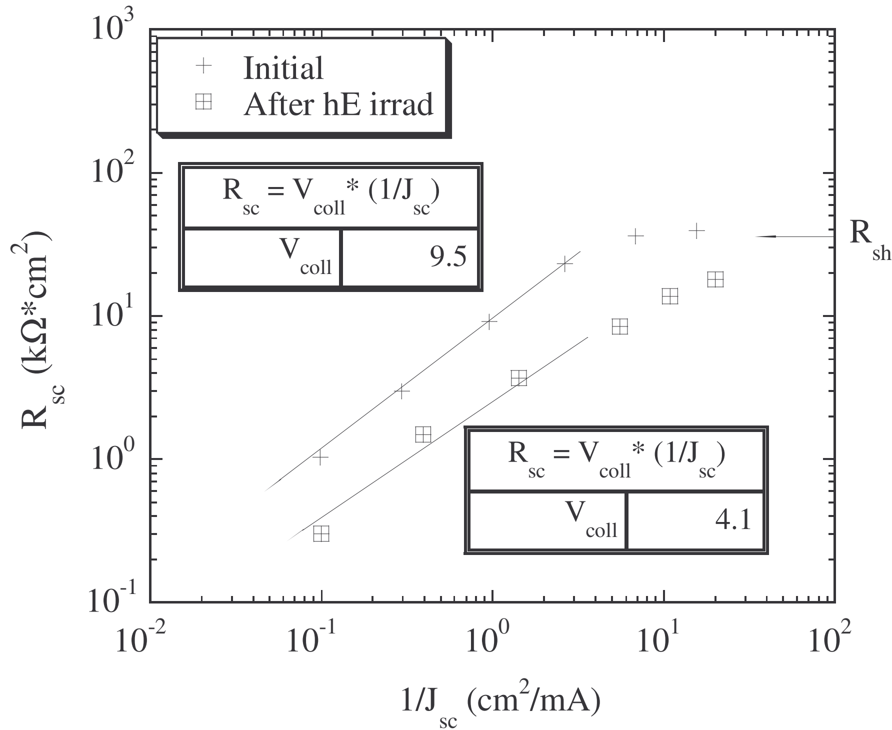

Figure 6.8 Short-circuit resistance R_{sc} as a function of the reciprocal the short-circuit current density for the nip sample of ϕ_c = 70 %, before and after irradiation with high-energy protons. The shunt resistance is not modified (within measurement errors) by high-energy proton irradiation.

As previously mentioned, the decrease of the collection voltage observed is consistent with the External Quantum Efficiency (EQE) measurements performed, where a reduction was observed in the “red” part of the spectra, indicating a loss in the carriers’ collection efficiency. We will show in the next section that the reduction of V_{coll} can be directly attributed to an increase of the defect density in the crystalline phase of the intrinsic layer, as monitored by the defect-related absorption α(0.8 eV).

c) Defect-related absorption

In the previous paragraphs we have shown that μc-Si:H solar cells degrade under high-energy proton irradiation. More particularly, we have observed that the fill factor is the electrical parameter that is most affected by high-energy proton irradiation. We showed in the previous section that the decrease of FF can be attributed to a reduction of the collection voltage and, consequently, to a reduced $\mu\tau$-product (i.e. τ drops due to increased recombination). Here, we will confirm that an increase in the defect density of the crystalline phase, as monitored the absorption coefficient at 0.8 eV, is indeed observed.

More precisely, we will show that in case of high-energy protons, the relative proton-induced increase in defect-related absorption $\Delta\alpha$(0.8 eV) increases linearly with the crystalline volume fraction. This observation agrees well with our assumption that proton-induced defects are created in the crystalline phase of the μc-Si:H intrinsic layer of the solar cells.

Moreover, it must be mentioned that the Urbach parameter E_0 is observed not to be modified when the solar cells are irradiated with high-energy protons. This means that high energy protons do lead to an increased defect-related absorption, but without modification of the static disorder in the material, as optically monitored by the value of E_0. On the other hand, we will show in § 6.6 that E_0 increases when low-energy protons are implanted within the intrinsic layer of the devices.

Figs. 6.9 (a) and (b) present the defect-related absorption α(0.8 eV) as a function of the Raman crystallinity factor ϕ_c for the nip and the pin dilution series, resp, in initial and irradiated state. It is shown that the relative increase of α(0.8 eV) is larger for high Raman crystallinity factors ϕ_c. Furthermore, we observe that α(0.8 eV) is minimal in the initial state for ϕ_c ~ 40-50 %; this minimum is maintained after high-energy proton irradiation:

(a)

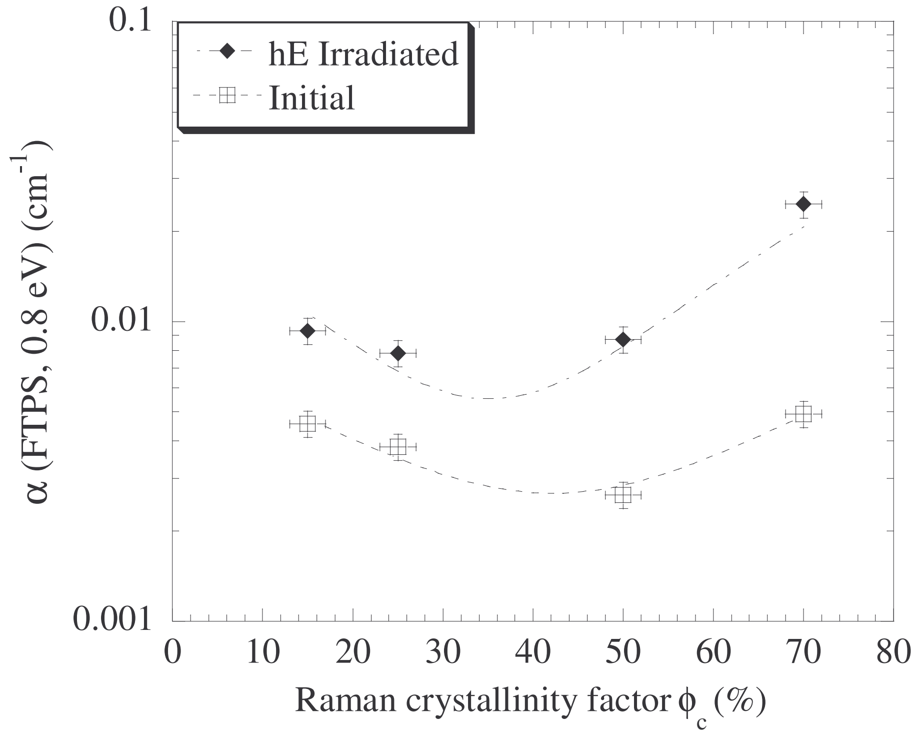

(b)

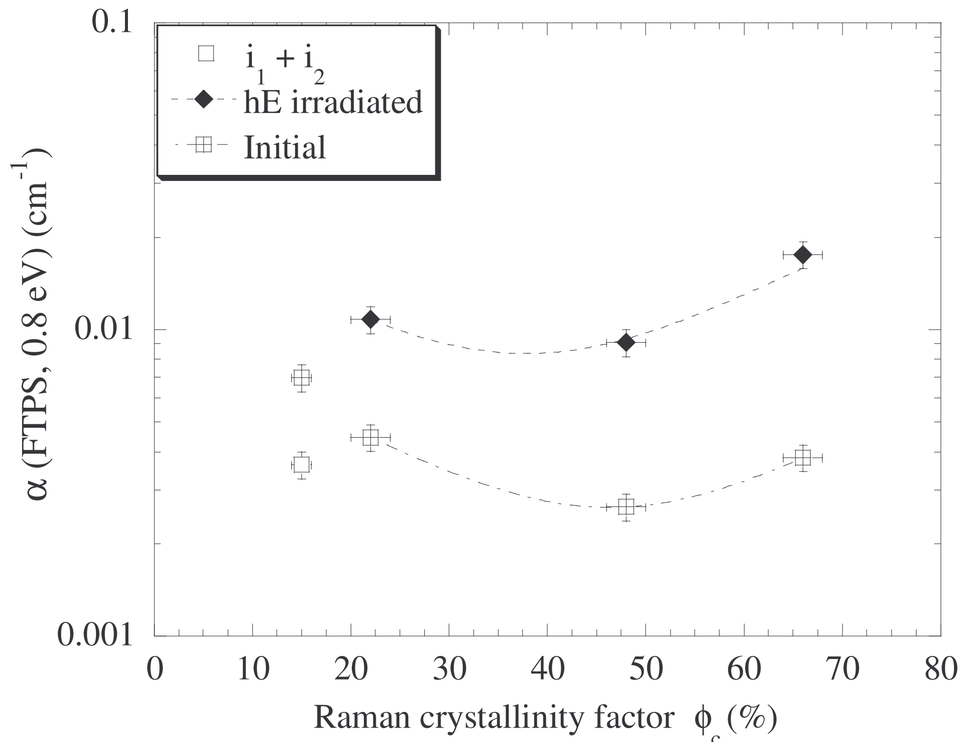

Figure 6.9. Defect-related absorption in initial state and after high-energy proton irradiation as a function of the Raman crystallinity factor ϕ_c, for (a) the nip dilution series, (b) the pin dilution series. The dotted lines are merely guides for the eyes.

Now, if we look at the relative increase of defect-related absorption with high-energy proton irradiation, we observe that Δα(0.8 eV) is proportional to the crystalline volume fraction, as can be seen in Fig. 6.10:

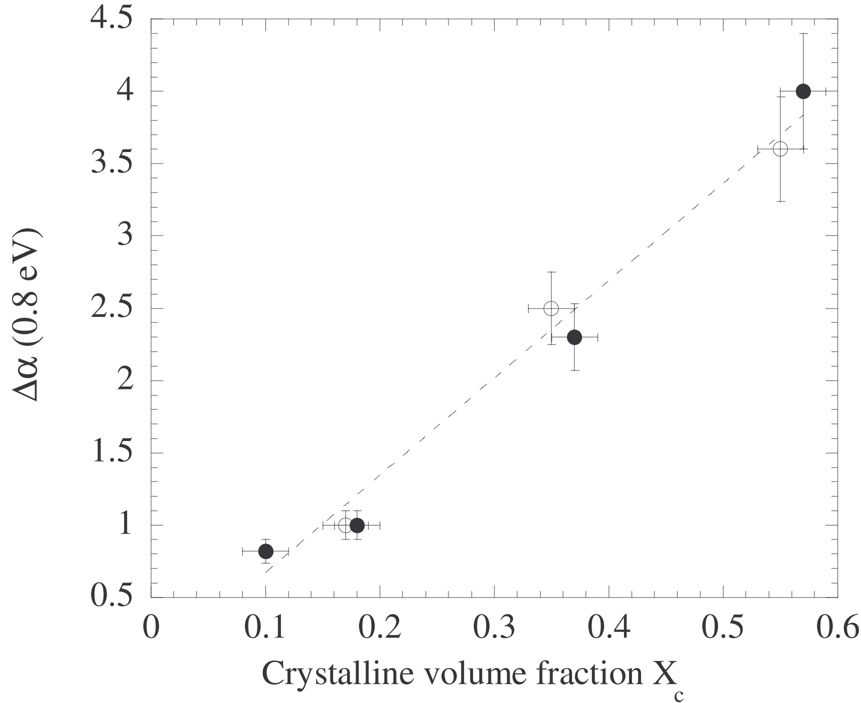

Figure 6.10. Relative increase in defect-related absorption after high-energy proton irradiation, as measured on the nip dilution series, as a function of the i-layer crystalline volume fraction X_c. The dotted line is a proportional fit.

The crystalline volume fraction X_c is defined (see also Chapter 5) as:

$$X_c = \frac{V_c}{V_{tot}} \tag{6.2),}$$

where V_c and V_{tot} are the crystalline volume and the total volume of the sample, respectively. X_c can be directly calculated from the Raman crystallinity factor ϕ_c, see [18] for details on the calculation procedure.

The relative increase of defect-related absorption, thus, increases proportionally to the crystalline volume fraction:

$$\Delta\alpha\,(0.8\,eV) \propto \frac{V_c}{V_{tot}} \tag{6.3}$$

This result confirms that the "bulk" of the crystalline phase of the μc-Si:H material is, indeed, affected by the high-energy proton irradiation.

As previously mentioned, the decrease of the collection voltage V_{coll}, and the consequent decrease of FF with high-energy proton irradiation is due to an increase

of the defect density in the i-layer. Indeed, Fig. 6.11 shows that V_{coll} is inversely proportional to the value of α(0.8 eV), as measured after low-energy irradiation. A similar observation was made in the case of light-induced degradation.

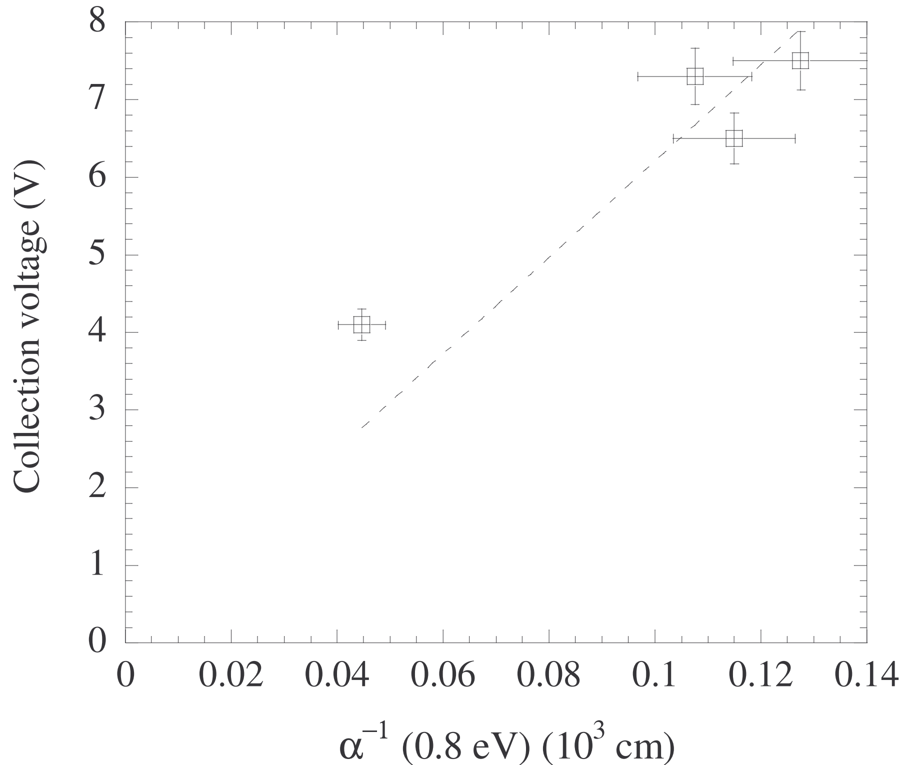

Figure 6.11. Collection voltage as a function of the reciprocal of the defect-related absorption after high-energy proton irradiation (nip series). The dotted line is a proportional fit.

In the case of light-soaking, as well as in the case of high-energy proton irradiation, the fill factor is the electrical parameter of the μc-Si:H solar cells that degrades the most. Nevertheless, the creation of defects does not affect the fill factor the same way for both types of degradation, as can be seen in Fig. 6.12, with the relative decrease of FF as a function of the relative increase of defect-related absorption. We observe that defects, as induced by high-energy proton irradiation, have a more detrimental effect on the fill factor than light-induced defects: $m = \Delta FF/\Delta\alpha$ is 2 times larger for high-energy proton-induced defects. This could suggest that proton-induced and light-induced defects have different capture cross-sections (see the discussion of Chapter 5, p.94):

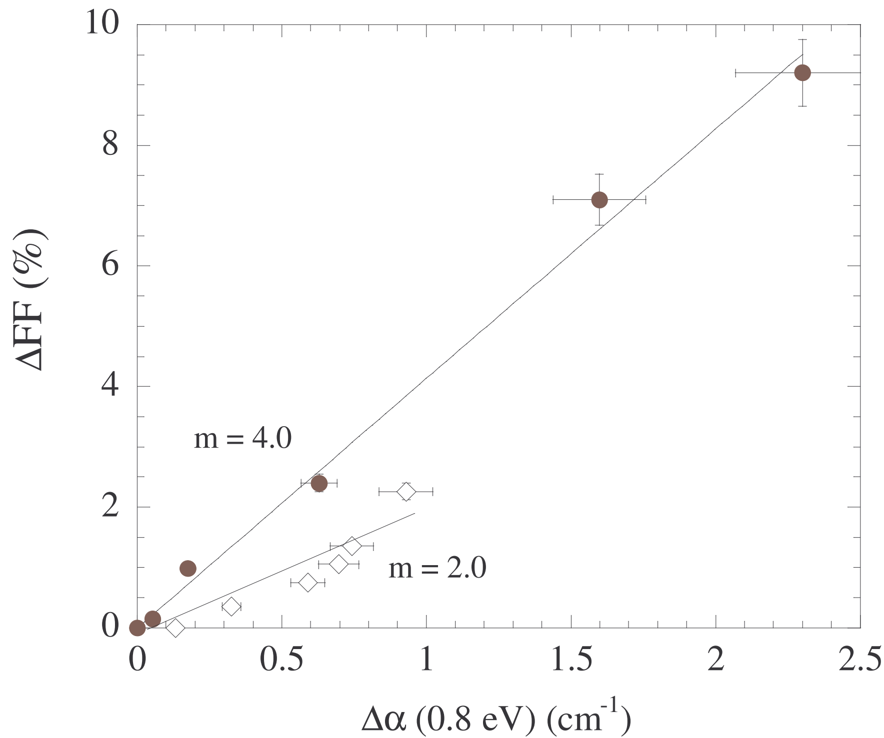

Figure 6.12. Relative loss of fill factor versus relative increase of defect-related absorption for the nip solar cell with $\phi_c = 50\%$ after (a) high-energy proton irradiation (black dots), (b) light-soaking (empty diamonds). The lines are proportional fits.

6.5.2 Defect Annealing

Now that we have looked at the degradation, as induced by high-energy proton irradiation, on the electrical parameters and on defect-related absorption, we will show that this degradation is completely reversible under thermal annealing. Fig. 6.13 shows the effect of high-energy proton irradiation and of subsequent annealing steps on the relative efficiency $\Delta\eta$ of the solar cells of the nip series.

The nip dilution series presents relative efficiency losses between 26%, for the highly crystalline nip cell ($\phi_c = 70\%$), and 11% for the one which is mainly amorphous ($\phi_c = 15\%$). We observe total recovery (+/- 1%) after the last annealing step at 180°C. Similar results were obtained for the pin series (not presented here).

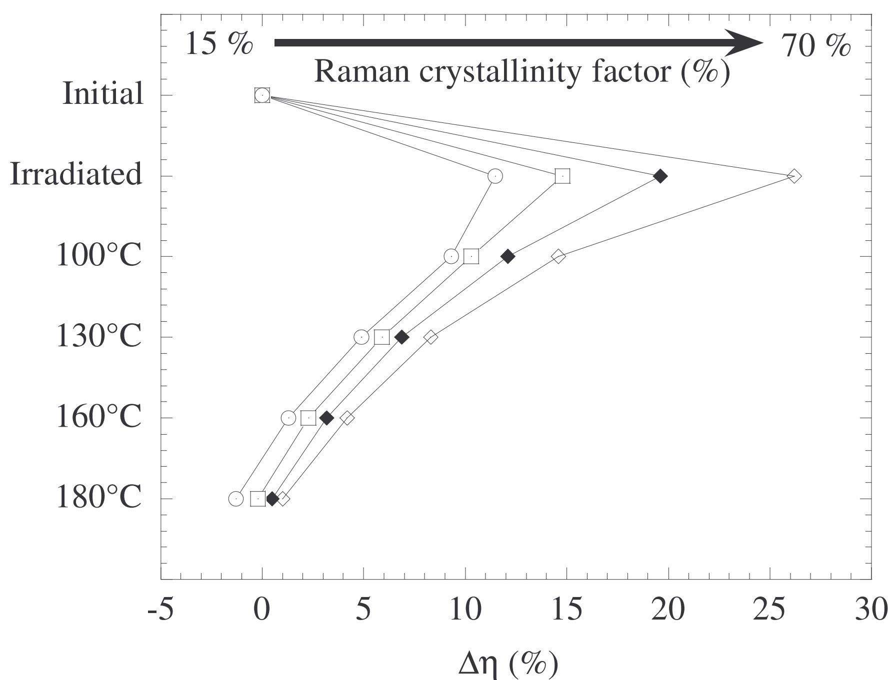

Figure 6.13. Relative efficiency as a function of high-energy proton irradiation and step-wise annealing for the nip dilution series.

Similarly to Δη, Δα(0.8 eV) also shows total recovery with thermal annealing, after annealing at 160°C and above:

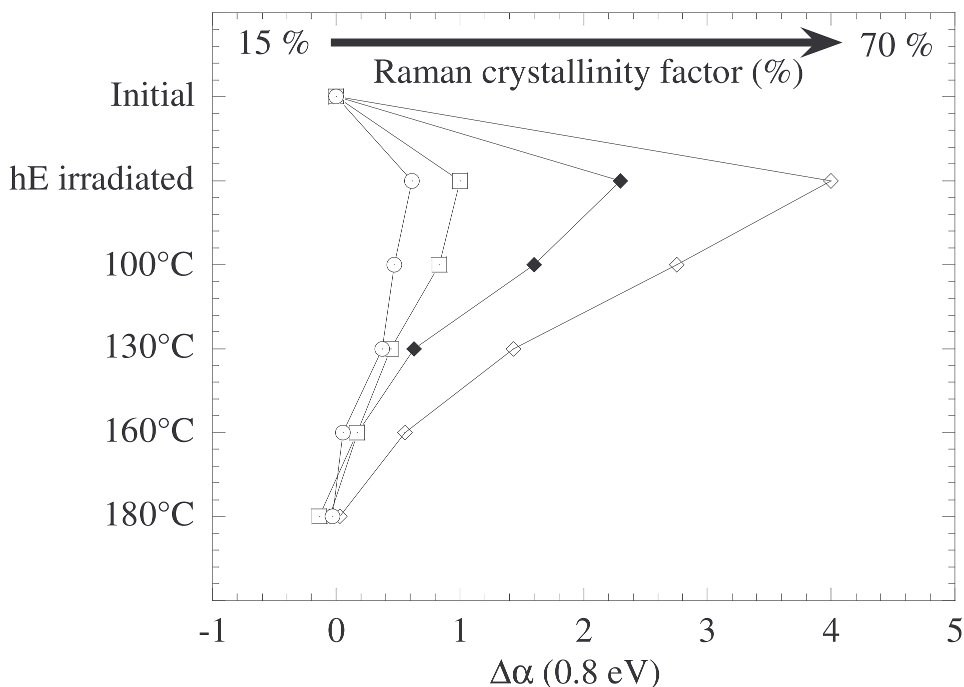

Figure 6.14. Relative defect-related absorption as a function of high-energy proton irradiation and step-wise annealing for the nip dilution series

We, thus, observe that high-energy proton irradiation leads to similar effects on the device electrical parameters as light-soaking, studied in the previous chapter; however, there are also 2 major differences between both types of degradation:

- In the case of light-soaking, the degradation decreases with crystallinity, whereas, in case of high-energy proton irradiation, the degradation becomes more pronounced with higher crystallinity;
- In the case of high-energy proton irradiation, the short-circuit current density suffers some reduction with $4\% < \Delta J_{sc} < 9\%$; in the case of light-soaking: $\Delta J_{sc} \leq 2\%$. The loss in external quantum efficiency occurs, in both cases, in the long wavelength region of the AM 1.5 spectrum (≥ ~ 600 nm).

From the similarities mentioned above, let us assume that the dynamics of annealing of high-energy proton-induced defects can, similarly to the case of light-induced defects, be described by a stretched exponential function, as introduced in the previous Chapter. The defect-related absorption is then expressed by:

$$\alpha(0.8\,eV)(t) = \alpha_{ss}(0.8\,eV) \cdot \exp\left[-\left(\frac{t}{\tau}\right)^{\beta}\right] \qquad (6.4),$$

where α_{ss} is the steady-state value of defect-related absorption (after high-energy proton irradiation), τ is a characteristic annealing time of the defects and t is the annealing time; τ is a function of the annealing temperature, through the expression:

$$\tau = \tau_0 \cdot \exp\left(\frac{E_a}{kT_a}\right) \qquad (6.5),$$

with E_a the activation energy and T_a the annealing temperature.

Then, by assuming that β is constant over the range of annealing temperatures used, the activation energy can simply be derived from equs. (6.4) and (6.5):

$$\left(\log\left[\frac{\alpha_0(0.8\,eV)}{\alpha_{10h}(0.8\,eV)}\right]\right)^{1/\beta} = C(\tau_0) \cdot \exp(-\frac{E_a}{kT_a}) \qquad (6.6)$$

Let us plot this logarithmic ratio as a function of $1/T_a$:

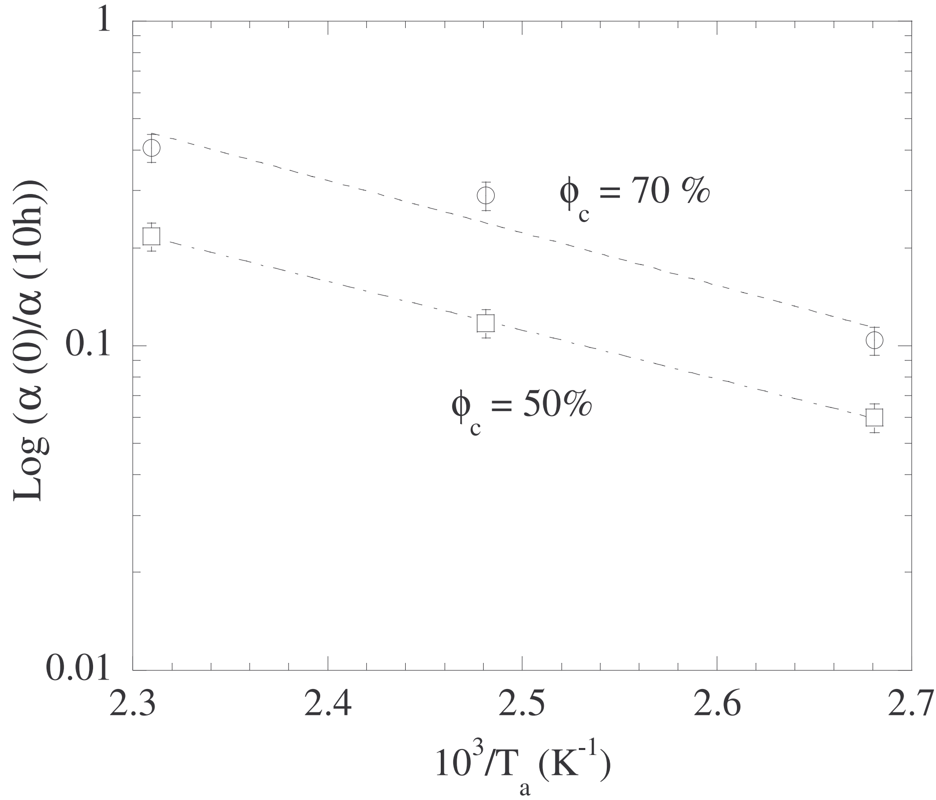

Figure 6.15. Logarithmic value of the ratio of the defect-related absorption after high-energy proton degradation and subsequent 10h annealing, as a function of the reciprocal of the annealing temperature for two nip solar cells of different crystallinity. The dotted lines are fits to equ. (6.6).

As previously mentioned, we suggest here that high-energy protons degrade the crystalline phase of the intrinsic layer incorporated into our μc-Si:H solar cells. Since α(0.8 eV) monitors the defect density in the crystalline phase (when the spectra are calibrated at 1.35 eV as in our work) we may assume that the defects are directly created in the crystalline phase and do not dispersively diffuse (as in the case of light-soaking, see § 5.10). We, thus, assume that $\beta \sim 1$ and we obtain from the fits of Fig. 6.15 the activation energy E_a for the annealing of the high-energy proton-induced defects: E_a is equal to 0.3 eV. In comparison, the activation energy for the annealing of light-induced defects in μc-Si:H is equal to 0.5 eV, as established in Chapter 5. This would suggest that the defects caused by high-energy proton irradiation are easier to anneal than those created by light-soaking. Nevertheless, measurements of the annealing kinetics, such as those done after light-soaking, should be performed to ascertain this assumption. The characteristic time τ is observed to depend on the crystallinity: from the fits to equ. (6.6) we obtain that $\tau_0 \sim 9 \cdot 10^{-3}$s for $\phi_c = 50\%$. For light-induced degradation, we also observed that $\tau = \tau(\phi_c)$, but we obtained an annealing characteristic time around 10 times larger with $\tau_0 \sim 9 \cdot 10^{-2}$ s for $\phi_c = 50\%$.

6.5.3 Model for high-energy proton defect creation and annealing in μc-Si:H

Amorphous silicon is known to present a better radiation hardness as compared to crystalline silicon [95]. According to Kishimoto et al. [105], the radiation hardness of a-Si:H is related to the "flexibility" of the amorphous network. On the other hand, the displacement damages created in the crystalline lattice are much more detrimental to the electrical properties. Based on these observations, we assumed that high-energy proton irradiation of μc-Si:H solar cells would lead to the creation of defects in the crystalline phase of the material. We have thereby shown that the relative increase of defect-related absorption, as induced by high- energy proton irradiation, is indeed proportional to the crystalline volume fraction. We, thus, think that high-energy proton-induced defects are created within the crystalline phase, where they are directly measured by α(0.8 eV). We, furthermore, propose that high-energy proton irradiation leads mainly to ionization damages and strong local recombination; this is confirmed by the fact that (a) the Urbach parameter is not modified by high-energy proton irradiation, (b) the degradation is reversible under thermal annealing. Finally, we suggest that the low activation energy measured for the defect annealing, E_a = 0.3 eV, is probably linked to the presence of hydrogen at grain boundaries, as evidenced in Infrared spectra [17].

6.6 Low-energy proton irradiation

In this paragraph, we will study the effect of the irradiation of μc-Si:H solar cells with protons of low energy (E = 405 keV). In this case, the protons (H^+) are implanted within the intrinsic layer of the μc-Si:H solar cells. We will show that the degradation is, similarly as in the case of high-energy protons, higher for highly crystalline cells. But, when compared with both light-induced and high-energy proton-induced degradation, the electrical parameters of the solar cells are much more affected by low-energy proton irradiation; dramatic relative efficiency losses up to 70% are measured here. Also, low-energy proton-induced degradation is shown to be only partially reversible under thermal annealing. The static "disorder" of μc-Si:H is increased by the low-energy proton irradiation, as indicated by an increase in the Urbach parameter E_0.

6.6.1 Proton degradation as a function of crystallinity

a) <u>Electrical parameters</u>

The effect of low-energy proton irradiation on the efficiency of the solar cells is presented in Fig. 6.16, with the relative efficiency loss $\Delta\eta$ as a function of i-layer average crystallinity ϕ_c (for the definition of $\Delta\eta$ see equ. (6.1):

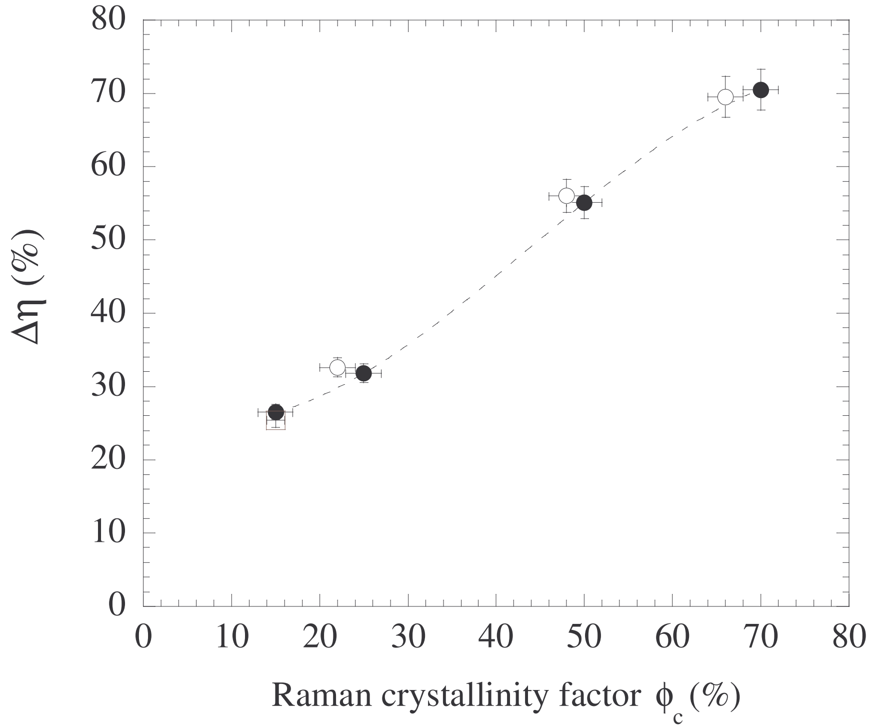

Figure 6.16. Relative low-energy proton-induced efficiency loss $\Delta\eta$ versus intrinsic layer Raman crystallinity factor ϕ_c for both series of cells (black dots: nip series, empty dots: pin series). The square symbol represents the pin cell with i-layer dilution profile. Dashed lines are merely guides for the eye.

Highly µc-Si:H cells suffer from a very strong degradation with a relative efficiency decrease of up to 70 %, while mainly amorphous cells show a relative efficiency reduction of around 30 %. Thus, the higher is the i-layer crystallinity, more affected are the cells by low-energy proton irradiation. This is a general rule that was observed for high-energy proton irradiation as well. Relative losses of the electrical parameters V_{oc}, FF and J_{sc} are all observed to increase with increasing i-layer crystallinity. Surprisingly, J_{sc} is the parameter that is the most affected by low-energy proton irradiation. A relative decrease of J_{sc} of 53 % is, thus, measured for the nip cell with the highest crystallinity, together with a relative decrease of FF and V_{oc} of 26 % and 18 %, resp.

The relative loss of J_{sc} is presented as a function of Raman crystallinity factor in Fig. 6.17. Fig. 6.18 shows the external quantum efficiency curves (EQE) in initial state, after low-energy proton irradiation and after annealing at 180°C, for the highly crystalline nip cell (ϕ_c = 70 %); from the EQE curve, one can obtain, by integration, the value of J_{sc}. Such as high relative decrease of J_{sc} was not observed after high-energy proton irradiation and light-soaking. We suggest that the reduction in J_{sc} is due to displacement damages created in the "crystalline" lattice.

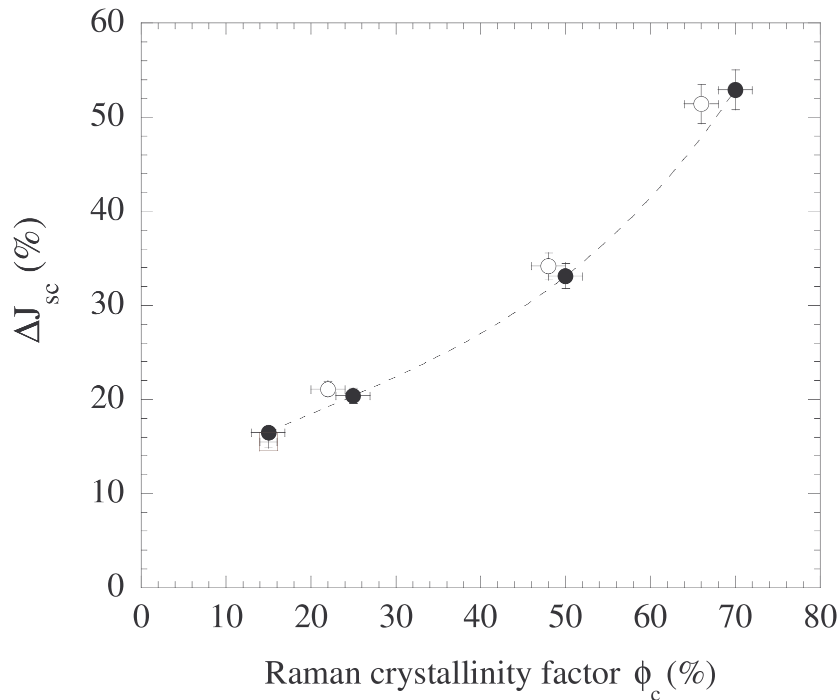

Figure 6.17. Relative low-energy proton-induced loss of short-circuit current density as a function of Raman crystallinity factor ϕ_c for both dilution series (black dots: nip series, empty dots: pin series). The square symbol represents the pin cell with the i-layer dilution profile. The dotted line is merely a guide for the eye.

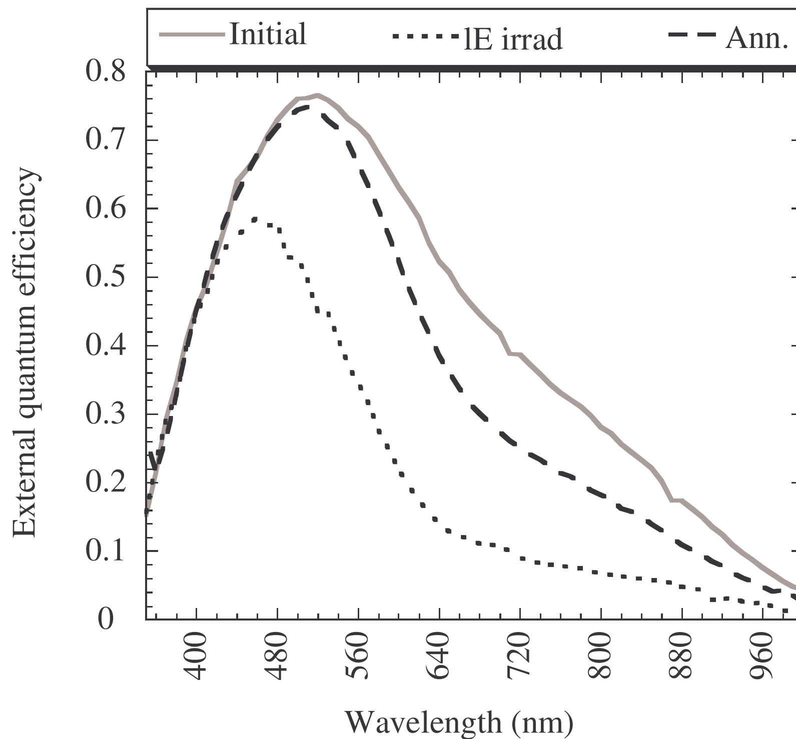

Figure 6.18. External quantum efficiency curves for initial and irradiated (low-energy p^+) states, and after annealing at 180°C, for the 70 % crystalline nip cell.

According to our basic upper limits calculations presented in Chapter 3, a relative decrease of J_{sc} could be related to a gap broadening due to proton (i.e. H^+) implantation but we can exclude this assumption because of the so high values measured for the relative decrease of J_{sc}. Furthermore is observed that EQE is reduced over the whole wavelength range by low- energy p^+ irradiation, with the main reduction occurring in the long wavelength response. In comparison to high-energy protons, we, thus, observe a supplementary deterioration of the p-i interface by low-energy protons. This is not surprising since protons are, in the low-energy case, also implanted at the p-i interface for both nip and pin solar cells (even if the latter are irradiated from the n side, low-energy protons are also implanted at the i-p interface). Moreover, the reduction of EQE is only partially reversible under the thermal annealing steps performed.

The relative loss of fill factor is presented as a function of Raman crystallinity factor in Fig. 6.19, whereas the relative loss of open-circuit voltage is shown in Fig. 6.20. For both electrical parameters, the highest degradation is measured on the devices of high crystallinity.

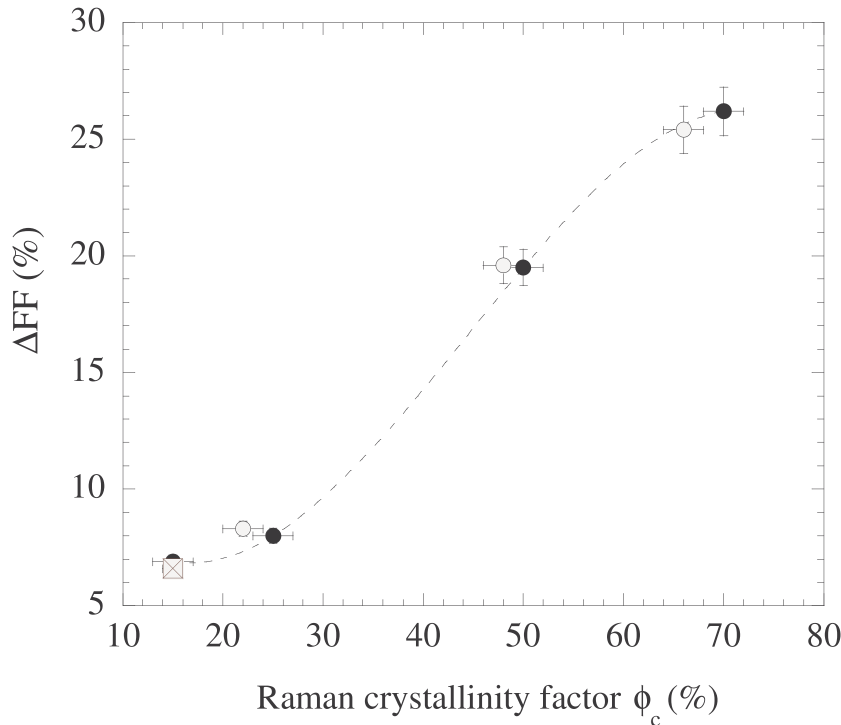

Figure 6.19. Relative low-energy proton-induced loss of fill factor as a function of Raman crystallinity factor ϕ_c for both dilution series of cells (black dots: nip series, empty dots: pin series). The square symbol represents the pin cell with the i-layer dilution profile. The dotted line is merely a guide for the eye.

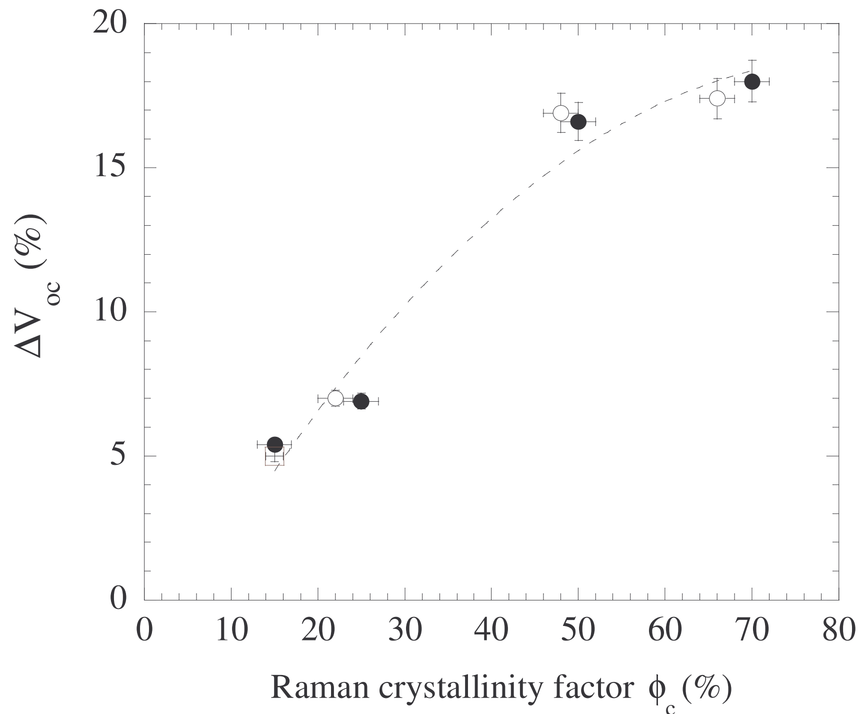

Figure 6.20. Relative low-energy proton-induced loss of open-circuit voltage as a function of Raman crystallinity factor ϕ_c for both dilution series of cells (black dots: nip series, empty dots: pin series). The square symbol represents the pin cell with the i-layer dilution profile. The dotted line is merely a guide for the eye.

b) Shunt resistance and collection voltage

In this paragraph, we will show that low-energy proton irradiation leads to a reduction in the collection voltage, as well as to a decrease in the shunt resistance. In the case of high-energy protons, only the collection voltage was affected by irradiation. Here, in the case of low-energy protons, Fig. 6.21 shows that the shunt resistance is also decreased by a factor ~ 4, whereas the collection voltage decreases from V_{coll} = 9.5 V to V_{coll} = 3.0 V for the nip solar cell with ϕ_c = 70%.

We suggest that the decrease of the shunt resistance is linked to the "crystalline lattice" damages created by the atoms that are displaced by low-energy protons. The series resistance R_s was not measured in our work; an increase of R_s could indicate that the resistivity of the TCO is also affected by low-energy proton irradiation.

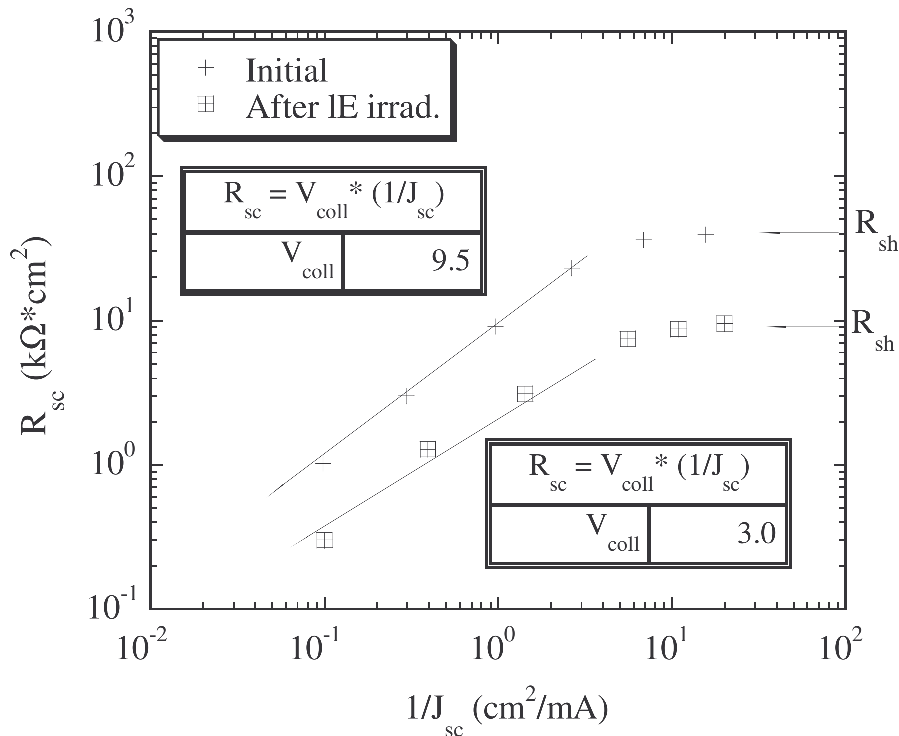

Figure 6.21. Short-circuit resistance R_{sc} as a function of the reciprocal of the short-circuit current density for the nip sample with ϕ_c = 70 %, before and after irradiation with low-energy protons. Note that both the collection voltage and also the shunt resistance are decreased.

c) <u>Defect-related absorption</u>

The relationship between defect-related absorption (α (0.8 eV)), in initial and irradiated states, and crystallinity is presented in Fig. 6.22 for (a) the nip dilution series, (b) the pin dilution series. The trend is very similar for both dilution series: the highly crystalline cells show an increase of α (0.8 eV) of a factor 12, while α(0.8 eV) is lower for the solar cells with ϕ_c between 40 and 50%. This "minimum" in defect-related absorption was already observed when the solar cells where light-soaked and irradiated with high-energy protons. The pin cell with an intrinsic layer hydrogen dilution profile shows a lower defect-related absorption than the nip cell of similar crystallinity, in the initial but also irradiated state.

(a)

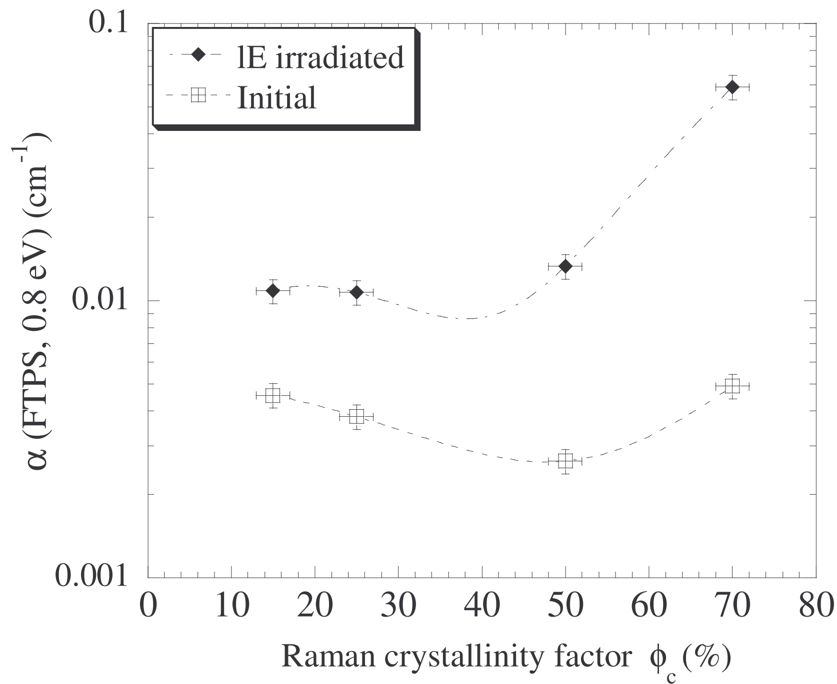

(b)

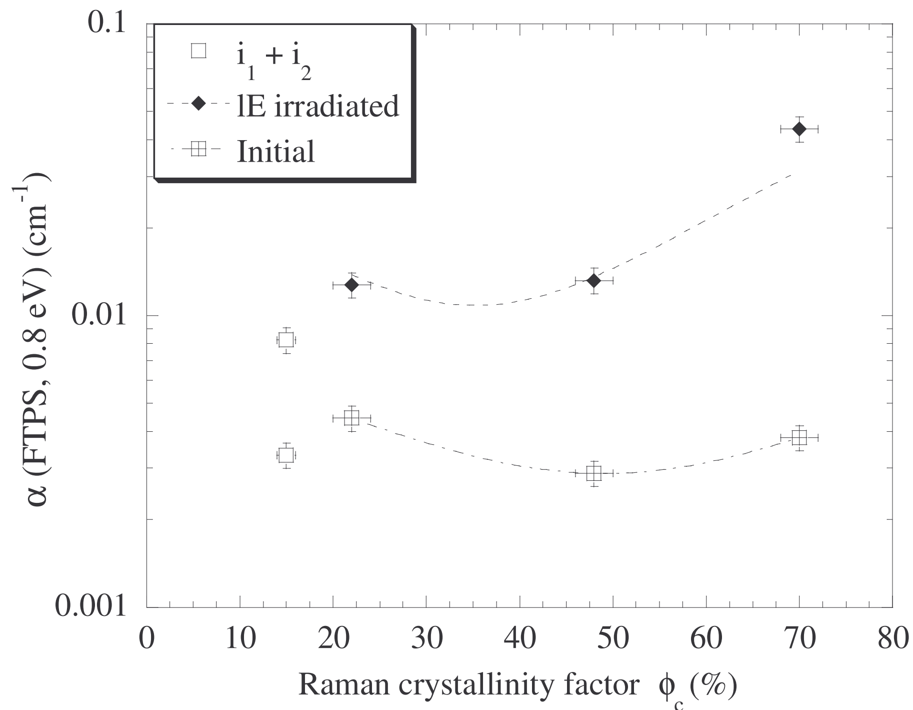

Figure 6.22. Defect-related absorption in initial state and after low-energy proton irradiation, as a function of the Raman crystallinity factor ϕ_c for (a) the nip dilution series, (b) the pin dilution series. The dotted lines are merely guides for the eye.

The relative increase of α(0.8 eV) due to low-energy proton irradiation is, similarly as in the case of high-energy protons (see Fig. 6.10), proportional to the crystalline volume fraction, see Fig. 6.23. Nevertheless, the coefficient of proportionality is almost 3 times larger in the case of low-energy protons, confirming that more defects are created:

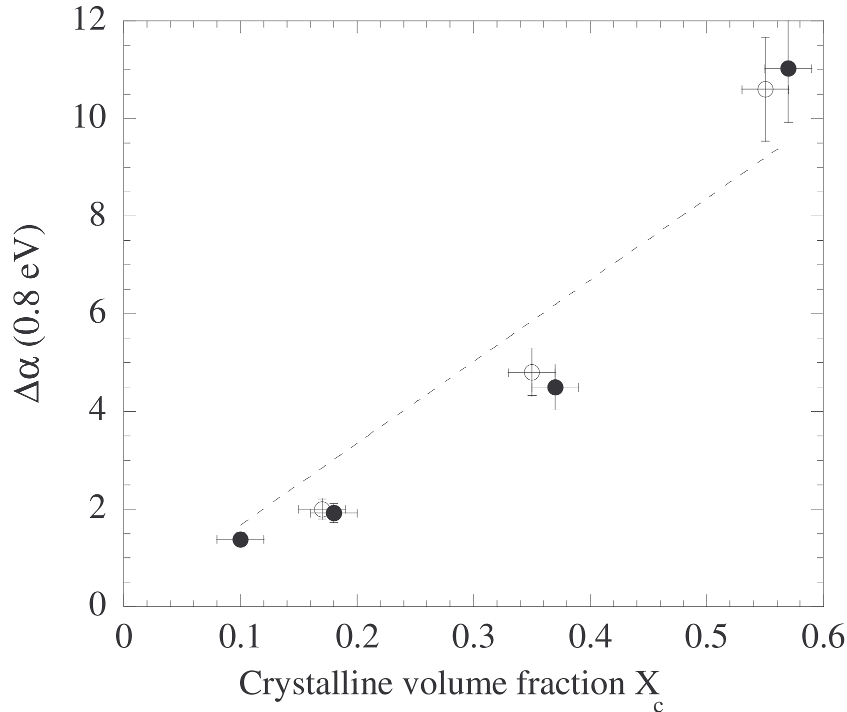

Figure 6.23. Relative increase of defect-related absorption due to low-energy proton irradiation, as measured in the nip dilution series, plotted as a function of the i-layer crystalline volume fraction X_c. The dotted line is a proportional fit.

In contrast with light-soaking and high-energy proton irradiation, the fill factor is not, in the case of low-energy proton irradiation, the parameter that degrades the most. Here, it is the short-circuit current density that shows the largest reduction. Nevertheless, in order to compare the three types of defects created by (a) light-soaking, (b) high-energy proton irradiation and (c) low-energy proton irradiation, we will, once again, look at the relative decrease of FF as a function of the relative increase of α(0.8 eV) in Fig. 6.24.

We observe that low-energy protons affect the fill factor in a very similar way as high-energy protons (i.e. the value of the slope $m = \Delta FF/\Delta\alpha$ is almost the same). Nevertheless, in the case of low-energy proton irradiation, the situation is different, since the relative increase of defect density is only partially reversible under the thermal annealing steps performed. Indeed, after the last annealing step, $\Delta\alpha$(0.8 eV) is still equal to 2 for the nip sample with $\phi_c = 70\%$ (see Fig. 6.27).

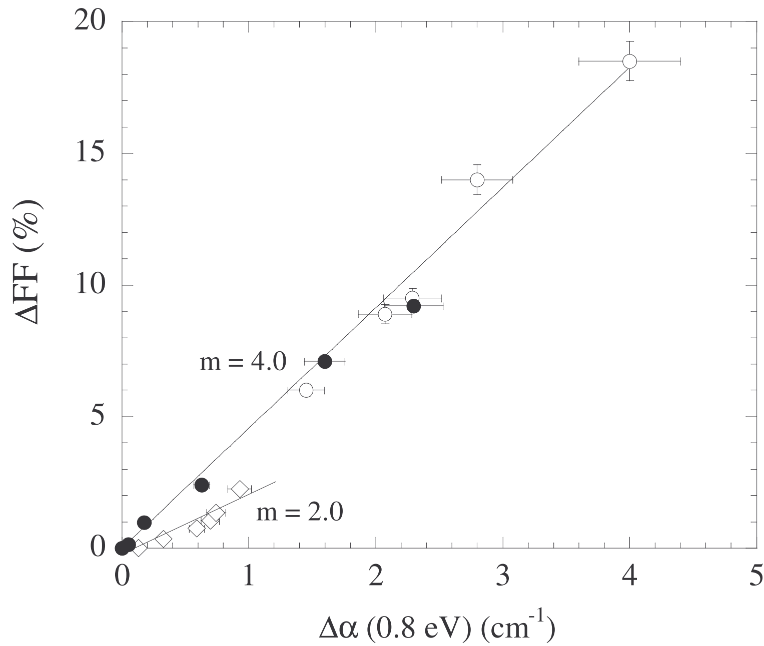

Figure 6.24. Relative loss of fill factor versus relative increase of defect-related absorption for the nip solar cell with ϕ_c = 50 % in the case of (a) light-soaking (empty diamonds), (b) high-energy proton irradiation (empty dots), (c) low-energy proton irradiation (black dots).

Finally, we again note that V_{coll} is inversely proportional to the value of α(0.8 eV) after low-energy proton irradiation, i.e. an increase of defect density is responsible for the decrease of the collection voltage:

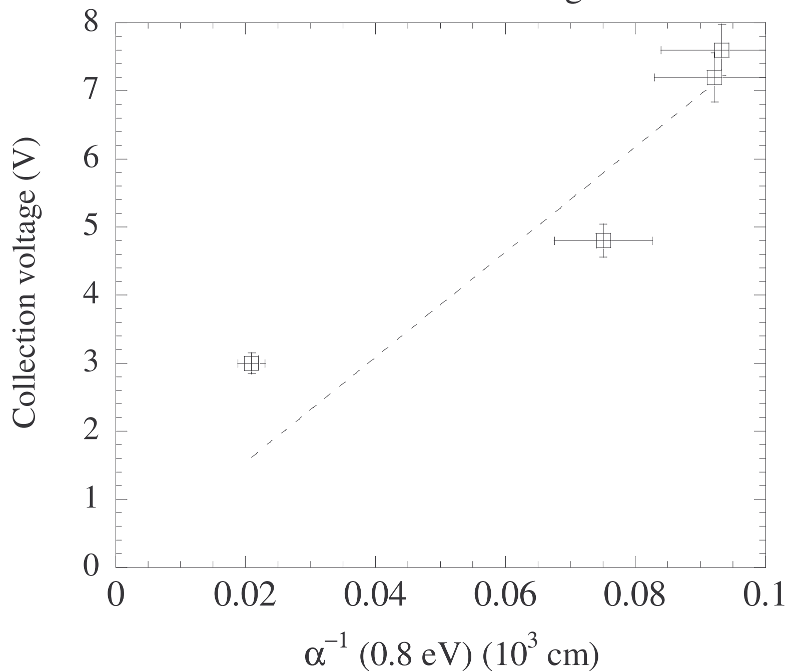

Figure 6.25. Collection voltage as a function of the reciprocal of the defect-related absorption after low-energy proton irradiation (nip series).

6.6.2 Defect annealing

In this paragraph, we will show that the degradation of the electrical parameters of the devices, as induced by low-energy proton irradiation, is only partially reversible under thermal annealing. Similarly, the defect-related absorption α(0.8 eV), that was increased by low-energy proton irradiation, does not return to its initial value: for the highly crystalline nip sample (ϕ_c = 70%) , the relative increase of α(0.8 eV) is still within a factor 2 after the last annealing step. The effect of subsequent annealing steps on the relative efficiency can be seen in Fig. 6.26 for the nip series. The pin series shows a similar trend (not presented here). Total recovery is not observed, even after annealing at 180°C. Normalized defect-related absorption presents a similar trend, as can be seen in Fig. 6.27.

The degradation due to low-energy proton irradiation is, thus, fundamentally different from the one induced by high-energy proton irradiation, which is completely reversible under thermal annealing. Furthermore, the Urbach parameter E_0 increases under low-energy proton irradiation, whereas it doe not change under irradiation by high-energy protons. This increase of E_0 means that the network's static disorder increases when low-energy protons are implanted within the intrinsic layer of the µc-Si:H solar cells. This observation is in agreement with the creation of displacement damages (lattice damages) as induced by low-energy protons.

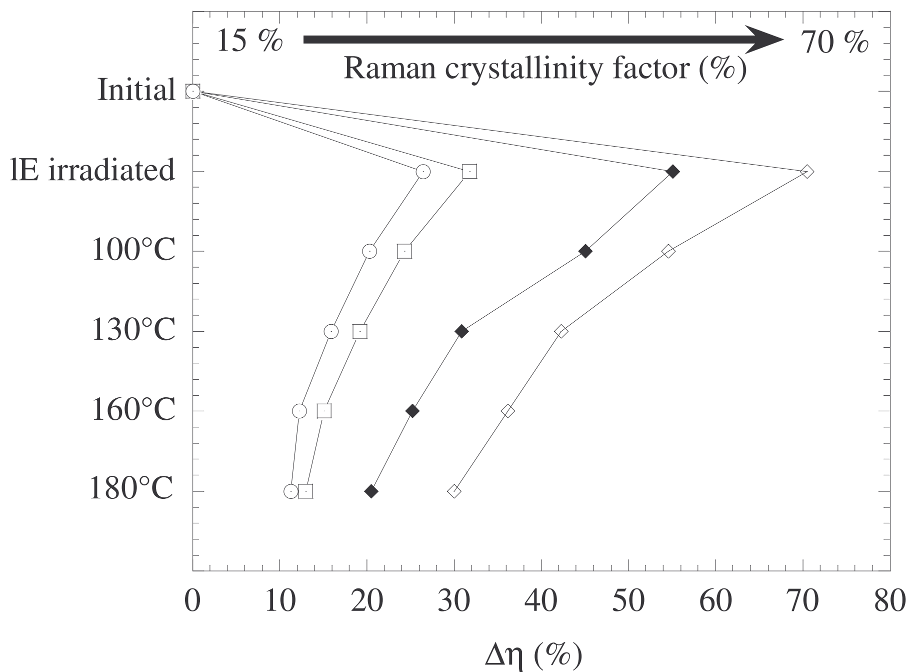

Figure 6.26. Relative efficiency as a function of low-energy proton irradiation and step-wise annealing for the nip dilution series.

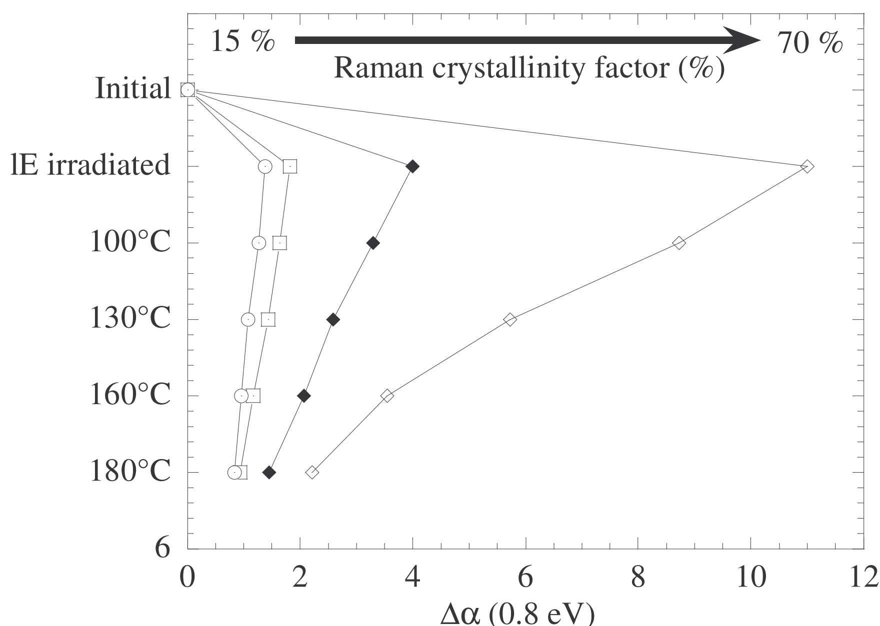

Figure 6.27. Relative defect-related absorption as a function of low-energy proton irradiation and step-wise annealing for the nip dilution series

Fig. 6.28 shows α(0.8 eV) and the Urbach parameter E_0 as a function of irradiation and annealing steps for the 70% crystalline nip cell: we observe that both parameters vary in a very similar way, and, after annealing at 180°C, neither α(0.8 eV) nor E_0 return to their initial values.

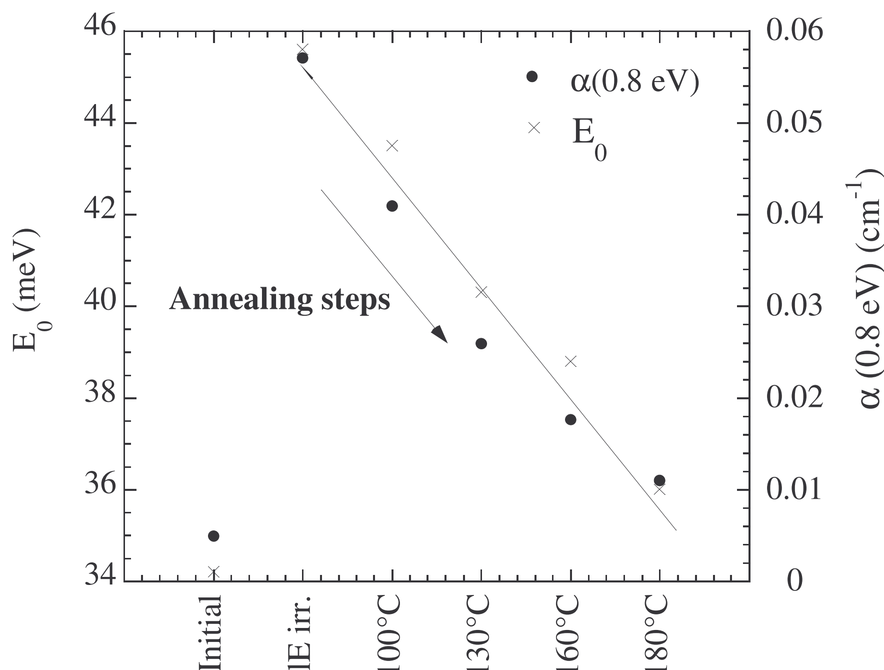

Figure 6.28. Defect-related absorption α(0.8 eV) and Urbach parameter E_0 as a function of low-energy proton irradiation and subsequent annealing steps for the 70% crystalline nip cell (E_0: crosses, α(0.8 eV): black dots).

Let us assume now that for low-energy proton irradiation, the dynamics of defect annealing can, similarly to the case of light-induced degradation and also to the case of high-energy proton irradiation, be described by a stretched exponential function. If once again, we assume that the dispersive parameter β is constant over the range of annealing temperatures used, the activation energy can be derived in a simple manner from the slope of the logarithmic plot as represented in Fig. 6.29.

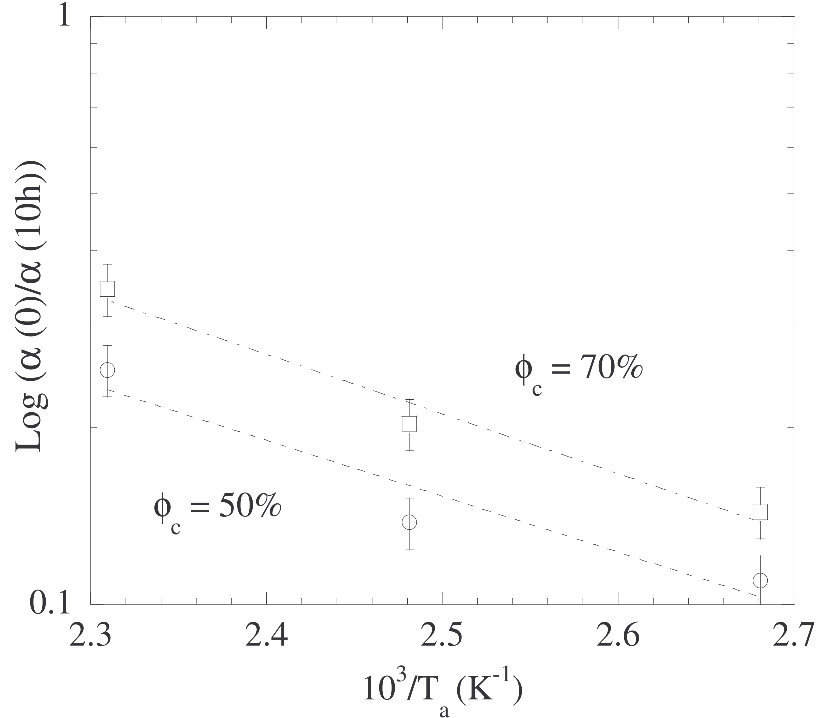

Figure 6.29. Logarithmic value of the ratio of the defect-related absorption after low-energy irradiation and after subsequent 10h annealing as a function of the reciprocal of the annealing temperature for two nip solar cells of different crystallinity. The dotted lines are fits to equ. (6.6).

By assuming once again that $\beta \sim 1$, which would be the case for non-dispersive diffusion, we obtain that the activation energy E_a for annealing low-energy proton-induced defects is equal to $E_a \sim 0.2$ eV, i.e. its value is very close to $E_a = 0.3$ eV, as measured when annealing the defects created by high-energy protons. In comparison, the activation energy for the annealing of light-induced defects in μc-Si:H is equal to 0.5 eV, as established in Chapter 5. For $\phi_c = 50\%$, we obtain for the annealing of defects induced by low-energy protons a characteristic time $\tau_0 \sim 1 \cdot 10^{-3}$ s, a value which is around 10 times shorter than the characteristic time assessed when annealing the defects induced by high-energy protons.

6.6.3 Model for low-energy proton defect creation and annealing in μc-Si:H

We observed that short-circuit current density is the parameter most affected by low-energy proton irradiation: it is observed that the external quantum efficiency is

reduced over the whole wavelength range, with the main reduction occurring in the long wavelength response. The short wavelength decrease is a consequence of the proton implantation at the p-i interface, while the long wavelength reduction represents an increase of the recombination centers in the bandgap. The decrease of external quantum efficiency is observed to be only partially reversible under the thermal annealing steps performed.

These observations, as well as the strong deterioration of the electrical parameters measured here confirms that the implantation of low-energy protons is much more destructive than exposure to protons with higher energies, as was indeed expected. We suggest that the defects created by low-energy protons may correspond to two distinct types of defects:

1. Ionization defects in the crystalline phase, leading to an increase of $\alpha(0.8 \text{ eV})$, reversible under the performed steps of thermal annealing; this type of defects represents the majority of the defects created when the solar cells are irradiated with high-energy protons. These defects lead to (a) an increased recombination in the i-layer, (b) a decrease of the collection voltage, and (c) a reduction of the collection efficiency for wavelength over 600 nm;

2. Displacement defects (damages to the lattice) created in the crystalline phase, also leading to an increase of $\alpha(0.8 \text{ eV})$, which are not reversible under the applied thermal annealing steps. Lattice damages due to proton implantation are created in the intrinsic layer, but also at the p-i and n-i interfaces of the solar cells. These defects lead to a decrease of the collection voltage of the intrinsic layer and also to a reduction of the shunt resistance of the solar cell. The collection efficiency is reduced over the whole spectrum. The non-reversible increase of the Urbach parameter observed confirms that the network's static disorder of the μc-Si:H i-layer is increased: these permanent atomic displacement defects affect bandtail states also.

6.7 Comparison of light-induced and proton-induced degradation in μc-Si:H solar cells

Let us now compare, in Table 6.1, the effect of light-soaking and high- and low-energy proton irradiation on (a) the defect-related absorption $\alpha(0.8 \text{ eV})$, (b) the Urbach parameter E_0, (c) the activation energy E_a for defect annealing, and (d) the proportionality factor $m = \Delta FF/\Delta\alpha(0.8 \text{ eV})$, as measured for the nip solar cell with ϕ_c = 50%. The last column of Table 6.1 indicates whether the degradation was reversible or not under the thermal annealing steps performed:

Type of degradation	α(0.8 eV)	E_0	E_a (eV)	τ_0 (ϕ_c = 50%) (s)	m (%)	Reversible
Light-soaking	↗	=	0.5	~10^{-1}	2.0	yes
High-energy p^+	↗	=	0.3	~10^{-2}	4.0	yes
Low-energy p^+	↗	↗	0.2	~10^{-3}	4.0	partially

Table 6.1. Table of comparison for the three types of degradation observed in our work: light-soaking (Chapter 5) as well as high- and low-energy proton irradiation and their effect on (a) the defect-related absorption α(0.8 eV), (b) the Urbach parameter E_0, (c) the activation energy E_a for defect annealing, (d) the proportionality factor m = $\Delta FF/\Delta\alpha$(0.8 eV) (± 0.5%), as measured for the nip solar cell with ϕ_c = 50%. The last column indicates the reversibility of the three types of degradation.

We, thus, observe that all three types of degradation lead to an increase of the defect-related absorption, which is assumed, in our work, to monitor the defect density in the crystalline phase. However, α(0.8 eV), as measured by Fourier-transform photocurrent spectroscopy (FTPS), is not an individual signature for one particular type of defects. Indeed, the sub-bandgap absorption coefficient spectrum is rather "flat" (see e.g. Fig. 5.13 in the previous Chapter) and no absorption line is observed, as in infrared spectroscopy for example. In fact, the absorption coefficient as measured by photocurrent spectroscopy is due to several optical transitions which all lead to photocurrent generation. The value of photon energy considered here (0.8 eV) is about 2/3 of the gap and therefore various electronic transitions can be involved, such as: (a) transitions between the conduction band and defects situated close to the valence band, (b) transitions from the valence band to defects close to the conduction band. The situation is, thus, a little different than in a-Si:H, where the defect-related absorption is measured closer to midgap at 1.2 eV.

The Urbach parameter is observed to remain constant when the µc-Si:H solar cells are light-soaked and irradiated with high-energy protons. On the other hand, when protons of lower energy are used, E_0 increases and never returns to its initial value: we attribute this increase to the creation of static disorder in the nanocrystals, such as related with the apparition of vacancies. Light-induced and high-energy induced defects can be fully thermally annealed; the activation energy

for both types of defects is observed to be rather low in μc-Si:H: $E_a = 0.5$ eV and 0.3 eV. For comparison, $E_a = 1$ eV for annealing light-induced defects in a-Si:H. Since we assumed that defect annealing is hydrogen mediated (see also § 5.10), we suggest that the high amount of hydrogen in μc-Si:H, as compared to a-Si:H, could justify the lower activation energy values measured.

The characteristic time τ for defect annealing was observed to depend on the crystallinity in the three types of degradation: in the case of light-induced degradation we explained this dependency in terms of diffusion. Here, τ_0 is observed to be lower for high- and low-energy proton-induced degradation than for light-induced degradation. We suggest that proton-induced defects, directly created in the crystalline phase, can be more rapidly annealed out than light-induced defects (created in the amorphous phase) because of the high amount of hydrogen present at the nanocrystals interface. This observation, as well as the values obtained for the activation energy, should be confirmed by additional kinetics measurements. Finally, we observed that the relative increase of defect density as induced by high- and low-energy proton irradiation more severely affects the fill factor than light-soaking. This could suggest that defects created inside the crystalline phase are more detrimental to the fill factor than passivation defects created at the nanocrystals surface. Nevertheless, further work should be carried out to ascertain this assumption.

6.8 Conclusions

Pin and nip microcrystalline silicon solar cells were shown to suffer from a strong degradation when exposed to low-energy protons which are implanted within the intrinsic layer. The damage as created by these implanted protons is shown to be only partially reversible under thermal annealing steps of 10h up to 180°C, contrary to light-induced defects. The implantation of low-energy protons within the intrinsic layer as well as at the p-i interface, causes a dramatic decrease of the solar cell short-circuit current density. This is then the electrical parameter of the devices which suffers the largest relative loss. We could demonstrate that the defects created within the i-layer adversely affect the fill factor, whereas both interface and bulk i-layer defects are responsible for the loss in short-circuit current density. From our observation of the partial recovery of the electrical parameters after thermal annealing, we suggest that at least two types of defect are created by low-energy protons. This could be a combination of displacement defects, resulting in an increased, permanent, static disorder within the material plus ionization defects, which would be fully thermally reversible. This suggests that low-energy protons create defects that act as recombination centers (deep defects) and increase static disorder (i.e. modify bandtail states energy distribution).

When the devices are exposed to protons of higher energy ($E > 1$MeV), the relative decrease of the electrical parameters of the solar cells is less

dramatic than in the case of low-energy proton irradiation. High-energy proton degradation of microcrystalline silicon solar cells results approximately in a relative degradation of the electrical parameter of the same order of magnitude as after light-soaking. This degradation is reversible under thermal annealing. Furthermore, in the case of 2 MeV protons, the fill factor is, in a similar manner as in the case of light-soaking, the parameter that shows the largest decrease. High-energy proton degradation is, thus, in some way, the reciprocal of the light-induced degradation, as a function of Raman crystallinity. Indeed, in the case of protons, the degradation is shown to be more pronounced for μc-Si:H with higher Raman i-layer crystallinity. We were, thus, able to "selectively" degrade the amorphous phase (and, subsequently, the surface of the nanocrystals) with photons, and the crystalline phase with high-energy protons. However, the exact microscopic nature of the defects is not known yet.

By using Fourier-transform photocurrent spectroscopy together with J(V) curves, we were able to evaluate the total defect density and to quantify its impact on the decrease of the fill factor. The measurement of the annealing kinetics of the defects revealed that, whatever their microscopic nature, the light-induced defects anneal out following a stretched exponential behavior. This observation suggest that annealing of light-induced defects in μc-Si:H solar cells is similar to that observed in a-Si:H. Consequently, we propose that dispersive diffusion of hydrogen is the fundamental microscopic mechanism that leads to the observed temperature-induced decrease of the total defect density under thermal annealing in μc-Si:H. However, a complete modeling of the H-diffusion process in the amorphous phase and in the nanocrystalline phase is not yet available.

From our experimental observations, we can conclude that:

- Light-soaking leads to the creation of defects in the amorphous phase; these defects somehow diffuse to the nanocrystals surface, where they deteriorate the passivation. Here, their density can be measured optically by Fourier-Transform photocurrent spectroscopy and it is observed that $\Delta\alpha$(0.8 eV) decreases with the ratio of the amorphous volume over the crystalline volume of the intrinsic layer. Light-soaking leads to an increased recombination within the intrinsic layer, which is responsible for the predominant degradation of the FF among the electrical parameters of the device. The kinetics of defects creation and annealing is fitted by a stretched exponential with a dispersive parameter $\beta < 1$ and an activation every E_a for annealing the defects that is lower than in a-Si:H. The light-induced defects are fully reversible under thermal annealing;
- High-energy proton irradiation leads to the creation of defects within the crystalline phase: their relative density increases proportionally to the material's crystalline volume fraction. Here again, it is the fill factor which is the electrical parameter showing the more pronounced degradation. The relative decrease in

FF can be fully attributed to the increased recombination within the intrinsic layer, as monitored by the defect-related absorption. From our observations, high-energy proton-induced defects are more detrimental to the fill-factor than light-induced defects. Here again, the annealing of high-energy proton-induced defects is thermally activated and the degradation totally reversible.

- Low-energy proton irradiation leads to the creation of lattice damages that affect the device permanently. Low-energy protons are implanted within the intrinsic layer of the μc-Si:H solar cells, with the p-i and i-n interfaces being also damaged. An increase of the optical Urbach parameter is observed that can be attributed to an increased static disorder in the material. We suggest that the observed dramatic decrease of the short-circuit current density is due to the increased recombination within the i-layer but as well to the damaged interfaces. One can even imagine that implanted hydrogen may lead to a modified carriers transport path within the material. Localized defects such as dangling bonds, which are predominantly caused by ionization damage in c-Si, are also created by low-energy protons in a similar manner as for high-energy protons. Contrary to lattice damages, they are reversible under thermal annealing.

In order to gain further insights into the exact microscopic nature of the various types of high- and low-energy proton-induced defects, defect annealing kinetics should be investigated in more details. Also, in a similar way as for light-soaking defects in μc-Si:H solar cells, Electron Spin Resonance (ESR) measurements should also be performed to identify more precisely the type of defects created by proton irradiation.

7. Final Conclusions

This thesis work was focused on microcrystalline silicon (μc-Si:H) solar cells and the characterization of the material's electro-optical properties within a complete device. Such characterization results in supplementary difficulties as compared with material's characterization in layers. Nevertheless, this approach was motivated by the fact that the physical-chemical nature of the underlying layers on the nucleation and microcrystalline growth of the intrinsic layer renders the comparison between "simple" layers and complete devices rather unreliable.

In this work, we first presented a simple model for the calculation of the upper limits of the electrical parameters of μc-Si:H pin junction solar cells. Thereafter, diagnostic tools of problematic cells (i.e. cells presenting low fill factor values) were introduced, that allowed to distinguish between the effect of non-optimal individual solar cell structuration and the effect of non-optimal electro-optical parameters. Finally, the detailed study of the stability of μc-Si:H solar cells under three different sources of degradation (namely light-soaking, high- and low-energy proton irradiation) allowed us to distinguish the effect of the degradation of amorphous and crystalline phases on the solar cells' properties.

First, we calculated the upper limits for the electrical parameters (J_{sc}, V_{oc}, FF, η) of single-junction solar cells, as a function of the material's bandgap energy. Three different models were considered for the calculation of these limits: two based on the pn junction theory fostered by experimental observations, and one more simple but original model, established for pin junctions. We showed that the largest gains still to be achieved regarding the conversion efficiency of present μc-Si:H solar cells should be made on the short-circuit current density. The upper limits for the conversion efficiency of tandem (double-junction) solar cells were also calculated as a function of the two materials' bandgap combination: we demonstrated that the "micromorph" (a-Si:H/μc-Si:H) tandem solar cell indeed represents an optimum combination of materials, validating the research carried out on this topic at the University of Neuchâtel since 1994.

Then J(V) measurements carried out at variable illumination (i.e. the VIM technique) allowed us to efficiently separate the effects of an increase of recombination (i.e. a decrease of the active material's "quality"), a low shunt resistance and a high series resistance, on the reduction of the fill factor with respect to an ideal (theoretical) FF value. A photogenerated carriers "collection" model, originally developed for a-Si:H solar cells was, thus, adapted to μc-Si:H solar cells, and the relationships established for the fill factor losses confirmed by actual measurements on various solar cells (dilution series, gas series and individual solar cells). We more particularly showed that the large majority of the pin and nip solar cells presented in this work were suffering from low collection

voltage values, probably due to diverse types of contamination. Indeed, contamination results in an increased recombination and/or electric field deformation. In addition, VIM measurements and assessment of $\mu^0\tau^0$-products confirmed that the p-i and n-i interfaces of μc-Si:H solar cells are very defective.

The stability of μc-Si:H solar cells under light-soaking was then studied in detail: we showed that μc-Si:H solar cells degrade in a "softer" and slower way, as compared to a-Si:H solar cells. Nevertheless, like in a-Si:H, the degradation is completely reversible under thermal annealing. We demonstrated that light-induced degradation of the electrical properties of the solar cells is consequent to an increase of defect density in the intrinsic layer. This is revealed by an increase of defect-related absorption α(0.8 eV), as well as a reduction of the collection voltage of the device. The amplitude of the light-induced degradation is a function of the crystalline volume fraction of the intrinsic layer, monitored by the Raman crystallinity factor ϕ_c. More precisely, we showed that the light-induced relative increase of defect-related absorption is a function of the ratio of the amorphous volume over the crystalline volume of the intrinsic layer. The fill factor was the electrical parameter presenting the largest light-induced decrease. We showed that the absolute loss of fill factor could be well quantified by the reduction in the collection voltage and by the increase of defect density in the i-layer of the solar cell. From the measured kinetics of defect creation and annealing, we suggest that light-induced defects, first created in the amorphous phase, diffuse dispersively to the nanocrystals' surface, where they deteriorate the passivation and consequently the electrical transport properties.

When irradiated with protons, we showed that μc-Si:H solar cells degrade and recover differently depending on the energy of the incident proton beam. In the case of high-energy protons, the degradation is completely reversible under thermal annealing, whereas with low-energy proton irradiation, permanent damage is created. In the latter case, the low-energy protons (H^+) are implanted within the intrinsic layer, instead of merely crossing it. The amplitude of the degradation is observed, in a similar manner to light-induced degradation, to depend on the crystallinity of the photoactive layer of the device. But, in the case of proton irradiation, the solar cells with the highest crystallinity are those showing the largest degradation. More precisely, we showed that the relative increase of defect - related absorption, as induced by high- and low-energy protons, is proportional to the crystalline volume fraction.

In this work we presented, for the fist time, a systematic application of Fourier-Transform Photocurrent Spectroscopy (FTPS) to the study of different types of defects in μc-Si:H. We showed that FTPS and the absorption coefficent at 0.8 eV could be used to quantify the density of recombination centers in complete μc-Si:H solar cells. However, we were unable to establish the exact microscopic nature of

the defects, as induced by the three different degradation mechanisms studied here. Indeed, α(0.8 eV) is not a defect-related signature, its value only gives information on the defect density in the intrinsic layer (more particularly, under our assumptions, α(0.8 eV) is proportional to the defects density in the crystalline phase. Since various optical transitions contribute to the absorption at 0.8 eV, the exact energy level of the recombination centers within the gap cannot be established. Thus, in order, to identify the exact nature of the defects created when the μc-Si:H solar cells are light-soaked or irradiated with protons, Electron Spin Resonance (ESR) measurements should be performed. Indeed, this characterization technique gives a characteristic value (the g value) that is unique for each defect.

References

[1] D.M. Chapin et al., J. Appl. Phys. 25 (1954), 676

[2] S. Veprek et al., Sol. State Comm. 11 (1968), 683

[3] J. Meier et al., Appl. Phys. Letters 65 (7) (1994), 860

[4] E. Vallat-Sauvain et al., J. Appl. Phys. 87 (2000), 3137

[5] J. Bailat et al, J. Appl. Phys. 93 2003, 5727

[6] U. Kroll et al., J. of Non-Cryst. Solids 227-230 (1998), 68

[7] S. Klein et al., Thin Solid Films 430/1-2 (2003), 202

[8] J. Hüpkes et al. Thin Solid Films 502 (2006), 286

[9] J. Bailat et al., to be published in the Proc. of the 4th WCEPC, Hawaï (2006)

[10] S. Faÿ et al., Ph.D. thesis, University of Neuchâtel (2003)

[11] J. Bailat et al, Ph.D. thesis, University of Neuchâtel (2004)

[12] A. Shah et al., Solar Energy Mat. & Sol. Cells 78 (2003), 469

[13] D. L. Staebler and C. R. Wronski, Appl. Phys. Lett. 31/4 (1977), 292

[14] J. Meier et al., Proc. of the 3rd WCPEC, Osaka (2003), 2801

[15] See e.g. "Photovoltaics: Energy for the New Millenium, The National Photovoltaics Program Plan, 2000-2004", DOE/GO-10099-940 (January 2004).

[16] K. Yamamoto et al., to be published in the Proc. of the 21st EU PVSEC, Dresden (2006)

[17] U. Kroll et al., J. Appl. Phys. 80 (1996), 4971

[18] C. Droz et al., Ph.D. thesis, University of Neuchâtel (2003)

[19] M. Vanecek, Journ. of Non-Cryst. Solids 266-269 (2000), 519

[20] U. Graf, Ph. D. thesis, University of Neuchâtel (2005)

[21] E. Vallat-Sauvain, Proc. of the 21st ICANS, Lisbon (2005) to be published in Journ. of Non-Cryst. Solids

[22] A. C. Boccara et al., Appl. Phys. Letters 36 (1980), 130

[23] M. Vanecek et al., Solid State Comm. 39 (1981), 1199

[24] N. Wyrsch, Ph.D. thesis, University of Neuchâtel (1992)

[25] J. D. Cody, Journ. of Non-Cryst. Solids 141 (1992), 3

[26] M. Vanecek et al., Appl. Phys. Letters 80 (2002), 719

[27] J. Bailat et al, Proc. of the 19th EU PVSEC, Paris (2004), 1541

[28] W. Shockley and H. J. Queisser, J. of Appl. Phys. 32 (3) (1961), 510

[29] A. Shah, Matériaux Electroniques Amorphes, Vol. 1&2, 3rd Edition, Neuchâtel (1995)

[30] M. Sze, Physics of Semiconductor Devices, 2nd Edition, Wiley, New Dehli (1983)

[31] C. Miazza, Ph.D thesis, University of Neuchâtel (2006)

[32] M. Illegems, Dispositifs à Semiconducteur, Part. 1&2, EPFL (1993)

[33] M.A. Green, Solar Cells, Prentice Hall (1982)

[34] H. Kiess and W. Rehwald, Sol. Energy Mat, & Sol. Cells 38, 1995, 45

[35] K. H. Böhm et al., Z. Astrophysik 43, 1957, 95

[36] A. Luque et S. Hegedus, “Handbook of Photovoltaic Science and Engineering”, John Wiley & Sons Ltd (2003)

[37] M. B. Prince, J. of Appl. Phys 26 (1955), 534

[38] J. J. Loferski, J. of Appl. Phys 27 (1956), 777

[39] J. Steinhauser et al., Proc. of the 20th EU PVSEC, Barcelona (2005), 1608

[40] D. Dominé et al, to be published in the Proc. of the 4th WCPEC, Hawaï (2006)

[41] J. Merten et al., IEEE Trans. on Elec. Devices 45 (2) (1998) 423

[42] W. Kusian et al., Proc. of the 9th ECPSEC (1989), 52

[43] S. Tchakarov et al., J. Appl. Phys. 94 (11) (2003), 7317

[44] R. A. Street, “Hydrogenated Amorphous Silicon”, Cambridge University Press (1991)

[45] A. Luque, A. Marti, Phys. Rev. Letters 78 (1997), 5014

[46] T. J. Coutts, Proc. of the 12th Int. PVSEC, Jeju, Korea (2001), 277

[47] J. Deng et al., Appl. Phys. Letters 82 (2003), 3023

[48] B. Ross et al., to be published in the Proc. of the 4th WCPEC, Hawaï (2006)

[49] J. Merten, Ph.D thesis, Universitat de Barcelona, Spain (1996)

[50] C. Hof, Ph.D. thesis, University of Neuchâtel, Switzerland (1999)

[51] J. Hubin et al, Phil. Mag B 72 (6) (1995), 589

[52] R. S. Crandall, J. of Appl. Phys 54 (12) (1983), 7176

[53] F. Meillaud et al., to be publ. in the Proc. of the 4th WCPEC, Hawaï (2006)

[54] N. Beck et al., J. of Appl. Phys. 79 (1996), 9361
[55] H. Schade, seminar given at the Institute of Microtechnology, Neuchâtel (2006)
[56] A. Shah et al, Thin Solid Films 502 (1-2) (2006), 292
[57] H. Matsuura et al., J. Appl. Phys 58 (1985), 1578
[58] J. M. Pearce et al., Proc of the 29th IEEE PVSC, New York, USA (2002), 1098
[59] B. Rech, Ph.D. thesis, Forschungszentrum Jülich (1997)
[60] J. Deng et al, Proc. of the MRS Symp., Vol. 808, A8.8.1 (2004)
[61] J. Deng et al., Proc. of the MRS Symp., Vol. 862, A11.4.1 (2004)
[62] J. Deng and C.R. Wronski, Journ. of Appl. Phys. 98 (2005), 024509
[63] S. Klein et al., Proc. of the 19th EUPVSEC, Paris (2004), 1579
[64] R. S. Crandall, Semiconductors and Semimetals B 21 (1984), 245
[65] M. Goerlitzer et al, J. of Appl. Phys.80 (9) (1996), 5111
[66] M. Goerlitzer et al, Ph.D. thesis, University of Neuchâtel (1998)
[67] J. Kocka et al., Journ. of Non-Cryst. Solids 299-302 (2002), 355
[68] W. B. Jackson et al., Appl. Phys. Letters 42 (1983), 105
[69] H. Curtins and M. Favre, Advances in Disordered Semiconductors, Vol. 1, World Scientific publishing company, Singapore, editor H. Fritzsche (1988), 329
[70] M. Favre, Ph.D. thesis, University of Neuchâtel (1993)
[71] T. Roschek et al., Thin Solid Films 451-452 (2004), 466
[72] K. Morigaki et al., Solid State Comm. 33 (1980), 851
[73] N. M.Amer et al., Physica 117B & 118 B (1983), 897
[74] V. Terrazzoni-Daudrix, Ph.D. thesis, University of Neuchâtel (2004)
[75] J. Kuendig et al., Sol. Energy Mat. & Sol. Cells 79 (2003), 425
[76] G. Yue et al., Journ. of Appl. Phys. 98 (2005), 074902
[77] H. Branz, Solid State Comm. 105 (6) (1998), 387
[78] R. Flückiger et al., J. Appl. Phys. 77 (1995), 712
[79] H. Liu et al., Sol. State Comm. 58 (1986), 601
[80] B. Yan et al., Appl. Phys. Letters 85 (11) (2004), 1925
[81] I. Hirabayashi et al., Jpn. Journ. Appl. Phys. 19 (1980), L 357

[82] J. I. Pankove et al., Appl. Phys. Letters 37 (1980), 705

[83] M. Stutzmann et al., Phys. Rev. B 32 (1) (1985), 23

[84] C. Wronski et al., to be published in the Proc. of the 4th WCPEC, Hawaï (2006)

[85] D. Redfield and R. H. Bube, Appl. Phys. Letters 54 (11) (1989), 1037

[86] W. B. Jackson and J. Kakalios, Phys Rev B 37 (2) (1988), 1020

[87] K. Morigaki and F. Yonezawa, Journ. of Non-Cryst. Solids 164-166 (1993), 215

[88] F. Meillaud et al., Proc. of the 31st IEEE PVSC, Orlando, USA (2005), 1412

[89] F. Meillaud et al., Proc. of the 20th EUPVSEC, Barcelona, Spain (2005), 1509

[90] B. Yan et al., Appl. Phys. Letters 85 (11) (2004), 1955

[91] H. Keppner et al., Solar En. Mat. & Solar Cells 34 (1994), 201

[92] A. Laades et al., Proc of the 19th EUPVSEC, Paris (2004), 1170

[93] A. L. Baia Neto et al., Journ. of Non-Cryst. Solids 299-302 (2002), 274

[94] N. Hata et al., Journ. of Non-Cryst. Solids 164-166 (1993), 231

[95] J. Kuendig et al, Solar Energy Mat. & Sol. Cells 79 (2003), 425

[96] J. Kuendig, Ph.D. thesis, Swiss Federal Institute of Technology (EPFL) (2003)

[97] S. Guha et al., Proc. of the 2nd WCPEC (1998), 3609

[98] R. Schwarz et al., Proc. of the 18th IEEE PVSEC (1985), 903

[99] C. E. Byvick et al., Proc of the 17th IEEE PVSEC (1984), 155

[100] M. Yamaguchi, Solar Energy Mat. & Sol. Cells 68 (2001), 31

[101] N. Wyrsch et al, Proc. of the MRS Symp. Vol 862 (2005), A15-4

[102] http:/www.srim.org

[103] F. Meillaud et al., Journ. of Non-Cryst. Solids 352 (2006), 1851

[104] H. Tada et al., Solar Cell Radiation Handbook, 3rd Ed., JPL Publ. (1982)

[105] N. Kishimoto et al., J. Nucl. Mater 258-263 (1998), 1908

Acknowledgements

First, I would like to thank Pr. A. Shah for giving me the chance to carry out this thesis work in the Thin-film silicon group. I greatly appreciated his encouragement and very constructive advices concerning my work, as well as the discussions we had about other topics than thin-film silicon solar cells. Also, thank you to Pr. C. Ballif for the very interesting discussions we had and for supporting my work.

I wish to thank my referees Pr. M. Lux-Steiner and Pr. A Tiwari for joining the examination board and for the time devoted to critically reading and correcting this thesis. Special thanks go to Dr. M. Vanecek for his comments and for welcoming me for two weeks in his research group at the Czech Academy of Sciences in Prague. Also, I warmly thank Dr. H. Schade for kindly accepting to comment the Chapters 3 and 4.

Very special thanks go to my project leader Dr. E. Vallat-Sauvain for her availability, enthusiasm, and very warm support during the years spent in the Thin-film silicon group. Thank you very much for the extra time spent to read and comment my thesis chapters.

Of course, I would like to thank all my colleagues at the Institute, in particular X. Niquille, D. Dominé, J. Bailat et M. Dubey who always accepted to deposit the μc-Si:H solar cells I needed. I also acknowledge C. Droz, J. Steinhauser, S. Olibet, C. Miazza, F. Freitas, R. Schluechter, J. Guillet and N. Wyrsch, for their very interesting and useful advices on technology and characterization. Thanks to S. Rosset, L. Fesquet and M. Python for helping me to develop experimental set-ups which were necessary for my work. I also wish to thank S. Faÿ, C. Buecher, V. Terrazzoni-Daudrix, U. Graf, L. Feitknecht, C. Denizot and M. Nagel for the very nice time spent together at lunch time, talking about everything except thin-film solar cells! Warm thanks go to G. Choong and F. Jeanneret for the good atmosphere in our office; to the "administrative" team: B. Khan, J. Benjac, S. Piffaretti and M. Racine for always being in a good mood; to H. Laaroussi for helping me solve all the computer problems I had (also in a good mood!). And…thanks to anybody I unfortunately forgot at the Institute or somewhere else.

I wish to thank Y. Gonin and F. Munnik for the proton irradiation performed at the CAFI (Centre d'Analyse par Faisceau Ionique), Le Locle, Switzerland.

Finally I would like to thank my family, and more particularly my parents, for their constant support during all my studies from the age of 5 to 28! Very warm thanks go to my husband Frederic for his kindness, positivism and support. And, thank you Sam for the time spent together playing and walking in the vineyard.

Annexe 1

Light-soaking study of two dilution series deposited on LPCVD-ZnO

Samples

Two dilution series of μc-Si:H cells were deposited by very-high frequency PECVD in both pin and nip configurations on transparent conducting oxide (TCO) layers on AF-45 glass substrates. The TCO layers on both sides of the pin or nip structures were 2.4 μm thick ZnO layers deposited by low pressure chemical vapor deposition (LPCVD). The deposition parameters of the doped layers were kept constant within a series. The only parameter varied was silane concentration used for the deposition of the intrinsic layer with crystallinity comprised between 10% and 81% for the pin and 22% and 62% for the nip series. The pin and nip series were deposited in two different systems, a single and a double chamber system respectively. The pin dilution series was observed to suffer a stronger light-induced degradation than the nip series; we attribute this difference to a probable contamination of the pin series (by dopants) during its deposition in the single-chamber system.

Characterization techniques

The characterization techniques employed are identical to those that were already introduced:

- Open-circuit voltage (V_{oc}) and fill factor (FF) were obtained from J(V) measurements under the AM 1.5 sun simulator at 25°C, whereas short-circuit current density (J_{sc}) was obtained from the integration of the external quantum efficiency measurement;
- The Fourier transform photocurrent spectroscopy (FTPS) technique was used to measure sub-bandgap absorption spectra of the intrinsic layers as incorporated within the solar cells;
- Micro-Raman spectroscopy was performed with a HeNe laser excitation beam (633 nm) to evaluate the average crystallinity factor of the intrinsic layer. It must be mentioned here that the Raman crystallinity factors of the solar cells do not vary with light-soaking; the degradation observed is, thus, not due to modifications of the microstructure.

Light-soaking and annealing conditions

Both series were light-soaked at open-circuit for 1000 hours at a temperature of 50°C, under an AM 1.5-like spectrum (100 mW/cm^2). They were then annealed, under nitrogen flow, for 10 hours at increasing temperatures: 70°C, 100°C, 130°C, 160°C and 180°C.

FTPS spectra of pin and nip cells

FTPS spectra of initial and degraded states of two pin cells, one with a crystallinity of 10% and the other one of 81% are presented in Fig. A.1 (a) and (b) resp. We observe that defect-related absorption varies very differently according to crystallinity: for the cell with $\phi_c = 10\%$ the defect-related absorption is increased by a factor more than 10 between initial and degraded state, whereas for cell with $\phi_c = 81\%$ it is only increased by a factor 2:

(a)

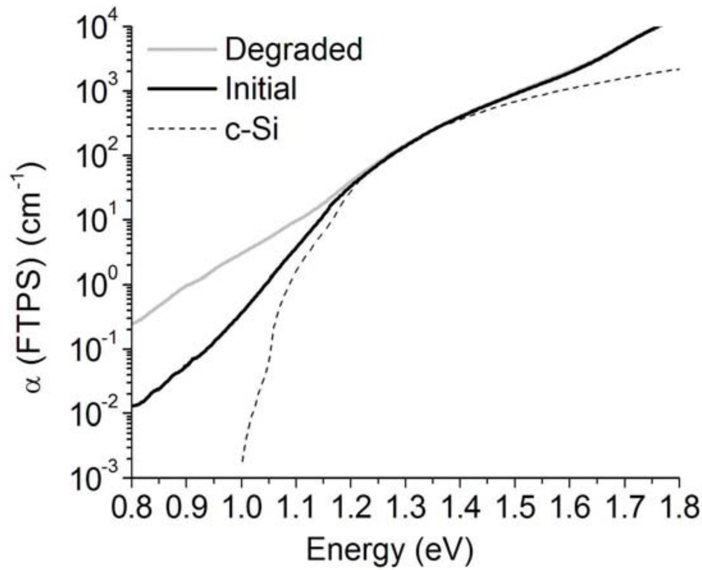

(b)

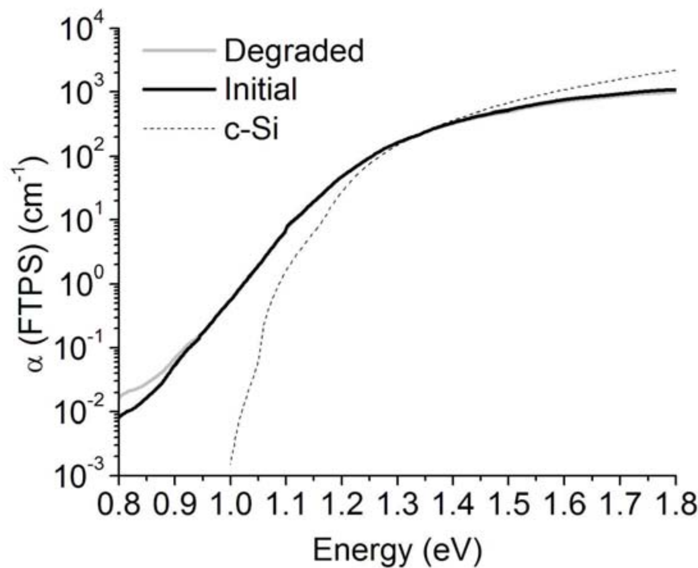

Figure A.1. Degraded and initial state FTPS spectra for pin cell with (a) $\phi_c = 10\%$, (b) $\phi_c = 81\%$.

The effects of annealing steps on the FTPS spectra can be seen in Fig. A.2 for the pin cell with $\phi_c = 10$ %. There is almost no variation of the FTPS spectra until the annealing at 130°C, but then there is a total recovery either after 160°C or 180°C.

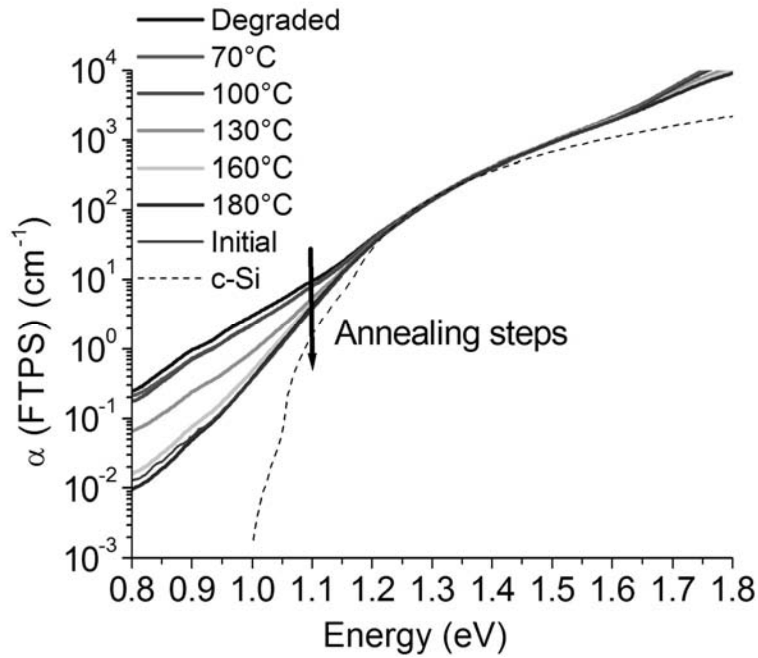

Figure A.2. FTPS spectra of the pin cell with $\phi_c = 10\%$ in initial and degraded state, as well as after each annealing.

Normalized defect-related absorption, defined as $\alpha(0.8\ eV)/\alpha(0.8\ eV)_{inital}$ is shown in Figure A. 3 (a) and (b) for the pin, respectively the nip dilution series as a function of annealing steps. One observes that pin and nip series present similar trends with a total recovery after 160°C or 180°C annealing.

(a)

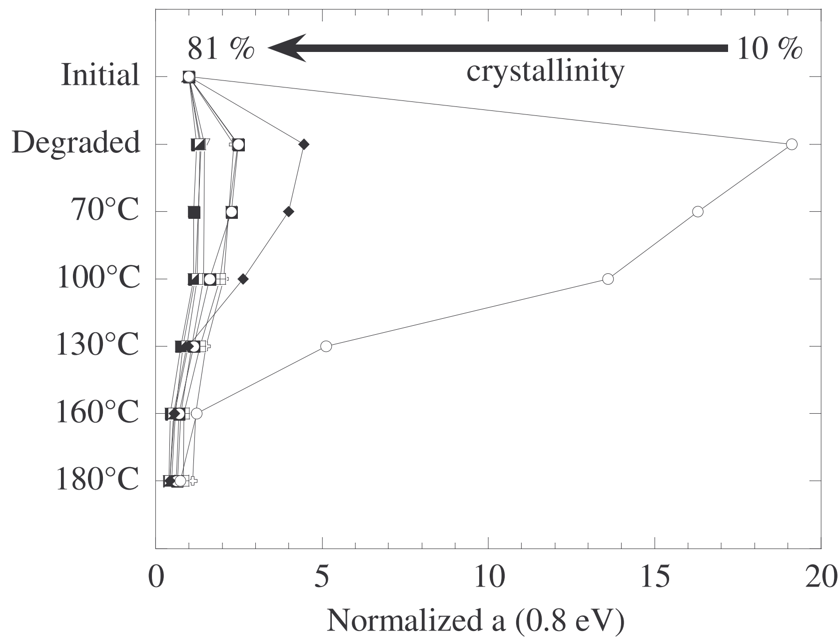

(b)

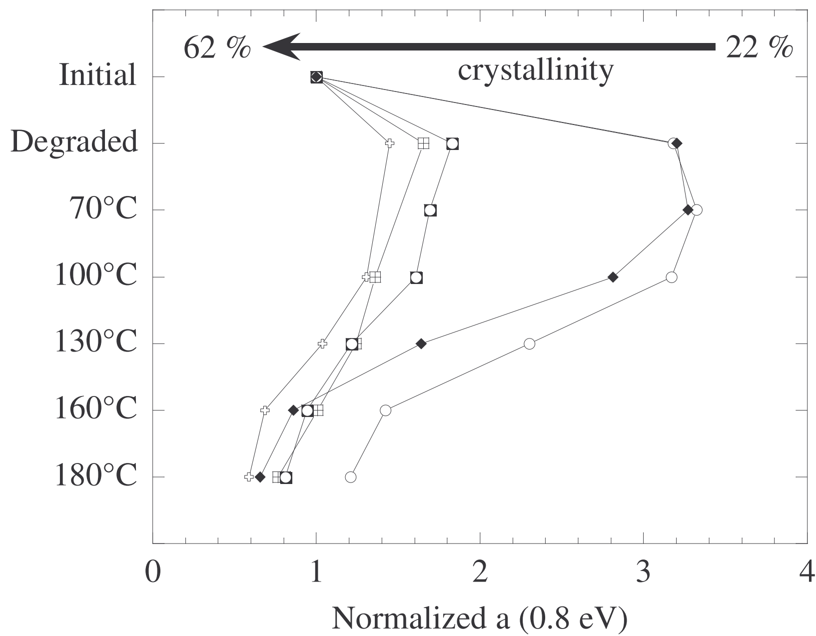

Fig. A.3. Normalized defect-related absorption as a function of annealing steps for the (a) pin dilution series, (b) nip dilution series

In Figs. A.4 (a) and (b), the relationship between defect-related absorption and crystallinity is presented for pin and nip series respectively. Again, nip and pin series present very similar trends and it appears that highly μc-Si:H cells present very small variations of α (0.8 eV). This observation is in agreement with those reported previously in this thesis on the two other dilution series. Defect-related

absorption is shown to be minimum for pin as well as for nip cells with medium crystallinity ($\phi_c \sim 50\%$) , for initial but also degraded state. It means that even if the defect density of these "best cells" increases with light-soaking its value is still lower than that of highly microcrystalline cells.

(a)

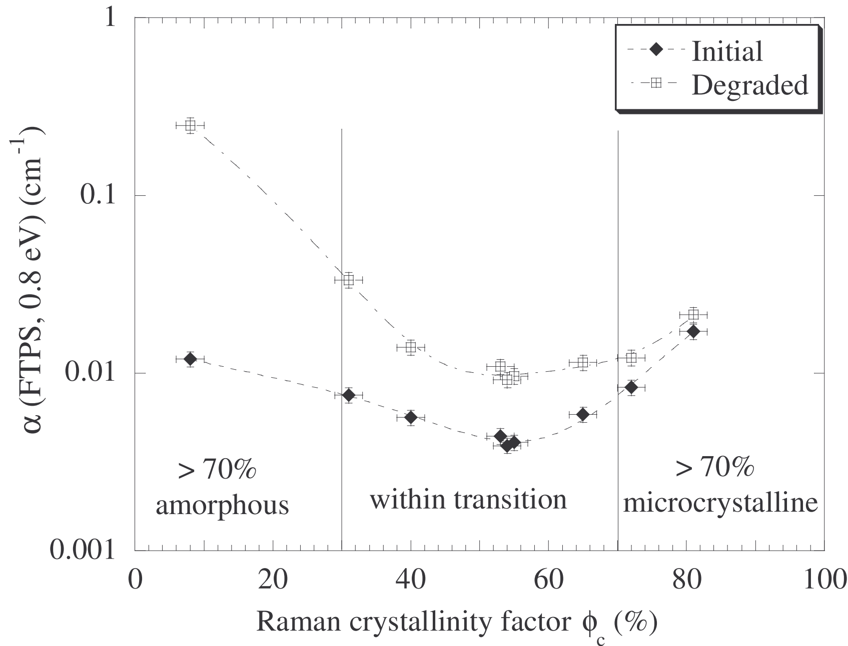

(b)

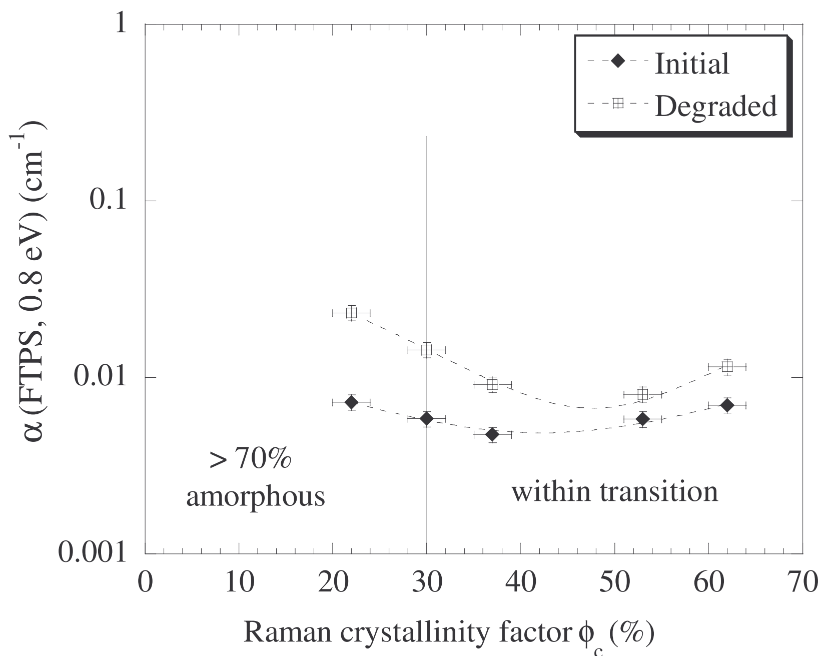

Figure A.4. Defect-related absorption in initial and degraded state as a function of i-layer Raman crystallinity factor for the (a) pin dilution series, (b) nip dilution series

Electrical parameters

The effect of light-soaking and annealing steps on the solar cell normalized efficiency (ratio of $\eta/\eta_{initial}$) is presented in Figs. A.5 (a) and (b). The pin cell with ϕ_c = 10 % shows an efficiency reduction of 47 %, while the efficiency of the nip cell with ϕ_c = 22 % decreases by 25 %. We observe that the dynamics of efficiency recovery is quite similar to that of the defect-related absorption: total recovery appears after annealings at 160°C or 180°C. Some cells even show higher efficiencies after the last annealing than they initially had.

(a)

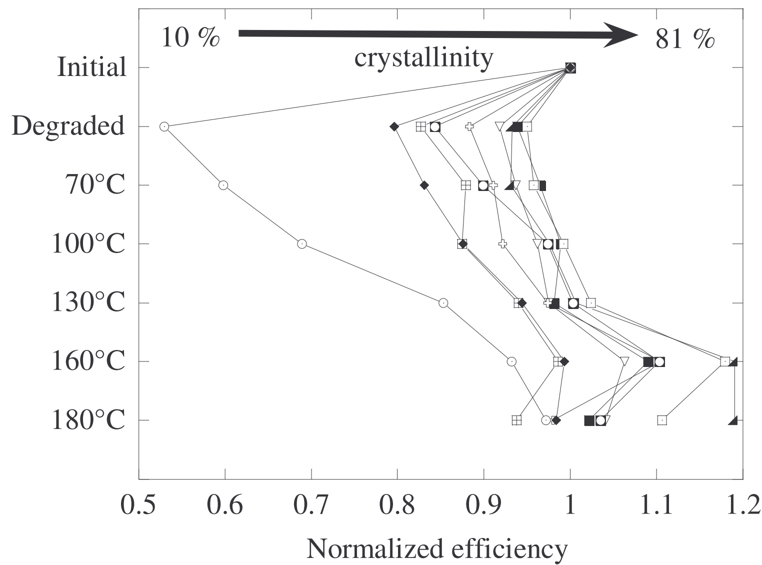

(b)

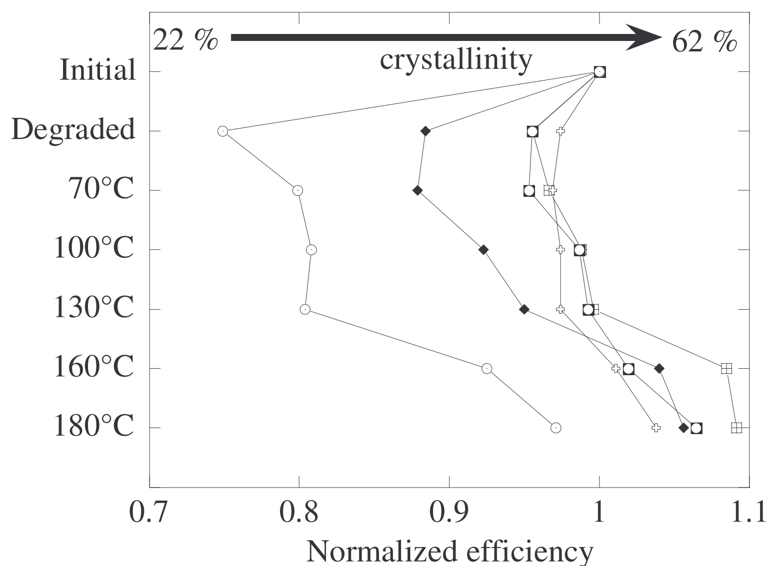

Figure A.5. Normalized efficiency as a function of subsequent annealings for the (a) pin dilution series, (b) nip dilution series

The effect of light soaking and annealing step at 180°C on open-circuit voltage V_{oc}, short-circuit current density J_{sc} and fill factor FF is presented in Figs. 6.A (a) for the mainly amorphous pin cell (ϕ_c = 10 %), as well as (b) for the mainly amorphous nip cell (ϕ_c = 22 %). V_{oc} is observed to be stable under light soaking for both cells, while FF and J_{sc} are affected. This trend can be extended to all pin and nip cells, but FF and J_{sc} are sensitive in a different manner depending on the cell configuration, as shown in Figs A.7 and A.8.

(a)

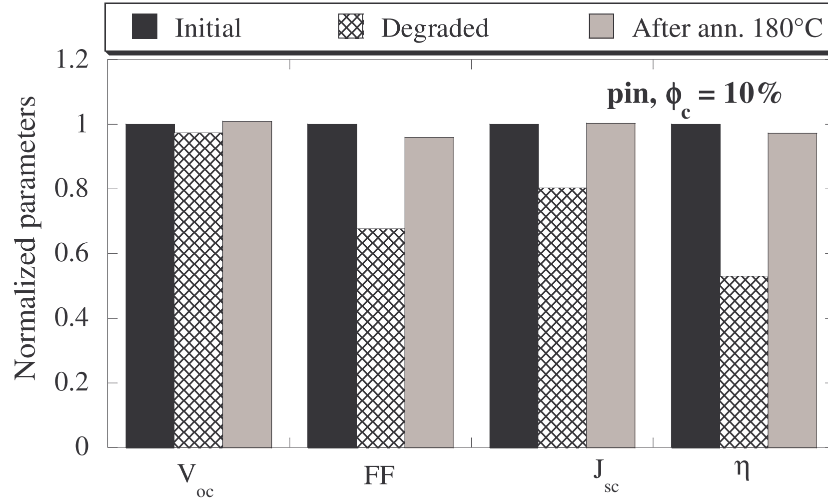

(b)

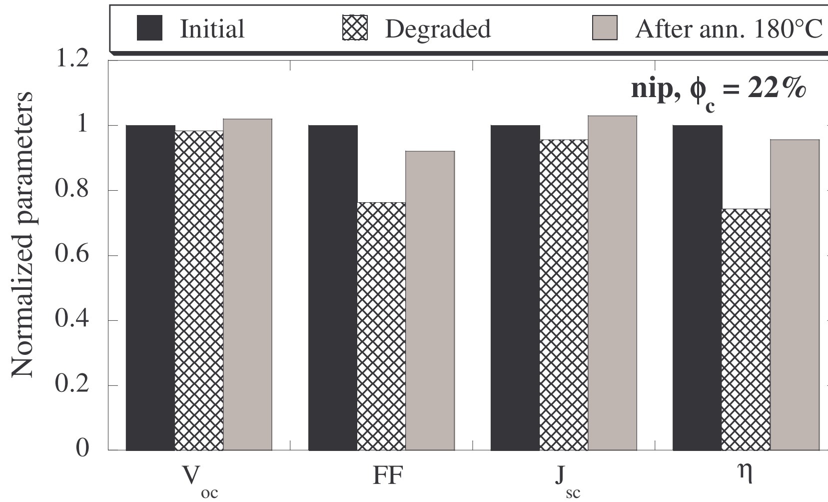

Figure A.6. V_{oc}, FF, J_{sc} and η in the initial and degraded states and after the annealing at 180°C for the mainly amorphous (a) pin cell, (b) nip cell.

Fig. A.7 presents the relative fill factor losses defined as:

$$\Delta FF = \left(FF_{init} - FF_{deg}\right)/FF_{init} \quad (A.1)$$

as a function of the Raman crystallinity factors of the cells for both series. ΔFF

decreases with crystallinity: variations of FF < 5% are observed for the cells with a Raman crystallinity factor > 30%. These small variations are accompanied by an increase of a factor 2 to 4 of defect-related absorption

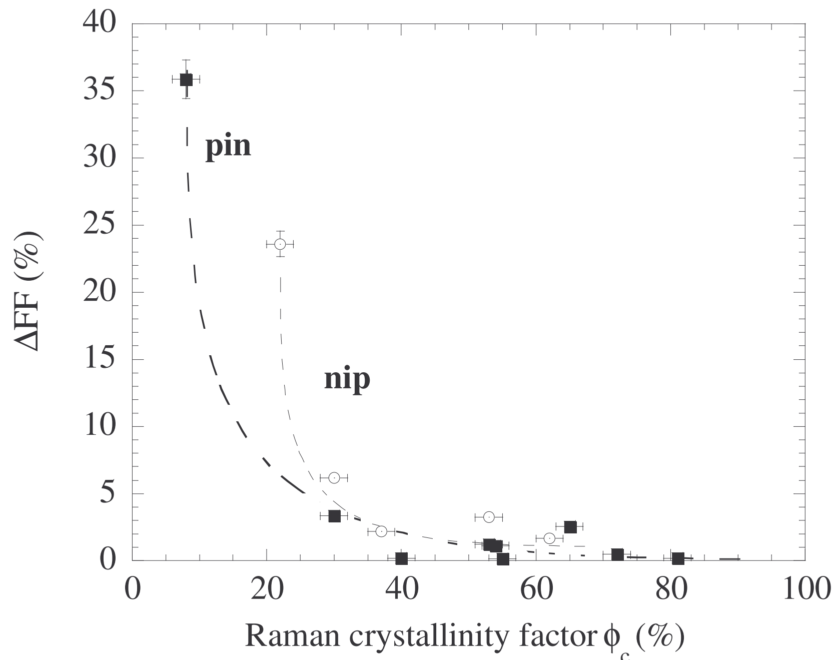

Figure A.7. Relative light-induced loss of FF as a function of i-layer Raman crystallinity factor for both dilution series of cells

The relationship between ΔJ_{sc}, defined similarly to ΔFF, and the crystallinity of the cells is presented in Fig. A.8 for both series:

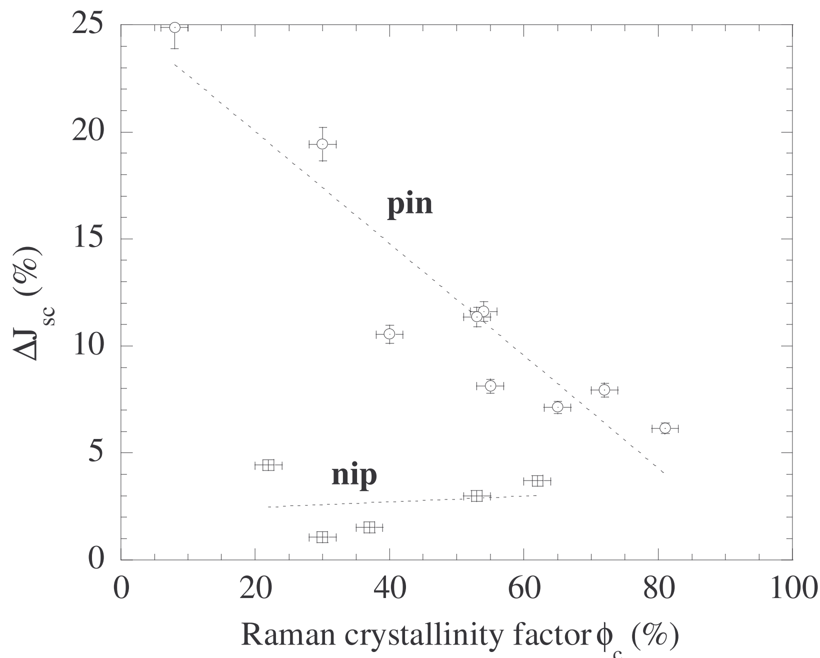

Figure A.8. Relative light-induced loss of J_{sc} as a function of i-layer Raman crystallinity factor for both dilution series of cells.

It appears that the nip cells are more stable, with $\Delta J_{sc} < 5\%$. The larger degradation of both the short-circuit current density and the fill factor of the pin cells, as compared to the nip cells, is attributed to a contamination of the intrinsic layer during the deposition in a single chamber. Indeed, a contamination by dopants (boron) could lead to a reduction in the electric field within the intrinsic layer and, thus, to a reduction of the collection voltage. The relative decrease of the electrical parameters, as well as the increase of defect-related absorption α(0.8 eV) measured on the present nip series, are of comparable order of magnitude as the results presented on the nip series of Chapter 5. We, thus, suggest that contamination (by boron and probably also by oxygen, as mentioned in chapter 5) both affect the stability of μc-Si:H and, maybe, increase the light-induced degradation in μc-Si:H solar cells.